DISSERTATION

SUBMITTED TO THE

COMBINED FACULTIES FOR THE NATURAL SCIENCES AND MATHEMATICS

OF THE RUPERTO-CAROLA UNIVERSITY OF HEIDELBERG, GERMANY

FOR THE DEGREE OF

DOCTOR OF NATURAL SCIENCES

Put forward by

M.Sc. Vincent Lami

Born in Komárno (Slovak Republic)

Oral examination: 16.10.2019

VISUALISING THE VERTICAL ENERGETIC LANDSCAPE IN ORGANIC PHOTOVOLTAICS

Referees: **Prof. Dr. Yana Vaynzof**

Prof. Dr. Annemarie Pucci

Visualisierung der vertikalen Energielandschaft in organischer Photovoltaik

Das Ziel dieser Doktorarbeit ist das Erlangen eines besseren Verständnisses der Energieniveaus in organischen, mehrlagigen Bauelementen. Der erste Teil dieser Arbeit beschäftigt sich mit einer neuen Klasse von nicht-fullerenen Akzeptoren in organischen Solarzellen, den sogenannten *N*-Heteroazenen. Eine gezielte Variation der Seitenketten erlaubt eine Verdreifachung der Effizienz, teilweise durch eine verbesserte Oberflächenbeschaffenheit der Schichten. Messungen mit transienter Absorptionsspektroskopie zeigen eine ungewöhnliche, vom elektrischen Feld abhängige Ladungsseparation im Gegensatz zu gewöhnlichen Fulleren-Akzeptoren. Im zweiten Teil dieser Arbeit wird die Entwicklung einer neuartigen Methode dargestellt, welche es ermöglicht die Anpassung der Energieniveaus zu untersuchen. Hierfür wird ultraviolette Photoemissionsspektroskopie mit einem essenziell schadenfreiem Ätzen mittels Argon Cluster-Atomen kombiniert. Wir zeigen die Effektivität unserer Methode für mehrere hochmoderne, leistungsfähige Photovoltaik-Systeme und demonstrieren, dass deren geschätzte photovoltaische Bandlücken hervorragend sowohl mit der Energie der Charge-Transfer-Komplexen übereinstimmen, als auch mit den zugehörigen Leerlaufspannungen korrelieren. Zudem stellen wir die Vielseitigkeit unserer Methode dar, indem wir die Auswirkung von Degradation auf die Entwicklung der Energetik, vertikale Schichtenbildung, Injektionsbarrieren in verborgenen Schichten, Seitenkettenvariationen, Molekül-dotierung und die energetische Anpassung in ternär gemischten Systemen untersuchen. Zusammengefasst, diese Arbeit demonstriert das Potenzial und die vielfältige Verwendbarkeit unserer neuartigen Methode, die für ein besseres Verständnis der vertikalen Zusammensetzung und energetischen Anpassung in dünnen, organischen Filmen genutzt werden kann. Dieses Verständnis hat eine entscheidende Rolle für die zukünftige Entwicklung optoelektronischer, organischer Bauelemente.

Visualising the Vertical Energetic Landscape in Organic Photovoltaics

The aim of this thesis is to achieve a better understanding of the energetic alignment in organic multi-layered devices. The first part of this thesis is dedicated to the investigation of a new class of non-fullerene acceptor materials, *N*-Heteroacenes, in organic solar cells. Intentionally varying the side chain structure enables a threefold increase in device performance, partly due to an improved active layer morphology. In addition, by employing transient absorption spectroscopy, an uncommon electric field-dependent charge separation is found, starkly different than for the case of conventional fullerene acceptors. In the second part of this thesis, a novel method for the investigation of energy level alignment in organic layers is developed, based on combining ultra-violet photoemission spectroscopy and essentially damage-free argon gas cluster etching. The efficacy of the technique is shown on several state-of-the-art high-performance photovoltaic systems, with estimated photovoltaic gaps being in excellent agreement with charge transfer state energies, and in direct correlation with corresponding open-circuit voltages. Furthermore, the versatility of the technique is exemplified by its application to study the evolution of the energetic alignment upon environmental degradation, vertical stratification, injection barriers at buried interfaces, side-chain variation, molecular doping and the energetic alignment in ternary blend systems. This work demonstrates the potential and wide applicability of our novel technique for understanding the vertical composition and energetic alignment in organic thin films. This understanding is crucial towards the future development of optoelectronic organic devices.

List of Publications

Publications Included in this Thesis

[1] **V. Lami**, D. Leibold, P. Fassl, Y. J. Hofstetter, D. Becker-Koch, P. Biegger, F. Paulus, P. E. Hopkinson, M. Adams, U. H. F. Bunz, S. Huettner, I. Howard, A. A. Bakulin and Y. Vaynzof, *N*-Heteroacenes as a New Class of Non-Fullerene Electron Acceptors for Organic Bulk-Heterojunction Photovoltaic Devices. *Sol. RRL* **1**, 1700053 (2017).

[2] **V. Lami**, A. Weu, J. Zhang, Y. Chen, Z. Fei, M. Heeney, R. H. Friend and Y. Vaynzof, Visualising the Vertical Energetic Landscape in Organic Photovoltaics. *Joule* (2019). doi:10.1016/j.joule.2019.06.018

[3] J. Zhang, M. H. Futscher, **V. Lami**, F. U. Kosasih, C. Cho, Q. Gu, A. Sadhanala, A. J. Pearson, B. Kan, G. Divitini, X. Wan, D. Credgington, N. C. Greenham, Y. Chen, C. Ducati, B. Ehrler, Y. Vaynzof, R. H. Friend and A. A. Bakulin, Sequentially Deposited versus Conventional Nonfullerene Organic Solar Cells: Interfacial Trap States, Charge-Transfer States, and Vertical Stratification. *in review*, (2019).

[4] A. Wittmann, G. Schweicher, K. Broch, J. Novak, **V. Lami**, Y. Vaynzof, E. McNellis, J. Sinova, K. Takimiya, S. Watanabe, J. Takeya and H. Sirringhaus, Tuning Spin Current Injection at Ferromagnet/Non-Magnet Interfaces by Molecular Design. *in review*, (2019).

[5] H. Shekhar, **V. Lami**, O. Solomeshch, A. Fenigstein, L. Tomer, L. Becky, Y. Vaynzof and N. Tessler, Doping induced performance enhancement in inverted small molecule organic photodiodes operating below 1V reverse bias - Towards compatibility with CMOS for imaging applications. *Org. Electron.* **67**, 1–9 (2019).

[6] **V. Lami**, Y. J. Hofstetter, J. Butscher and Y. Vaynzof, Origin of open-circuit voltage tuning in ternary organic solar cells. *in preparation*, (2019).

Additional Publications

[1] E. H. Menke, D. Leibold, **V. Lami**, Y. J. Hofstetter, M. Mastalerz and Y. Vaynzof, Triptycene-trisaroyleneimidazoles as non-fullerene acceptors - Influence of side-chains on solubility , device morphology and performance. *Org. Electron.* **47**, 211–219 (2017).

[2] P. Fassl, **V. Lami**, A. Bausch, Z. Wang, M. T. Klug, H. J. Snaith and Y. Vaynzof, Fractional deviations in precursor stoichiometry dictate the properties, performance and stability of perovskite photovoltaic devices. *Energy Environ. Sci.* **11**, 3380–3391 (2018).

[3] A. Weu, T. R. Hopper, **V. Lami**, J. A. Kreß, A. A. Bakulin and Y. Vaynzof Field-Assisted Exciton Dissociation in Highly Efficient PffBT4T-2OD:Fullerene Organic Solar Cells. *Chem. Mater.* **30**, 2660–2667 (2018).

[4] D. Leibold, **V. Lami**, Y. J. Hofstetter, D. Becker, A. Weu, P. Biegger, F. Paulus, U. H. F. Bunz, P. E. Hopkinson and A. A. Bakulin, Triptycenyl - phenazino - thiadiazole as acceptor in organic bulk- heterojunction solar cells. *Org. Electron.* **57**, 285–291 (2018).

[5] P. Fassl, S. Ternes, **V. Lami**, Y. Zakharko, D. Heimfarth, P. E. Hopkinson, F. Paulus, A. D. Taylor, J. Zaumseil and Y. Vaynzof, Effect of Crystal Grain Orientation on the Rate of Ionic Transport in Perovskite Polycrystalline Thin Films. *ACS Appl. Mater. Interfaces* **11**, 2490–2499 (2019).

[6] A. Weu, J. A. Kress, F. Paulus, D. Becker-Koch, **V. Lami**, A. A. Bakulin and Y. Vaynzof, Oxygen-Induced Doping as a Degradation Mechanism in Highly Efficient Organic Solar Cells. *ACS Appl. Energy Mater.* **2**, 1943–1950 (2019).

[7] D. D. Tune, H. Shirae, **V. Lami**, R. J. Headrick, M. Pasquali, Y. Vaynzof, S. Noda, E. K. Hobbie and B. S. Flavel, Stability of Chemically Doped Nanotube–Silicon Heterojunction Solar Cells: Role of Oxides at the Carbon–Silicon Interface. *ACS Appl. Energy Mater.* acsaem.9b01050 (2019). doi:10.1021/acsaem.9b01050

[8] L. M. Falk, K. P. Goetz, **V. Lami**, Q. An, P. Fassl, J. Herkel, F. Thome, A. D. Taylor, F. Paulus and Y. Vaynzof, Effect of Precursor Stoichiometry on the Performance and Stability of MAPbBr 3 Photovoltaic Devices. *Energy Technol.* ente.201900737 (2019). doi:10.1002/ente.201900737

[9] D. Becker-Koch, M. Albaladejo Siguan, **V. Lami**, F. Paulus, H. Xiang, Z. Chen, Y. Vaynzof, The double-edged sword of oxygen exposure of PbS quantum dot solar cells, *in review* (2019)

[10] M. A. Siguan, D. Becker-Koch, A. D. Taylor, Q. Sun, **V. Lami**, P. G. Oppenheimer, F. Paulus, Y. Vaynzof, Efficient and Stable Hybrid Triple-Cation Perovskite/PbS Quantum Dot Solar Cells, *submitted* (2019)

List of Conference Presentations

[1] **V. Lami**, P. E. Hopkinson, and Y. Vaynzof, Development of a new method to probe the electronic structure of organic photovoltaic materials in a bulk heterojunction, Poster - DPG Spring Meeting 2017, Dresden, Germany

[2] **V. Lami** and Y. Vaynzof, Direct Measurement of the Energetic Landscape of Solution-Processed Organic Photovoltaic Devices, Poster - MRS Fall Meeting 2018, Boston, USA

[3] **V. Lami**, A. Weu, J. Zhang, Y. Chen, Z. Fei, M. Heeney, R. Friend, and Y. Vaynzof, Visualising the Vertical Energetic Landscape in Organic Photovoltaics, Oral presentation - DPG Spring Meeting 2019, Regensburg, Germany

[4] **V. Lami**, A. Weu, J. Zhang, Y. Chen, Z. Fei, M. Heeney, R. Friend, and Y. Vaynzof, Visualising the Energetic Landscape of Organic Photovoltaic Devices and the Effects of Degradation, Oral presentation - EMRS Spring Meeting 2019, Nice, France

Contents

Abbrevations **xii**

1 Introduction **1**

2 Theoretical Background **7**

2.1 Physics of Solar Cells 7

2.1.1 Characteristic Properties and the Power Conversion Efficiency . 7

2.1.2 Efficiency Limits 10

2.1.2.1 Solar Irradiation 11

2.1.2.2 Photovoltaic Efficiency Limit 12

2.2 Excitations and Loss Mechanisms in Organic Photovoltaic Materials . . 13

2.2.1 Excitons in Organic Materials 14

2.2.1.1 Organic Materials 14

2.2.1.2 Excitons in Organic Solar Cells 16

2.2.1.3 The Bulk Heterojunction (BHJ) Solar Cell 16

2.2.1.4 Exciton Movement 17

2.2.1.5 Exciton Types 19

2.2.1.6 Spin Statistics in Excitons 19

2.2.2 Recombination Mechanisms 21

2.2.2.1 Geminate Recombination 23

2.2.2.2 Non-Geminate Recombination 24

2.2.3 Intensity Dependent Solar Cell Parameters 26

2.2.3.1 Effects on the Short-Circuit Current 26
2.2.3.2 Effects on the Open-Circuit Voltage 26
2.3 Energy Level Alignment at Interfaces in Organic Semiconductors 28
2.3.1 Introduction 28
2.3.2 Electronic Structure of Organic Materials 29
2.3.2.1 Effect of Charges on the Electronic Structure 29
2.3.2.2 Difference Between Optical and Electronic Gaps 30
2.3.3 Energy Level Alignment at Organic/Passivated Substrate Interfaces 30
2.3.3.1 The Integer Charge-Transfer (ICT) Model 31
2.3.3.2 The ICT Model on Organic/Conducting Substrate Interfaces 32
2.3.3.3 The cases of PEDOT:PSS and ZnO 33
2.3.4 Organic/Organic Interfaces 34
2.3.5 Energetic Alignment at Organic/Metal Interfaces Manufactured by Chemisorption 35
2.3.5.1 The Push-Back Effect 36
2.3.5.2 Chemisorption Induced Dipole 37
2.3.6 Band Bending 37
2.3.6.1 Gap States - Replacing the ICT model? 38
2.3.6.2 Insights from Simulations 39
2.4 Energetic Losses 42
2.4.1 Introduction 42
2.4.2 The Impact of the Photovoltaic Gap E_g^{PV} 43
2.4.3 The Influence of the Choice of Electrodes 44
2.4.4 DOS Broadening 45
2.4.5 Charge Transfer (CT) States 46
2.4.5.1 Correlation to Open-Circuit Voltage (V_{OC}) 49
2.5 Summary 51

3 Materials and Methods 53

3.1 Materials and Solvents . . . 53

3.1.1 Non-Fullerene Acceptors in Organic Photovoltaic Devices . . . 53

3.1.2 Substrates . . . 58

3.2 Fabrication Methods . . . 58

3.2.1 Substrate Cleaning . . . 59

3.2.2 Film and Device Fabrication . . . 59

3.2.3 Device Architectures . . . 59

3.2.3.1 Standard Architecture . . . 59

3.2.3.2 Inverted Architecture . . . 60

3.2.3.3 Bilayer Films . . . 60

3.2.4 Specific Material Preparation Methods . . . 60

3.2.4.1 PEDOT:PSS . . . 60

3.2.4.2 ZnO Preparation . . . 61

3.2.4.3 P3HT and $PC_{60}BM$ . . . 61

3.2.4.4 PffBT4T-2OD:$PC_{70}BM$ . . . 61

3.2.4.5 PBDB-T:NCBDT . . . 61

3.2.4.6 PFBDB-T:C8-ITIC . . . 62

3.2.4.7 DRCN5T:$PC_{70}BM$ . . . 62

3.2.4.8 DNTT Spintronic Layers . . . 62

3.2.4.9 Doped $PC_{60}BM$ Layers . . . 62

3.2.4.10 PBDB-T-2Cl:ITIC-2F:$PC_{70}BM$ . . . 62

3.2.4.11 PTB7:$PC_{70}BM$:ICBA . . . 62

3.3 Experimental Methods . . . 62

3.3.1 Photoemission Spectroscopy . . . 62

3.3.1.1 Ultra-Violet Photoemission Spectroscopy (UPS) . . . 63

3.3.1.2 X-Ray Photoemission Spectroscopy (XPS) . . . 65

3.3.2 Depth Profiling . . . 65

3.3.2.1 Gas Cluster Ion Beams . . . 65

3.3.2.2 Comparison of the Introduced Damage between Cluster and Monoatomic Modes . . . 67
3.3.3 Atomic Force Microscopy . . . 68
3.3.4 Grazing-Incidence Wide-Angle X-Ray Scattering . . . 69
3.3.5 Photoluminescence Spectroscopy . . . 69
3.3.6 UV-vis Spectroscopy . . . 70
3.3.7 Photothermal Deflection Spectroscopy . . . 71
3.3.8 Transient Absorption Measurements . . . 72
3.3.9 DekTak Profilometer . . . 72
3.3.10 Device Characterization . . . 73
3.3.10.1 Solar Simulator . . . 73
3.3.10.2 External Quantum Efficiency . . . 73
3.3.10.3 Sample Holder and Environmental Rig . . . 74

I Non-Fullerene Acceptor Molecules: *N*-Heteroacenes 77

4 *N*-Heteroacenes: a Novel Class of Non-Fullerene Acceptors 79
4.1 Intorduction . . . 79
4.2 Optoelectronic Properties . . . 80
4.3 Photovoltaic Device Performance . . . 82
4.4 Morphological Properties . . . 84
4.5 Photophysics . . . 85
4.5.1 Field-Dependent Charge Dynamics . . . 89
4.5.2 Bimolecular Recombination . . . 90
4.6 Summary . . . 90

II Damage-Free UPS Depth Profiling 93

5 Visualising the Vertical Energetic Landscape in Organic Photovoltaics 95
5.1 Introduction . . . 95

5.2 Method Development . . . 97
5.2.1 Why Gas Cluster Ion Beams? . . . 97
5.2.1.1 Monoatomic vs. Cluster Etching . . . 98
5.2.2 UPS Depth Profiling . . . 100
5.2.2.1 Fitting Procedure . . . 101
5.2.2.2 Depth Profiling of a P3HT:$PC_{60}BM$ Bulk Heterojunction 102
5.2.2.3 Excluding Preferencial Etching . . . 105
5.2.2.4 Depth Profiling of a P3HT/$PC_{60}BM$ Bi-layer . . . 105
5.2.3 Determining Energetic Landscapes . . . 106
5.2.3.1 Energetic Landscape of P3HT:$PC_{60}BM$ Bulk Heterojunction and P3HT/$PC_{60}BM$ Bi-layer . . . 108
5.2.3.2 Energetic Landscapes of Other High-Efficiency Photovoltaic Systems . . . 109
5.2.4 A Comparison of Estimated Photovoltaic Gaps from Different Approaches with Device V_{OC}s . . . 110
5.3 Summary and Outlook . . . 114

6 Application of UPS Depth Profiling in Various Systems 117
6.1 Evolution of BHJ Energetics Upon Degradation in Oxygen and Light . . 117
6.1.1 Evolution of the Energetic Landscape upon Degradation . . . 118
6.2 Vertical Stratification in Sequentially vs. Conventionally Deposited BHJs 120
6.3 Additional Material Systems . . . 123
6.3.1 Change in Energetics in a Spintronic System . . . 123
6.3.2 Change in Energetics Upon Interlayer Doping . . . 125
6.4 Origin of Open-Circuit Voltage Tuning in Ternary Organic Solar Cells . . 126
6.4.1 PBDB-T-2Cl:ITIC-2F:$PC_{70}BM$ . . . 127
6.4.1.1 Device Performance . . . 127
6.4.1.2 XPS Depth Profiling: Compositional Profiles . . . 128
6.4.1.3 UPS Depth Profiling: Correlation between V_{OC} and E_g^{PV} 129
6.4.2 PTB7:$PC_{70}BM$:ICBA . . . 130

6.4.2.1 UPS Depth Profiling: Correlation between V_{OC} and E_g^{PV} 131
6.4.2.2 The Superiority of UPS over XPS Depth Profiling: Compositional Profiles . . . 132
6.5 Summary . . . 133

7 Conclusions and Outlook **135**

III Appendix **139**

A The Fitting Program *LaFit* **141**
A.1 File Requirements for Data Import . . . 141
A.2 Main Functions . . . 142
A.2.1 UPS Data Fitting . . . 144
A.2.1.1 HOMO Onset Fitting . . . 144
A.2.1.2 SECO Onset Fitting . . . 145
A.2.1.3 Fitting of UPS Depth Profiles . . . 145
A.2.2 Material Percentage Determination . . . 147
A.2.2.1 Material Percentage from an XPS Depth Profile . . . 147
A.2.2.2 Material Percentage from a UPS Depth Profile . . . 148
A.2.3 Energetic Diagram . . . 148
A.3 Example Files and *MatLab* Codes . . . 149
A.3.1 Example Files for Data Import . . . 149
A.3.2 Important *MatLab* Codes . . . 150

B Supplementary Figures **159**

Bibliography **213**

Danksagung/Acknowelegements **217**

Abbrevations

AFM	atomic force microscopy
Ag	silver
Al	aluminium
Alq3	aluminum-tris(8-hydroxychinolin)
AM	air mass
Ar	argon
Au	Gold
BE	binding energy
BHJ	bulk heterojunction
BL	bi-layer
BR	bimolecular recombination
c-Si	crystalline silicon
C	carbon
C_{70}	[5,6]-Fullerene-C70
C8-ITIC	(2Z)-2-[(8-(E)-[1-(dicyanomethylidene)-3-oxo-1,3-dihydro-2H-inden-2-ylidene]methyl-6,6,12,12-tetraoctyl-6,12-dihydrothieno[3,2-b]thieno[2″,3″:4′,5′]thieno[2′,3′:5,6]-s-indaceno[2,1-d]thiophen-2-yl)methylidene]-3-oxo-2,3-dihydro-1H-inden-1-ylidenepropanedinitrile
Ca	calcium
CB	conduction band
CBP	4,40-N,N0-dicarbazolyl-biphenyl
CO_2	carbon dioxide
Cr	chromium

Cs	caesium
CS	charge-separated state
CT	charge transfer
CuPc	copper phthalocyanine
CV	cyclic voltammetry
D/A	donor/acceptor
DFT	density functional theory
DNTT	dinaphtho[2,3-b:2,3-f]thieno[3,2-b]thiophene
DOS	density of states
DRCN5T	2,2′-[(3,3‴,3⁗,4′-tetraoctyl[2,2′:5′,2″:5″,2‴:5‴,2⁗-quinquethiophene]-5,5⁗-diyl)bis[(Z)-methylidyne(3-ethyl-4-oxo-5,2-thiazolidinediylidene)]]bis-propanedinitrile
EA	electron affinity
EDX	energy dispersive x-ray
$\mathbf{E_F}$	Fermi energy
EG	electronic gap
EL	electroluminescence
ε_0	vacuum permittivity
ε_r	relative permittivity
EQE	external quantum efficiency
ETL	electron transport layer
F	fluorine
FET	field-effect transistor
FF	filling factor
FRET	Förster resonant energy transfer
FWHM	full width half maximum
GaAs	gallium arsenide
GCIB	gas cluster ion beam
GIWAXS	grazing-incidence wide-angle x-ray scattering

H	hydrogen
He	helium
HOMO	highest occupied molecular orbital
HTL	hole transport layer
I_D	dark current
I_{ph}	photo-current
I_{sh}	shunt current
IC	internal conversion
ICBA	indene-C60 bisadduct
ICT	integer charge-transfer
IMFP	inelastic mean free path
IP	ionization potential
IPES	inverse photoemission spectroscopy
IR	infrared
ISC	intersystem crossing
ITIC-2F	3,9-bis(2-methylene-((3-(1,1-dicyanomethylene)-6,7-difluoro)-indanone))-5,5,11,11-tetrakis(4-hexylphenyl)-dithieno[2,3-d:2',3'-d']-s-indaceno[1,2-b:5,6-b']dithiophene
ITO	indium tin oxide
IV	current-voltage
J_{sc}	short circuit current density
k_B	Boltzmann constant
LUMO	lowest unoccupied molecular orbital
m-MTDATA	4,4,400-tris[3-methyl-phenyl(phenyl)amino]triphenylamine
MIM	metal-insulator-metal
MoO_x	molybdenum oxide
MPP	maximum power point
N-DMBI	(4-(1,3-dimethyl-2,3-dihydro-1H-benzoimidazol-2-yl)phenyl)dimethylamine
N	nitrogen

NFA	non-fullerene acceptor
NIR	near-infrared
O	oxygen
OFET	organic field effect transistor
OG	optical gap
OLED	organic light emitting diode
OPV	organic photovoltaic
OSC	organic solar cell
P3HT	poly(3-hexylthiophene)
PBDB-T	poly[(2,6-(4,8-bis(5-(2-ethylhexyl)thiophen-2-yl)-benzo[1,2-b:4,5-b′]dithiophene))-alt-[5,5-(1′,3′-di-2-thienyl-5′,7′-bis(2-ethylhexyl)benzo[1′,2′-c:4′,5′-c′]dithiophene-4,8-dione)]
PBDB-T-2Cl	poly[(2,6-(4,8-bis(5-(2-ethylhexyl-3-chloro)thiophen-2-yl)-benzo[1,2-b:4,5-b′]dithiophene))-alt-(5,5-(1′,3′-di-2-thienyl-5′,7′-bis(2-ethylhexyl)benzo[1′,2′-c:4′,5′-c′]dithiophene-4,8-dione))
$PC_{60}BM$	[6,6]-Phenyl-C61-butyric acid methyl ester
$PC_{70}BM$	[6,6]-Phenyl-C71-butyric acid methyl ester
PCE	power conversion efficiency
PDS	photothermal deflection spectroscopy
PEDOT	poly(3,4-ethylenedioxythiophene)
PES	photoemission spectroscopy
PFBDB-T	poly[(2,6-(4,8-bis(5-(2-ethylhexyl)thiophen-2-yl)-benzo[1,2-b:4,5-b′]dithiophene))-alt-(5,5-(1′,3′-bis(4-fluorothiophen-2-yl)-5′,7′-bis(2-ethylhexyl)benzo[1′,2′-c:4′,5′-c′]dithiophene-4,8-dione
PFESA	poly(perfluor- oethylene sulfonic acid)
PffBT4T-2OD	poly[(5,6-difluoro-2,1,3-benzothiadiazol-4,7-diyl)-alt-(3,3‴-di(2-octyldodecyl)-2,2′,5′,2″,5″,2‴-quaterthiophen-5,5‴-diyl)]
PL	photoluminescence
PLQE	photoluminescence quantum efficiency
PSS	poly(styrene sulfonic acid)
PTB7	poly(4,8-bis[(2-ethylhexyl)oxy]benzo[1,2-b:4,5-b′] dithiophene-2,6-diyl3-fluoro-2-[(2-ethylhexyl)carbonyl]thieno[3,4-b]thiophenediyl)

PV	photovoltaic
$\mathbf{E_g^{PV}}$	photovoltaic gap energy
Py	permalloy
$\mathbf{R_s}$	series resistance
$\mathbf{R_{sh}}$	shunt resistance
S	sulphur
SAM	self-assembled monolayer
SC	solar cell
SECO	secondary electron cut-off
Si	Silicon
SIMS	secondary ion mass spectrometry
SQ	Shockley-Queisser
SRH	Shockley-Read-Hall
SVD	singular value deconvolution
TA	transient absorption
TiN	titanium nitride
TIPS-TAP-1T	triptycenyl-tetraazapentacene
TIPS-TAP-2T	bistriptycenyl-tetraazapentacene
TIPS-TAP	triisopropylsilyle-thynyl-tetraazapentacene
TSC	ternary solar cell
UHV	ultra-high vacuum
UPS	ultra-violet photoemission spectroscopy
UV	ultra-violet
VB	valence band
$\mathbf{V_{bi}}$	built-in potential
VC	vibrational cooling
VL	vacuum level
$\mathbf{V_{OC}}$	open-circuit voltage

VR	vibrational relaxation
w.r.t.	with respect to
Φ	work function
W-M	Wannier-Mott
XPS	x-ray photoemission spectroscopy
ZAD	zinc acetate dihydrate
ZnO	zinc oxide

Twenty years from now you will be more disappointed by the things you didn't do than by the ones you did do. So throw off the bowlines. Sail away from the safe harbour. Catch the trade winds in your sails.

Mark Twain

1 Introduction

Due to a rapid rise in world population, industrialization and economic growth, especially in India and China, there is also a rise in energy demand. Up to date, this demand has been mostly met by burning fossil fuels, causing increasing levels of carbon dioxide (CO_2) to accumulate in the atmosphere, acting together with other gases as a greenhouse: these "greenhouse" gases let short-wave solar radiation through the Earth's atmosphere, but they partly prevent long-wave energy re-radiation into space and hence trap the heat. [1] The burning of fossil fuels has already resulted in an increase of atmospheric CO_2 concentrations from $\sim$ 340 ppm to $\sim$ 410 ppm in the last 40 years. [2] In the same time period, an annual average surface temperature increase of $\sim$ 0.8 $^{\circ}C$ has been observed. [3] Political steps, such as the Paris agreement in 2015, [4] have been taken to prevent a temperature rise exceeding 2 $^{\circ}C$ above pre-industrial levels. In Germany, the share of renewable energies in electrical power generation has increased from $\sim$ 9 % to over 40 % from 2002 to 2018 as shown in **Fig. 1.1**, [5] however, this is not the case for the rest of the world, with a worldwide average value of $\sim$ 9 % in 2018. [6] Analysis of the overall world power generation between 2010 and 2015 has shown that the growth rate of renewable energy sources between 2015 and 2020 needs to be at least twice as high as it was in the first 5 year period. [7] In order to overcome this tremendous challenge, renewable, carbon-neutral energy technologies are highly desired, with solar power being one of the most promising candidates.

The amount of solar energy hitting the Earth's surface is about 96000 TW per year. It is, however, impossible to capture the overwhelming majority of this energy. Assuming a 2 % land-only coverage, with solar panels with a 12 % power conversion efficiency (PCE) on average, this number reduces to $\sim$ 67 TW. This is, however, still more than twice the total projected global energy demand of $\sim$ 30 TW for the year 2050. [8] In comparison, the globally installed solar power capacity was about 400 GW in 2017, and it could potentially surpass 1 TW in 2022, [9] and $\sim$ 7 TW in 2050. [10] An even greater increase, however, could be achieved by considering economic incentives. While the payback time, the time required to produce enough energy to offset the energy invested during fabrication, of currently established, conventional crystalline silicon (c-Si) solar cell technologies is about 2 years, for organic solar cells (OSCs) this time was about 0.4 years already in 2013. [8] Additionally, flexibility, low production cost and light-weight (due to the high absorption coefficients of OSCs) make them

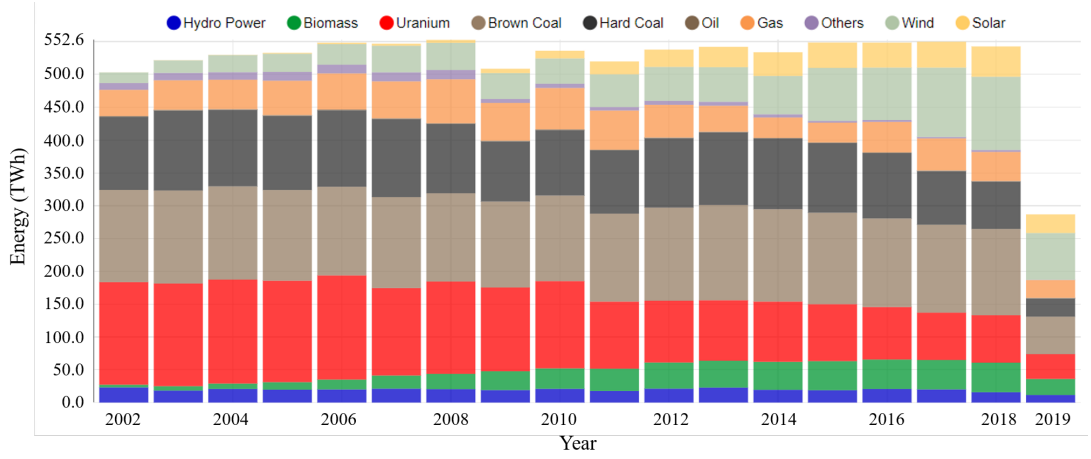

Figure 1.1: Net public electricity generation in Germany from 2002 until July 2019 with respective contributions of different energy sources. Adapted from [5] and modified, 2019, Copyright © Fraunhofer-Gesellschaft.

potential candidates for future applications, [11] with great improvements in device efficiencies being made in the last 20 years, shown in **Fig. 1.2** reaching impressive values of 16.5 %. [12]

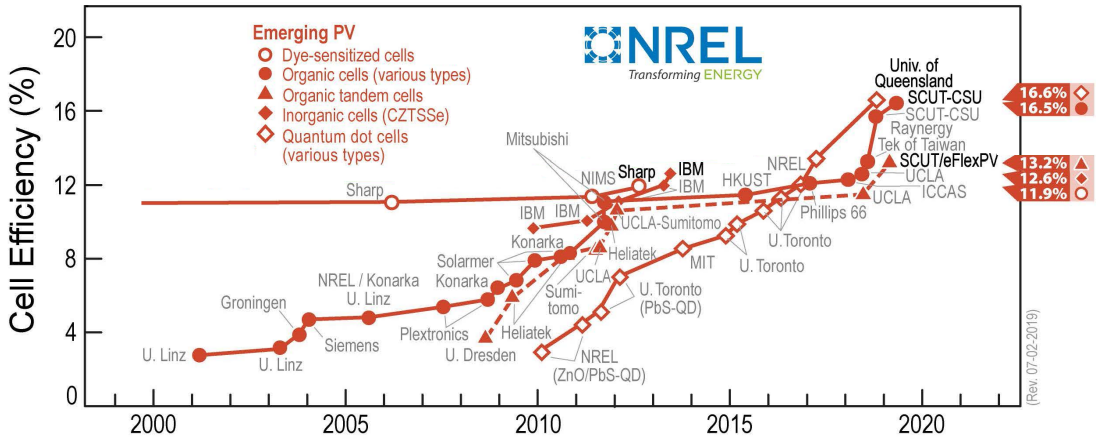

Figure 1.2: Solar cell efficiency chart of emerging photovoltaic (PV) technologies in the last 20 years, including organic and tandem solar cells (SCs). Adapted from [13] and modified.

In order to maintain momentum and enable further improvements in OSC efficiency, it is vital to identify and understand factors governing their performance. Organic photovoltaic (OPV) devices are composed of an electron-rich donor and an electron-poor acceptor material. [14] Although both should contribute to the generated photocurrent effectively in order to achieve high-performance devices, the development of new donors has received more attention than that of new acceptors in the past few decades, [15] with most OSCs employing fullerenes as acceptor. The focus in

material development, however, has recently shifted to organic non-fullerene acceptors (NFAs) due to several advantages when compared to fullerenes. [16–20] The latter have a 3D character and thus isotropic charge transport, delocalized electronic states, high electron mobilities, and good intermixing, however, they also have less desirable qualities such as weak absorption in the visible and near-infrared (NIR) regions, thermal and photo-chemical instability and a time-consuming purification, contributing to high production costs. [21] Fortunately, NFAs offer the possibility to address these deficiencies: their chemical structure and therefore their electron affinity can be varied over a wide range, while at the same time they can exhibit increased visible–NIR absorptivity, and in some cases even their synthesis is easier. [15, 18, 22–27] On the down side, in the case of planar, 2D molecules, they tend to show inherently anisotropic crystal structures and thus non-isotropic charge transport, which can complicate electron-transport in these layers. [18, 20, 28] Nevertheless, efforts in NFA research have increased the PCE of OSC devices to > 16 %. [12]
OSCs consist, apart from the active layer comprising the donor and acceptor materials, of a variety of stacked layers, including electrodes, transport, and blocking layers. Consequently, a more profound understanding of elementary processes such as charge generation, transport, recombination, injection and extraction is challenging. However, in order to improve OPV devices even further, these processes need to be understood. In particular, they are determined by the energetic alignment of the individual layers of the device, e. g. the highest occupied molecular orbital (HOMO) and the lowest unoccupied molecular orbital (LUMO) for each component. At present, such information is only evaluated for isolated, single layers, which does not account for the critical effects of the interface when blended, such as band bending or dipole formation. The exact position of these energy levels is, however, of crucial importance when interpreting device physics and especially when searching for new materials, since donor and acceptor need to be complementary when blended: their energetic alignment will determine whether effective charge separation will take place or not, thus influencing the resulting device PCE. Apart from the energetic landscape, compositional distribution can also play a crucial role in determining how well charges can be transported to the electrodes for collection. This aspect is still not well understood for more complicated systems consisting of more than two materials in the active layer, such as is the case for ternary solar cells (TSCs). Even though increased efforts have been made to understand and address these issues, a clear understanding is still lacking.

This thesis is aimed to address these issues in the following way:

- First, we investigate a new class of NFAs, N-Heteroacenes, with varying side chains and examine thus the differences between a 2D and a 3D molecule. We show that planar molecules result in strong aggregation due to crystallization, and thus an anisotropic electron transport, resulting in poor device performance. We also show that the addition of side chains to planar molecules breaks their

tendency to crystallize and results in a 3-fold efficiency increase. Finally, while addressing the photophysics of this material system, we show that while the internal field, caused by the electrodes, does not change charge separation behaviour for fullerene based systems, it has an impact on our N-Heteroacene and potentially on all NFA based systems. [20]

- Next, we focus on accurately assessing the energetic landscape in OPV devices. To accomplish this, we develop a technique employing ultra-violet photoemission spectroscopy (UPS) in combination with Argon gas cluster ion beam (GCIB) sputtering, which allows for damage-free depth profiling and thus an accurate determination of the vertical energetic alignment of multiple layers as a function of depth. [29–34] In doing so, we determine the HOMO levels simultaneously for all materials present in the device and the corresponding vacuum level. Furthermore, we can estimate the LUMO level from optical measurements, resulting in a complete energetic picture. To examine the utility of this methodology, we apply it to a variety of organic material systems, in both bi-layer (BL) and bulk heterojunction (BHJ) structures, including both fullerene and non-fullerene acceptors. With this technique we are able to determine important parameters, such as the HOMO-HOMO offset (driving force for charge separation) and the "photovoltaic gap" (the energetic difference between the LUMO of the acceptor and the HOMO of the donor). While minimizing the former is a prerequisite for low voltage losses, [35] the latter is used to predict the potential open-circuit voltage (V_{OC}) of the corresponding device; [36–42] both being thus important indicators of the PCE. In addition to the energetic landscape, we obtain compositional information with a high vertical depth resolution, allowing us to investigate effects such as doping or intermixing. Generally, this method has vast applications to the field of organic electronics, and can be applied to the study of energetic landscapes of any type of multi-layered device, including solution-processed devices, which, unlike devices with evaporated layers, cannot be addressed *in situ*. [34]

- Finally, we show a variety of application possibilities of our technique, such as probing the changes in energetic landscape upon degradation and thus the temporal evolution of electronic and compositional profiles after device operation. We find that during degradation in 20 % oxygen and light exposure, oxygen p-dopes the active layer of our OPV devices; however, in a highly composition dependent, non-homogeneous manner. With this information, our method opens up a new way to quantify energy losses in OPV systems and to develop new routes for their suppression. [34] Additionally, we show that UPS depth profiling can successfully distinguish materials showing dissimilar electronic structure even when the components are comprised from the same elements, which is not possible with any other technique known up to date. Furthermore, we investigate a sequentially deposited and a doped material system, and show that our technique indeed allows for the investigation of intermixing as well as dop-

ing. [43, 44] Next, we investigate the charge injection and transport in a material system with slightly varied side chains. [45] Finally, we show that our methodology is also applicable for ternary systems, allowing for compositional and energetic depth profiles for more complex OPV devices.

To accomplish this, we will first discuss the fundamental physics of solar cells, charge recombination, and energetic alignment, as well as their impact on device performance in **Chapter 2**, followed by a description of all materials and methods used in **Chapter 3**. Next, we will summarize our results for the investigated NFA system of N-Heteroacenes in **Chapter 4**, and continue with our developed UPS depth profiling method and its applications in **Chapter 5** and **6**, respectively. A summary and outlook including potential future projects are given in **Chapter 7**.

2 | Theoretical Background

The main aim of this thesis is to discuss the development of a new technique capable of measuring the overall energetic landscape in OPV devices. With this, the goal is to achieve a better understanding of the changes which occur when materials are blended, how this affects the energetics alignment within the active layer, and finally how the overall device performance is influenced. Ultimately, this will improve both our understanding of the working principle of OSCs and the performance of SCs. This chapter begins by discussing the basic physics of SCs, followed by a detailed description of excitons and recombination types in organic layers. These are directly related to the internal losses in the device. Next, the current knowledge of transport levels and energetic alignment in OPV devices is explained in great detail. Finally, as all of these parameters correlate with and influence the device performance, especially the open-circuit voltage (V_{OC}), a detailed overview on energetic losses leading to reduced device V_{OC}s are discussed.

2.1 Physics of Solar Cells

A solar cell is fundamentally a diode, which is inherently non-perfect and will thus have unwanted resistances and leakage currents. Important device parameters such as the short circuit current density (J_{sc}), V_{OC} and filling factor (FF) will be introduced in the context of diodes. At last, we will discuss the limitations to solar cell efficiency including the maximal power provided by the sun.

2.1.1 Characteristic Properties and the Power Conversion Efficiency

The equivalent circuit of a solar cells is schematically shown in **Fig. 2.1**. When describing its current, the SC can be subdivided into the dark current (I_D), photo-current (I_{ph}) and shunt current (I_{sh}). While I_D is determined by the diode properties of a solar cell, I_{ph} and I_{sh} are determined by photo-induced charge carrier generation and device imperfections, respectively, [46] and is thus summarized as:

$$I = I_D + I_{sh} + I_{ph} \tag{2.1}$$

According to the Shockley theory, [47] I_D has an exponential dependence on the output voltage V_{output} and can be expressed as:

$$I_D = I_0 \left[exp\left(\frac{qV_{output}}{nk_BT} \right) - 1 \right] \tag{2.2}$$

where I_0 is the reverse saturation current,[1] q the elementary charge, k_BT the thermal energy and n the ideality factor, describing the diode properties of the SC. An ideality factor of 1 would signify a negligible charge carrier recombination, while in real devices this factor is greater than 1, typically between 1 and 2. [48]
In addition to the Shockley's theory, one needs to include the solar cells series resistance (R_s) and shunt resistance (R_{sh}), which are, in case of a real OPV device, non-negligible. While R_s mainly constitutes the resistance of interfacial contacts, the active layer itself and the electrodes, R_{sh} arises from numerous kinds of leakage currents, including losses caused by impurities. [11] The output voltage in **Eq. 2.2** becomes thus $V_{output} = V - IR_s$, with V being the applied voltage. I_{sh} can be simply expressed by *Ohm's law* ($V = IR_S + I_{sh}R_{sh}$), and by substituting into **Eq. 2.1**, the overall current I can be written as:

$$I = \frac{R_{sh}}{R_{sh} + R_s} \left\{ I_0 \left[exp\left(\frac{q(V - IR_s)}{nk_BT} \right) - 1 \right] + \frac{V}{R_{sh}} \right\} - I_{ph} \tag{2.3}$$

In order to have a better comparison between solar cells, the current I is often divided by the area of illumination A, yielding in the current density $J = I/A$.

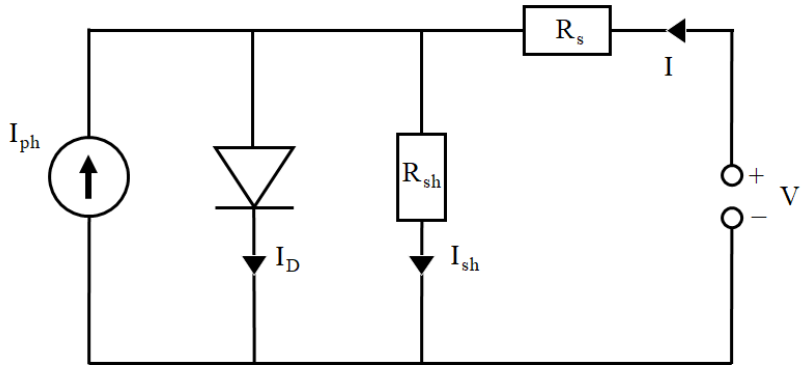

Figure 2.1: Equivalent circuit for a solar cell: the device is operated at a voltage V, and has a series and shunt resistance R_s and R_{sh}, including a shunt current I_{sh}. The overall current I comprises the current from the diode I_D and the generated photocurrent I_{ph}. [46]

Typically, solar cells are characterized by measuring the current-density with respect to the applied voltage, resulting in so called JV curves, such as plotted in **Fig. 2.2**. The most important characteristic parameter of such a curve are the J_{sc}, V_{OC} and the

[1] In inorganic semiconductors, such as p-n junctions, its value typically denotes the current contributed by minority charge carriers, [48] while in OPV devices it originates from thermal exciton excitations. [49]

FF.

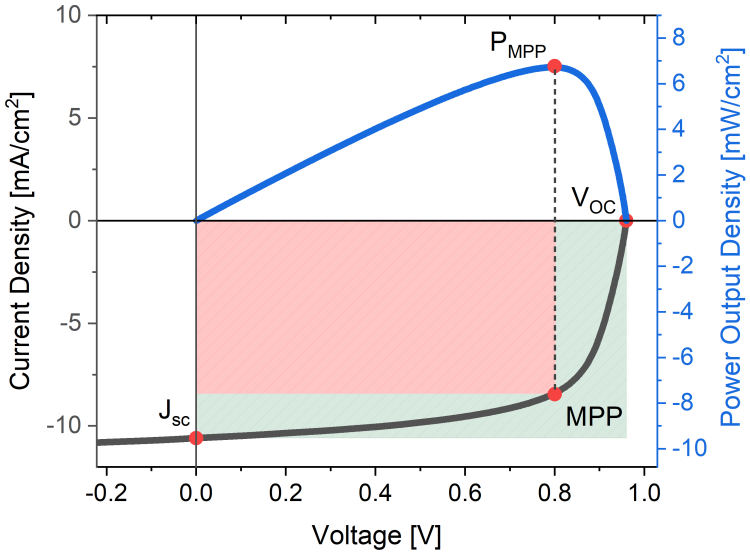

Figure 2.2: Exemplary JV curve (black) and the corresponding power output density (blue) for a solar cell. The short circuit current density (J_{sc}), open-circuit voltage (V_{OC}), maximum power point (MPP) and the power output density at the MPP, P_{MPP} are denoted with red dots. The P_{MPP} corresponds to the area of the red rectangle, while the P_{MPP} for a perfect diode would correspond to the area of the green rectangle.

The J_{sc} is defined as the current-density when no voltage is applied. Under the assumption of an ideal diode, *e.g.* $R_s \to 0$ and $R_{sh} \to \infty$, J_{sc} equals the photo-current J_{ph} according to **Eq. 2.3**.

$$J_{sc} = J(V = 0) \approx -J_{ph} \tag{2.4}$$

The V_{OC} is defined as the applied voltage at which there is no measured current flowing through the device, and it reads according to **Eq. 2.3**:

$$V_{OC} = V(J = 0) = \frac{nk_BT}{q} ln\left(\frac{J_{ph}}{J_0} + 1\right) \tag{2.5}$$

The FF describes the shape of the JV curve, which is mainly governed by R_s and R_{sh}, as shown in **Fig. 2.3**. It is defined by the ratio of the green and red rectangles in **Fig. 2.2** and is thus given as:

$$FF = \frac{V_{MPP} \cdot J_{MPP}}{V_{OC} \cdot J_{sc}} = \frac{P_{MPP}}{V_{OC} \cdot J_{sc}} \tag{2.6}$$

where V_{MPP}, J_{MPP} and P_{MPP} are the voltage, current density and power density at the MPP. The FF is thus maximal, when the the current-voltage (IV) curve is perfectly rectangular and the area of green and red rectangles is equal.

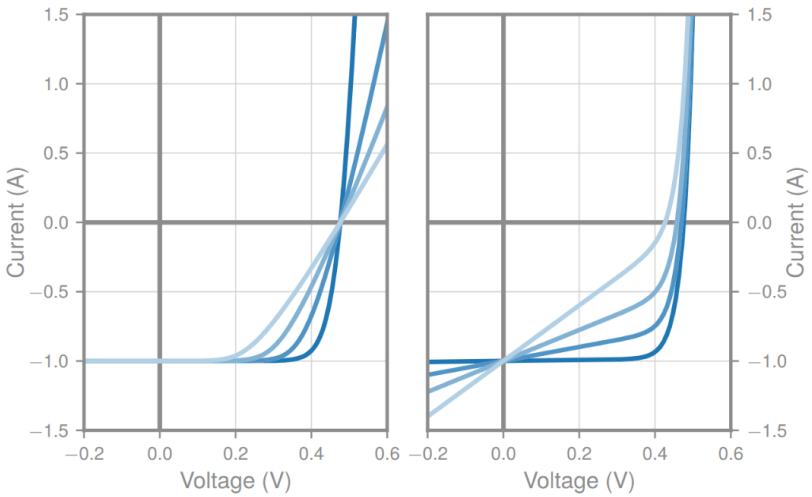

Figure 2.3: Simulated IV curves for increasing R_s ($R_{sh} \rightarrow \infty$) and decreasing R_{sh} ($R_s = 0$) values from dark to light blue, on the left and right, respectively. This shows the importance of a high R_{sh} (and thus a low leakage due to impurities) and a low R_s (and thus a low resistance of interfacial contacts). Adapted from [50].

With that, the PCE of a solar cell is defined as the generated power at MPP divided by the overall incident power density $P_{incident}$:

$$PCE = \frac{P_{MPP}}{P_{incident}} = \frac{FF \cdot V_{OC} \cdot J_{sc}}{P_{incident}} \tag{2.7}$$

The PCE of solar cells is thus the highest, when the FF, the V_{OC}, as well as the J_{sc} are maximized. This is the case, when both the leakage current and the resistance of interfacial contacts are minimized, or in other words, when as many of the incident photons are converted to electric current as possible.

2.1.2 Efficiency Limits

As described in the previous section, the PCE depends on the ratio of P_{MPP} to $P_{incident}$. While incident power density $P_{incident}$ is defined by the solar irradiation, not all of the incident photons will interact with the OPV device and generate electricity, leading to the finally extractable P_{MPP}. Hence, the energy potentially harvested by any solar energy converter is the thermal radiation coming from the sun. Furthermore, the PCE of a solar cell is determined by the maximum achievable (i) V_{OC} after accounting for fundamental intrinsic losses, such as Boltzmann and Carnot losses and thermalization and (ii) J_{sc} after accounting for emission losses and below bandgap radiation, as described by the Shockley-Queisser limit, described in **Sec. 2.1.2.2** below.

2.1.2.1 Solar Irradiation

Solar irradiation can be approximated by black body radiation with an average temperature of 5800 K, as shown in **Fig. 2.4** as a function of wavelength λ as a black line. The actual spectral irradiance of the sun outside the atmosphere of the earth, referred to as the air mass (AM) 0 spectrum, is plotted as a function of the wavelength λ in **Fig. 2.4** as a green line. This spectrum, however, slightly changes after crossing the earth's atmosphere. The AM number is defined as $1/cos(\alpha)$, with the angle of incidence α measured to the vertical at the earth's atmosphere. In other words, AM describes the *actual path* of a sunray divided by the *perpendicular path* through the earth's atmosphere. While the latter is also defined as AM 1, the standard spectrum for solar cell characterization is AM 1.5, characterising an angle of incidence of 48°, given in **Fig. 2.4** as a red line.

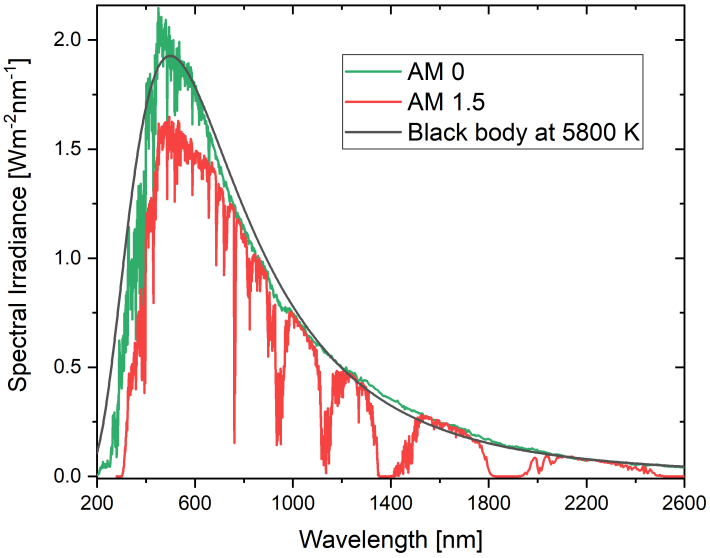

Figure 2.4: Spectral irradiance of the sun plotted as a function of the wavelength at just above the earth's atmosphere, also referred to as $AM\ 0$ (black line), and at the earth's surface at an incident angle of $\sim$ 48 $°C$, also referred to as $AM\ 1.5$ (red line). Adapted and replotted with permission from [51].

The maximum of this spectrum is located in the middle of the visible spectral range at $\sim$ 500 nm (2.5 eV). One interesting fact is, however, that this maximum is found in the infrared (IR) range at $\sim$ 1.4 eV (880 nm), when the spectrum is plotted as a function of photon energy $\hbar\omega$, with $\hbar$ and ω[2] being the Planck's constant and the light frequency, respectively. The reason for this is that the infinitesimal wavelength interval $d\lambda = -\frac{2\pi\, c}{\hbar\omega^2} d\hbar\omega = -\frac{\lambda^2}{2\pi\hbar\, c} d\hbar\omega$ does not correspond to a constant infinitesimal energy interval $d\hbar\omega$. The integral over the AM 1.5 spectrum, *i.e.* the total energy flux, is 100 $\frac{mW}{cm^2}$, which is a standard value used when measuring, and thus comparing, solar cells. It should be noted that on different locations on earth, the incident angle of the

[2] $\omega = 2\pi\frac{c}{\lambda}$, with c being the velocity of light.

incoming light, and thus the corresponding AM number, is also different; however, in order to ensure comparability, all solar cell efficiency values are measured using the AM 1.5 spectrum.

2.1.2.2 Photovoltaic Efficiency Limit

Considering only thermodynamic arguments, solar radiation to electricity conversion efficiencies close to the Carnot efficiency of 95 % may be achievable, with a heat source and a heat sink at 5800 K and 300 K, respectively. [42] When taking into account additional entropy losses, efficiencies up to 85 % would be still achievable based on a black body absorber. [48] For single band gap semiconductors, however, the maximum achievable efficiency is smaller. In 1961 Shockley and Queisser derived an efficiency limit for p-n junction solar cells by detailed balance. [52] Based on microscopic radiative processes in p-n junctions, assuming a 6000 K black body radiator, they derived a maximum efficiency of 30 % and an optimum absorber band gap of 1.1 eV. Several publications discuss and confirm this ultimate limit, [53–55] with only small variations resulting in a new limit of $\sim$ 33 % at an optimal bandgap of 1.34 eV at AM 1.5. [54] The latter analysis shows that energy loss happens due to the following processes: photon energy too low to excite the absorber ($\sim$ 31 %), intraband thermalization ($\sim$ 23 %), entropic losses ($\sim$ 12 %) and radiative recombination ($\sim$ 1 %), as summarized in **Fig. 2.5**.

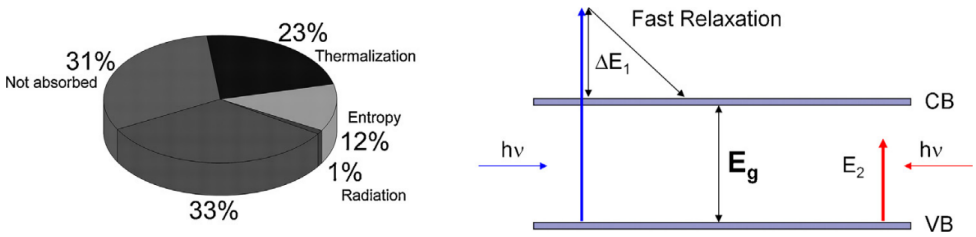

Figure 2.5: Summary of different energetic losses derived by *Archer et al.*, [54] and a corresponding energy level diagram showing photon energies (i) a lot higher, than the absorbers optical gap with an excess energy of ΔE_1, and (ii) with a lower energy E_2 being lower, than the absorbers optical gap and thus not resulting in absorption. Adapted from [42], Copyright © 2013 Elsevier Ltd.

The following assumptions have been made for the Shockley-Queisser (SQ) limit:

1. An electron-hole pair is generated by each absorbed photon.
2. The solar cell has a perfect charge collection.
3. Charge carrier recombination happens only radiatively.

The first two assumptions imply that each absorbed photon is converted into a collectable charge carrier. The third assumption ensures a maximum lifetime of photogenerated charge carriers and the highest achievable V_{OC}. [42]
The importance of the suppression of non-radiative recombination for solar cell performance has been discussed in several reports, [56, 57] showing, however, that even high

performance, small area devices operate relatively far away from the desired radiative decay only limit. [58] In order to make the effect of non-radiative recombination more explicit, one can plot the dependence of the efficiency-band gap relation as a function of the radiative recombination contribution, as shown in **Fig. 2.6**. If there is only radiative recombination, the maximum efficiency limit is at $\sim$ 33 %, as discussed above, however, if only $\sim 10^{-6}$ % of the charge carriers recombine radiatively, which is more realistically the case in state of the art devices, [58] the maximum efficiency limit shifts to $\sim$ 17 %.

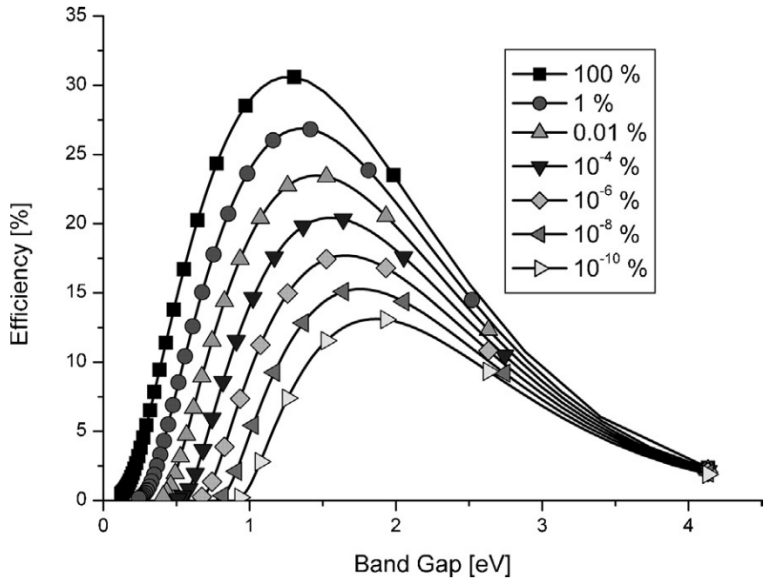

Figure 2.6: Theoretically reachable efficiency as a function of the absorbers band gap for different radiative recombination percentages. If recombination only happens radiatively (100 %), the efficiency limit is at $\sim$ 33 % as derived by *Archer et al.*, [54] but as its fraction decreases and non-radiative recombination starts to play a more and more important role, the maximum achievable efficiency decreases. Adapted from [42] and modified, Copyright © 2013 Elsevier Ltd.

2.2 Excitations and Loss Mechanisms in Organic Photovoltaic Materials

In order to be able to maximize device parameters such as V_{OC}, J_{sc}, FF and thus the PCE, one needs to have a better understanding on the physical and electronic structure of the materials of which thin film OSCs are made of. The theory for inorganic semiconductors is well developed, and it is often invoked to explain the behaviour or organic semiconductor devices. The two have, however, very different material properties. In inorganic semiconductors, such as silicon, electron-hole pairs created by photoexcitation will immediately dissociate into free charge carriers. In organic semiconductors, however, bound electron-hole pairs, called *excitons*, are created. [59] This

has been considered as the main contributor to recombination-based losses in OPV devices. [14, 60, 61] For this reason, we will discuss how organic layers are formed, how excitons are created and move, and finally, we will discuss exciton and charge carrier recombination losses, leading to a decreased device performance.

2.2.1 Excitons in Organic Materials

The difference in electron-hole pair dissociation properties originates from the low dielectric constant of organic materials compared to inorganic ones. [61] The dielectric constant, also referred to as relative permittivity (ε_r), of a material is a dimensionless factor, always given in relation to the vacuum permittivity ($\varepsilon_0 \approx 8.854 \cdot 10^{-12} Fm^{-1}$). It describes the response of a material to an electric field: the higher ε_r, the higher the screening of an electric field in the material. Hence, in a low ε_r material, excitons will have a higher binding energy (BE) due to a stronger Coulomb interaction between electron and hole. For comparison, while Silicon has a rather high $\varepsilon_r^{Si} \approx 12.1$, [62] organic materials have relative permittivities as low as $2-5$. [61, 63–65]

Excitons are quasiparticles, representing a collective excited state of an ensemble of atoms or molecules in an aggregate or in crystals. [66, p. 58] They can be created by light (photoexcitation) or can appear as a result of relaxation processes of high energy excited states. [67] They are neutrally charged, and can be characterized by their BE: that is, the energy required to separate them into a pair of free charge carriers. The low dielectric constant of organic semiconductors leads to strongly bound excitons, with a higher BE than the thermal energy at room temperature $k_B T \approx 25.26\ meV$[3] (with $T = 20\ ^\circ C$).

In the next sections, first, organic layer formation is discussed, followed by a general description of an exciton life-cycle in a representative OSC. With this, the concept of film morphology is introduced, including the principle of a BHJ solar cell. Exciton types, their migration, and the importance of their spin are explained in great detail, in order to form a basis for recombination mechanisms.

2.2.1.1 Organic Materials

From Atoms to Molecules The basic requirement for electrical conductivity of a film is the presence of delocalized charge carriers, capable of receiving energy. This delocalization in amorphous organic solids is much less pronounced than in their inorganic counterparts, such as crystalline Silicon (Si). Organic materials are mainly composed of carbon (C) atoms, while other low-atomic-number atoms, such as nitrogen (N), oxygen (O), and sulphur (S) are also common building elements. A bonding scheme of alternating single and double C-C bonds, *i.e. conjugation* is very common for these types of materials, as presented in **Fig. 2.7a**. This is a result of the so-called sp^2-hybridization, meaning that one valence electron which was originally in an s-orbital, has entered a p-orbital. The energy cost for this is compensated by the formation of a

[3] With $k_B \approx 8.617 \cdot 10^{-5}\ eVK^{-1}$ being the Boltzmann constant

σ bond, consisting of two electrons shared between C and hydrogen (H). This results in three covalent σ-bonds within a plane, and a remaining p_z orbital overlapping with the very same p_z orbital of neighbouring atoms, yielding a π-bond. Since this latter bond is highly delocalized over multiple molecules, and in the case of polymers over large segments of their chain, the HOMO and LUMO levels of the molecules are derived from occupied π-bonding (**Fig. 2.7b**) and unoccupied π^*-antibonding (**Fig. 2.7c**) orbitals, respectively, with the latter having a higher energy. [68] In a relaxed state, only the bonding orbital is expected to be occupied. They can become populated and depopulated without breaking apart, because of the significantly stronger σ-bonds.

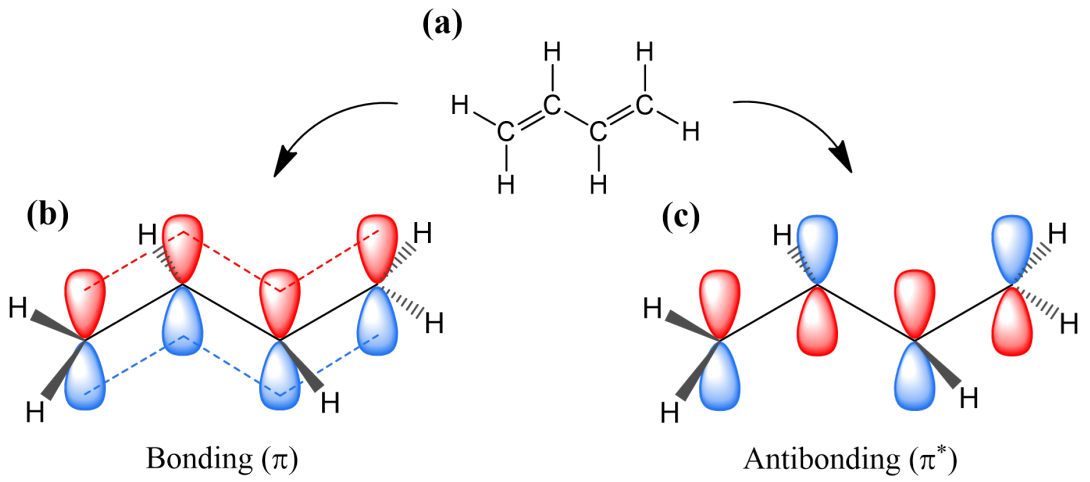

Figure 2.7: **(a)** Example of a conjugated $C = C - C = C$ bond in a chemical element representation. Schematics of the p_z orbitals resulting from conjugation in the **(b)** bonding and **(c)** antibonding state.

From Molecules to Thin Films When molecules or polymers form a solid film, individual molecules interact only by weak *van der Waals* forces, resulting in HOMOs and LUMOs completely localized on individual molecules or molecular chains. [69] The implication of this is that the electronic structure of such films is largely determined by that of individual molecules, leading to a strong limitation of classical band theory at room temperature. The HOMO level is approximately equal to the energy needed to ionize a molecule in a thin film, defined as the ionization potential (IP). It is important to realize, though, that the removal of an electron from such a system will affect the corresponding molecule: it will be positively charged and its electronic structure will differ from that of a neutral molecule. The energy gained when adding an additional electron to a neutral molecule is defined as the electron affinity (EA), which has a similar energy to that of the LUMO. [70, 71]

2.2.1.2 Excitons in Organic Solar Cells

For the separation of high BE excitons in organic materials, extra energy is needed, which can be provided by an optimized intermixing of donor and acceptor materials and a advantageous film architecture. This will be the topic of this section. A schematic diagram of the energy levels, with the corresponding HOMO and LUMO levels of a typical bi-layer donor-acceptor system is shown in **Fig. 2.8a**, with the corresponding spatial picture in **Fig. 2.8b**. Upon photon absorption, an exciton is created (*(1)* in **Fig. 2.8**), which is bound by a Coulomb force and will thus not dissociate under ambient conditions. It can, however, diffuse through the donor material (*(2)* in **Fig. 2.8**). In case it reaches a donor/acceptor (D/A) interface, it can dissociate into an electron on the acceptor and a hole on the donor molecule due to the driving force constituted by the difference in the LUMO energies of donor and acceptor, [72] (*(3)* in **Fig. 2.8**). This whole transfer mechanism can also happen in the opposite direction from the acceptor to the donor. [73] After the free charges percolate to the electrodes, they can be extracted. (*(4)* in **Fig. 2.8**)

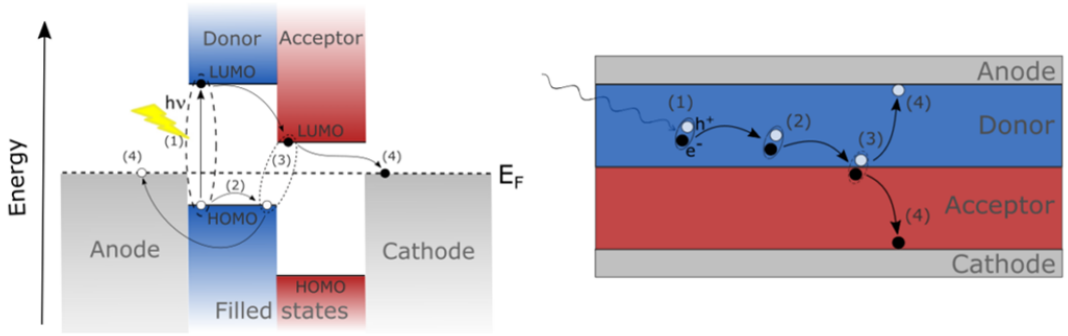

Figure 2.8: **(a)** Energy level and **(b)** spatial representation of a typical donor(blue)/acceptor(red) bi-layer device including exciton generation (1), diffusion (2), separation (3), and percolation as well as extraction (4). Adapted from [74].

2.2.1.3 The Bulk Heterojunction (BHJ) Solar Cell

Film morphology and thickness are tremendously important in OSCs. While process *(2)* in **Fig. 2.8** requires as much D/A interface area as possible, process *(4)* is limited by free pathways for separated charge carriers to the corresponding electrodes. The bi-layer structure, first introduced by *Tang et al.* in 1986, [75] satisfies the latter requirement, but the existence of only one interface between donor and acceptor strongly restricts the exciton dissociation process *(2)*. The overall film thickness also plays an important role: if the films are too thin, light absorption is limited, while if the films are too thick, excitons created further away from the D/A interface than the exciton diffusion length recombine before they reach the interface. [76] To overcome this issue, the BHJ concept was introduced, [77] where the donor and acceptor materials are intimately mixed, forming a bicontinuous network with small-scale phase separation. [78]

In the ideal case, a film thickness of $100 - 200\ nm$ is thick enough to absorb the majority of incident photons and thin enough to collect most of the charges. [79] There is, however, no general consensus on how the ideal BHJ nano-morphology should look like. **Fig. 2.9** shows 4 different scenarios: while a very fine dispersion of donor and acceptor (**Fig. 2.9a**) would lead to an efficient charge generation but poor charge transport, a bi-layer structure (**Fig. 2.9b**) would have the opposite effect. An ideal structure, good for both charge generation and transport can theoretically be achieved in two dimensions as shown in **Fig. 2.9c**, with domain sizes two times the exciton diffusion length L_D. [80] Such a structure is, however, very hard to fabricate. BHJ solar cells (**Fig. 2.9d**) provide a good trade-off between charge generation and transport, while being relatively easy to fabricate.

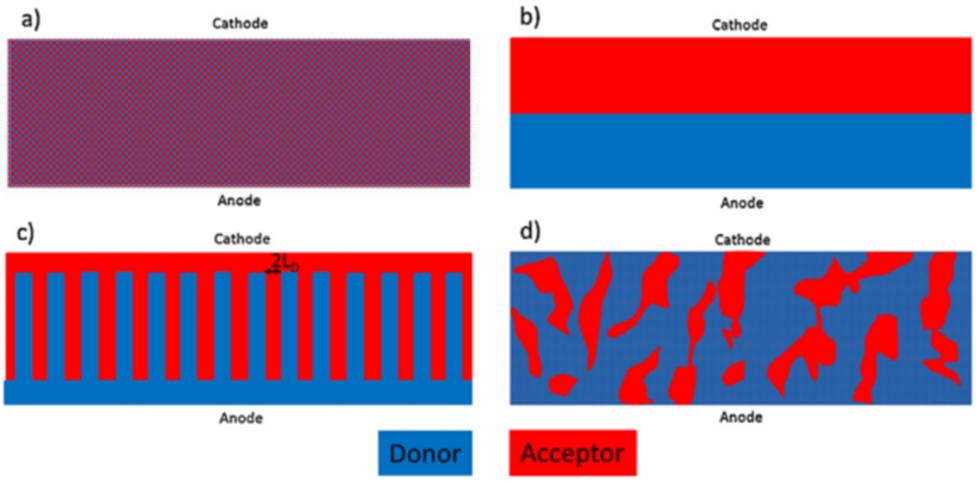

Figure 2.9: Schematic representation of different donor(blue)-acceptor(red) nano-morphologies: **(a)** A very fine mixture of donor and acceptor materials, **(b)** a perfect bi-layer, **(c)** ideal morphology for a 2D SC, with domain sized two times the exciton diffusion length L_D, and **(d)** representation of a real device BHJ. Adapted from [42] and modified,

2.2.1.4 Exciton Movement

In order to achieve a more detailed understanding on the previously described processes, we discuss possible exciton transport mechanisms, i.e. the exciton movement. Let us consider an exciton, located on a donor molecule. One possible pathway of exciton relocation to an acceptor molecule is by non-radiative energy transfer, leaving the donor in the ground state and putting the acceptor in the exited state. This energy transfer happens either through space (Förster) or through a bond (Dexter), as shown schematically in **Fig. 2.10a** and **b**, respectively. [81] Exciton separation is also possible by electron transfer (**Fig. 2.10c**), resulting in a negatively and a positively charged acceptor and donor molecule, respectively. Finally, a transfer mechanism is also possible by radiative exciton recombination and subsequent photon re-absorption by another

molecule.

When there is a significant overlap between the donor emission and acceptor absorption spectra, *Förster resonant energy transfer (FRET)* can take place via dipole-dipole electromagnetic interaction (**Fig. 2.10a**). This energy transfer is typically observed for a molecular distance of $r \sim 1 - 5\ nm$, since its efficiency decreases with r^{-6}. [82, 83] FRET occurs on a nanosecond time scale, [84] and applies only for singlet excitons. [85]

An actual electron exchange between molecules takes place during *Dexter energy transfer* (**Fig. 2.10b**). [86] This mechanism allows for spin functions on both molecules to change simultaneously; hence, all types of allowed and spin-forbidden transitions may occur, including both singlet and triplet exciton transfer. [87] The electron exchange is based on the overlap of molecular orbitals, with a probability thus exponentially decreasing with molecule distance, as would be expected for a tunneling mechanism. Dexter energy transfer typically occurs on a microsecond scale. [85] For singlet excitons, in terms of efficiency, FRET usually outperforms Dexter energy transfer. [88]

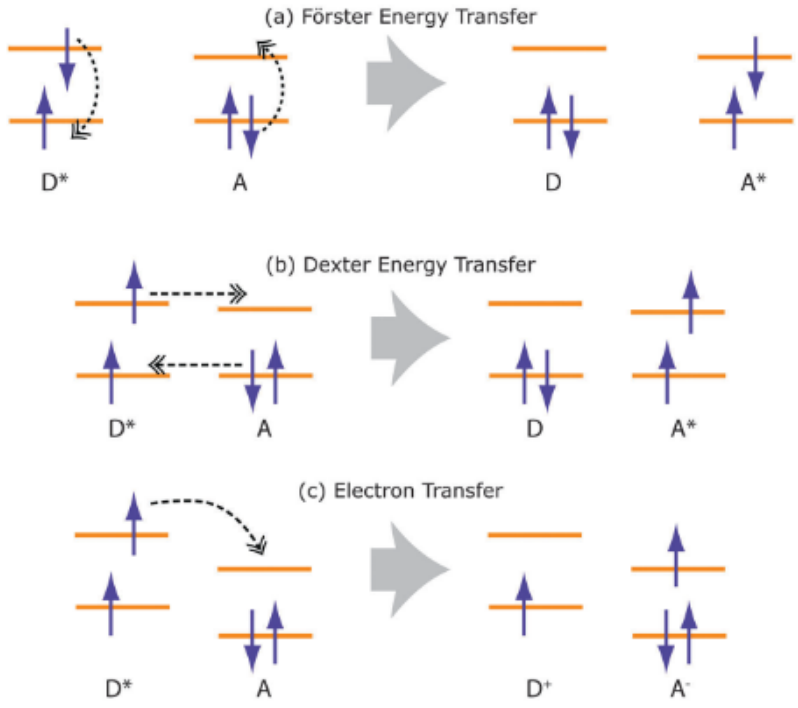

Figure 2.10: Possible exciton transfer and CT state formation mechanisms. Orange, horizontal lines denote HOMO and LUMO energies on the donor (D) and acceptor (A) molecules, with blue arrows representing electrons with corresponding upward or downward spins. Initial and final situations are represented on the left and right, respectively for **(a)** Förster energy transfer, **(b)** Dexter energy transfer and **(c)** Electron transfer from an excited donor molecule (D*) to a neutral acceptor (A). Black dashed arrows represent the rearrangement of the electronic configuration in the corresponding energy transfer mechanisms. Reproduced from [88] with permission from The Royal Society of Chemistry. Copyright © 2015.

An actual *electron transfer* is schematically shown in **Fig. 2.10c**, for which the exciton binding energy needs to be overcome. If, for example, the LUMO (HOMO) of the ac-

ceptor is significantly lower (higher) than that of the excited donor, then electron (hole) transfer can take place at the D/A interface. After this short-range interaction, the donor and acceptor molecules are positively and negatively charged, respectively. [88]

2.2.1.5 Exciton Types

All exciton movement mechanisms are strongly dependent on the BE and other properties of the corresponding exciton. There are three main classes of excitons classified according to their BE or size: *Frenkel*, *Wannier-Mott (W-M)* and *charge transfer (CT) excitons*. A schematic representation of these is shown on **Figure 2.11**.

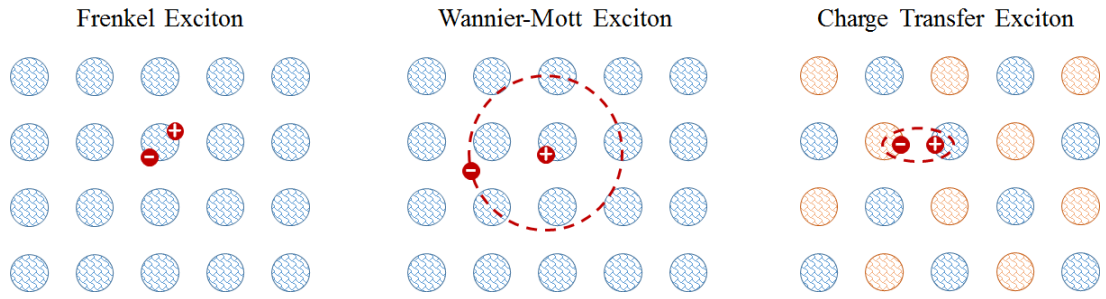

Figure 2.11: Schematics of Frenkel, Wannier-Mott and Charge Trasfer excitons from the left to the right.

Frenkel excitons are present in solids that are made by weakly interacting units, such as molecular crystals and organic semiconductors. The neutral excited state carried around by the exciton is molecular-like, and thus always localized on a single molecule.

W-M excitons are present in densely packed materials, such as covalent solids and inorganic semiconductors. The exciton radius is in this case much larger than the lattice constant and exciton propagation can be described by the relative motion of electron and hole and that of their centre of mass. This system resembles a hydrogen atom where the proton is now a positron. [66, p. 58]

CT excitons are localized on different molecules and thus the distance between electron and hole corresponds to 1-2 times the molecular distance. They are of crucial importance for OSCs, since they are considered as an intermediate state in the creation of free charge carriers by light absorption. [89]

2.2.1.6 Spin Statistics in Excitons

The majority of organic molecules have an electrically neutral ground state with a net spin of zero. [88] After photo-excitation of the ground state, an electron gets excited into a energetically higher state. Possible decay and transition mechanisms will determine whether the electron can or cannot contribute to the overall photocurrent in an OPV devices and will thus determine its performance. We will therefore discuss the majority of such pathway in the following section.

Electronic states with a net spin of *zero* or *one* are called *singlets* or *triplets*, respectively. The BE of singlet excitons is usually on the order of $0.3 - 0.5\ eV$; [90–92] while triplet excitons exhibit higher BE values due to the attractive exchange interaction between the electron and hole of the same spin orientation. [86]

Most organic molecules possess an electrically neutral ground state $\mathbf{S_0}$ with a net spin of zero. Possible electronic states and transitions are shown in a *Jablonski diagram*, in **Figure 2.12**. All shown states are positioned vertically by their energy and grouped horizontally by their spin multiplicity. At this point it should be pointed out that this diagram is not complete: it neglects, for example, for energy migration through the density of states, singlet–singlet annihilation, and singlet fission, and it does not contain coupling with the environment. In real molecules, such coupling is responsible for transition energy renormalization and vibrational cooling (VC), *i.e.* internal energy dissipation to the environment. [66, p. 90]

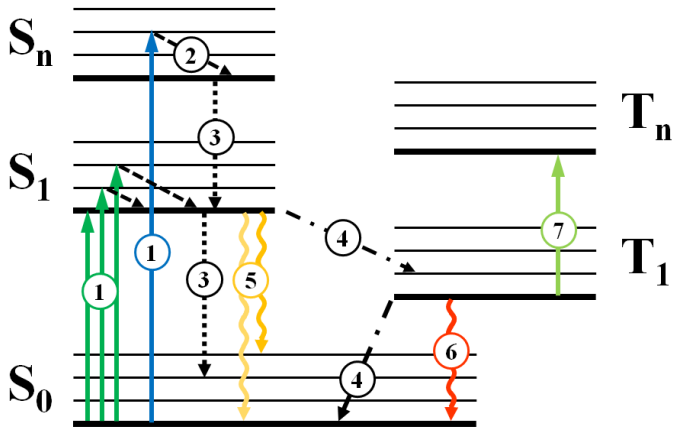

Figure 2.12: Jablonski diagram of electronic transitions in organic semiconductors. Arrows with numbers represent (1) absorption, (2) vibrational relaxation, (3) non-radiative relaxation/-transition, (4) intersystem crossing, (5) fluorescence, (6) phosphorescence and (7) photoinduced absorption. **S** and **T** represent singlet and triplet states, respectively.

Green arrows (**1**) represent absorption of a photon that brings a molecule from the ground state $\mathbf{S_0}$ to the first singlet excited state $\mathbf{S_1}$, or to its higher vibrational states. Transitions to higher singlet excited states are also possible and are represented with a blue arrow (**1**).

Dashed-line arrows (**2**) represent vibrational energy redistribution (down conversion) or vibrational relaxation (VR) of absorbed electrons, initially stored in few optically coupled modes. As a result, the electronic state will appear to be *"relaxed"* in contrast to the initial excited state, however the excess energy at this point is still stored in the molecule. Its vibrational population distribution corresponds to a higher temperature than that of the environment, the molecule is thus still *"hot"*. [66, p. 91] VR typically happens on the $\sim$ *ps* time scale, as also shown in **Table 2.1**.

Internal conversion (IC) (dash line arrows (**3**)) and intersystem crossing (ISC)

(dash-dot line arrow (**4**)) are both non-radiative transitions between states of same spin multiplicity and different spin manifolds, respectively. Typical depopulation rates for these processes can be found in **Table 2.1**. *Fluorescence* (yellow wavy arrows (**5**)) and *phosphorescence* (red wavy arrows (**6**)) are both radiative transitions resulting in the emission of light. These transitions as also called photoluminescence (PL) when they are initiated by photon absorption. These radiative and non-radiative transitions compete with each other, and the outcome of this competition is of crucial importance for the performance of an OSC. While radiative recombination results in an emitted photon, which can get re-absorbed, non-radiative recombination results typically in lattice vibration (a phonon) and is thus an irreversible thermal loss.

Table 2.1: Typical non-radiative depopulation rates for the most common molecular processes. The *"Label"* column refers to the notation in the *Jablonski diagram (Figure 2.12)*. Values adapted from [66, p. 89], Copyright © John Wiley & Sons, 2012.

Process	Label	Typical depopulation rates $[s^{-1}]$	Time scale
VR	**2**	$10^{12} - 10^{13}$	$(0.1 - 1)\ ps$
IC ($S_n \rightarrow S_1$)	**3**	$10^{12} - 10^{14}$	$(0.01 - 1)\ ps$
IC ($S_1 \rightarrow S_0$)	**3**	$10^{8} - 10^{10}$	$(0.1 - 10)\ ns$
ISC ($S_1 \rightarrow T_1$)	**4**	$10^{6} - 10^{11}$	$10\ ps - 1\ \mu s$
ISC ($T_1 \rightarrow S_0$)	**4**	$10^{4} - 10^{1}$	$0.1\ ms - 0.1\ s$

Finally, a light green arrow (**7**) represents the absorption of a photon that brings state $\mathbf{T_1}$ to a higher triplet excited state $\mathbf{T_n}$. This process can be used for the detection of triplet excitons, as in photo-induced transient absorption (TA) experiments. [86] Singlet excitons can in some cases undergo a fission process resulting in two triplet excitons. This process is, however, not discussed further in this thesis; additional information can be found in [93] and references therein.

2.2.2 Recombination Mechanisms

Having discussed the different exciton types, their movement and their importance for PV cells in the previous sections, we can now consider possible processes that can occur on their way to the collecting electrodes more in detail. A simplified overview of the whole photovoltaic process in OPVs for the case of light absorption in the donor molecule is presented in **Fig. 2.13** with a typical historical sequel from the left to the right. First, an exciton is created upon photon absorption, which can freely move within the donor molecule with a diffusion length of only about 10 nm, typical for organic materials. [94] Ideally, it migrates to a D/A interface where it might be separated; however, it has been shown in several reports that before reaching the charge-separated state (CS) they undergo a CT state. [95–97] This occurs when the electron is already spatially located on the LUMO band of the acceptor while the hole is still on the HOMO band of the donor. We note, that in this situation, the charges are still bound by Coulomb force. In the ideal case, CT state separation will take place, and

the free charge carriers (CS) percolate towards the corresponding electrodes and get collected by them, generating photocurrent. This mechanism is often supported by the asymmetry of the electrode work functions, resulting in an internal electric field driving the free charge carriers towards the corresponding electrodes, where they can be collected. However, in reality a lot can go wrong during the processes. Each gen-

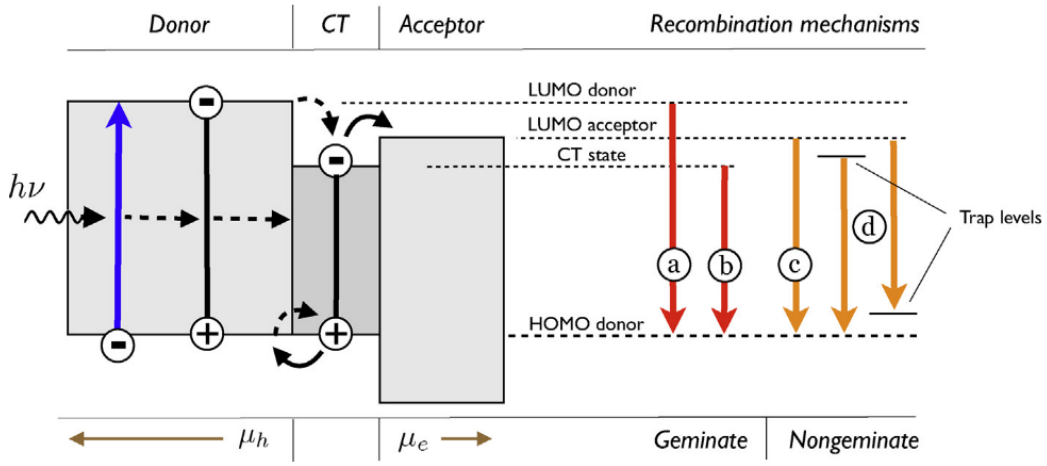

Figure 2.13: From left to right: an incoming photon with energy $h\nu$ (wavy arrow) is absorbed and results in an excitation of an electron at the HOMO level of the donor, forming an exciton. After diffusion to the D/A interface, the CT state is formed with an electron on the acceptor and hole on the donor, subsequent to exciton dissociation, where electron and hole are not bound by Coulomb force anymore. Free electron and hole can drift through the acceptor and donor phases, respectively, to the corresponding contacts. The four most common recombination mechanisms are represented with red (ⓐ and ⓑ) and yellow (ⓒ and ⓓ) arrows on the right, representing geminate and non-geminate loss channels, respectively: ⓐ exciton decay right after excitation, ⓑ CT state recombination, ⓒ bimolecular recombination of a free electron and a free hole and ⓓ trap assisted recombination of a free charge carrier with an oppositely charged trap within the band gap. Reproduced with permission from [14]. Copyright © 2013 Elsevier Ltd.

erated exciton has only a few nanoseconds (See **Table 2.1**) to reach a D/A interface before recombining to the ground state. If the domain sizes are not small enough, such that time is not sufficient for reaching such an interface, it is likely that the exciton will recombine. (Process ⓐ in **Fig. 2.13**) Excitons that make it to the interface and form a CT state may still recombine instead of reaching CS. (Process ⓑ in **Fig. 2.13**) These processes can be referred to as *geminate*[4] *recombination* processes, indicating that the recombining electron-hole pair was originating from a single photon event. There are a lot of factors playing a role in the competition between free charge carrier generation and geminate recombination, such as CT state delocalization and the internal electric field. [14]

After the CS is reached, recombination of an electron with another oppositely

[4]The Latin word geminus means twins, indicating that both charge carriers involved in the recombination process were "born" from the same photon.

charged free carrier on its way to the corresponding electrode is still possible. This recombination mechanism is referred to as *non-geminate recombination*, since the recombining charge carriers do not necessarily originate from the same photon. It includes both *bimolecular recombination (BR)* (Process ⓒ in **Fig. 2.13**), as well as *trap-assisted recombination* (Process ⓓ in **Fig. 2.13**). In the latter, one of the recombining charges is energetically trapped prior to recombination. Non-geminate recombination is the primary loss mechanism in most of the efficient OPV devices and it can be influenced by a variety of factors such as phase separation, layer thickness, energetic disorder and charge carrier mobilities.

2.2.2.1 Geminate Recombination

Geminate recombination includes both exciton relaxation to the ground state before it can reach a D/A interface and interfacial recombination. Typically, interfacial recombination occurs after CT state formation. In both cases, however, the driving force for recombination is the Coulomb attraction between electron and hole. Geminate recombination is considered as a monomolecular process, since the number of geminate pairs scales linearly with the number of absorbed photons, and thus, an only through geminate recombination limited system would scale linearly with light intensity.

Exciton Relaxation to the Ground State Exciton migration, necessary for their separation, is often described via diffusion only, as also described in **Sec. 2.2.1.2**. However, recent studies show an ultrafast free charge carrier generation, within 100 fs, which is far too fast to be explained by diffusion, [98–100] but rather by delocalized excited states. [101] Interestingly, this ultrafast process depends on domain size in a similar manner as what one would expect assuming diffusion. [99] The concept of delocalization is not only important for exciton relaxation but also for V_{OC} loss interpretation, as we will discuss later.

CT Relaxation to the Ground State It has been shown for fullerene derivatives that when an exciton reaches a D/A interface, charge transfer to the bound CT state (by Coulomb force) is initiated by the energetic offset between the two materials. [102–105] Hence, a large research effort has been made to increase these energetic offsets at interfaces even for NFAs, [106, 107] where often an offset value of 0.3 eV was the universal target value for efficient exciton separation. [42] It has been shown, however, for various fullerene and NFA systems that far lower offset values can also result in efficient exciton separation. [35] Further studies proposed that mixed phases, [108] charged defects, [109] or entropy gains [105, 110] may contribute to the free energy gradient and thereby help charge separation. Understanding the nature of this energetic offset is of crucial importance when selecting donor and acceptor materials. Dissociation into the CS state competes with transfer to the triplet CT state and geminate recombination to the ground state. The former can serve as a deactivation pathway if its energy is more

than 0.1 eV lower than that of the singlet CT state; [38, 103] otherwise, the latter will be the dominant loss mechanism.

The role of electronic delocalization and "hot" CT states has not yet been fully understood and the question whether charge transfer from the CT state to CS happens only through the CT ground state, or also from its excited hot states, is an open debate. On the one hand, there is evidence that hot, delocalized CT states can enable more efficient CS generation due to an enhanced entropy resulting from increased effective electron–hole pair separation. [103, 105, 111–113] Interestingly, the probability of populating hot CT states increases with increasing energetic offsets between donor and acceptor. [14] On the other hand, systems have been reported in which hot CT states are not essential to the CS generation process, [114–117] at least not at room temperature. It has been suggested that in systems with a sufficiently delocalized CT ground state, there is no need for the extra energy of hot CT states, and that the degree of delocalization is a function of both molecular and film properties, such as reorganization energy, [112, 113] LUMO degeneracy, [118] and energetic alignment of donor and acceptor. [119] A dependency of charge separation efficiency on the electric field has been also observed for some material systems, depending on the system of choice and even on processing conditions. [20, 120–123]

2.2.2.2 Non-Geminate Recombination

After a geminate pair is successfully separated, the internal field will drive the charges toward the electrodes. However, as the applied bias increases, the driving force and consequently the charge collection efficiency decreases until it reaches zero when the applied bias equals V_{OC}. [100] At such low internal fields, non-geminate recombination starts to play a crucial role, and it can originate from three fundamentally different mechanisms: *bimolecular*, *trap-assisted* (monomolecular) and *Auger* (trimolecular) *recombination*. [14]

Bimolecular Recombination BR includes the recombination of a free electron with a free hole, and it is the most important loss channel in BHJ OPV devices. [124]
It is limited by the rate at which free charge carriers find each other, and is thus mobility dependent, as described by the *Langevin* expression: [14]

$$R_L = \frac{q}{\varepsilon}(\mu_n + \mu_p)(np - n_i^2) \tag{2.8}$$

Here, q is the elementary charge, ε the dielectric constant, n_i the intrinsic carrier concentration and n (p) and μ_n (μ_p) the charge density and mobility of electrons (holes), respectively. This expression has been observed to be valid in OPV devices; [125] however, is has also been questioned by reports which show a field- and morphology-dependent mobility. [120, 126] It is thus important to realize that the mobilities introduced in **Eq. 2.8** refer to values in blend films, which can differ from mobilities of the individual materials measured separately. On the contrary, it has been shown that the

overall BR in OSCs generally decreases with increasing mobility, because of improved charge collection and thus reduced charge carrier density ($n \cdot p$ in **Eq. 2.8**). [127] A minimum mobility of $10^{-8}\ V/m^2s$ for both electrons and holes can serve as a rule of thumb for good device performance, as empirically determined by *Proctor et al*. [14]
Since measurement values of R_L are often smaller than expected from **Eq. 2.8**, [128] the Langevin-reduction factor ζ has been introduced for the net BR rate R_{BI}. By neglecting for n_i and assuming $n = p$:

$$R_{BI} = \gamma_{BMR} n^2 \tag{2.9}$$

where γ_{BMR} is the BR coefficient defined as $\gamma_{BMR} = \frac{\zeta}{\varepsilon}(\mu_n + \mu_p)$and has typical values between 0.01 and 1. [129–131] This reduction in Langevin recombination has been attributed to increased phase separation, [132] spatial variations of electron and hole carrier densities, [133] and neglecting the contribution of the lower mobility charge carrier. [134] BR primarily happens at the D/A interface, and it likely occurs via CT states. [104] Hence, the very same factors decreasing geminate recombination may also be responsible for decreasing bimolecular loss channels. [135]

Trap-Assisted Recombination This loss channel is a first order process involving one electron (hole) recombining with a trapped and thus localized hole (electron). The recombination rate is mainly determined by the density of traps and by how quickly the free carrier can find the trapped one. This process is know in inorganic semiconductors as Shockley-Read-Hall (SRH) recombination, and its rate is given by: [136]

$$R_{SRH} = \frac{C_n C_p N_{tr}(np - n_i^2)}{C_n(n + n_1) + C_p(p + p_1)} \tag{2.10}$$

where C_n (C_p) is the probability rate of an electron (hole) getting trapped by an empty trap, N_{tr} is the density of electron traps and $n_1 \cdot p_1 = n_i^2$. In organic devices, where $n \approx p$ and $np \gg n_1 p_1$, and in the case of electron trapping ($C_p \ll C_n$), **Eq. 2.10** reduces to: [137]

$$R_{SRH} = C_p N_{tr} p, \text{ with } C_p = \frac{q}{\varepsilon}\mu_p. \tag{2.11}$$

Due to this dependency on hole mobility, trap-assisted recombination is also thermally activated and dictated by free carrier transport. [137] Since this happens through isolated domains, trapped carriers must be within hopping distance of a D/A interface in order to efficiently recombine with the free charge carriers. Otherwise, if they are further away, they are likely to be thermally re-emitted.
Generally, the majority of efficient OPV systems do not appear to be limited by trap-assisted recombination, [100] and trapping is only important in systems where chemical impurities are introduced, such as it is often the case during degradation.

Auger Recombination A further possible non-gemiate loss channel is Auger recombination, which is a three particle process. [138] In this case, after the recombination,

the freed-up energy is transferred to a third electron which is then excited to a higher energetic state, happening at the following rate:

$$R_{Auger} = (\Gamma_n n + \Gamma_p p)(np - n_i^2) \tag{2.12}$$

where Γ_n and Γ_p are the Auger coefficients. Auger recombination happens only at a charge carrier density, higher than it is the case in OSCs, it has been thus not directly observed in OPV devices, [59] we will thus not describe this mechanism further.

2.2.3 Intensity Dependent Solar Cell Parameters

Intensity-dependent current-voltage studies can help to understand first-order (monomolecular) and second-order (bimolecular) recombination processes in BHJ OPV devices, [139] important for a deeper understanding of recombination kinetics and thus the optimization of solar cell performance. First- and second-order recombination are dominant at short circuit and open-circuit conditions, respectively: as we move from short circuit to open-circuit, the external voltage V is increased, leading to a decreased internal voltage ($V_{int} = V_{bi} - V$, with V_{bi} being the built-in potential), resulting in an increased carrier density and thus a transition from first- to second order recombination kinetics. [140] This is important to keep in mind, when interpreting IV curves of OPV devices. Let us now discuss these two regimes in more detail.

2.2.3.1 Effects on the Short-Circuit Current

Light intensity-dependent measurements at short circuit, carried out by *Cowan et al.* [139] on numerous material systems resulted in an experimental observation of $J(V) \approx I^{\alpha}$, where $\alpha \approxeq 1$. This holds for all tested systems for all currents where $-0.5 < V < V_{MPP}$, where V_{MPP} is the voltage at maximum power point, and thus also for J_{sc} where the applied voltage equals zero. Testing thus J_{sc} for different light intensities (I) results in the coefficient α, being a measure for recombination processes happening at short circuit. They claim that in this voltage range, monomolecular recombination dominates and that $\alpha \equiv 1$ when all carriers are swept out prior to recombination. It could also mean, however, that no recombination is happening in the device. [141] Powers less than 1 could result from space charge effects, BR, variations in the continuous distribution in the density of states or variations in electron and hole mobilities. [139, 142, 143]

2.2.3.2 Effects on the Open-Circuit Voltage

In early reports, [144, 145] the temperature dependence of V_{OC} was explained by making use of the description of an ideal diode, such as a p-n junction Si solar cell, for which the V_{OC} reads: [146]

$$V_{oc} = \frac{k_B T}{q} ln\left(\frac{J_{sc}}{J_0} + 1\right) \tag{2.13}$$

where J_0 is the reverse bias saturation current density described in great detail in [146]. **Eq. 2.13** is, however, only valid for an ideal diode since it is derived under the assumption that the photo-current J_{ph} of the device equals the J_{sc} for any applied voltage. This is, however, often not the case for OPV devices. [147] To overcome this problem, an ideality factor n is often introduced to the right side of **Eq. 2.13**. [102]

Another approach is to derive the V_{OC} from the number of charge carriers and their recombination. When an OPV device is under illumination at open circuit, the current is zero and hence all photogenerated charge carriers recombine within the cell. The resulting V_{OC} is then equal to the difference between the quasi-Fermi levels of the phase separated donor and acceptor domains, [139] resulting in:

$$V_{oc} = \frac{1}{e}\left(E_{LUMO}^{Acceptor} - E_{HOMO}^{Donor} - \Delta\right) - \frac{k_B T}{e} ln\left(\frac{n_e n_h}{N_c^2}\right) \tag{2.14}$$

where e is the electron charge, $k_B T$ the thermal energy, n_e and n_h the electron and hole densities in the acceptor and donor at open-circuit, respectively, and N_c the density of conduction states, which is assumed to be equal for both the acceptor and donor. The energetic shift Δ, introduced by *Cowan et al.* [139], is associated with disorder. At finite temperatures, due to Fermion statistics and thus disorder, the quasi-Fermi levels move away from the HOMO and LUMO into the gap, decreasing the built-in potential (V_{bi}). [139]

At open-circuit, since the overall current is zero and all charge carriers recombine, the electron and hole densities n_e and n_h within the device are equal and can be written as n_{oc}. The generation rate G of excitons at open-circuit equals their recombination and can be thus written as: [139]

$$G = \frac{n_{oc}}{\tau_r} + \gamma n_{oc}^2 \tag{2.15}$$

where τ_r is the monomolecular recombination lifetime and γ is the BR coefficient.

At open-circuit the latter term is dominant, leading to a generation rate of $G \approx \gamma n_{oc}^2$. This can now be plugged in **Eq. 2.14** and by taking into account that γ and N_c are independent on light intensity I while single photon processes and G are linearly dependent on it, [147] one gets for the change in V_{OC}:

$$\delta V_{OC} \propto \frac{k_B T}{q} ln(I) \tag{2.16}$$

On the contrary, if monomolecular recombination would be the main contributor at open-circuit conditions, **Eq. 2.15** would simplify to $G \approx \frac{n_{oc}}{\tau_r}$, resulting in:

$$\delta V_{OC} \propto \frac{2k_B T}{q} ln(I) \tag{2.17}$$

In summary, measuring the slope of δV_{OC} vs. I can help to understand recombination processes under open-circuit conditions. Pure bimolecular and monomolecular recom-

binations are indicated by a slope of $1 \cdot \frac{k_B T}{q}$ and $2 \cdot \frac{k_B T}{q}$, respectively. Other pre-factors can indicate a mixture of these two recombination types. A slope higher than $\frac{k_B T}{q}$ can also result from trap-assisted recombination. [137] One should pay attention when interpreting results since this technique only delivers reasonable results at intensities at which the dark current is low and does not perturb the V_{OC} dependence. This can be double-checked by monitoring the change in FF: if this significantly drops at low intensities, than the dark current is too high and the results could be misleading. [14]

2.3 Energy Level Alignment at Interfaces in Organic Semiconductors

2.3.1 Introduction

In this section we will mainly discuss how energy levels in organic materials align. The weak *van der Waals* forces[5] between individual organic molecules, such as polymers or small molecules, result in completely localized HOMO and LUMO levels in solid films. [69] The resulting electronic structure of the overall film thus reflects that of an individual molecule or single polymer chain. On the one hand, this is also the reason why density functional theory (DFT) calculations of individual molecules can be applied to estimate the overall energetics. On the other hand, usual band theory including band transport, as applied for inorganic materials, is not applicable at room temperature, [69] except for highly crystalline, high-mobility organic materials. [148]

OPV devices, however, consist of not one but multiple layers, including organic semiconductors, dielectrics, metals or other types of conducting electrodes. The electronic structure and thus the energetic alignment between these interfaces will strongly affect the overall performance of OPV devices, influencing mainly charge *injection*, *extraction* and *transport*. [149] Transport properties depend for example on molecular orientation across the interface and the relative positions of the relevant electronic transport levels across this boundary region. These levels are the Fermi level of the metal or conducting electrode, and the HOMO and LUMO levels in an organic semiconductor for holes and electrons, respectively. Injection barriers for the corresponding charge carriers are defined by differences between these levels. An adequate measurement of these is, however, non-trivial, especially due to interfacial effects.

When an organic material is brought into contact with another material, the adsorption process can be very different depending on the interaction strength between these two layers. This process is not only dependent on the materials themselves, but also on the preparation method and the order in which the materials were brought

[5] A more detailed description can be found in **Chapter 2.2.1.1**.

into contact. [150–152] In order to be able to predict the energy-level diagram for a particular interface, the method of interface formation needs to be known. Although there is no universal model for describing energetic alignment of all existing interfaces, models successfully predicting different subsets of interface types do exist. In the next sections, we will discuss 3 different types of interfaces:

1. *Organic/passivated substrate* interfaces
2. *Organic/organic* interfaces on a passivated surface
3. *Organic/clean metal* interfaces

The first two are almost non-interacting interfaces, such as contaminated or passivated metal surfaces (any metal prepared or treated under ambient conditions), and π-conjugated molecules and polymers (e.g. PEDOT:PSS). [153] In these two cases there will be barely any charge transfer between the surfaces. [69] The third category includes stronger, but still only weakly interacting interfaces, such as it is the case, when evaporating organic materials on top of non-reactive clean metals, or vice versa. [154]

This section starts with a discussion of some general facts important to understand organic interfaces, including the impact of charges on organic molecules and the difference between optical and electronic gaps. Next, the three interface types introduced above are discussed in more detail including the integer charge-transfer (ICT) model and the importance of gap states. Note, that there is a difference between the CT state termed in previous sections (referring to an exciton with hole and electron being located on the HOMO of the donor and the LUMO of the acceptor, respectively), and the ICT model (which introduces extra sub band gap states, as discussed more in detail later on).

2.3.2 Electronic Structure of Organic Materials

In this section, two main effects not present in inorganic semiconductors will be discussed, both arising from the substantially lower dielectric constant of organic materials: the impact of charge carriers and the exciton BE on the energy levels.

2.3.2.1 Effect of Charges on the Electronic Structure

It is important to keep in mind that the occupation of a molecule by a charge carrier has important consequences regarding the electronic structure of this molecule: [89]

(1) This central charge polarizes the surrounding molecules, which in turn stabilize the central charge. This stabilization is on the order of $1 - 1.5\ eV$, depending on several factors including molecular arrangement and polarizability of the molecule. [155–157]

(2) The central charge also leads to an atomic and electronic reorganization of the hosting molecule, resulting in an atomic as well as a lattice relaxation. The coupling between charge and atomic relaxation, often termed electron- (hole-) phonon interaction, further lowers the energy of the molecular ion by $\sim 0.1eV$. Additionally, the lattice relaxation contributes in the range of 10 meV. [156]

Polarization of the surrounding medium is expected to depend significantly on the exact position of the occupied molecule. Next to a metal surface for example, polarization is higher due to the considerably higher polarizability of the metal, resulting in a difference on the order of 0.2 eV for small molecules. [157] Conversely, the opposite effect occurs at the surface of an organic film due to an incomplete surrounding. Consequently, the HOMO and LUMO energy positions are expected to vary from interface to bulk to surface. [149]

2.3.2.2 Difference Between Optical and Electronic Gaps

In the first investigations of organic semiconductors their electronic structure was treated in analogy to inorganic materials and, as a consequence, the energetic difference between HOMO and LUMO (the energy gap) was measured with optical absorption spectroscopy. [158, 159] It is important to realize, however, that there is a difference between the optical gap (OG) and the electronic gap (EG) in these materials: [69] in optical absorption experiments, an electron–hole pair is created by photon absorption and the OG is derived from the absorption onset. While in inorganic materials, this electron-hole pair immediately dissociates into free charge carriers, in organic materials it may still be bound due to Coulomb interaction forming thus an exciton. Therefore, the measured OG is smaller than the EG by exactly the exciton binding energy. In the case of strongly localized *Frenkel excitons*, the binding energy may be as large as 1 eV. [158] A possible way of determining the EG is by UPS, x-ray photoemission spectroscopy (XPS) and inverse photoemission spectroscopy (IPES). [158, 160, 161].

2.3.3 Energy Level Alignment at Organic/Passivated Substrate Interfaces

Most of the interfaces covered in this thesis will be described in the following section. Most commonly used passivated substrates processed under ambient conditions include indium tin oxide (ITO), PEDOT:PSS, and zinc oxide (ZnO). The latter two serve as hole transport layer (HTL) and electron transport layer (ETL), transporting only holes and electrons, while blocking the opposite charges, respectively. Energetic alignment at such interfaces determines charge injection and extraction. In the case of minimal interaction at these interfaces, simple vacuum level alignment can be expected, described by the Schottky–Mott limit (**Fig. 2.14b**). This occurs when the interface formation process does not induce any interfacial states in the HOMO-LUMO gap of the organic semiconductor. [162] A deviation from this limit is expected when the work function (Φ) of the metal is either lower or higher than the organic material's

HOMO or LUMO, respectively (**Fig. 2.14a** and **c**). In both cases the ICT model predicts an excessive charge exchange. [149] In this section we will discuss a these effects and models describing them in more detail.

2.3.3.1 The Integer Charge-Transfer (ICT) Model

The ICT model describes interfaces at which the hybridization between substrate wave functions and π-electronic molecular orbitals is negligible: interfaces formed under ambient conditions, solution processed layers, organic/organic interfaces and interfaces formed on substrates passivated by oxides or hydrocarbons. [69] The energy of a positive (negative) ICT state E_{ICT+} (E_{ICT-}) is defined as the *energy required to take away one electron from* (*energy gained when one electron is added to*) the organic molecule producing a fully, electronically and geometrically, relaxed state. This way, new states appear in the previously forbidden band gap between the HOMO and LUMO. Utilizing this effect, *Braun et al.* [69] proposed a sharp transition between a Fermi-level pinning and a vacuum level (VL) alignment regime (Schottky–Mott limit) as summarized in **Table 2.2** and visualized in **Fig. 2.14**. In the VL alignment regime, the work function of the organic material Φ_{ORG} is dependent on that of the metal substrate Φ_{SUB}, whereas in the Fermi-level pinning regime, where Φ_{SUB} is greater as E_{ICT+} or smaller as E_{ICT-}, this is not the case and charge transfer takes place. This has been shown to be true in multiple studies, [69, 153, 163] for a variety of different substrates (including aluminium (Al), Si, Gold (Au), ITO and PEDOT:PSS) and organic materials (including poly(3-hexylthiophene) (P3HT)).

Table 2.2: The three different regimes for energy level alignment predicted by the ICT model, as also schematically drawn on **Fig. 2.14**. Note, that in this case Φ_{SUB} is the real substrate work function after taking into account the push-back effect. Adapted from [69].

Label on Fig. 2.14	Initial energetics	Alignment type
(a)	$\Phi_{SUB} > E_{ICT+}$	Fermi level pinning to E_{ICT+}, Φ_{ORG} independent of Φ_{SUB}
(b)	$E_{ICT-} < \Phi_{SUB} < E_{ICT+}$	Vacuum level alignment, Φ_{ORG} dependent on Φ_{SUB}
(c)	$\Phi_{SUB} < E_{ICT-}$	Fermi level pinning to E_{ICT-}, Φ_{ORG} independent of Φ_{SUB}

In the first case (**Fig. 2.14a**), when $\Phi_{SUB} > E_{ICT+}$, bringing the organic material in contact with the substrate will result in charge transfer: electrons will spontaneously begin to flow towards the substrate, thereby increasingly positively charging the organic material, creating thus a potential dipole. This process continues until an electron transfer through this interface costs no energy, i.e., Φ_{SUB} and E_{ICT+} together with the introduced dipole are equal. In such a case a further increase of Φ_{SUB} would not change the alignment in any way, but would only introduce a greater dipole at the VL.

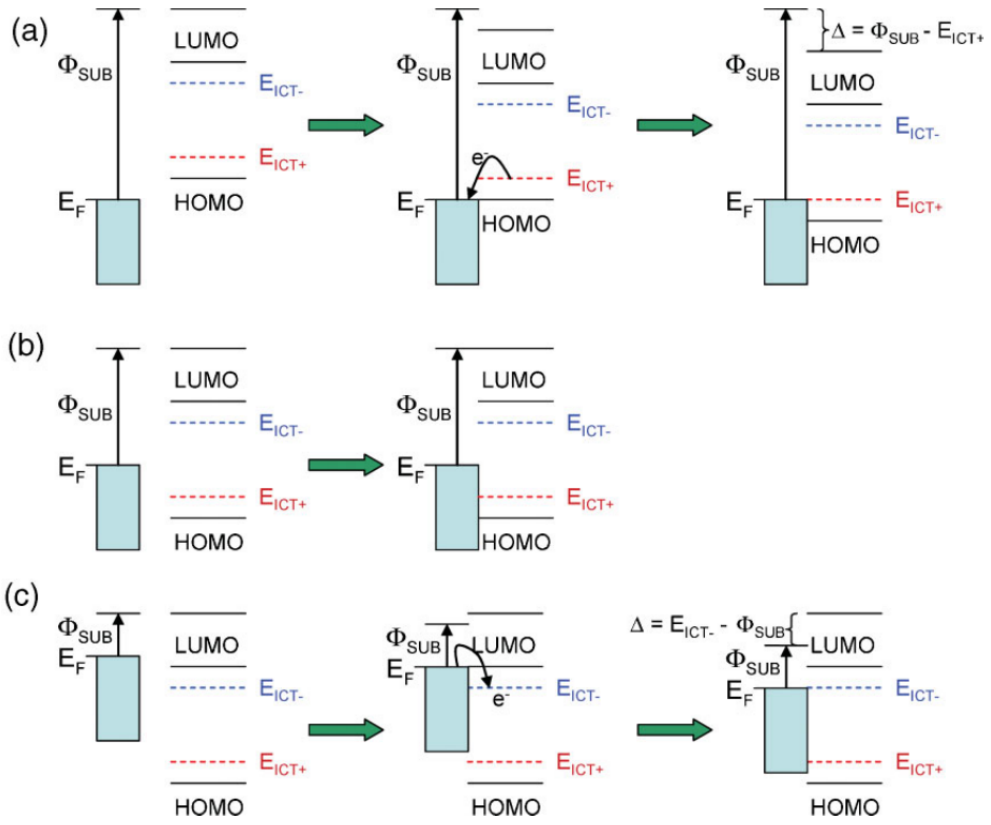

Figure 2.14: Schematics of the ICT model and the three regions it predicts depending on the substrate work function Φ_{SUB}: **(a)** Fermi level pinning to the positive charge transfer state E_{ICT+} in case it is smaller than Φ_{SUB}, **(b)** vacuum level alignment in the case when Φ_{SUB} is between the positive and negative integer charge transfer states and **(c)** Fermi level pinning to the negative charge transfer state E_{ICT-} in case it is greater than Φ_{SUB}. Reproduced with permission from [69]. Copyright © 2009 WILEY-VCH Verlag GmbH & Co. KGaA, Weinheim

In the Schottky-Mott limit (**Fig. 2.14b**), when $E_{ICT-} < \Phi_{SUB} < E_{ICT+}$ no charge transfer occurs. A charge transfer would be only possible by hole creation in the organic material and electron creation in the substrate or vice versa. However, the first is energetically unfavourable because $\Phi_{SUB} < E_{ICT+}$, and the latter due to $\Phi_{SUB} > E_{ICT-}$. Hence, no charge transfer takes place and there is a vacuum level alignment, without any offset.
Finally (**Fig. 2.14c**), when $\Phi_{SUB} < E_{ICT-}$, the very same thing happens as in the first case, but in the opposite direction: a dipole at the interface in the other direction is created by an electron transfer from the substrate into the organic material.

2.3.3.2 The ICT Model on Organic/Conducting Substrate Interfaces

The predictions made by the ICT model have been tested for a variety of material systems, with one particular material system covering all three proposed energy level

alignment regimes (equivalently marked in **Fig. 2.15**): [164]

(a) Fermi level pinning to E_{ICT+} (Ohmic contact)

(b) VL alignment (Schottky barrier) and

(c) Fermi level pinning to E_{ICT-} (Ohmic contact).

In their study, *Crispin et al.* spin-coated an alternating polyfluorene, called "APFO-Green1", on top of different substrates (such as barium oxide, oxidized Al, plasma cleaned Au, ITO, etc.) with a variety of Φ_{SUB}. This study is particularly interesting since it gives experimental evidence for all three by the ICT model proposed alignment regimes, marked with (a), (b), and (c) in both **Fig. 2.14** and **Fig. 2.15**.

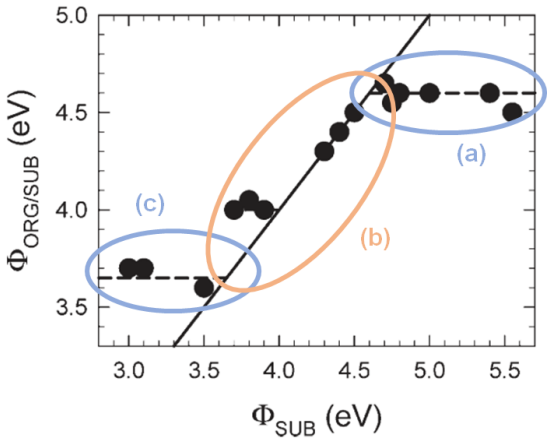

Figure 2.15: Work function of the organic material $\Phi_{ORG/SUB}$ deposited on a variety of substrates with Φ_{SUB} for the exemplary organic molecule *APFO-Green1*. [164] Solid and dashed lines with a slope 1 and 0, respectively, are added as guides for the eye. Reproduced with permission from [69]. Copyright © 2009 WILEY-VCH Verlag GmbH & Co. KGaA, Weinheim

2.3.3.3 The cases of PEDOT:PSS and ZnO

Since most of the solar cells and films investigated in this thesis were prepared on Glass/ITO/PEDOT:PSS or Glass/ITO/ZnO substrates, they are discussed more in detail below.

PEDOT:PSS PEDOT:PSS is a conducting polymer with its Fermi level aligned to the underlying substrate and a constant Φ independent of the choice of substrate or of possible intermediate layers. [165]

ZnO ZnO has a constant Φ, surface roughness, and morphology independent of layer thickness. [166] The conductivity of ZnO can be enhanced by oxygen desorption, induced for example by UV exposure. [166] Such exposure also introduces slight changes in surface stoichiometry. [167] Interestingly, the overall Φ of ZnO can be

controlled over wide ranges (up to 2.8eV) by adsorbing self-assembled monolayers (SAMs) on its surface. [168] This happens in a way that is phenomenologically similar to work function changes of metals. However, $\Delta\phi$ relies on two complementary mechanisms due to an electron transfer to the adsorbed SAM: band bending in the ZnO itself and formation of a dipole at the interface. [169]

2.3.4 Organic/Organic Interfaces

Organic heterojunctions can be considered as nearly non-interactive due to the weak interaction between molecules. Hence, the ICT model for metal/organic interfaces introduced above should also hold true, and has been indeed successfully applied to various cases of multiple layers comprised of organic semiconductors. [69] However, in the case of organic/organic interfaces, not only is their energetic position with respect to the substrate Fermi level important, but also the relative position of their ICT state energies. [154] This has been very nicely visualised by depositing the same stack of two organic materials on top of two different substrates and showing that the resulting energetic alignment is not only substrate dependent, but is also greatly influenced by the order in which the organic layers were deposited.

The deposition of the organic materials 4,40-N,N0-dicarbazolyl-biphenyl (CBP) and 4,4,400-tris[3-methyl-phenyl(phenyl)amino]triphenylamine (m-MTDATA) on either ITO/PEDOT:poly(perfluor- oethylene sulfonic acid) (PFESA) or Si with a thin native oxide on top in this and in reversed order results in completely different final energetics as shown in **Fig. 2.16 and 2.17**, respectively.

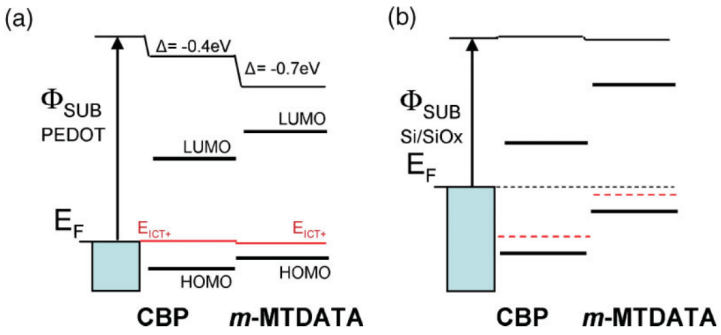

Figure 2.16: Schematic energy level alignment including Φ_{SUB}, HOMO and LUMO levels and integer charge transfer energies derived from UPS measurements, [154] for the bi-layer systems: **(a)** $PEDOT : PFESA/CBP/m-MTDATA$ and **(b)** $Si/SiO_x/CBP/m-MTDATA$. The energetic alignment follows the predictions of the ICT model. Note, that the only difference to **Fig. 2.17** is the deposition order of the organic materials. Reproduced with permission from [69]. Copyright © 2009 WILEY-VCH Verlag GmbH & Co. KGaA, Weinheim

Fig. 2.16(a) shows that the deposition of CBP on PEDOT:PFESA introduces a dipole of 0.4 eV and a Fermi level alignment to E_{ICT+} of CBP. The deposition of m-MTDATA on top of this stack, with the lowered VL, introduces another dipole of 0.7 eV and a realignment of the Fermi level to E_{ICT+} of m-MTDATA. Interestingly, when the same stack was deposited on top of Si (**Fig. 2.16(b)**), no changes in the VL were observed

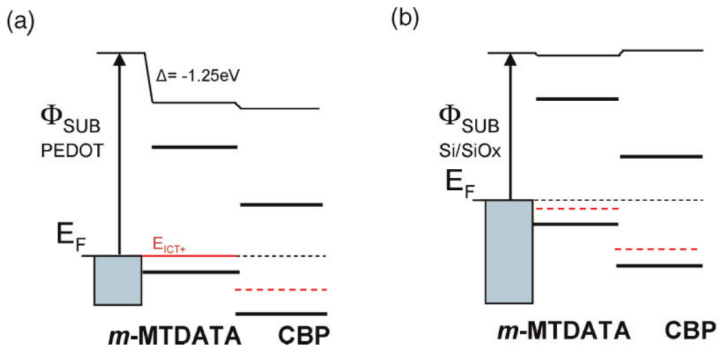

Figure 2.17: Schematic energy level alignment including Φ_{SUB}, HOMO and LUMO levels and integer charge transfer energies derived from UPS measurements, [154] for the bi-layer systems: **(a)** $PEDOT : PFESA/m-MTDATA/CBP$ and **(b)** $Si/SiO_x/m-MTDATA/CBP$. The energetic alignment follows the predictions of the ICT model. Note, that the only difference to **Fig. 2.16** is the deposition order of the organic materials. Reproduced with permission from [69]. Copyright © 2009 WILEY-VCH Verlag GmbH & Co. KGaA, Weinheim

because the substrate Fermi level was in between both E_{ICT} levels for both materials. Since the latter argument holds true independent of organic material deposition order, no changes in the VL were expected when depositing the organic materials vice versa on top of Si (**Fig. 2.17(b)**). The situation changes, however, when changing the deposition order on top of the PEDOT:PFESA substrate (**Fig. 2.17(a)**). In this case, the deposition of m-MTDATA introduces a dipole of 1.25 eV and a Fermi level alignment to E_{ICT+} of m-MTDATA. Further deposition of CBP does not introduce any dipoles to the VL, since the new Fermi level with the lowered VL lies in between the E_{ICT} levels of CBP.

Considering the above discussed cases, the HOMO and LUMO level positions of these materials depend on (i) the work function of substrate used and on (ii) the deposition order, failing thus energy-level alignment symmetry. [69] It is the equilibration of the Fermi level across the full layer stack that determines energy-level alignment, and not the electronic coupling at the individual interfaces. Furthermore, energetic alignment can be also influenced by film morphology, which can influence the charge carrier delocalization in films and thus the charge transfer energies, and by degradation, which can change the chemical structure of individual layers and interfaces.

2.3.5 Energetic Alignment at Organic/Metal Interfaces Manufactured by Chemisorption

Energy level alignment of thermally evaporated metals or organic materials on organic layers or clean metal films, respectively, often differs from strictly non-interactive interfaces, vacuum level alignment and consequently the ICT model. [163, 170–172] This can lead to a restriction of the Fermi level movement, potentially caused by

several phenomena: [149]

- *Metal-induced gap states in the semiconductor:* The metal wavefunction for ultra-high vacuum (UHV) deposited metals can penetrate into the first few molecular layers of the organic material, resulting in a quasi-continuum of states. [173, 174] This will reduce charge transfer at the interface, and consequently the alignment will be less dependent on Φ_{SUB}, which will limit the Fermi level movement. [175, 176]

- *Push-back effect:* The work function of metals can be changed by contamination or for example an organic monolayer (SAM). [150] Normally, the wave function of electrons in the metal extends out into the vacuum, which is changed when depositing an organic material on top: metal electrons are pushed back into the metal due to the repulsive force of the occupied electron orbitals of the deposited material. The same applies in the case of contamination on top of metal surfaces.

- *Defect formation:* Defects at metal/organic interfaces can be chemical or structural in nature, introducing new discrete energy levels in the semiconductor gap. [176] These new states will exchange charges with the substrate and, again, limit the Fermi level movement at the interface. Additionally, when evaporating metal on organic materials, the metal atoms will often diffuse into the organic film, resulting in a rough interface. [151, 152]

All these effects add up and result in a final energetic alignment. The overall energetic picture will be very complicated; however, when evaporating organic materials on metals, one can just view the metal surface and the first few organic layers as a new substrate and assume that the following organic layers will not interact with this surface any more. For further estimations, one can use the ICT model as described above in **Sec. 2.3.3.1**. In this work, however, no results for organic material evaporation are shown, and we will thus only mention a few effects which could be of interest for completeness. More details on such interfaces can be found elsewhere ([69, 172]).

2.3.5.1 The Push-Back Effect

The work function of most metals can be found in literature, measured with different techniques. The work function of Au, for example, is commonly measured with UPS and its value is typically $\Phi_{Au} = (5.2 \pm 0.1)\ eV$. [69] This value, however, is obtained for atomically clean surfaces prepared and measured under UHV conditions at a typical pressure of $10^{-9} mbar$ or better. This is 2-4 orders of magnitude lower than the pressure of $\sim 10^{-6} mbar$ typically used for metal deposition. Most metal films prepared at this higher pressure are slightly oxidized. Furthermore, exposure to air results in thin (saturated) hydrocarbon layers, which is typical for Au and ITO, [69] leading to a reduction of Φ_{Au} by up to $\sim 1\ eV$. [177] Additionally, the processing

temperature also influences the final work function. [178] Even though there is almost no charge exchange between the hydrocarbon contamination and the metal surface, the metal work function is still modified. [69] This mechanism is called the push-back effect. Interestingly, this effect applies for both cases: metal evaporated on top of organic films or vice versa. [179]
One can also make use of this effect by a purposeful change of Φ by for example SAMs. [180] Such modifications of Φ can be of great importance regarding carrier extraction and injection. Interestingly, the change in work function is not only dependent on the used SAM, but also on the underlying metal. [170]

The extent of the dipole induced by SAMs can be estimated by: [181]

$$\Delta\phi = \frac{eN\mu}{\varepsilon_0\varepsilon} \tag{2.18}$$

where e is the elementary charge, N the area density of dipoles on the surface, μ the dipole moment of the isolated molecules forming the monolayer, ε_0 the vacuum permittivity and ε the *effective* relative dielectric constant with typical values between 2 and 3. This equation only holds true when the molecules are not sitting on top of each other, but rather build one layer (*island growth*); otherwise, a dipole-dipole depolarization can take place.

2.3.5.2 Chemisorption Induced Dipole

The formation of a chemical bond at an interface will change the electron density on the adsorbate, and thus introduce a partial charge transfer between the two layers. The direction of this is determined by the chemical potentials of the two layers: μ_{SUB} and μ_{ORG}, with charges flowing from higher to lower chemical potentials. For a metal, this equals its work function, while for organic materials, the middle of their IP and EA is a good estimate. The amount of transferred charge can be then estimated by: [182]

$$\Delta N = \frac{\mu_{SUB} - \mu_{ORG}}{2 \cdot (\eta_{SUB} + \eta_{ORG})} \tag{2.19}$$

with η_{SUB} and η_{ORG} being the absolute hardness of the substrate and the organic material. This quantity is inversely proportional to the density of states (DOS) at the Fermi level: harder materials will thus accept less charge. [170]

2.3.6 Band Bending

While the concept of band bending is well understood for inorganic semiconductors, it is not fully understood for organic materials. Band bending occurs when charge is exchanged between interfaces, which is theoretically only the case for organic materials in close vicinity of a metal surface. [69] Nevertheless, band bending over more than just a few atomic layers has been demonstrated for π-conjugated molecules on

metal surfaces. [183] Such band bending can occur when, for example, the films are slightly doped by impurities from synthesis or induced by the atmosphere. The latter was studied with a controlled amount of exposure to oxygen, yielding an increased p-doping and a depletion region of up to 20 nm. [184] The more organic molecules are purified or the less they get exposed to the atmosphere, the less band bending should their interfaces show. [69] There are other approaches, however, to describe band bending.

2.3.6.1 Gap States - Replacing the ICT model?

The ICT model described in the previous sections is a useful tool for energetic alignment approximation. However, it assumes a band like electronic structure, which is not the case for organic materials, where delocalization results in hopping like transport. [149] The difference between the HOMO (LUMO) and the introduced E_{ICT+} (E_{ICT-}) is generally of the order of $400 - 600$ meV measured by UPS (IPES) and has been interpreted as described in **Sec. 2.3.3.1** by the ICT model. [153, 185] This interpretation implies, however, that the extraction (injection) of a photo-induced electron measured by UPS (IPES) is of the same order ($400 - 600$ meV). Nonetheless, theoretical computations show $3 - 4$ times lower molecular deformation energies for such photoemission spectroscopy (PES) measurements, casting doubts on the validity of the ICT model. [149]

The presence of a significant density of gap states, exponentially decreasing from the HOMO edge on, has been concluded by various techniques, including scanning Kelvin probe [186, 187] and high-sensitivity PES. [188] In this picture, charge carrier transport in organic materials is described in terms of *hopping* between delocalized, Gaussian distributed states and *trapping* in deeper, more localized trap states. The idea of trapping also explains why the charge carrier mobility increases when increasing the number of charge carriers introduced to the system: detrapping requires time and energy and therefore, once a trap is filled it stays this way for a little while. That also means that traps can be filled up. Hence, at lower carrier densities, trapping decreases charge carrier mobility, while as traps get more and more filled up, they become inactive and charge carrier mobility thus increases. The energy required for detrapping depends on the density and depth of the traps below the LUMO or above the HOMO for electrons or holes, respectively.
But what does it mean for interfaces? As already mentioned above, Fermi level pinning was frequently observed slightly above the HOMO or below the LUMO between electrodes and organic materials. Looking at this fact from the gap state perspective, it is fully consistent with the idea of gap state densities. As the substrate work function approaches, and thus the Fermi level moves through the upper (downer) tail of the gap states at the HOMO (LUMO), it also moves through an increasing density of filled (empty) tail states, which become depleted (filled) and positively (negatively) charged. This will result in a significant charge transfer, however, only at the interface and not in the bulk of the organic layer, resulting in *"band bending"* at the metal/organic inter-

face. [149, 189]

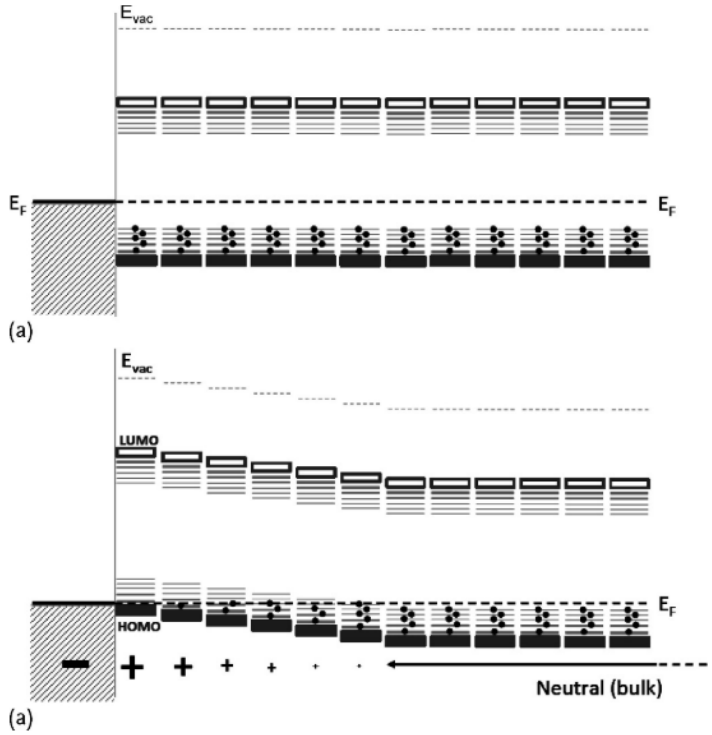

Figure 2.18: Energetic alignment at a metal/organic interface, emphasizing the role of gap states. **(a)** Vacuum level alignment case, where the substrate work function is well within the band gap of the organic material. **(b)** As the substrate work function approaches the HOMO of the organic material, a charge transfer is induced resulting in a bending of both the transport levels, HOMO and LUMO, and the vacuum level. Reproduced with permission from [149]. Copyright © 2013, Wiley-VCH.

2.3.6.2 Insights from Simulations

Organic layers are never free standing entities and are always prepared on conducting substrates with a constant Fermi level and an infinite reservoir of charges. Electronic equilibrium across the entire junction and thus a common Fermi energy (E_F) needs to be given; otherwise, charge carriers could not freely move through the junction. [154] There are two energetic alignment types: (i) interface dipoles due to charge transfer between molecules at the interface and (ii) band bending due to extended space-charge regions on either side of the interface. [190]

So far, deviations from VL alignment have been explained by Fermi level pinning to the corresponding ICT energies. *Oehzelt et al.* developed a model in which organic materials are discretized into laterally homogeneous sheets at an interval Δz, with each sheet having material-specific properties. [191] HOMO and LUMO levels are approximated by Gaussian energy distributions, reflecting disorder. [192]

In their model, they assume an occupied DOS and an aligned VL, resulting in a depth-resolved charge-density profile $\rho(z)$. After that, the one dimensional Poisson equation is solved, yielding $V(z)$, and the original $\rho(z)$ is shifted by $-eV(z)$. This procedure is iterated until convergence is reached.

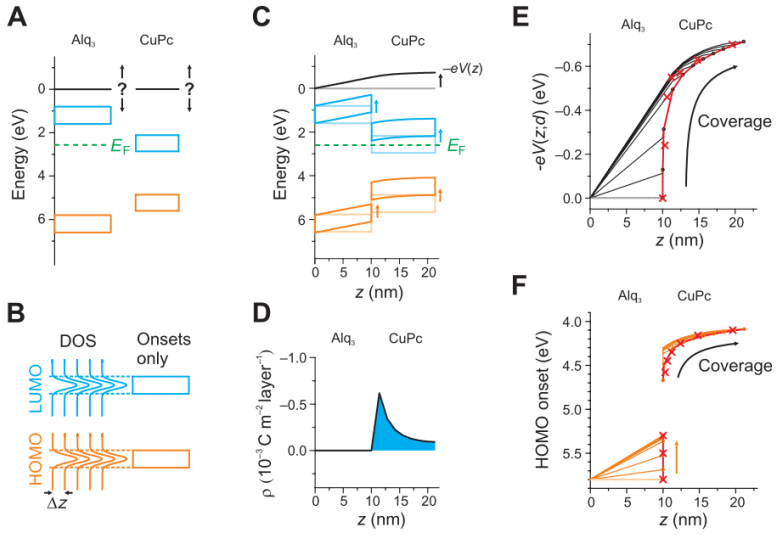

Figure 2.19: Simulation of the energetic level alignment of an organic heterojunction, consisting of $Alq3$ and $CuPc$, carried out by *Oehzelt et al.* [191] **(A)** Schematics of the initial energetics subsequent to deposition, with a substrate Fermi level of $E_F = 2.6\ eV$ represented by a green dashed line. **(B)** Illustration of the assumed Gaussian distribution of the DOS of both the HOMO and LUMO levels, separated with the discretization interval Δz, as well as their simple box representation for more clarity. **(C)** Simulated energetic alignment after contact formation between $Alq3$ and $CuPc$, including the vacuum level alignment, represented by $-eV(z)$. **(D)** Corresponding density of charges $\rho(z)$. **(E)** Comparison of measured (red crosses) and simulated (black dots) vacuum level endpoints $-eV(d)$ for the corresponding layer thickness d and calculated vacuum level progression $-eV(z)$ for different overall thickness d (black lines). **(F)** Resulting experimental (red crosses) and simulated (orange dots) HOMO levels for $Alq3$ and $CuPc$ upon increasing $CuPc$ coverage d and calculated HOMO level progression inside the heterojunction for different coverage thickness d (orange lines). Reproduced with permission from [191], Science Advances, open access. Copyright © 2015, Martin Oehzelt, Kouki Akaike, Norbert Koch and Georg Heimel.

Their results (**Fig. 2.19**) show no dipole formation and no transferred charge at an exemplary organic/organic interface (copper phthalocyanine (CuPc) on top of aluminum-tris(8-hydroxychinolin) (Alq3)), but rather an accumulation of charges in the top interface, resulting in a plate capacitor with the bottom organic layer, and a bending of the potential (**Fig. 2.19A-D**). In order to obtain these results, no ICT states were needed. Another important finding is that since UPS measurements only access the very top $1-3\ nm$ of the layer and represent thus only the "endpoints" $V(d)$, they do not give information about the local potential $V(z < d)$ inside the heterostructure. [193] In their results, no step-like increase in VL (surface dipole) is present, but rather a slow increase of it (**Fig. 2.19E**), being also valid for the corresponding HOMO

levels of the organic materials (**Fig. 2.19F**).

They also apply their simulation method for a material combination often used in OSCs, where both the HOMO and LUMO of one of the materials lie energetically deeper or higher than those of the other material, schematically shown in **Fig. 2.20A** and **B** on the very left. Five different scenarios are then simulated, in which the E_F of the substrate is sweeped through from the lowest lying HOMO up to the highest lying LUMO considering both materials. This results in very different scenarios regarding VL, HOMO and LUMO bendings: positive, no, and negative shifts. The fact that for the very same organic material system, all three possible scenarios occur, highlights again the importance of Φ_{SUB}. [191]

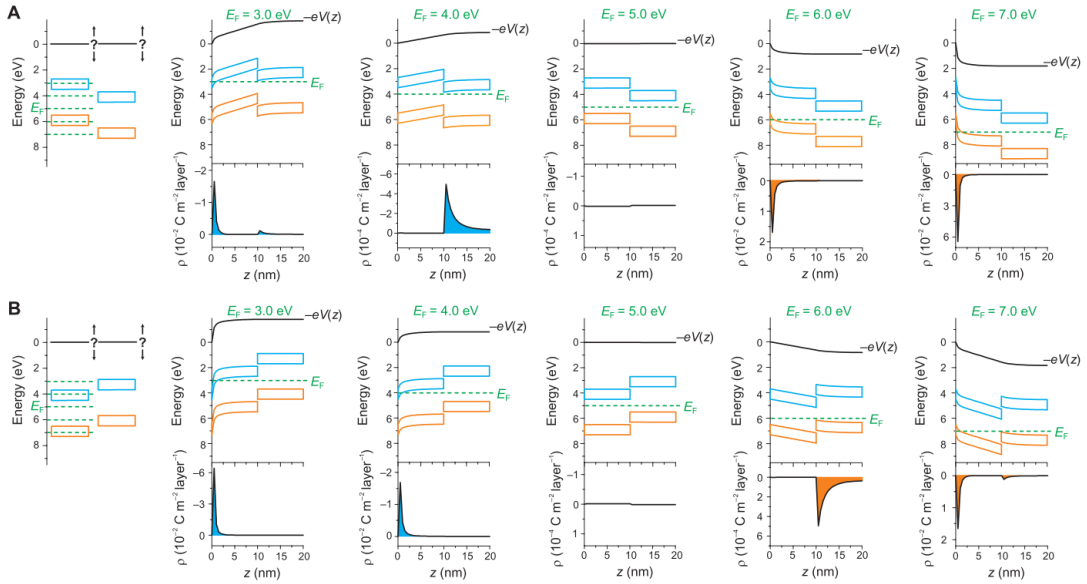

Figure 2.20: Calculated energy level alignments for a heterojunction where both the HOMO and LUMO levels of the material on top are **(A)** lower or **(B)** higher, compared to the bottom material. Initial energetic situation (such as in **Fig. 2.19A**), final energetic alignment (such as in **Fig. 2.19C**) and density of electrons in the LUMO (blue) and holes in the HOMO (orange) (such as in **Fig. 2.19D**) are shown for different substrate Fermi levels indicated by green dashed lines in the initial energetic alignment on the very left. Reproduced with permission from [191], Science Advances, open access. Copyright © 2015, Martin Oehzelt, Kouki Akaike, Norbert Koch and Georg Heimel.

In summary, the fact that this model predicts both surface dipoles and band bending without the introduction of any kind of ICT states in itself is intriguing. This model also predicts all 3 scenarios (positive/no/negative surface dipole) for the very same material system depending only on Φ_{SUB} and highlighting again the importance of the substrate work function.

2.4 Energetic Losses

2.4.1 Introduction

After understanding exciton generation, migration, separation, recombination, as well as energetic alignment in organic materials and the basics of solar cell operation in OPV devices, this section is dedicated to provide an interconnection of all these topics and thereby to explain energetic and consequent V_{OC} losses in OSCs. A decreased V_{OC} results also in a lower overall device performance, that is, a decreased PCE (as predicted by **Eq. 2.7**). Minimizing these losses is thus of crucial importance for an efficient OPV device design.

Let us again consider a D/A energetic diagram, as shown in **Fig. 2.21A**: The smallest optical gap of the two constituent materials (for convenience, that of the donor) is denoted with E_g. After light absorption, excitons first need to migrate to a D/A interface, where they can form a CT state with the energy E_{CT}, depending on energetic alignment, before they can be separated. After reaching the CS, free charge carriers will be collected at the electrodes, unless they recombine on their way. The non-ideality of these processes will lead to losses in V_{OC}, wherein the overall energetic loss ($E_{loss} = E_g - V_{OC}$) can be subdivided into energetic losses incurred during charge generation ($E_g - E_{CT}$) and recombination ($E_{CT} - V_{OC}$), as schematically shown in **Fig. 2.21B**.

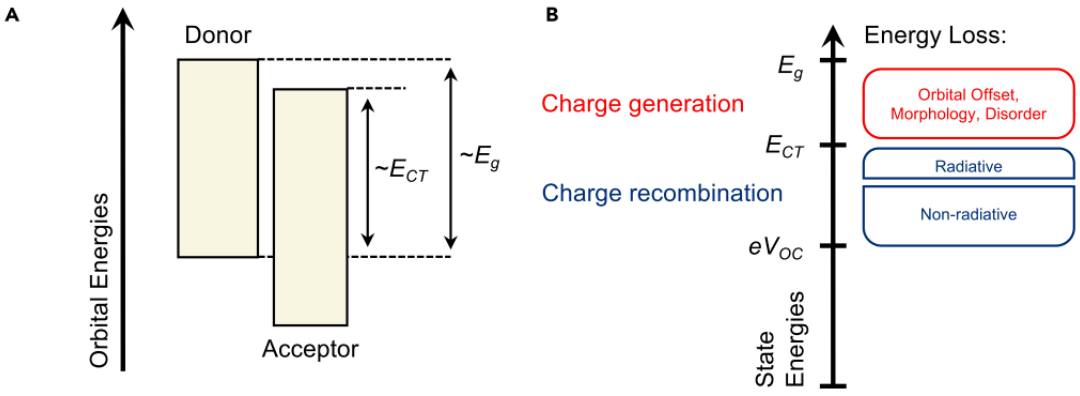

Figure 2.21: (A) Energetic diagram illustrating orbital energies for a typical D/A system. The smallest optical energy gap of the two constituent materials is denoted by E_g, while the difference between the HOMO of the donor and LUMO of the acceptor, also corresponding to the CT state energy, is denoted by E_{CT}. **(B)** The overall energy loss (E_{loss}) can be subdivided into charge generation ($E_g - E_{CT}$) and charge recombination ($E_{CT} - V_{OC}$) induced losses. Reproduced with permission from [194]. Copyright © 2017 Elsevier Inc.

In the next sections, various parameters affecting the V_{OC} of OPV devices, such as the HOMO and LUMO level positions of the donor and acceptor, the choice of the electrode materials, density of states including energetic disorder, and the CT state will be extensively discussed.

2.4.2 The Impact of the Photovoltaic Gap E_g^{PV}

V_{OC} denotes the voltage at which the total current is zero, resulting from a balance between charge carrier generation and recombination in the active layer. We note that this equality only holds for the sum of electron and hole currents ($I_e + I_h$), but not for both individual currents if, for example, electron and hole mobilities are imbalanced. [104] At V_{OC}, the internal field V_{bi} is cancelled out by the accumulation of charge carriers at the corresponding electrodes, constituting a potential difference, corresponding to the V_{OC}. [36] The absence of an electric filed results in an enhanced recombination. This has been already introduced in **Eq. 2.14**, which includes a disorder and a temperature dependent term, the sum of which is often referred to as a "typical loss in optimized solar cells" and has been empirically estimated to be 0.3 V by *Scharber et al.*. [42] Hence, the V_{OC} if often empirically estimated by:

$$eV_{oc} = \left(E_{LUMO}^{Acceptor} - E_{HOMO}^{Donor}\right) - 0.3V \tag{2.20}$$

Thus, one of the most common ways in literature to estimate the upper limit for the V_{OC} is by the energetic difference of the HOMO level of the donor and LUMO level of the acceptor, referred to from now on as the *photovoltaic gap energy* (E_g^{PV}). [36–41] It has been demonstrated by *Scharber et al.* [37] that varying the HOMO level of a polymer over a wide range while not changing the acceptor in PEDOT:PSS based devices results in a linear correlation with V_{OC}, as shown in **Fig. 2.22**. One needs to add, however, that the HOMO levels were estimated in this study by cyclic voltammetry (CV) measurements, carried out in solution, and can thus not accurately represent the energetics in films.

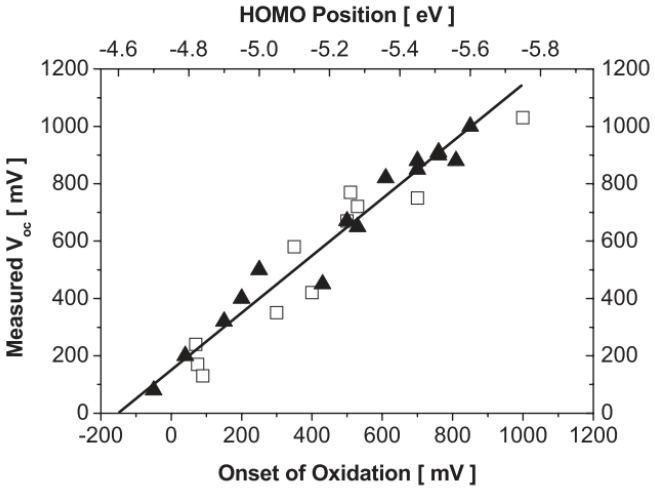

Figure 2.22: Measured V_{OC} values of various polymer:fullerene BHJ OSCs as a function of HOMO level of the corresponding polymer measured by CV in solution. The presented data is fitted linearly with a slope of 1. Reproduced with permission from [37]. Copyright © 2006 WILEY-VCH Verlag GmbH & Co. KGaA, Weinheim

2.4.3 The Influence of the Choice of Electrodes

The energy level alignment between an electrode and organic material will be either Ohmic or Schottky type in the Fermi level pinning or VL alignment regime, respectively. On the one hand, if one of the electrodes has an Ohmic contact, the V_{OC} will be only slightly influenced by changes in the electrode work function, and additionally, disorder and recombination at the contact will be reduced. [11, 36] On the other hand, for a Schottky type contact classical metal-insulator-metal (MIM) theory can be applied, [150] and the V_{OC} can be thus approximated by the electrode Φ difference and the degree of band bending at the electrodes. Additionally, recombination at the organic-electrode interface is more likely to occur. [76] Both these situations are schematically summarized in **Fig. 2.23** with V_{OC-1} and V_{OC-2} representing the energetic differences determining the V_{OC} in the case of Ohmic and Schottky contacts, respectively.

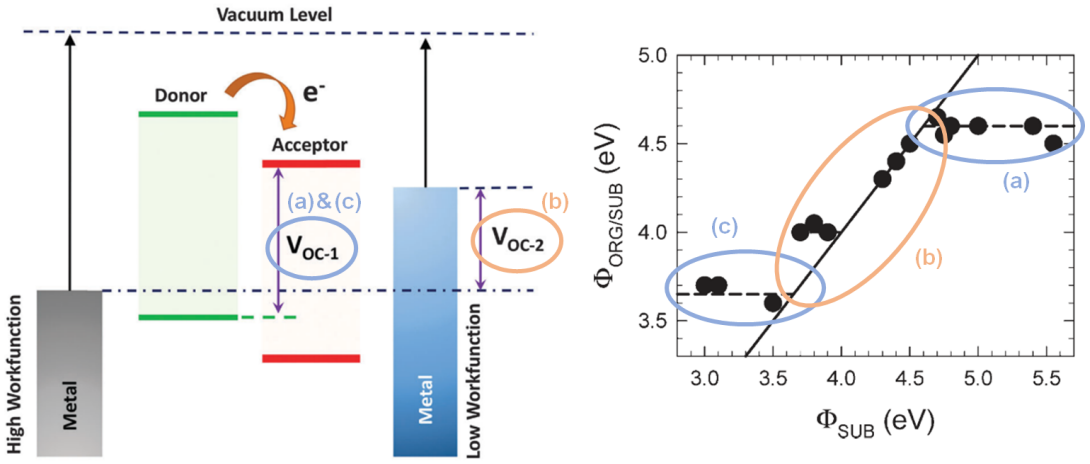

Figure 2.23: Visualising the values of importance when electrode-organic material contacts are Ohmic (V_{OC-1}) or Schottky type (V_{OC-2}) on the left. In the first case, Fermi level pinning can be observed and the V_{OC} will be only slightly dependent on the electrode Φs, V_{OC-1} is thus represented by the E_g^{PV} of the D/A system. While in the case of a Schottky type contact, where electrode work functions are well within the donor and acceptor band gap, the electrode Φ difference, denoted here with V_{OC-2}, will also play a role. However, only in first approximation, since it does not account for various effects such as band bending. Reproduced from [11] with permission from The Royal Society of Chemistry. Copyright © 2016. The two cases are also compared with **Fig. 2.15** (Reproduced with permission from [69]. Copyright © 2009 WILEY-VCH Verlag GmbH & Co. KGaA, Weinheim) for clarity.

It should be noted, however, that both cases are only approximations and serve only as rules of thumb when comparing electrodes: they do not account, for example, for light intensity and thus carrier density effects, which can influence the device V_{OC}. [139, 195] The selectivity of ETLs and HTLs (how fast and selectively they can extract one specific type of charge), strongly influences the device V_{OC}, but does not necessarily change the energetic alignment. [196] Finally, both the degree of disorder and morphology in the active layer affect device V_{OC}, but are not addressed in the

approximations made above. [197, 198]

2.4.4 DOS Broadening

Another approach, often used in literature, is to estimate the V_{OC} from the splitting of electron and hole quasi-Fermi energy levels ($E_{Fn} - E_{Fp}$ in **Fig. 2.24**), as it is commonly done for inorganic semiconductors. [199] For organic material systems, however, this approach needs to be corrected due to disorder-induced gap tail states, which will shift the electron (hole) quasi-Fermi level down (up) and will further reduce the V_{OC}. [102] Consequently, the role of energetic disorder should be taken into account when approximating the V_{OC}. [200] The shape of the DOS is mostly described by a Gaussian distribution for organic materials. [201, 202] It has been suggested by *Garcia et al.* that a decrease in V_{OC} is induced by recombination through tail states, as schematically shown with an arrow (A) in **Fig. 2.24**. [200, 203] Additionally, the broadening of the DOS will decrease the electron-hole quasi Fermi-level splitting due to electrons (holes) being in the bottom (top) tail of the Gaussian distribution, exhibiting a width of $\sigma = (2-4)k_BT$. Furthermore, the authors suggest that in addition to electron-hole recombination, an electron can also recombine via hopping to nearby unoccupied localized states, as schematically shown with an arrow (B) in **Fig. 2.24**.

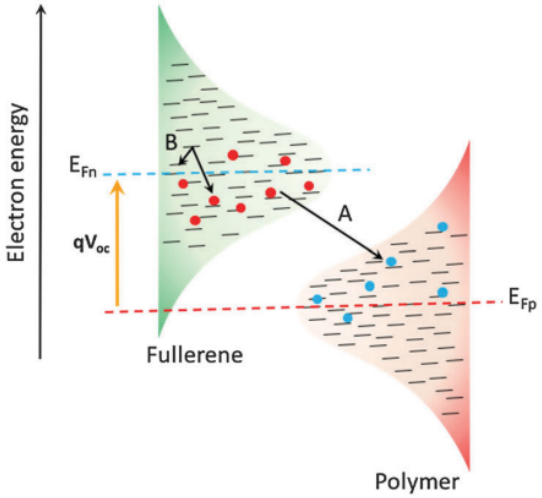

Figure 2.24: Schematic representation of the Gaussian broadening of the DOSs for the LUMO of the acceptor (fullerene) and HOMO of the donor (polymer), including various occupations states for thermalized electrons (red) and holes (blue), with quasi-Fermi levels E_{Fn} and E_{Fp}, respectively. Two possible loss mechanism pathways, including electron-hole recombination (arrow A) and electron energy loss to nearby vacant states (arrow B), are also given. Reproduced from [11] with permission from The Royal Society of Chemistry. Copyright © 2016.

Simulations done by *Blakesley et al.* verified that an increasing energetic disorder results in either a drop in V_{OC} or an enhanced density of traps. [195] We note that disorder is not only a molecular property, but will also depend on film preparation. [204] *Heumueller et al.* investigated solar cell degradation, observing a DOS broadening over

time. [202] They propose a redistribution of charge carriers in a broadened DOS, with a suppressed broadening in the case of more crystalline materials with a higher charge carrier density. Two possible mechanisms for the V_{OC} loss induced by degradation are proposed as schematically shown in **Fig. 2.25**: either due to a reduced charge carrier density and hence an increased (trap-assisted) recombination without any change in the DOS broadness, or vice versa with a broadened DOS but an unchanged charge carrier density. Furthermore, they also suggest that any material system with high charge carrier density is more stable against disorder-induced V_{OC} losses. [202]

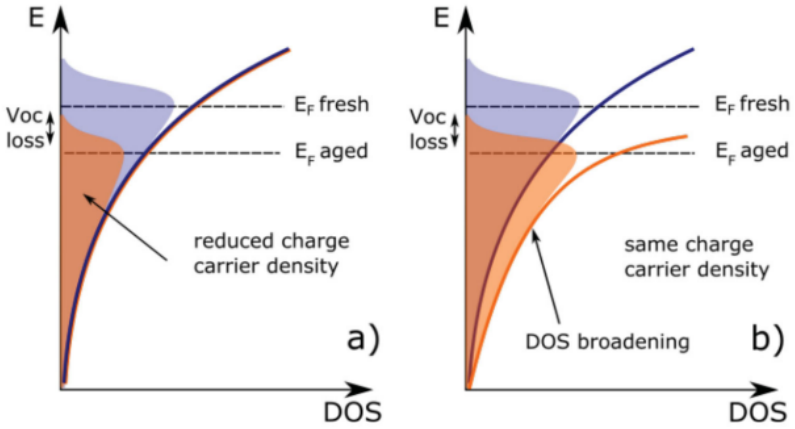

Figure 2.25: *Heumueller et al.* suggested, that V_{OC} losses due to degradation are induced either by **a)** a reduced charge carrier density caused by an increased recombination with an unchanged DOS, or by **b)** a broadened DOS with a constant charge carrier density. Reproduced with permission from [202]. Copyright © 2015 WILEY-VCH Verlag GmbH & Co. KGaA, Weinheim

2.4.5 Charge Transfer (CT) States

Before charge separation, excitons will undergo an intermediate state, with a bound electron and hole (by Coulomb force) on the acceptor LUMO and donor HOMO, respectively. The energetic difference of the two levels has been defined previously as the photovoltaic gap E_g^{PV}. This expression, however, ignores that the electron and hole are still in a bound state and thus have a binding energy on the order of 0.5 eV. [205] Therefore, this intermediate state, including the exciton BE, is often referred to as the CT state with energy E_{CT}, [104] first described by *Mulliken et al.* [206] Since then, its existence has been shown in numerous studies. [114, 205, 207, 208] In addition to the Coulomb binding energy, [102, 209] polarization effects and delocalization, caused by for example aggregation or crystallization, will also affect E_{CT}. [97, 210]

Detecting the CT State The CT state only exists on a D/A interface and it can be characterized by the appearance of new absorption and emission peaks with ener-

gies lower than the optical band gaps of the donor and acceptor materials. [205] Typically, in thin films with blended donor and acceptor, the absorption of the CT state is $10^2 - 10^3$ times weaker than that of the pure materials; it is, however, still detectable with photothermal deflection spectroscopy (PDS). [211] Other than that, the radiative decay of CT states can be detected by both PL [212] and electroluminescence (EL), [213] and their absorption $A(E)$ and emission $N(E)$, described as functions of the excitation energy E are related by: [48]

$$N(E) \propto A(E) \cdot E^2 \cdot exp\left(-\frac{E}{k_B T}\right) \tag{2.21}$$

Thus, if CT absorption has been observed, also emission can be expected and vice versa. Experimental observations show that both the high-energy part of the CT emission and low-energy part of the CT absorption follow a Gaussian shape, broadened by temperature as well as the reorganization energy λ, and can be thus written as: [205, 214, 215]

$$N(E) \propto E \cdot exp\left[\frac{-(E_{CT} - \lambda - E)^2}{4\lambda k_B T}\right] \tag{2.22}$$

and

$$A(E) \propto \frac{1}{E} \cdot exp\left[\frac{-(E_{CT} + \lambda - E)^2}{4\lambda k_B T}\right] \tag{2.23}$$

The reorganization energy is related to nuclear deformations at and near the D/A interface, [216] with values on the order of 0.1 eV or even higher. [214] One can thus expect absorption and emission peak positions at $E_{CT} + \lambda$ and $E_{CT} - \lambda$, respectively. In addition, both E_{CT} and λ are temperature dependent when taking disorder into account. [217, 218]

The Impact of CT State Energy E_{CT} When an exciton approaches a D/A surface it will undergo a CT state formation prior to separation. Interestingly, if the acceptor singlet state is lower in energy than the CT state, the CT energy will not affect the device V_{OC}. [104] This, however, is not the case for most organic material systems, and excitons will undergo the CT state, as shown with ① in **Fig. 2.26**. This will optimally result in a CS (②), denoted here as free charge carrier state (FC), which is, unlike the CT state, not bound to the ground state any more, and in which charges can freely migrate through the active layer. [205] The CT state can, however, also repopulate the donor's S_1 (the original donor HOMO) or triplet state, as denoted with ③ and ④, respectively.

The exact mechanism of CT state formation (①) is under debate. On the one hand, studies exist showing that the driving energy between E_{CT} and the LUMO of the donor is of great importance when it comes to CT creation, showing a vibrational relaxation to the donor singlet ground state prior to electron transfer to the CT state. [219, 220]

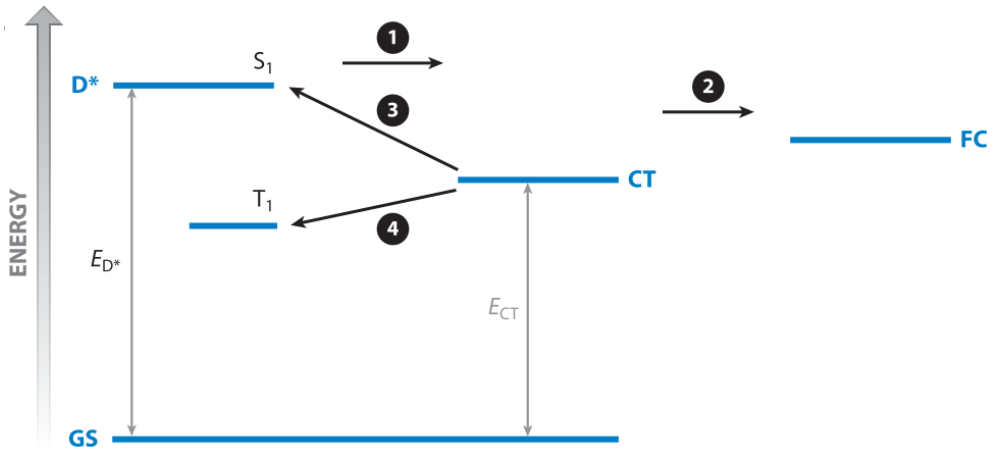

Figure 2.26: Energetic diagram showing the free charge carrier (FC) generation process, starting with an excitation of the donor molecule from its ground state GS into its S_1 state $D*$. During FC generation, excitons have to pass through the CT state, which is still bound to GS. Numbers from ① to ④ represent intermediate processes such as the photoinduced electron transfer (①), CT state dissociation into FC (②), repopulation of S_1 (③), and population of donor triplet states (④). The horizontal scale represents the electron-hole separation distance. Reproduced with permission from [205]. Copyright © 2016, ANNUAL REVIEWS.

On the other hand, studies show a CT state creation on the $10 - 100\ fs$ timescale, including an oscillating transfer with a $(25\ fs)^{-1}$ frequency, suggesting an effective electron transfer to the CT state independent of the very same driving energy. [221, 222]

Several studies reported a correlation between driving energy and the yield of created free charge carriers, explained by the fact that the CT state still needs to overcome the electron-hole binding energy. The question whether the excess energy of charge carriers provided in "hot" (vibrationally not yet relaxed) CT states, as already discussed in **Sec. 2.2.2.1**, is beneficial for reaching CS is still not answered. On the one hand, *Bakulin et al.* have shown that free charge carrier generation is possible on a timescale faster than CT state thermalization, indicating that excess energy can indeed help charge separation. [111] On the other hand, it has been shown in various studies, that free charge carrier generation is independent of the excess energy of the excited CT state. [205, 223, 224]

The lower the LUMO-LUMO offset between donor and acceptor, the lower the energetic loss introduced by orbital offsets, and the lower the driving force for charge separation. As a consequence, the absorption and emission bands of the pure materials and the CT state begin to overlap and a back transfer to the donor singlet state (③) becomes more likely. [223, 225] It has been reported that if the difference in the EL peak position (and consequently the CT state energy) and E_g of the smaller band gap material is smaller than $\sim 0.35\ eV$, the blend will exhibit a higher geminate recombination and thus a reduced V_{OC}. [226]

An additional loss mechanism comprising donor triplet state population (④) prior to ground state decay has been proposed for material systems with a slightly

higher CT state energy than the energy of these triplet states. [227] If the energetic difference is, however, larger than 0.3 eV, the losses can be suppressed. [228] It has been also suggested that an increased spatial donor-acceptor separation minimizes recombination losses through this triplet loss channel. [229]

2.4.5.1 Correlation to Open-Circuit Voltage (V_{OC})

While in the DOS model, V_{OC} is directly attributed to a loss in energetics due to the tail states, in the case of CT states, the V_{OC} loss occurs due to interface recombination. [195] It has been shown long ago that the charge-carrier lifetime and the V_{OC} of OPV devices is highest when all non-radiative pathways are eliminated and charges recombine only radiatively. [52] Radiative recombination of free charge carriers can be directly measured by EL and is dominated by intermolecular CT emission, since the recombination of a free hole and an electron occurs through the CT state. The external quantum efficiency (EQE) of EL emission η_{EL} is on the order of 10^{-6}, and thus strongly limits the V_{OC} as discussed below. [213]

Approaching the V_{OC} from the Dark Saturation Current As introduced in **Sec. 2.1.1** in **Eq. 2.5**, the V_{OC} derived from the Shockley equation is given as:

$$Voc = \frac{nk_BT}{q} \cdot ln\left(\frac{J_{ph}}{J_0} + 1\right) \tag{2.24}$$

where J_0 is the dark saturation current. Its value is typically determined by recombination and injection of free charge carriers. [102, 230] *Vandewal et al.* implemented the generalized Planck law about the relationship between absorptance and emission spectrum determined by Würfel et al. [231] and the correlation between photovoltaic performance and electroluminescence determined by Rau et al. [232] into **Eq. 2.2** yielding: [102]

$$J_0 = \frac{q}{EQE_{EL}} \int EQE_{PV}(E)\phi_{BB}(E)dE \tag{2.25}$$

Here, EQE_{EL} is the overall EL EQE obtained by integrating $EQE_{EL}(E)$ over all photon energies, EQE_{PV} is the EQE measured for solar cells at short circuit conditions, and $\phi_{BB}(E)$ the black body radiation at room temperature ($T = 300\,^{\circ}C$) integrated over all incidence angles, which exponentially decreases with photon energy.[6] [233] By plugging **Eq. 2.25** into **Eq. 2.24**, one can calculate the V_{OC} by measuring EQE_{EL} and EQE_{PV} and compare it with experimentally determined values, as shown in **Fig. 2.27**.

Higher EQE_{EL} values thus correspond to an enhanced V_{OC}: in some systems, increasing EQE_{EL} by a factor of 10 will result in an increase in V_{OC} of $\sim$ 58 mV at room

[6] $\phi_{BB} \approx \frac{2\pi E^2 k_B T}{c^2 h^3} exp\left(-\frac{E}{k_B T}\right)$, with c and h being the speed of light and the Planck constant.

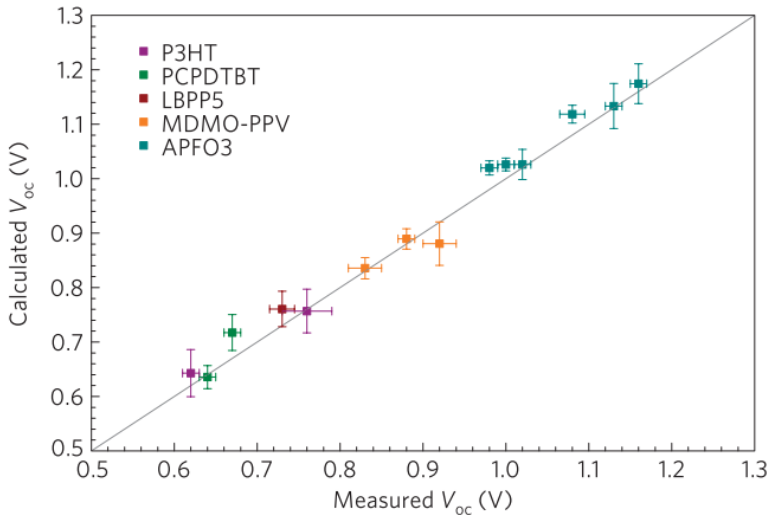

Figure 2.27: V_{OC} values calculated according to **Eq. 2.5** from EQE_{EL} and EQE_{PV} measurements and plotted as a function of V_{OC}s measured for OSCs. Different colours represent different polymers (mixed with fullerenes), while layer preparation conditions for measured and calculated V_{OC} values were always the same. A 1-to-1 correspondence is represented with a grey line. Reproduced with permission from [102]. Copyright © 2009, Springer Nature.

temperature, due to an elimination of radiative recombination pathways. [102]

Approaching the V_{OC} Directly from E_{CT} By assuming a detailed balance between qV_{OC} and the chemical potential difference of free electrons and holes, [234] and further assuming that free charge carrier generation occurs through relaxed CT state dissociation and not directly, [205] the V_{OC} can be written as:

$$qV_{OC} = E_{CT} - k_B T ln\left(\frac{kN_{CTC}}{G}\right) \tag{2.26}$$

where G, N_{CTC} and k are the the photogeneration rate, the density of charge transfer complexes and the decay rate constant, respectively. By inserting $\eta_{EL} = k_{rad}/k$, with k_{rad} being the radiative part of the overall CT decay, **Eq. 2.26** is modified to:

$$E_{CT} - qV_{OC} = k_B T ln\left(\frac{k_{rad}N_{CTC}}{G}\right) + k_B T ln\left(\eta_{EL}^{-1}\right) \tag{2.27}$$

The relationship between V_{OC} and E_{CT} has been shown in various studies, [38, 102, 225] and is summarized in **Fig. 2.28**.

Possible strategies to reduce V_{OC} losses could be a reduction of N_{CTC}, k_{rad} or an enhancement of η_{EL}. *Vandewal et al.* found experimental evidence that a 10-fold reduction of interfacial area from 10 % to 1 % had no influence on CT state energy. Yet, the reduced D/A interface area also reduced N_{CTC}, slightly enhancing thus the device V_{OC}, as schematically shown in **Fig. 2.29**. [235] The effect of k_{rad} on the V_{OC} is minimal and hence it should be varied over orders of magnitude, while keeping η_{EL} constant,

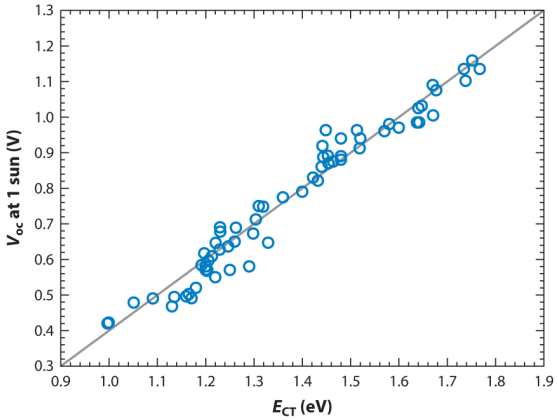

Figure 2.28: Real device V_{OC}s for a variety of material systems incorporating fullerenes, plotted as a function of measured E_{CT}, with a grey line representing a linear fit with a slope of 1 and an offset of 0.6 eV. Reproduced with permission from [205]. Copyright © 2016, ANNUAL REVIEWS.

in order to have a significant effect on the V_{OC}. [236, 237]

Removing non-radiative pathways would increase η_{EL}, [238] which in turn would result in tremendous enhancements in device V_{OC}, since a typical value of $\eta_{EL} \approx 10^{-6}$ corresponds to a voltage loss of $\sim 0.36\ eV$, according to **Eq. 2.27**. Replacing fullerenes with NFAs could be a possible way to achieve higher V_{OC}s, which has been shown by *Bartynski et al.* with a material system yielding an overall loss of only 0.37 eV. [239]

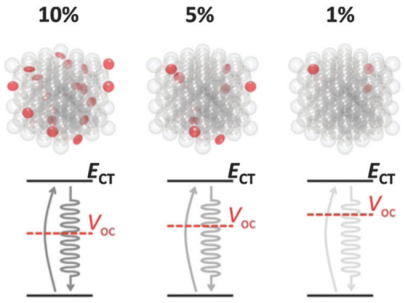

Figure 2.29: Schematic representation of the impact of D/A interfacial area on device V_{OC}. While reducing the interfacial area has no impact on E_{CT}, it results in an enhanced device V_{OC}. Reproduced from [11] with permission from The Royal Society of Chemistry. Copyright © 2016.

2.5 Summary

In this chapter, first the working principle of SCs was introduced including important device parameters such as the J_{sc}, V_{OC}, FF and PCE. Additionally, the standard solar spectrum used for generalized SC characterization was explained and the main factors limiting device efficiency were discussed showing a maximum reachable value for

single-junction OSCs of $\sim$ 33 % when excluding non-radiative recombination.

Next, excitons in organic materials are explained including their migration, separation and recombination. The concept of a BHJ thin film is introduced, where a trade-off between a large D/A interface area, possible pathways for free charge carriers and a relatively easy fabrication is made. An insight into a variety of transition mechanisms is also provided including absorption, vibrational relaxation, internal conversion (IC), intersystem crossing (ISC), and photoluminescence (PL) - all being important when interpreting loss mechanisms in complete OPV devices. Furthermore, geminate and non-geminate recombination types are introduced with focus on mono- and bimolecular processes, also referred to as first- and second-order processes. We correlate these two to the device parameters J_{sc} and V_{OC} by discussing their dependency on light and temperature and conclude that while the change in J_{sc} depends more on monomolecular, the change in V_{OC} is rather governed by bimolecular processes.

In the next section, the energetic alignment of organic/organic and organic/metal interfaces is explained by the ICT model, gap states and by Gaussian broadened density of states (DOS). Interfaces are subdivided into ultra clean metal interfaces fabricated under UHV conditions resulting in reactive interfaces, and into passivated layers including contaminated metals by exposure to ambient conditions and π-conjugated polymers such as PEDOT:PSS. Furthermore, the difference between the optical and electronic gap, resulting from the exciton binding energy, is highlighted.

Last but not least, by combining the previous sections, the current understanding of energetic losses and with that V_{OC} losses (originating from charge generation and recombination) is elucidated in great detail. Next, the impact of the photovoltaic gap energy (E_g^{PV}) and the choice of electrodes are discussed. Furthermore, V_{OC} losses are explained by the broadening of the DOS caused by disorder and delocalization. Additional losses arising from device degradation are explained by either a further DOS broadening or a reduced charge carrier density. Finally, current studies about the correlation of V_{OC} and the CT state energy are presented including CT state detection possibilities.

All in all, this chapter was dedicated to give a basic understanding on how fundamental physical processes such as charge generation, recombination and transport can influence OPV device performance, especially the open-circuit voltage (V_{OC}).

3 | Materials and Methods

In this chapter an overview of all materials and solvents used in this thesis is given, followed by specific preparation and fabrication methods. Finally, all relevant measurement techniques for this thesis are introduced and explained.

3.1 Materials and Solvents

Since the discovery of organic semiconductors in 1954 by Inokuchi [240], they have been extensively investigated and are widely used today as photoconductors in laser printers, organic light emitting diodes (OLEDs), and have potential applications in optoelectronic and electronic devices, such as OSCs, and organic field effect transistors (OFETs). [241] In order to fabricate devices, organic materials are commonly dissolved in specific solvents, prior to layer deposition. In this thesis, the materials used for experiments are summarized in **Table 3.1** and **3.3** with their chemical structures in **Fig. 3.1** and **3.2**, while solvents are summarized in **Tables 3.5**.

3.1.1 Non-Fullerene Acceptors in Organic Photovoltaic Devices

Some of the materials used in this thesis are NFAs, which have several advantages compared to fullerenes, including larger absorption cross sections, [25, 242] extended absorption into the NIR, [243] and low costs of purification. [74] Due to the possibility of choosing donor and acceptor with complementary absorption regions, both electron and hole transfer from the donor and acceptor can favourably contribute to charge generation, respectively. [17] Furthermore, the tunability of NFA energy levels, makes minimization of energetic losses originating from orbital offsets possible. [25, 243] In addition, NFAs generally have a higher EQE_{PL} and, consequently, a lower non-radiative recombination contribution. The latter two effects generally yield a higher device V_{OC} and, thus, a higher overall performance. [244–246] All these differences between fullenere and non-fullerene electron acceptors result in different charge generation and recombination dynamics between the two and general rules made for the highly investigated and quite well understood fullerenes should be taken with care, when applying for NFAs.

Table 3.1: List of Materials used in this thesis. (Part 1)

Material	Provider/Synthesis	CAS Number
poly(3-hexylthiophene) (P3HT)	Sigma-Aldrich	156074-98-5
[6,6]-Phenyl-C61-butyric acid methyl ester ($PC_{60}BM$)	Sigma-Aldrich	160848-22-6
poly[(5,6-difluoro-2,1,3-benzothiadiazol-4,7-diyl)-alt-(3,3‴-di(2-octyldodecyl)-2,2′,5′,2″,5″,2‴-quaterthiophen-5,5‴-diyl)] (PffBT4T-2OD)	1-Material	-
poly[(2,6-(4,8-bis(5-(2-ethylhexyl)thiophen-2-yl)-benzo[1,2-b:4,5-b′]dithiophene))-alt-[5,5-(1′,3′-di-2-thienyl-5′,7′-bis(2-ethylhexyl)benzo[1′,2′-c:4′,5′-c′]dithiophene-4,8-dione)] (PBDB-T)	Ossila	1415929-80-4
[6,6]-Phenyl-C71-butyric acid methyl ester ($PC_{70}BM$)	Ossila	609771-63-3
zinc acetate dihydrate (ZAD)	Sigma-Aldrich	5970-45-6
NCBDT	By Jiangbin Zhang [247]	-
poly[(2,6-(4,8-bis(5-(2-ethylhexyl)thiophen-2-yl)-benzo[1,2-b:4,5-b′]dithiophene))-alt-(5,5-(1′,3′-bis(4-fluorothiophen-2-yl)-5′,7′-bis(2-ethylhexyl)benzo[1′,2′-c:4′,5′-c′]dithiophene-4,8-dione (PFBDB-T)	By Zhuping Fei [248]	-
(2Z)-2-[(8-(E)-[1-(dicyanomethylidene)-3-oxo-1,3-dihydro-2H-inden-2-ylidene]methyl-6,6,12,12-tetraoctyl-6,12-dihydrothieno[3,2-b]thieno[2″,3″:4′,5′]thieno[2′,3′:5,6]-s-indaceno[2,1-d]thiophen-2-yl)methylidene]-3-oxo-2,3-dihydro-1H-inden-1-ylidenepropanedinitrile (C8-ITIC)	By Zhuping Fei [248]	-
triisopropylsilyle-thynyl-tetraazapentacene (TIPS-TAP)	By Philipp Biegger [249]	-
triptycenyl-tetraazapentacene (TIPS-TAP-1T)	By Philipp Biegger [249]	-
bistriptycenyl-tetraazapentacene (TIPS-TAP-2T)	By Philipp Biegger [249]	-

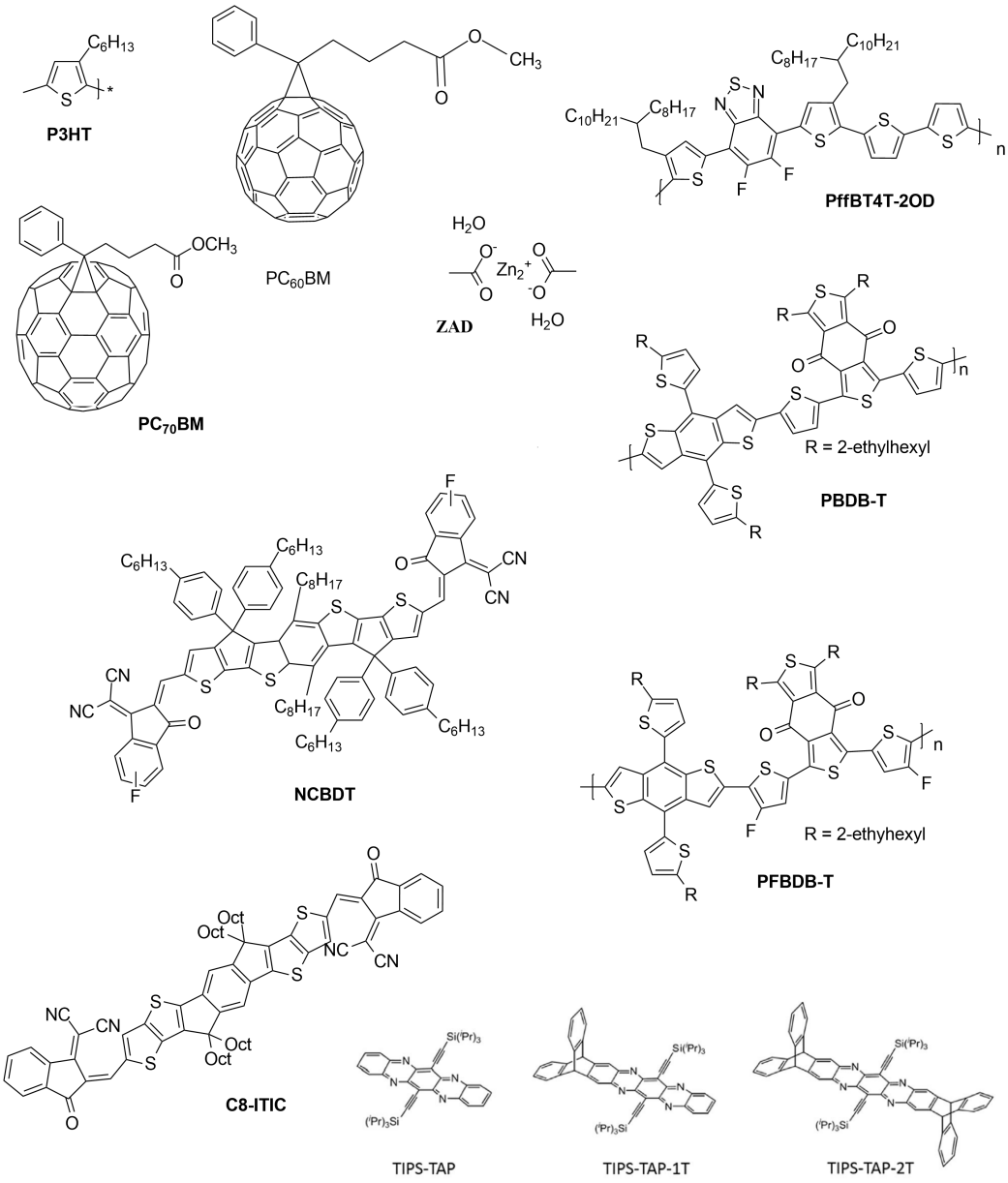

Figure 3.1: Chemical structure of the materials used in this thesis. (Part 1) Chemical structures for the TIPS-TAP derivatives adapted from [20], 2017 Copyright Wiley-VCH.

Table 3.3: List of Materials used in this thesis. (Part 2)

Material	Provider/Synthesis	CAS Number
2,2′-[(3,3‴,3‴″,4′-tetraoctyl[2,2′:5′,2″:5″,2‴:5‴,2‴″-quinquethiophene]-5,5‴″-diyl)bis[(Z)-methylidyne(3-ethyl-4-oxo-5,2-thiazolidinediylidene)]]bis-propanedinitrile (DRCN5T)	Ossila	1674394-69-4
3,9-bis(2-methylene-((3-(1,1-dicyanomethylene)-6,7-difluoro)-indanone))-5,5,11,11-tetrakis(4-hexylphenyl)-dithieno[2,3-d:2′,3′-d′]-s-indaceno[1,2-b:5,6-b′]dithiophene (ITIC-2F)	Ossila	2097998-59-7
poly[(2,6-(4,8-bis(5-(2-ethylhexyl-3-chloro)thiophen-2-yl)-benzo[1,2-b:4,5-b′]dithiophene))-alt-(5,5-(1′,3′-di-2-thienyl-5′,7′-bis(2-ethylhexyl)benzo[1′,2′-c:4′,5′-c′]dithiophene-4,8-dione)) (PBDB-T-2Cl)	Ossila	2239295-71-5
indene-C60 bisadduct (ICBA)	Sigma Aldrich	1207461-57-1
dinaphtho[2,3-b:2,3-f]thieno[3,2-b]thiophene (DNTT)	By Angela Wittmann [45]	-
[5,6]-Fullerene-C70 (C_{70})	By Himanshu Shekhar [44]	-
(4-(1,3-dimethyl-2,3-dihydro-1H-benzoimidazol-2-yl)phenyl)dimethylamine (N-DMBI)	By Himanshu Shekhar [44]	-

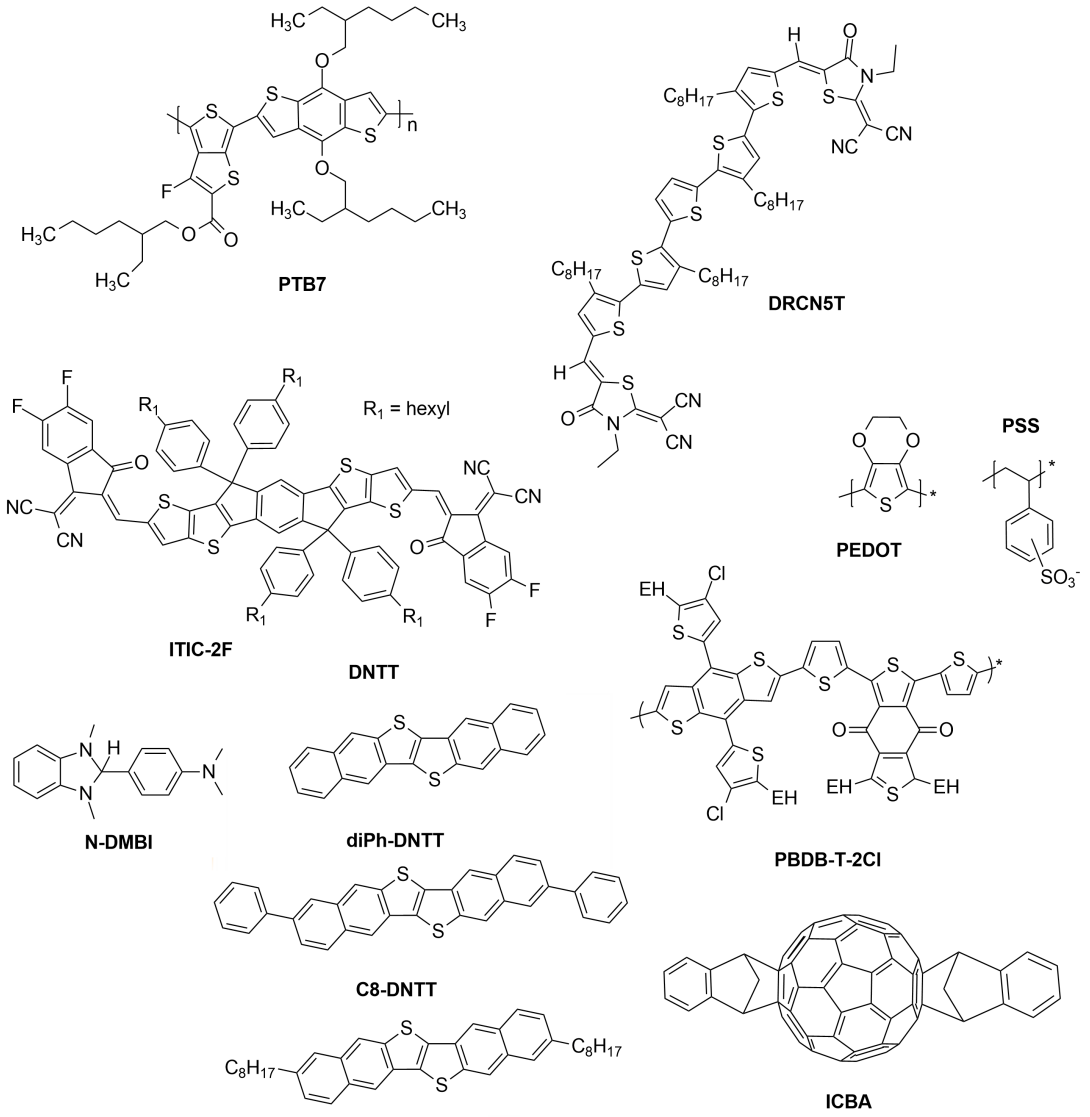

Figure 3.2: Chemical structure of the materials used in this thesis. (Part 2)

Table 3.5: List of Solvents used in this thesis.

Solvent	Provider	CAS Number
chloroform	Sigma-Aldrich	67-66-3
dichloromethane	Sigma-Aldrich	75-09-2
chlorobenzene	Sigma-Aldrich	108-90-7
1,8-diiodooctane	Sigma-Aldrich	24772-63-2
monoethanolamine	Sigma-Aldrich	141-43-5
2-methoxyethanol	Sigma-Aldrich	109-86-4
caesium carbonate	Sigma-Aldrich	534-17-8
1,2-dichlorobenzene	Sigma-Aldrich	95-50-1

3.1.2 Substrates

Solar Cell Substrates ITO substrates, with a sheet resistance of 15 Ωsq^{-1}, were bought from *PsiOTec Ltd.* Sodalime glass substrates, $12x12\ mm^2$ in size, were pre-patterned, resulting in central $7x12\ mm^2$ ITO stripes.

Substrates for PES Investigations Generally, PES can be only carried out on conducting substrates, functioning as a reservoir of charge carriers, necessary due to the high amount of photoelectrons removed from the system (layer surface) by the measurement itself. The very same *Glass/ITO* substrates, already described above for solar cells, were used for this purpose. After substrate cleaning and layer deposition, described below, a part of the layer was removed again with a metal tweezer in order to be able to connect the ITO conducting layer with the sample holder used for PES measurements.

Glass Substrates Microscope slides were bought from Thermo Scientific, are were used for UV-vis and PL measurements after they were cut into $\sim 12x12\ mm^2$ substrates.

Spectrosils PDS measurements require special, circular substrates, so called *spectrosils*, which were bought from UQG Optics. The diameter of these high purity, fused silica glass substrates is $\sim 12\ mm$. The transmission of spectrosils is very high in the ultra-violet (UV) region.

3.2 Fabrication Methods

In the following section, we will describe film preparation processes including cleaning, spin-coating and metal evaporation. Device architecture types are also introduced.

3.2.1 Substrate Cleaning

All substrate types, described in **Sec. 3.1.2** were cleaned the very same way following these steps:

1. Rinsing the substrates with Acetone on a Teflon holder
2. Sonicating in Acetone and 2-Propanol (wet to wet transfer) for 10 min each in an ultrasonic bath
3. Blow drying the substrates (N_2 gun)
4. Oxygen-plasma cleaning for 10 min at 0.4 $mbar$ and 100 W

3.2.2 Film and Device Fabrication

All organic layers were deposited by so called *spin-coating*. During this process, the substrate is held with a vacuum chuck, while it can be rotated at various spin speeds up to 10000 rpm. The final layer thickness d scales with the spin speed Ω and concentration c as $d \sim c/\sqrt{\Omega}$, resulting in typical layer thicknesses of $(20 - 200)$ nm. Films are either spin-coated (static coating) under ambient conditions or in a nitrogen filled glovebox (< 2 ppm O_2 and < 2 ppm H_2O).
Metal contacts and other interlayers (Au, silver (Ag), calcium (Ca), chromium (Cr), Al and molybdenum oxide (MoO_x)) are evaporated in a thermal evaporator on a rotational stage, at a base pressure of 10^{-6} $mbar$, at a rate varying from 0.02 to 0.15 nm/s, placed inside the nitrogen filled glovebox. Subsequent to evaporation, a metallic mask is laid on the top of the substrates, resulting in eight solar cell pixels with an area of 4.5 mm^2.

3.2.3 Device Architectures

3.2.3.1 Standard Architecture

Standard architectures were achieved by the following layers:

- *Glass/ITO substrates*: Cleaned as described in **Sec. 3.2.1**
- *PEDOT:PSS* films were deposited as described in **Sec. 3.2.4.1**, serving as the HTL.
- The *active layer* consists of multiple organic materials. First, all of them are individually dissolved in a nitrogen filled glovebox in either chloroform, chlorobenzene, dichloromethane at concentrations varying from 5 mg/ml to 30 mg/ml and kept on a hotplate at $(50 - 90)$ $^\circ C$ for at least 2 h. Then, the solutions are filtered through a 0.45 μm PTFE filter, and mixed at the desired donor to acceptor ratio. Finally, 80 μl of the solution is spin-coated with a spin speed of $(800 - 2500)$ rpm for 50 s and 2500 rpm for 5 additional seconds on the PEDOT:PSS covered substrate. Exact values for different material combinations are specified below.
- For the *top electrode evaporation*, the substrates were transferred to a thermal evaporator with a base pressure of $2 \cdot 10^{-6}$ $mbar$, where 10 nm Ca (ETL) and 80 nm Al

with a rate of $0.02 - 0.15\ nm/s$ were evaporated.

3.2.3.2 Inverted Architecture

Inverted architectures were achieved by the following layers:

- *Glass/ITO substrates*: Cleaned as described in **Sec. 3.2.1**
- *ZnO* was deposited by the sol-gel method, described in **Sec. 3.2.4.2**, serving as the ETL.
- The *active layer* was prepared the same way, as for the standard architecture, described in **Sec. 3.2.3.1**.
- For the *top electrode evaporation*, the substrates were transferred to a thermal evaporator with a base pressure of $2 \cdot 10^{-6}\ mbar$, where 10 nm MoO_x (HTL) and 80 nm Ag with a rate of $0.02 - 0.15\ nm/s$ were evaporated.

3.2.3.3 Bilayer Films

Bilayer films were prepared by float-casting. The donor and acceptor films were separately spin-coated on PEDOT:PSS and ZnO films, respectively. The PEDOT:PSS/donor films were then immersed in deionized water until the PEDOT:PSS film dessolved, leaving a floating donor film on top of the deionized water surface. The free floating donor film was then picked up by the ZnO/acceptor substrate. Next, the substrate was placed under vacuum ($10^{-1}\ mbar$) for a half an hour in order to ensure proper film formation and water evaporation. The films were not annealed to prevent intermixing.

3.2.4 Specific Material Preparation Methods

3.2.4.1 PEDOT:PSS

PEDOT:PSS is a polymer mixture consisting of hydrophobic PEDOT and hydrophilic PSS with positive and negative charges on them, respectively, leading to a stabilization of the whole mixture. This results in the formation of small agglomerates, a few nm in size, with PSS forming the shell. [149] The overall conductivity of PEDOT:PSS can be tuned from about $10^{-5}\ S/cm$ to 100 S/cm by changing the PEDOT to PSS ratio from 1 : 20 to 1 : 2.5. Material properties, such as the WF of PEDOT:PSS can be also tuned by changing the amount of residual water during fabrication from 4.8 eV (ambient conditions) to 5.6 eV (vacuum annealing). [250]

Preparation After a short ultrasonication of the PEDOT:PSS solution, it is filtered through a 0.45 μm PVDF filter and spin-coated at a spin speed of 2000 rpm, with an acceleration of 1000 rpm/s for 45 s in a fume hood (ambient air), resulting in a layer thickness of $\sim$ 70 nm. After spin-coating, the substrates were annealed at 140 $^\circ C$ for 10 min in order to as much residual water evaporate from the film as possible before

bringing the substrates into a N_2-filled glovebox. Finally, the substrates were annealed in the glovebox at 250 $°C$ for an additional 20 min.

3.2.4.2 ZnO Preparation

For ZnO deposition, a low-cost, sol-gel method, described by *Znaidi et al.* [251] including the three steps below was used.

- The *solution preparation* was done as described by Kwon et. al: [252] 0.46 mol of ZAD and the same amount of monoethanolamine were dissolved in 1 ml 2-methoxyethanol and heated and stirred over night at 70 $°C$ and 700 rpm, respectively. This solution was additionally caesium (Cs) doped by adding caesium carbonate with a molar ratio of 2 %.
- This solution (50 μl) was then *spin-coated* onto the substrates at a spin speed of 2000 rpm for 50 s and an acceleration of 1000 rpm/s, yielding in an approx. 40 nm thick ZnO layer.
- The spin-coated substrates were then *annealed* at 200 $°C$ for 30 min.

3.2.4.3 P3HT and $PC_{60}BM$

For the BHJ active layer, pre-weighted P3HT and $PC_{60}BM$ were dissolved in chlorobenzene at a concentration of 16 mg/ml. The solutions were mixed at a D/A ratio of 1:0.8 and spin-coated using a 0.45 μm PTFE filter at a spin speed of 1000 rpm for 60 s.
Bilayer films were manufactured as described in **Sec. 3.2.3.3**, with material concentrations of 8 mg/ml and 40 mg/ml for P3HT and $PC_{60}BM$, respectively.

3.2.4.4 PffBT4T-2OD:$PC_{70}BM$

PffBT4T-2OD and $PC_{70}BM$ were dissolved in an 1:1 mixture of chlorobenzene and 1,2-dichlorobenzene (with 3 volume % 1,8-diiodooctane) at a concentration of 16 and 19.2 mg/ml, respectively and kept on the hotplate at 90 $°C$. For the spin-coating step, a plastic chuck was used to avoid cooling of the substrates during film deposition. The substrates were post-annealed at 90 $°C$ for 5 minutes. These layers were prepared by Andreas Weu.

3.2.4.5 PBDB-T:NCBDT

PBDB-T and NCBDT were dissolved in chloroform at a concentration of 5 and 4 mg/ml, respectively. The mixed solution (1:1) was spin-coated at 1400 rpm for 20 s. The substrates were then placed in a glass Petri dish for solvent vapor annealing. Layers were prepared by Jiangbin Zhang, further preparation details are given elsewhere. [247, 253]

3.2.4.6 PFBDB-T:C8-ITIC

The PFBDB-T:C8-ITIC blend solution was dissolved in chlorobenzene at a concentration of 20 mg/ml and a ratio of 1 : 1.25 and annealed overnight at 50 $^{\circ}C$. The mixed solution was then spin-coated at 2400 rpm for 60 s. Layers were fabricated by Zhuping Fei, with more details on fabrication in [248].

3.2.4.7 DRCN5T:$PC_{70}BM$

DRCN5T and $PC_{70}BM$ were dissolved in chloroform, at concentrations of 15 and 12 mg/ml, respectively. Mixed solutions (1:1) were then spin-coated at 1700 rpm for 20 s. The substrates were post-annealed at 120 $^{\circ}C$ for 10 min and additionally solvent annealed for 1 min in a Petri dish, rich in chloroform vapour. Layers were fabricated by Andreas Weu.

3.2.4.8 DNTT Spintronic Layers

DNTT spintronic layers on a permalloy (Py) substrate were provided by Angela Wittmann. Layers were prepared as desribed in [45].

3.2.4.9 Doped $PC_{60}BM$ Layers

80 nm thick $PC_{60}BM$ (either undoped or doped with N-DMBI) were deposited on titanium nitride (TiN), additionally, a further 50 nm thick C_{70} layer was deposited on top by Himanshu Shekhar with further details in [44].

3.2.4.10 PBDB-T-2Cl:ITIC-2F:$PC_{70}BM$

All three materials were dissolved in a nitrogen filled glovebox in conduction band (with 1 volume % 1,8-diiodooctane) at a concentration of 10 mg/ml and mixed at desired mass ratios. Layers were spin-coated at a spin speed of 1000 rpm for 50 s and post-annealed at 100 $^{\circ}C$ for 10 min.

3.2.4.11 PTB7:$PC_{70}BM$:ICBA

All three materials were dissolved in a nitrogen filled glovebox in 1,2-dichlorobenzene (with 3 volume % 1,8-diiodooctane) at a concentration of 10 mg/ml and mixed at desired mass ratios. Layers were spin-coated at a spin speed of 1000 rpm for 50 s and post-annealed at 100 $^{\circ}C$ for 10 min. Layers were fabricated by Yvonne Hofstetter.

3.3 Experimental Methods

3.3.1 Photoemission Spectroscopy

PES measurements such as UPS and XPS were carried out in an UHV chamber of an ESCALAB 250Xi from ThermoFisher, with a base pressure of 10^{-10} $mbar$. UPS mea-

surements were performed using a double-differentially pumped helium (He) gas discharge lamp emitting *He I* radiation ($h\nu = 21.22\ eV$) with a pass energy of 2 eV and a bias of $-5\ V$, the latter to ensure secondary electron onset detection. In most graphs in this thesis, showing UPS spectra, the x axis represents the binding energy with respect to (w.r.t.) the Fermi level E_F. The Φ and the HOMO level w.r.t. E_F of the corresponding measured material is determined by the secondary electron cut-off (SECO), and by a linear fit of the low binding energy edge position, respectively. XPS measurements were performed using an XR6 monochromated Al $K\alpha$ x-ray source ($h\nu = 1486.6\ eV$) with a 650 mm spot size.
The measurement principle of both these techniques is schematically shown in **Fig. 3.3**, while more detailed descriptions are given in the next Sections.

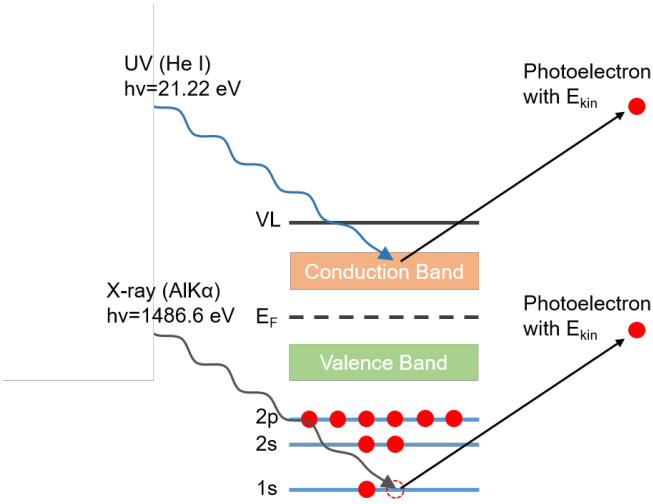

Figure 3.3: Measurement principle of the UPS and XPS techniques, both based on the photoelectric effect.

3.3.1.1 Ultra-Violet Photoemission Spectroscopy (UPS)

As schematically shown in **Fig. 3.3**, UV light absorption leads to an emission of photoelectrons from the valence band of organic materials. An entire spectrum has typically three features: (i) the photoemission onset consisting of the SECO originating from secondary electrons, (ii) DOS from valence band electrons, and (iii) a Fermi level step for metals. Secondary electrons are inelastically scattered within the sample, before leaving its surface, containing thus no meaningful information. Their onset, however, consists of electrons barely overcoming the VL of the sample and are thus a measure for the Φ of the material. One needs to keep in mind, that the measured spectra are only representative for top $\sim 2\ nm$ of the layer, due to the very low inelastic mean free path (IMFP), being a measure for the maximum escape depth of photoelectrons, at an excitation energy of $h\nu = 21.22\ eV$.

In order to be able to resolve the SECO, and to overcome the Φ of the detector, samples are negatively biased at $-5\ V$ to shift the vacuum level of the sample. This makes the recording of a metal reference spectrum necessary, mostly done for Au, as shown in **Fig. 3.4** as a blue spectrum. The position of the Fermi level in this measurement will define the overall Fermi level for all subsequent measurements. In our measurement setup, it was measured to be $E_F^{kin} = 26.15\ eV$. The measured kinetic energy at the SECO onset E_{SECO} in this spectrum will also define the Φ of the metal ϕ_{SUB}, as in:

$$\phi_{SUB} = h\nu + E_{SECO} - E_F^{kin} = 21.22\ eV + E_{SECO} - 26.15\ eV \tag{3.1}$$

When an organic material (red spectrum in **Fig. 3.4**) on top of a metal is measured, the Fermi level will be defined by the metal underneath, and will stay unchanged. The Φ of the organic material, denoted with $\phi_{ELP/SUB}$ can be determined equivalently to **Eq. 3.1**. Fitting the kinetic energy spectrum at the HOMO level onset, as described in **Sec. A.2.1.1**, will result in E_{HOMO} and its value defines the IP of the measured organic material as follows:

$$IP = h\nu - (E_{HOMO} - E_{SECO}) = 21.22\ eV - (E_{HOMO} - E_{SECO}) \tag{3.2}$$

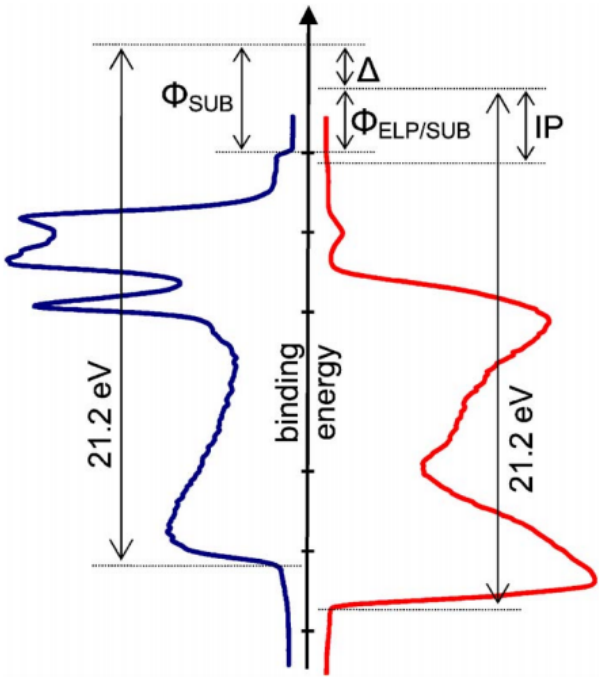

Figure 3.4: Example UPS spectra for a metal substrate (blue) with the work function ϕ_{SUB}, determined by its SECO onset and Fermi level E_F, and an organic thin layer on top (red) with the work function $\phi_{ELP/SUB}$ and thus a surface dipole of Δ. The Fermi level of the organic material is defined by the substrates E_F, and its HOMO onset together with its SECO onset is a measure for its IP. Spectra are plotted as a function of the binding energy, which is zero at the metals Fermi level. Adapted from [185], Copyright © 2006, AIP Publishing.

PES spectra can be generally plotted either as a function of the measured kinetic energy of electrons or of the binding energy of these electrons, whereas $E_F^{kin} = 26.15\,eV$ defines the zero point for the binding energy for an excitation energy of 21.22 eV.

3.3.1.2 X-Ray Photoemission Spectroscopy (XPS)

The working principle of XPS is very similar to that of UPS described above, but at a higher excitation energy of 1486.6 eV in our setup. With this, XPS probes core level electrons and is sensitive to the top $\sim$ 10 nm of the surface. The measured kinetic energy of electrons can be converted to corresponding binding energies analogue to the UPS setup and corrected for known element specific atomic sensitivity factors. The binding energy is specific for each element and also depends on its chemical environment and can thus be a measure for atomic composition. XPS spectra were fitted using the smart fitting algorithm provided by Avantage.

3.3.2 Depth Profiling

3.3.2.1 Gas Cluster Ion Beams

Supersonic Gas Expansion Cluster beam formation was first investigated by *Becker et al.* in 1956 in the field of intense molecular beams at low temperatures. [254] After several decades of research, cluster formation through supersonic gas expansion was discovered, [255] and it yielded in high intensity cluster beams. [29]

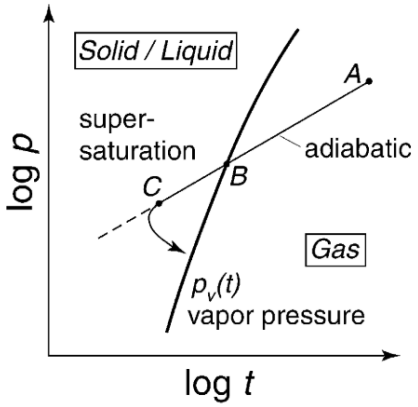

Figure 3.5: Phase diagram showing supersaturation during an adiabatic expansion. Reproduced with permission from [29], Copyright © 2001 Elsevier Science B.V. All rights reserved.

When a gas is directly expanding from a high-pressure source into vacuum through a small nozzle, the expansion will happen adiabatically, and the relative overall velocity of the gas atoms will be reduced. This will also lead to a temperature drop, and at the point of supersaturation (Point B in **Fig. 3.5**), gas condensation will take place. [255] This gas-fluid phase transition leads to a formation and growth of clusters. [29] Hence,

assuming spherical clusters with the radius r, the Kelvin's equation reads: [256]

$$ln\left(\frac{P_r}{P_0}\right) = \frac{2\sigma m}{k_B T_0 \rho} \cdot \frac{1}{r} \tag{3.3}$$

where P_r and P_0 are the vapour pressure and the saturated vapour pressure (that of a plane surface), and σ the surface tension, m and ρ the mass and density of the corresponding cluster atoms, k and T_0 the Boltzmann constant and the temperature. This leads to a critical radius for cluster formation r^*:

$$r^* = \frac{2\sigma m}{k_B T_0 \rho} ln(P_r/P_0) \tag{3.4}$$

Hence, all clusters formed have a radius $r > r^*$, whereas r^* is dependent on, among others, nozzle temperature and stagnation pressure and consequently the overall nozzle geometry.

Cluster Size The average cluster size is mostly determined by nozzle geometry, more specifically by gas flow, beam temperature and divergence. The most common nozzles for GCIB applications are the sonic, the Laval and the conical nozzle. [255] *Hagena et al.* introduced the *condensation parameter* Γ^*, serving as a semi-empirical scaling parameter, proportional to the average cluster size $n_a v$: [255, 257–259]

$$\Gamma^* = n_0 D^q T_0^{0.25q-1.5} \cdot \frac{1}{\Gamma_{ch}}, \text{ with } n_0 = \frac{p_0}{k_B T_0} \tag{3.5}$$

with n_0 being the number density, D the diameter of the nozzle, Γ_{ch} a characteristic scaling factor, making Γ^* non-dimensional, and q an experimentally derived gas dependent constant. Values for the latter two for various gases can be found elsewhere, [258] whereas values for argon (Ar) are given as $q_{Ar} = 0.85$ and $\Gamma_{ch}^{Ar} = 347 \cdot 10^{14}\ m^{-2.15} K^{-1.2875}$, leading to scaling parameter for Ar clusters of:

$$\Gamma^* = \frac{p_0 D^{0.85}}{\Gamma_{ch} k_B T_0^{2.2875}} \tag{3.6}$$

Typical cluster sizes range from several to a few thousand of atoms, in extreme cases even over a hundred thousand, [257] with a size distribution width (FWHM) of $\Delta n \approx n_{av}$. [260]

Further Processing After supersonic gas expansion described above, clusters will undergo a few more steps before they are used for surface modification:

- Stable cluster formation is ensured by multiple skimmers with differentially pumped vacuum regions, and additionally, the core portion of the flow field is screened out. Finally, the cluster beam gets transferred to UHV through a beam-defining collimator. [259]

- Clusters are charged by electron bombardment.

- The overall beam can thus be focused and accelerated by electrodes and size selected by an additional a magnetic field.

Monoatomic beams can be generated by directly introducing gas into the ionization region.

Surface Modification Capabilities The introduction of GCIBs opened up many opportunities regarding surface modification, such as thin film deposition, [260] surface smoothing, [29] and damage-free etching of organic materials. [261, 262] In **Chapter 5** in this thesis, we will make use of the latter.

3.3.2.2 Comparison of the Introduced Damage between Cluster and Monoatomic Modes

Molecular dynamics simulations are great tools for tracing collisions, which simultaneously occur within picoseconds between incident and target atoms on a nm scale, during a cluster ion impact. [263, 264] Such simulations suggest, that the major advantage between GCIBs and monoatomic beams is the possibility of shallow implantation effects in the former. Since GCIBs are made up of many atoms with a high energy density in a small volume, all of them interacting with the surface at the same time, their interaction results in a non-linear sputtering yield. Hence, doubled cluster kinetic energy does not imply a double as high sputtering yield. [265, 266] This also implies, that the damage caused by monoatomic and cluster ion beams can be fundamentally different, as shown for an exemplary case of three boron ion beam sizes B_1, B_{13} and B_{169} with the same kinetic energy of 7 keV on crystalline Si in **Fig. 3.6**. Interaction with the sample for these cases are fundamentally different: While monoatomic beams will trigger a cascade mechanism due to binary collisions, resulting in deep penetration depth and displacements, collision cascades induced by clusters take place simultaneously in a narrow top surface region. [33]

Interestingly, a GCIB can transport several orders of magnitude more atoms than a monoatomic beam at the same current density due to the fact, that clusters have a low charge to mass ratio: As we increase the cluster size to > 1000 atoms, keeping the overall kinetic energy constant, the incident energy per atom decreases to a several eV/atom. [29] Additionally, it is hard to realize monoatomic beams with an energy per atom as low as several eV due to space charge effects. In summary, GCIBs offer a great opportunity for surface smoothening and surface sensitive etching.
Further details on cluster ion sources are given in the cited references.

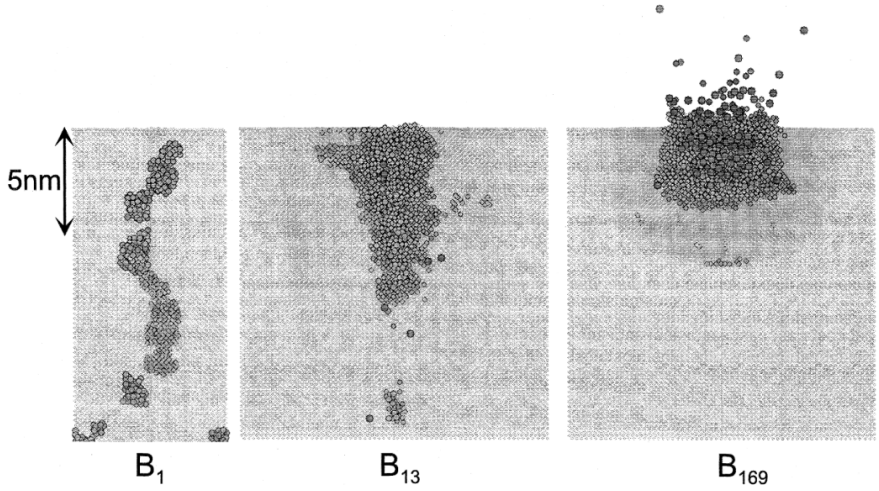

Figure 3.6: Molecular dynamics simulations, 385 fs after the impact of monoatomic (B_1), small (B_{13}) and large (B_{169}) boron clusters with the same acceleration energy of 7 keV on crystalline Si. Reproduced with permission from [266], Copyright © 1999 Elsevier Science B.V. All rights reserved.

3.3.3 Atomic Force Microscopy

In order to investigate the microstructure of organic surfaces, we applied atomic force microscopy (AFM), with its working principle schematically sketched in **Fig. 3.7**, operated in *tapping mode*.

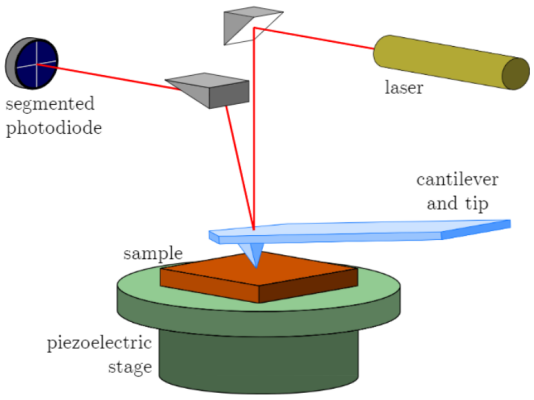

Figure 3.7: Schematics of the optical system of an AFM: Changes in canteliver height can be easily detected by a laser light, focused on a top of it and subsequently reflected to a photodiode. Adapted from [267].

A canteliver with a very small tip, $\sim 8\ nm$ in size, is rastered over the sample surface, while it is driven into a forced vibration with a frequency just below its eigenfrequency. At the same time, the height difference between sample and tip is controlled with a piezoelectric stage at a distance, where the tip can be affected by both the attracting van der Waals forces and the Pauli repulsion of the atoms in the layer. The sum

of these forces (Lennard-Jones potential) result in a shift of the tip's eigenfrequency resulting in an amplitude and phase modulation of the driven oscillation. This change can be then detected by a laser light, focused on the top of the tip, which is then aligned to the middle of a segmented photodiode after multiple reflection events. Measured data was evaluated by gwyddion.

3.3.4 Grazing-Incidence Wide-Angle X-Ray Scattering

Grazing-incidence wide-angle x-ray scattering GIWAXS measurements were carried out at the SAXS/WAXS beamline at the Australian Synchrotron. Highly collimated x-rays, with 10.2 keV kinetic energy, were aligned to the sample surface. Scattering patterns, at a distance calibrated using a silver behenate scattering standard, were collected from 0.11 to 0.4 ° incidence angle (αi) with a resolution of 0.02 °. This resolution was chosen in order to ensure enough sensitivity both at the surface and in the film. All 2D scattering patterns were converted to 1D, creating in as well as out plane cuts, using the software tool NIKA. [20] GIWAX measurements in this thesis were carried out by Sven Huettner.

3.3.5 Photoluminescence Spectroscopy

PL and the resulting photoluminescence quantum efficiency (PLQE) were measured in an integrating sphere (Ulbricht-sphere) with an entering and exiting ports, as schematically shown in **Fig. 3.8**.

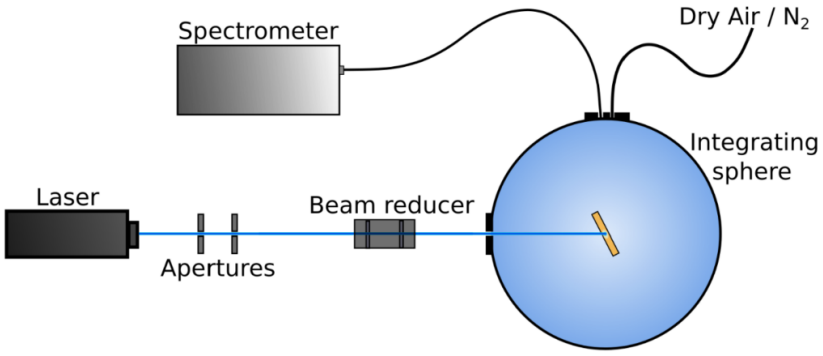

Figure 3.8: Schematic illustration of the PL setup: A laser beam is focused by numerous apertures and a beam reducer into an integrating sphere with a choosable atmosphere. After numerous light scattering events, the laser light is coupled out from the sphere, through an optical fibre, into a spectrometer. Adapted from [268].

A laser, with a spot size of $\sim 2mm$ and a variable monochromated wavelength, is focused into the entering hole of such an integrating sphere. The latter is covered with a highly reflective coating on the inside and acts thus like a hollow cavity: Light within the sphere is scattered diffusively over all angles, resulting in a linear dependency between the intensity of entering and exiting light. The exit port is coupled with an

optical fibre to a spectrometer enabling data analysis. Measurements in the integrating sphere can be performed in various atmospheres, such as pure N_2, ambient or dry air.

The PLQE can be calculated from four different PL measurements (**Fig. 3.9**), as introduced by *deMello et al.* [269]

- *Dark measurement*, in order to rule out the noise of the spectrometer.
- A *"No Sample"* measurement, determining the lasers overall optical power reaching the spectrometer, and to have a background for the next two measurements.
- An *"Off-Axis"* measurement, where only scattered light will hit the sample.
- An *"On-Axis"* measurement, where the sample is directly hit by the light after entering the sphere.

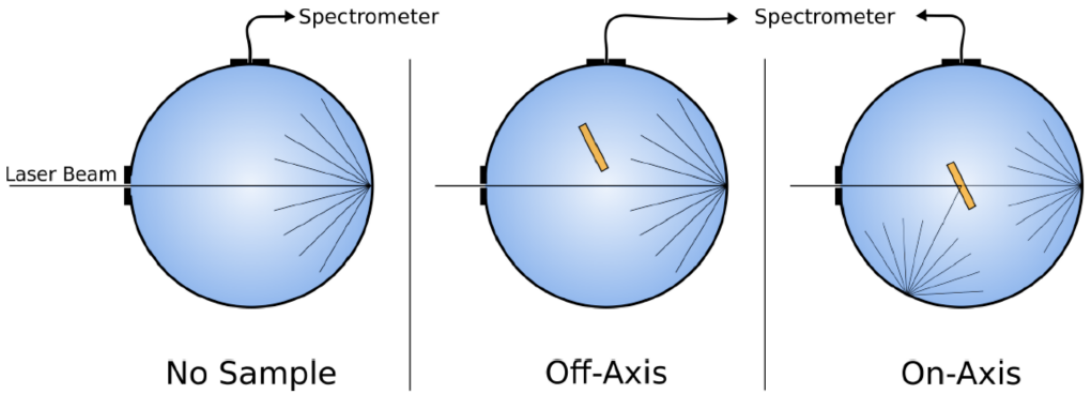

Figure 3.9: Schematic illustration of the *"No Sample"*, *"Off-Axis"* and *"On-Axis"* measurements crucial for PLQE determination. Adapted from [268].

When integrating up the *"On-Axis"* and *"Off-Axis"* spectra, one needs to differentiate between the areas under the PL peak (I_{on}/I_{off}) and under the original laser peak (L_{on}/L_{off}), resulting in the overall PLQE of:

$$PLQE = \frac{I_{on} - (1 - A) \cdot I_{off}}{L_{off} \cdot A}, \text{ with } A = 1 - \frac{L_{on}}{L_{off}} \tag{3.7}$$

3.3.6 UV-vis Spectroscopy

In UV-vis spectroscopy, with the clue in the name, mostly UV and visible, but also IR, light ($\sim 200 - 1200nm$), with a known intensity I_0, is sent through a monochromator, and directed through an aperture onto a sample of interest, as schematically shown in **Fig. 3.10**.

The light directed onto the sample will be either reflected, absorbed or transmitted. The latter, with intensity I, can be measured for every wavelength with a photoresistor and an amplifier, yielding the absorbance A of the sample. Assuming neglectable light

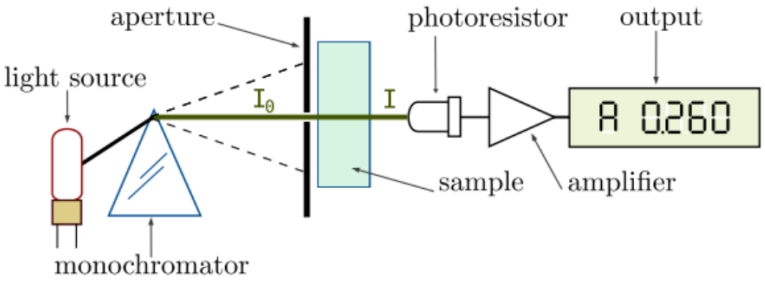

Figure 3.10: Schematic illustration of the UV-vis setup. Light from a light source is monochromated, resulting in a beam with intensity I_0 and a specific wavelength λ, which is then directed onto the sample of interest. Due to absorption in the sample, the light intensity will change to I, which can be measured by a photoresistor and an amplifier. Adapted from [267]

reflectance, the absorption coefficient $\alpha(\lambda)$ can be determined from the Lambert-Beer law, knowing the layer thickness d:

$$A = log_{10}(I_0/I) = log_{10}(e) \cdot \alpha(\lambda)d \tag{3.8}$$

UV-vis measurements will be used to determine optical band gaps of materials in this thesis, they are, however, not sensitive enough for sub-bandgap measurements, since their resolution for very low intensities are limited.

3.3.7 Photothermal Deflection Spectroscopy

PDS allows to measure absorbance of very thin films in the range of $\sim 350 - 1100\ nm$ with a very high sensitivity down to 10^{-5}. Additionally to material absorption data, this technique can provide valuable information on optical parameters, such as sub-bandgap states and Urbach energy, with its working principle shown in **Fig. 3.11**.

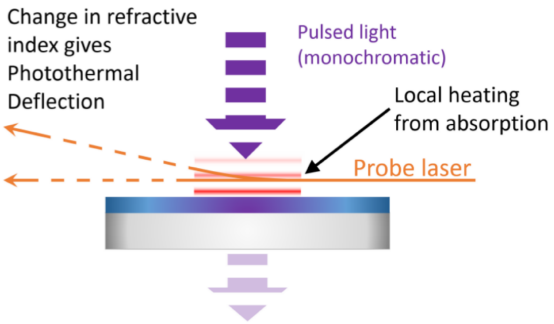

Figure 3.11: Schematics of the working principle of PDS. While a sample is locally excited by a pulsed light (purple dashed arrow), the absorbed light heats up the sample, generating heat waves (red lines). The temperature change just above the sample will change its refractive index, resulting in the reflection of a probe layer beam (orange arrow). Adapted from [270]

Generally, this technique makes use of the mirage effect: The material gets heated by absorption of a pulsed light at a certain wavelength (monochromated 150 W xenon

short arc lamp (Ushio Inc.), passing a filter wheel (FW102C, Thorlabs Inc.) and pulsed by a chopper (MC2000, Thorlabs Inc.)), which heats up the surrounding liquid (Fluorinert) and changes thus its refractive index. At the same time, a probe laser (633 nm) is directed just above the thin film surface and gets deflected by the heated up liquid, measurable with a lock-in amplifier and a photodetector.
The deflection angle ϕ of the probe laser depends linearly on the absorption coefficient $\alpha(\lambda)$ and the incident light intensity of the pump beam I_0: $\phi \sim \alpha(\lambda) I_0$. The overall PDS spectrum needs to be calibrated with a UV-vis spectrum. A more detailed description of the technique can be found elsewhere. [270, 271] PDS measurements in this thesis were carried out by David Becker-Koch.

3.3.8 Transient Absorption Measurements

TA spectroscopy as an ultrafast technique with a sub-100 fs time resolution, allowing for the detection of internal conversion, intersystem crossing, fluorescence and CT state formation. A pulse, 4 mJ in energy, was generated at a rate of 1 kHz with a regenerative Ti/Sapphire amplifier (Solstice, Spectra Physics), and was split into two parts with equal energy. One part was put through a mechanical delay stage, before it was focused onto a YAG substrate, in order to generate an IR probe and a reference light. The other part was used to pump an optical parametric amplifier in order to generate a 700 nm pump light with a final intensity of $\sim$ 20 nJ. Both parts, probe and pump, were focused on the sample into a 0.5 mm diameter spot, and both probe and reference spectra were detected using fibre spectrometers (Photonic Solutions). On each sample, both pure films and devices were measured. For the latter, the probe light was reflected from the metal electrode surface (so called pixels), while for films, probe and pump spots were chosen to be between device electrodes (between pixels). TA measurements shown in **Chapter 4** were carried out by Artem Bakulin at the Department of Chemistry, Imperial College London (UK).

3.3.9 DekTak Profilometer

For a quick layer thickness determination, samples were first scratched by a tweezer in order to locally remove a part of the layer, followed by Bruker DektakXT contact profilometer measurements. It consists of a vertically movable diamond tip stylus with a diameter of 12.5 μm and a horizontally movable sample stage. After the tip is brought into contact with the film, it slowly scans its surface, yielding in absolute values for height differences, down to a resolution of $\sim$ 10 nm. Measurements were levelled before extracting height information.

3.3.10 Device Characterization

3.3.10.1 Solar Simulator

Characterization of organic solar cells was done by an ABET AAA Sun 3000 solar simulator, schematically shown in **Fig. 3.12a**, as a light source and by following ASTM G-173 standards. The light source was calibrated by a reference silicon photodiode in order to simulate a 100 mW/cm^{-2} AM 1.5 (described in **Sec. 2.1.2.1**) spectrum.

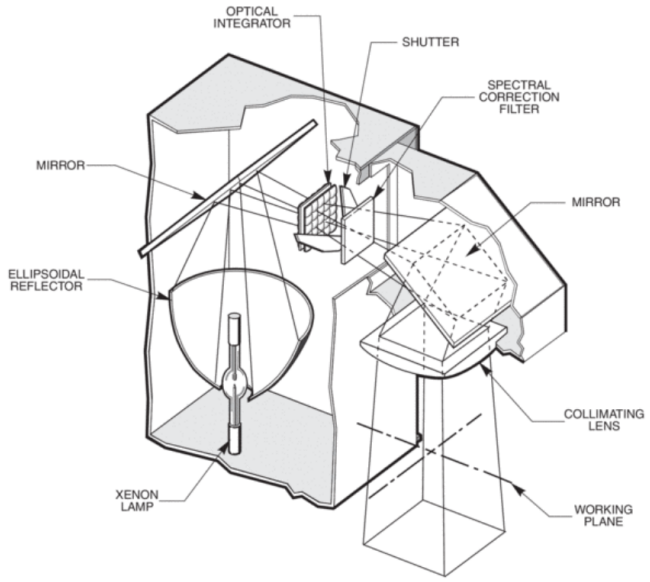

Figure 3.12: Cut-away view of a solar simulator with labelled components. Adapted from [272], Copyright 2019, Newport Corp.

Each pixel on a solar cell was characterized by a self-built arduino setup, a Keithley 2450 Source Measure Unit (SMU) and a LabView software. Current-voltage IV curves, described in **Sec. 2.1.1**, were measured in dark and light (under the solar simulator) from -1 V to 1 V in 0.05 V steps and an equilibration time of 25 ms. Prior to IV curve measurements, however, the light intensity of the solar simulator needed to be corrected by a spectral mismatch factor, measured by our EQE setup, described below.

3.3.10.2 External Quantum Efficiency

EQE of devices is measured under short circuit conditions, thus without applying an external bias, and its value indicates the percentage of incident photons which contribute to a measurable current at the electrodes, thus to the photocurrent, at a certain wavelength λ. It is determined by a self-built setup, as schematically shown in **Fig. 3.13**, where low intensity monochromated light ($(350-1050)$ nm) is separated by a beam splitter, and a part of it is focused on an individual solar cell pixel. The wavelength dependent sensitivity of the setup is calibrated by a NIST-traceable photodiode prior to each measurement.

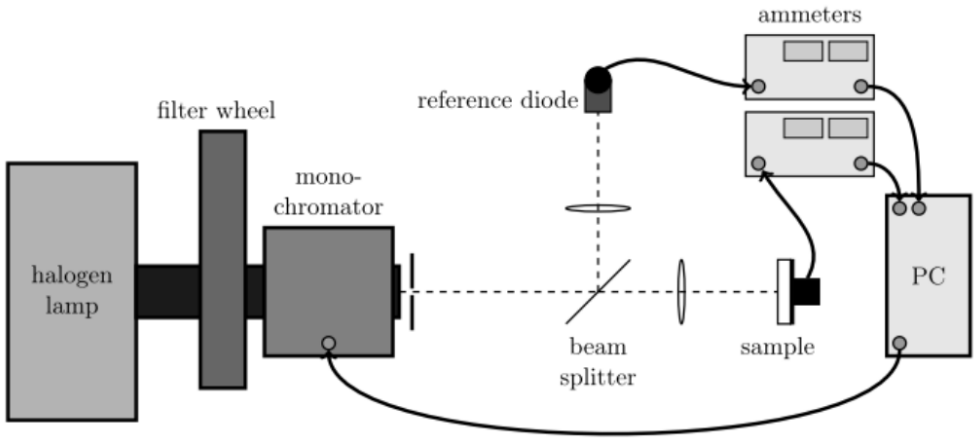

Figure 3.13: Schematics of the experimental setup for EQE measurements, including a halogen lamp, a filter wheel and a monochromator for light generation at certain wavelengths and a beam splitter, a reference diode and various measuring units for determination of the correct wavelength dependent EQE. Adapted from [267]

Knowing the photon flux of the solar spectrum (AM 1.5) and the EQE for the range of wavelengths, where the material combination used for solar cells absorbs, one can predict the J_{sc} of the solar cell by:

$$J_{sc}^{\text{predicted}} = e \cdot \int_{\lambda_1}^{\lambda_2} EQE(\lambda)\phi_{AM\ 1.5}(\lambda)\mathrm{d}\lambda \tag{3.9}$$

Additionally, in order to account for spectral differences, a spectral mismatch factor, as described by *Seaman et al.*, [273] was calculated. It accounts for differences between the AM 1.5 reference spectrum $\phi_{AM\ 1.5}$, the spectral irradiance of the solar simulator ϕ_{SS}, the spectral responsivity of the reference diode EQE_{RD} and the the EQE_{PV} spectrum of the corresponding PV device,[274] as in:

$$M = \frac{\int_{\lambda_1}^{\lambda_2} EQE_{RD}(\lambda)\phi_{AM\ 1.5}(\lambda)\mathrm{d}\lambda}{\int_{\lambda_1}^{\lambda_2} EQE_{PV}(\lambda)\phi_{AM\ 1.5}(\lambda)\mathrm{d}\lambda} \cdot \frac{\int_{\lambda_1}^{\lambda_2} EQE_{PV}(\lambda)\phi_{SS}(\lambda)\mathrm{d}\lambda}{\int_{\lambda_1}^{\lambda_2} EQE_{RD}(\lambda)\phi_{SS}(\lambda)\mathrm{d}\lambda} \tag{3.10}$$

3.3.10.3 Sample Holder and Environmental Rig

A sample holder and a home-built environmental rig (shown in **Fig. 3.14**) were designed by Dr. Paul Hopkinson and Andreas Weu, respectively, while both are described in great detail in [275]. The combination of both allows for a controlled atmosphere in the sample holder, while measuring IV or EQE curves, allowing thus for testing performance changes during degradation.

Pure N_2 (99.999%) is used as the carrier gas, and it can be mixed with both O_2 (99.99%) and H_2O (water containing bubbler) in a precisely controlled way, measured by sensors (EasyDew humidity sensor from Michell instruments and Cambridge Sen-

sotec 2100). The sample holder allows for measuring four solar cell substrates at the same time.

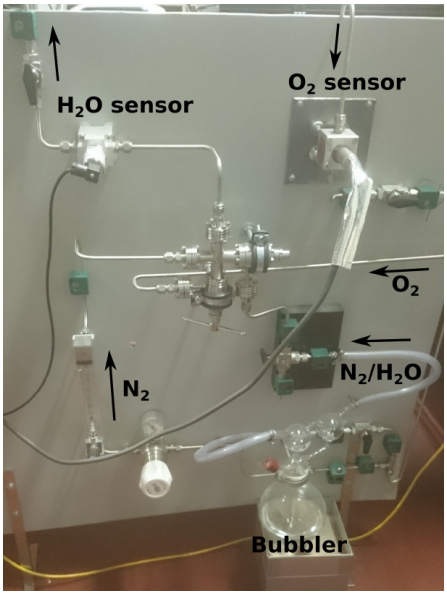

Figure 3.14: Photograph of the home-built environmental rig, including gas flow directions, marked with arrows, O_2 and H_2O sensors and the water filled bubbler. Adapted from [276]

Part I

Non-Fullerene Acceptor Molecules: *N*-Heteroacenes

4 | *N*-Heteroacenes: a Novel Class of Non-Fullerene Acceptors

This chapter is based on our recently published article "*N*-Heteroacenes as a New Class of Non-Fullerene Electron Acceptors for Organic Bulk-Heterojunction Photovoltaic Devices" in the journal Solar RRL. [20] This project was performed in collaboration with David Leibold and resulted in a further publication with the title "Triptycenyl-phenazino-thiadiazole as acceptor in organic bulk-heterojunction solar cells" in the journal Organic Electronics. [122]

4.1 Intorduction

There is a burning need for alternatives to fullerene derivatives mainly due to their low light absorption and high costs of purification. Non-fullerene acceptors (NFAs) offer a great opportunity to overcome these issues, as described in **Sec. 3.1.1**. Back in 2016, when we started to investigate NFAs, the choice of acceptor material was still mostly limited to fullerenes, [277] however, some progress in alternative acceptor compound development has already been made. [25] With *Bunz and co-workers*, we started to investigate a new class of materials: *N-Heteroacenes*. When we started to investigate this material system, only one publication in the literature had so far incorporated *N*-Heteroacenes as an acceptor moiety of a π conjugated donor, [278] however, no publications existed investigating *N*-Heteroacenes as acceptors in OSCs. One noteworthy example of this material system is TIPS-TAP, [279] which packs in a brickwork motif, when spin-coated into a film, resulting in high charge carrier mobilities, up to 13 $cm^2V^{-1}s^{-1}$ for electrons. [280–282] Due to this promising property and the lack of literature reports, we investigated TIPS-TAP and two of its derivatives TIPS-TAP-1T and TIPS-TAP-2T in BHJ OSCs. First, their optical and electronic properties are analysed (**Sec. 4.2**), followed by their performance in devices (**Sec. 4.3**), showing they can achieve a PCE of 2.5 %. Then, their morphological (**Sec. 4.4**) and photophysical (**Sec. 4.5**) properties are characterized underlining, that *N*-Heteroacene acceptors exhibit interesting photophysics, fundamentally differing from what has been observed so far in fullerene based systems. Finally, the results are carefully discussed and summarized and an overview of further improvements in NFA systems is given.

4.2 Optoelectronic Properties

As already mentioned above, three derivatives of tetraazapentacene: TIPS-TAP, TIPS-TAP-1T and TIPS-TAP-2T have been synthesised by *Bunz and co-workers*, based on previously reported procedures, [249, 280, 283] with chemical structures shown in **Fig. 4.1**. The only difference between these molecules are additional 1 or 2 *triptycene* side chains, in the case of TIPS-TAP-1T or TIPS-TAP-2T, respectively. Nevertheless, all of them are soluble in common solvents, such as toluene, chloroform, or chlorobenzene, and were purified by column chromatography and recrystallised in hexane, as described by *Biegger et. al*. [283]

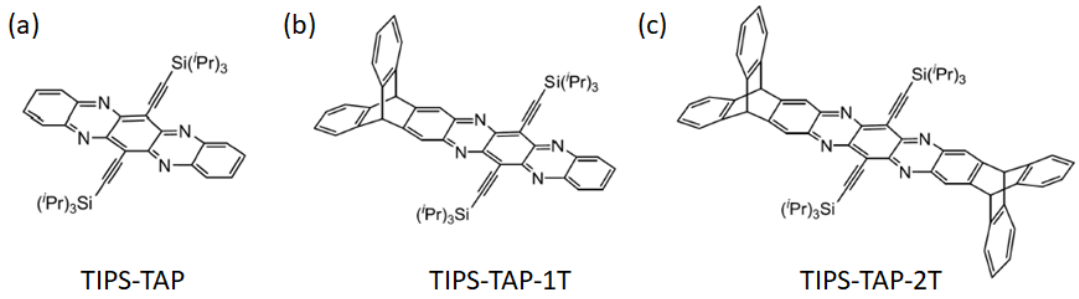

Figure 4.1: Chemical structures of **(a)** TIPS-TAP, **(b)** TIPS-TAP-1T and **(c)** TIPS-TAP-2T. Adapted from [20]. Copyright © 2017 WILEY-VCH Verlag GmbH & Co. KGaA, Weinheim.

In order to have a better understanding of these materials, we first characterised their optoelectronic properties: We performed UV–vis absorption measurements on all three acceptors in both solution and of thin films, as shown in **Fig. 4.2a-c**. Additionally, we also measured UV-vis absorption of a poly(4,8-bis[(2-ethylhexyl)oxy]benzo[1,2-b:4,5-b'] dithiophene-2,6-diyl3-fluoro-2-[(2-ethylhexyl)carbonyl]thieno[3,4-b]thiophenediyl) (PTB7) thin film (**Fig. 4.2d**), which we have chosen as the donor material for OPV devices, discussed further in the next Section. The absorption spectrum of TIPS-TAP shows strong variations when comparing the measurements in solution and thin film. The maximum absorption peak of the latter is red-shifted by $\sim$ 20 *nm* compared to the measurement in solution, indicating stark intermolecular interactions of the aromatic π-systems of TIPS-TAP and thus strong crystallisation in the solid state, in agreement with previous reports. [282] In the case of TIPS-TAP-1T and TIPS-TAP-2T, the change in absorption between solution and film is considerably reduced, indicating that the introduction of side chains significantly reduces crystallisation.

Energetic alignment in general will determine device physics, including charge transport, injection and extraction. A first estimation to energetics can be done by measuring the IP of individual materials by UPS. As we will see in the following Chapter, this can be sometimes a crude estimation, we will, however, stick to this approximation in this study. The DOS and thus the valence band with respect to the VL of the three ac-

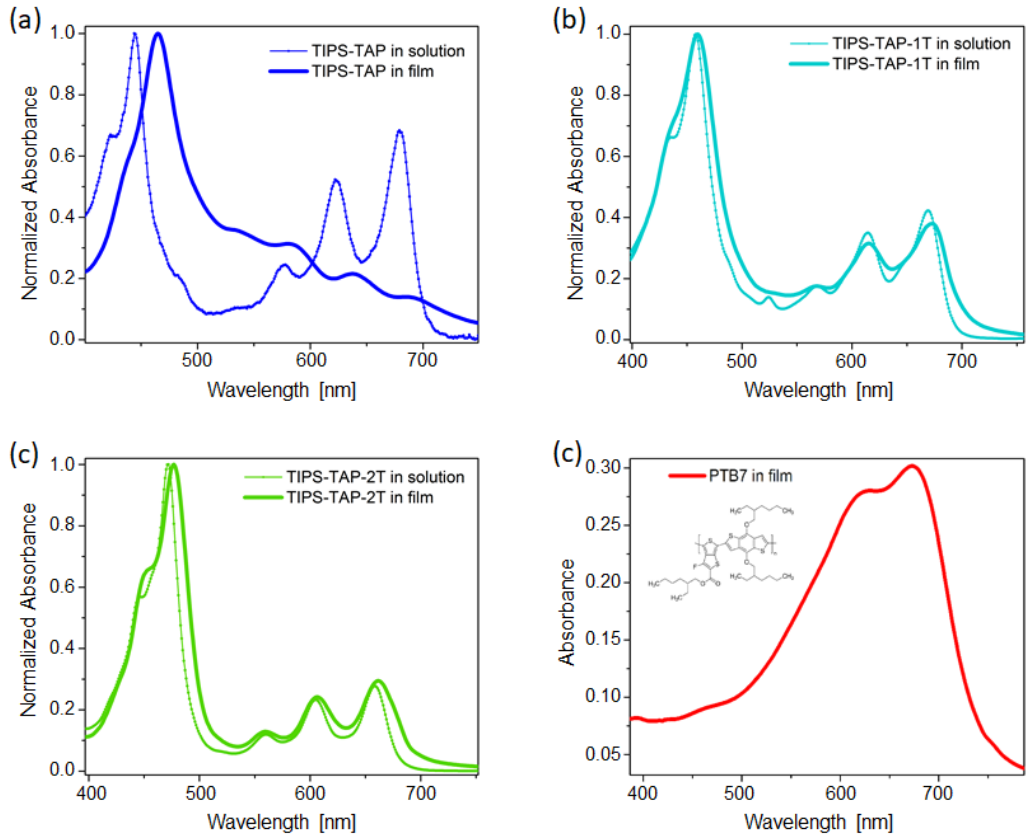

Figure 4.2: UV-vis absorption measurements in both solution and thin films of **(a)** TIPS-TAP, **(b)** TIPS-TAP-1T, **(c)** TIPS-TAP-2T and **(d)** PTB7 (thin film only). Adapted from [20]. Copyright © 2017 WILEY-VCH Verlag GmbH & Co. KGaA, Weinheim.

ceptors is shown in **Fig. 4.3a**. The corresponding IPs can be determined by fitting the low binding energy edge of the valence band for the corresponding materials. [171] We found the IPs to be 6.05 eV for TIPS-TAP and 5.8 eV for both TIPS-TAP-1T and TIPS-TAP-2T. Such a small decrease in the IP after introducing side chains is in agreement with previous studies including CV measurements and DFT calculations. [283] One often makes the assumption, that the optical and transport gaps in organic materials are the same, such as it is in the case of inorganic materials. [150] This is not always the case, as described in **Sec. 2.3.2.2**, it yields, however, a good approximation. This holds especially true when comparing similar systems, such as it is the case for our acceptor materials. The EAs can thus be estimated by adding the corresponding optical gaps to the measured IPs. As it can be seen in **Fig. 4.2**, the absorption onset in the measured UV-vis spectra are not sharp, suggesting that the absorption measurements are affected by crystallization induced light scattering. This makes data fitting rather difficult, we thus performed highly sensitive PDS absorption measurements on the same films (**Fig. 4.3b**). These measurements yielded optical gaps of 1.55 eV, 1.60 eV and 1.70 eV, for TIPS-TAP, TIPS-TAP-1T and TIPS-TAP-2T, respectively, in good agree-

ment with previous DFT calculation results. [283] All in all we are able to estimate the EAs of all three components, resulting in a complete energetic picture. The energy levels of the three acceptor molecules and that of PTB7 are summarized in **Fig. 4.3c**.

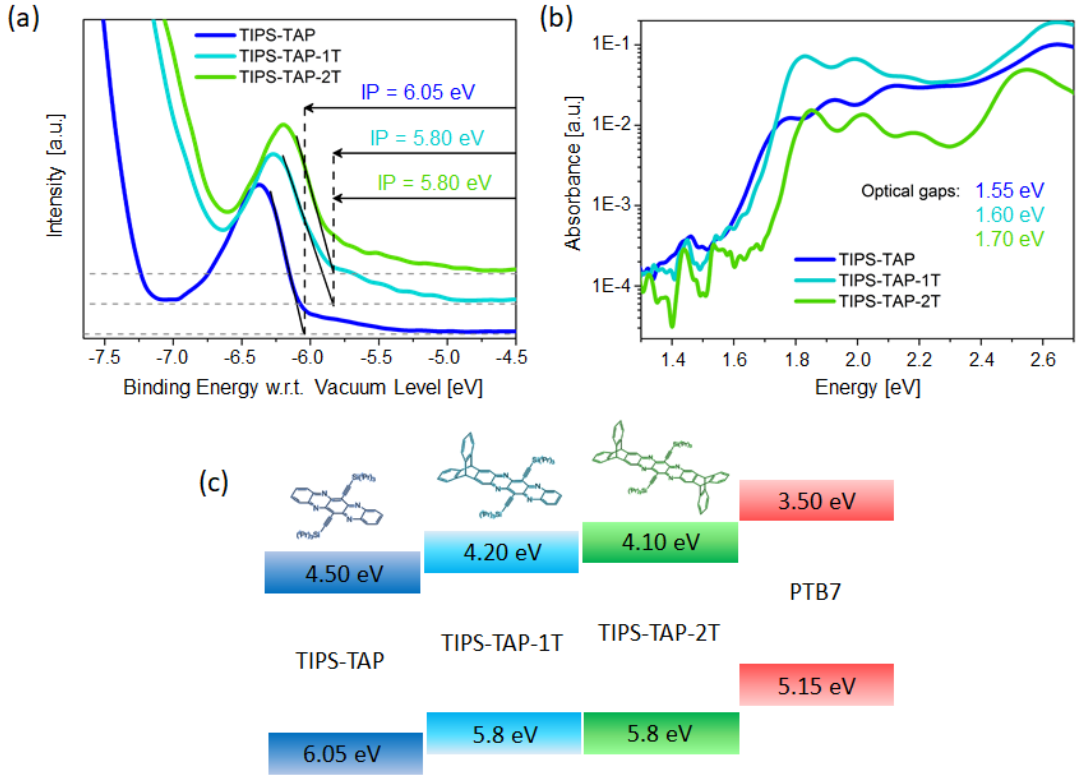

Figure 4.3: (a) UPS and **(b)** PDS measurements of TIPS-TAP (dark blue), TIPS-TAP-1T (light blue) and TIPS-TAP-2T (green). Resulting energy levels with indicated IP and EA values for the three acceptors and for PTB7 (Values from [74]), which was used as donor in OPV devices. Adapted from [20]. Copyright © 2017 WILEY-VCH Verlag GmbH & Co. KGaA, Weinheim.

4.3 Photovoltaic Device Performance

We chose PTB7 as the donor material for BHJ OPV devices, and fabricated these in a first investigation with a donor to acceptor ratio of 1:1. EQE spectra of these devices and corresponding IV curves are plotted in **Fig. 4.4 a** and **b**, respectively. EQE curves, when compared with the UV-vis absorption data (**Fig. 4.2**), show that both donor and acceptor (for all three compounds) contribute to the photocurrent. Devices with an active layer of PTB7:TIPS-TAP exhibit a rather moderate peak EQE of 18 %, which is only slightly improved when using TIPS-TAP-1T. However, when changing the acceptor to TIPS-TAP-2T, the EQE is significantly increased, achieving a maximum peak value of 46 %. This enhancement is consistent with the IV characteristics of devices, including the threefold increase in J_{sc}, when exchanging TIPS-TAP with TIPS-TAP-2T. This exchange results in an additional improvement of the V_{OC} from

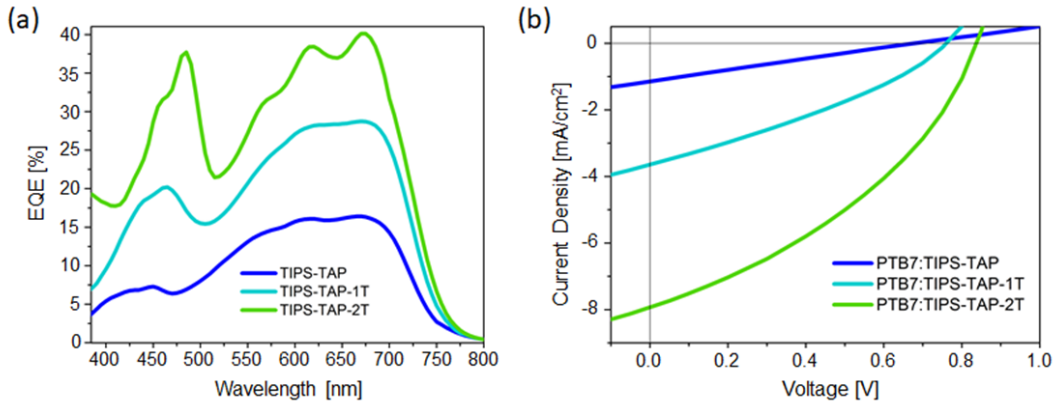

Figure 4.4: (a) EQE and **(b)** JV curves for PTB7:TIPS-TAP (dark blue), PTB7:TIPS-TAP-1T (light blue) and PTB7:TIPS-TAP-2T (green) devices. Adapted from [20]. Copyright © 2017 WILEY-VCH Verlag GmbH & Co. KGaA, Weinheim.

0.7 *V* in average for TIPS-TAP to 0.78 *V* and 0.85 *V* for TIPS-TAP-1T and TIPS-TAP-2T, respectively. This improvement can be related to the change in energetics for the latter two, especially to the reduced EAs. Finally, also the device FFs are increased for the latter two derivatives, they are, however, still very low, even for TIPS-TAP-2T (approaching only $\sim$ 37 %). In order to exclude the possibility of poor extraction layers or contact properties, we also fabricated OPV devices with $PC_{70}BM$ as acceptor material, yielding high FFs ($\sim$ 64 %) and an overall higher PCE of 7.79 %. [20] Further factors for this rather poor performance for TIPS-TAP derivatives and the low FFs, can originate from a variety of different parameters, such as poor charge transport, unfavourable blend morphology/microstructure or geminate/bimolecular recombination, and will be discussed in the following Sections in more detail. Nevertheless, we demonstrated, that *N*-Heteroacenes can indeed serve as NFAs in BHJ OSCs with a maximum PCE of 2.51 %, which was achieved for devices with PTB7 and TIPS-TAP-2T as donor and acceptor, respectively. Photovoltaic performances for all three compounds are summarized in **Table 4.1**.

Table 4.1: Photovoltaic parameters for BHJ OSCs with PTB7 as donor and TIPS-TAP, TIPS-TAP-1T and TIPS-TAP-2T as acceptor. Values are averaged over approximately 40 devices. The value in brackets for PCE denotes the maximum obtained value for each derivative. Reconstructed with permission from [20]. Copyright © 2017 WILEY-VCH Verlag GmbH & Co. KGaA, Weinheim.

	V_{OC} [V]	J_{sc} [mA/cm²]	FF [%]	PCE [%]
TIPS-TAP	0.70 ± 0.02	2.57 ± 0.14	37 ± 1	$0.67 \pm 0.06 (0.74)$
TIPS-TAP-1T	0.78 ± 0.01	3.39 ± 0.16	31 ± 1	$0.82 \pm 0.04 (0.91)$
TIPS-TAP-2T	0.85 ± 0.07	7.51 ± 0.28	36 ± 2	$2.28 \pm 0.15 (2.51)$

We also carried out donor to acceptor ratio variation studies for PTB7:TIPS-TAP-2T blends in the hope for even better performing devices. Corresponding EQE curves and photovoltaic device parameters are summarized in **Fig. 4.5**. The PCE of the devices varies with varying donor to acceptor ratio, but interestingly it shows a maximum for the already tested ratio of 1:1, with a performance very similar to that at a ratio of 2:1. The EQE spectra show a comparable contribution to the photocurrent from both donor and acceptor with a rather similar wavelength dependent efficiency of charge extraction for both ratios. Ratios below 2:1 as well as above 1:1 result in poorer performing devices, thus we chose a ratio of 1:1 for further investigations.

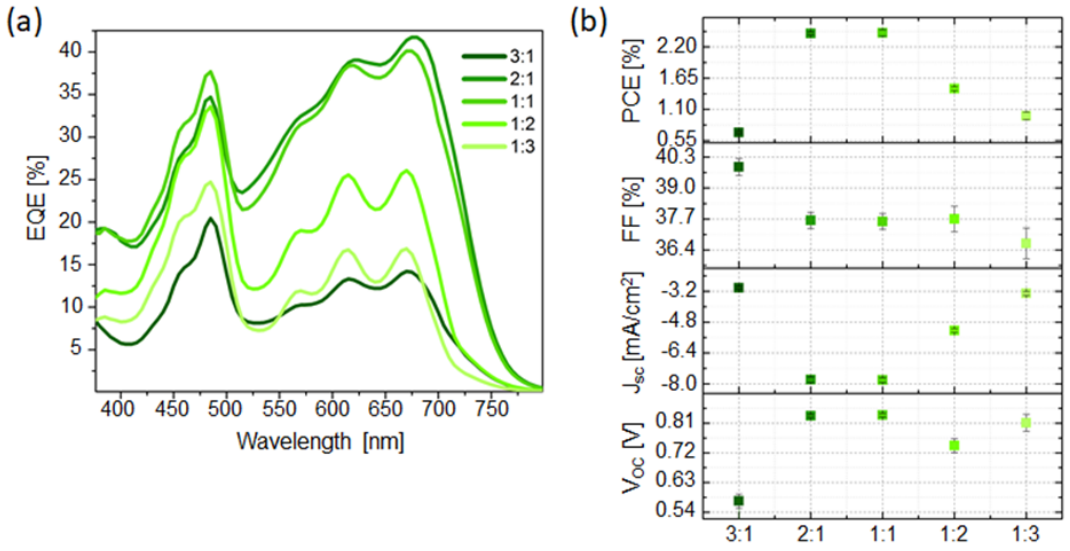

Figure 4.5: (a) EQE spectra and **(b)** averaged photovoltaic performance for a varying donor to acceptor ratio from 3:1 to 1:3, denoted with colours ranging from dark to light green, respectively. Reproduced with permission from [20]. Copyright © 2017 WILEY-VCH Verlag GmbH & Co. KGaA, Weinheim.

4.4 Morphological Properties

In order to better understand the photovoltaic behaviour of our cells, we characterized the film surfaces with polarized optical microscopy and AFM, both shown in **Fig. 4.6**. It can be clearly seen in the polarized microscope images, that in the case of PTB7:TIPS-TAP blends (**Fig. 4.6a**), small crystallites are formed, which we attribute to TIPS-TAP undergoing strong crystallisation during the film formation process. AFM measurements of the same film (**Fig. 4.6b**) showed a very rough microstructure ($RMS \approx 5.34\ nm$). Both microscopic techniques suggest a gross phase separation caused by strong intermolecular interactions between the TIPS-TAP molecules. Such a large-scale phase separation can result in low J_{sc} and FF of PV devices, leading thus to an overall drop of device performance.
When moving to acceptor molecules including *tripticene* side chains, both polarized

microscope images (**Fig. 4.6b** and **c**) and AFM micrographs (**Fig. 4.6e** and **f**) show very smooth and uniform surfaces with an RMS of approximately 0.5 nm for both TIPS-TAP-1T and TIPS-TAP-2T.

In order to further investigate film crystallinity and orientation, we performed grazing-incidence wide-angle x-ray scattering (GIWAXS) measurements on thin films of pristine acceptors as well as on blends with PTB7, as shown in **Fig. 4.7**. Pure TIPS-TAP films (**Fig. 4.7a**) exhibit a very high crystallinity and strong anisotropic orientation with high intensity $(00k)$ peaks, suggesting an edge-on molecular orientation towards the substrate. [282] Similar crystalline features can also be found in PTB7:TIPS-TAP blends, however, with somewhat reduced intensity compared with pristine acceptor films, showing that the solid state packing of TIPS-TAP remains unchained, but somewhat reduced. Such an edge-on orientation can be very beneficial for horizontal charge transport, such as it is needed in field-effect transistors (FETs), it is, however, detrimental to solar cells, where a vertical charge transport is desired. This unfavourable TIPS-TAP molecule orientation is probably also one of the reasons for a poor device performance.

Introducing *triptycene* units highly suppresses molecular crystallization as already suggested by polarized microscope images and AFM micrographs (**Fig. 4.6**) and confirmed by GIWAXS measurements (**Fig. 4.7**). The latter shows neither for TIPS-TAP-1T, nor TIPS-TAP-2T any clear crystalline features, which holds for both pristine and with PTB7 blended films. A crystal structure has been reported previously for solution grown TIPS-TAP-2T single crystals, [283] in our thin films on the contrary, no such crystallization occurs. Without this crystallization, thin films are more likely to have a higher intermixing and thus an increased surface smoothness, such as already suggested by AFM measurements shown above. Our results show, that crystallization is suppressed for both TIPS-TAP-1T and TIPS-TAP-2T, resulting in fully amorphous films and thus likely in a similar BHJ morphology, however, the corresponding device performances are very different. This suggests, that a further morphological fine-tuning is necessary in order to find a balance between small phase separated and pure material domains for efficient charge separation and transport, respectively.

4.5 Photophysics

While morphological differences between PTB7:TIPS-TAP-1T and PTB7:TIPS-TAP-2T devices are minimal, their PV performance is highly different, the latter showing a more than doubled J_{sc} with respect to the first. In order to find the origin of these dissimilarities, we investigated the photophysics by examining charge generation and recombination in PTB7:acceptor blends: We measured TA spectroscopy in the near-IR spectral region, in which only photo-induced absorption features of charges and excitons are present. As measured TA spectra of a PTB7:TIPS-TAP film are shown in **Fig. 4.8** at short (1 ps) and long (> 2 ns) delay times. The observed spectra shape is significantly changing with time, whereas the early and late features can be assigned

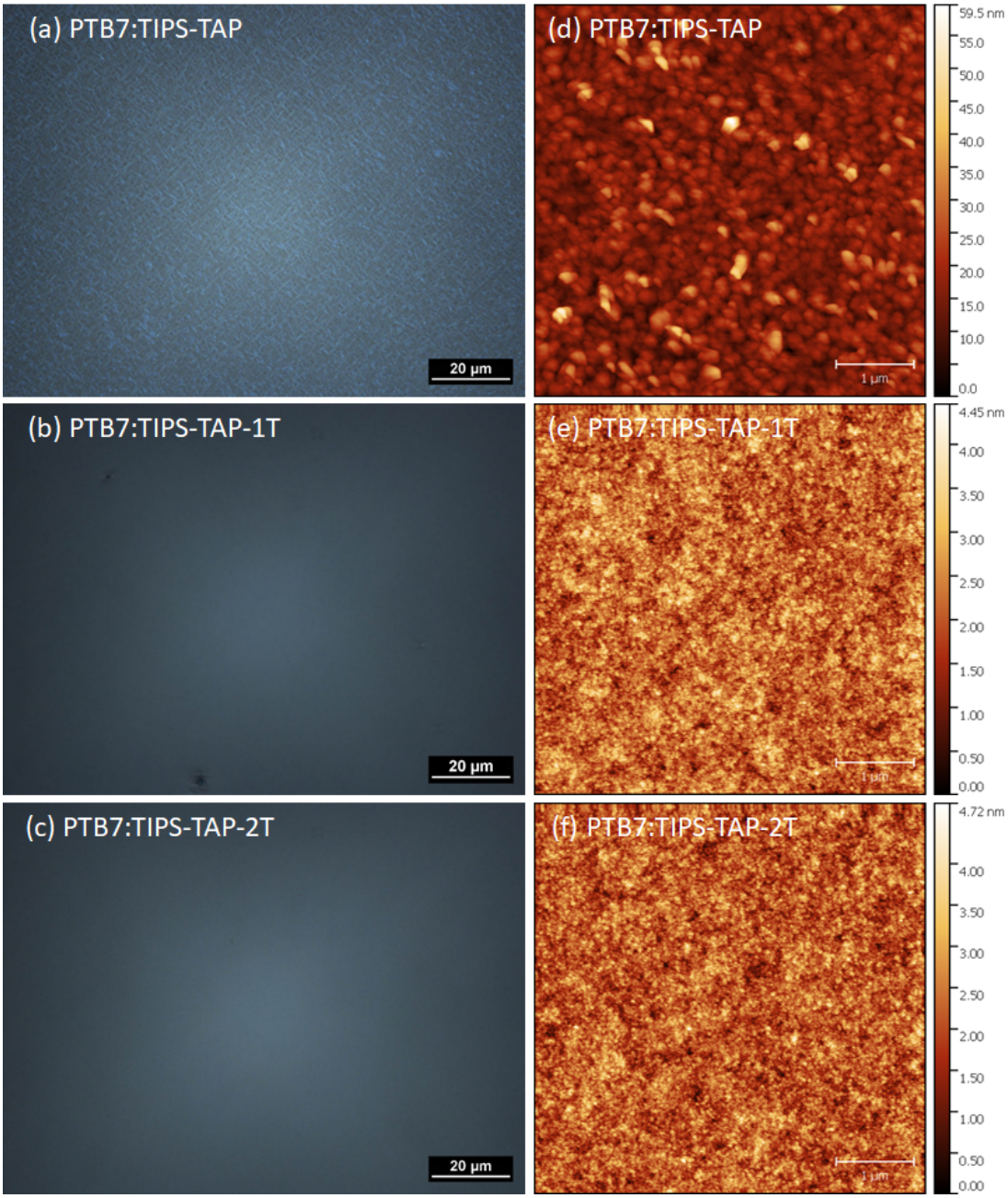

Figure 4.6: Polarized microscope pictures (left) and AFM micrographs (right) of the following blends: PTB7:TIPS-TAP (**(a)** and **(d)**), PTB7:TIPS-TAP-1T (**(b)** and **(e)**) and PTB7:TIPS-TAP-2T (**(c)** and **(f)**). Adapted from [20]. Copyright © 2017 WILEY-VCH Verlag GmbH & Co. KGaA, Weinheim.

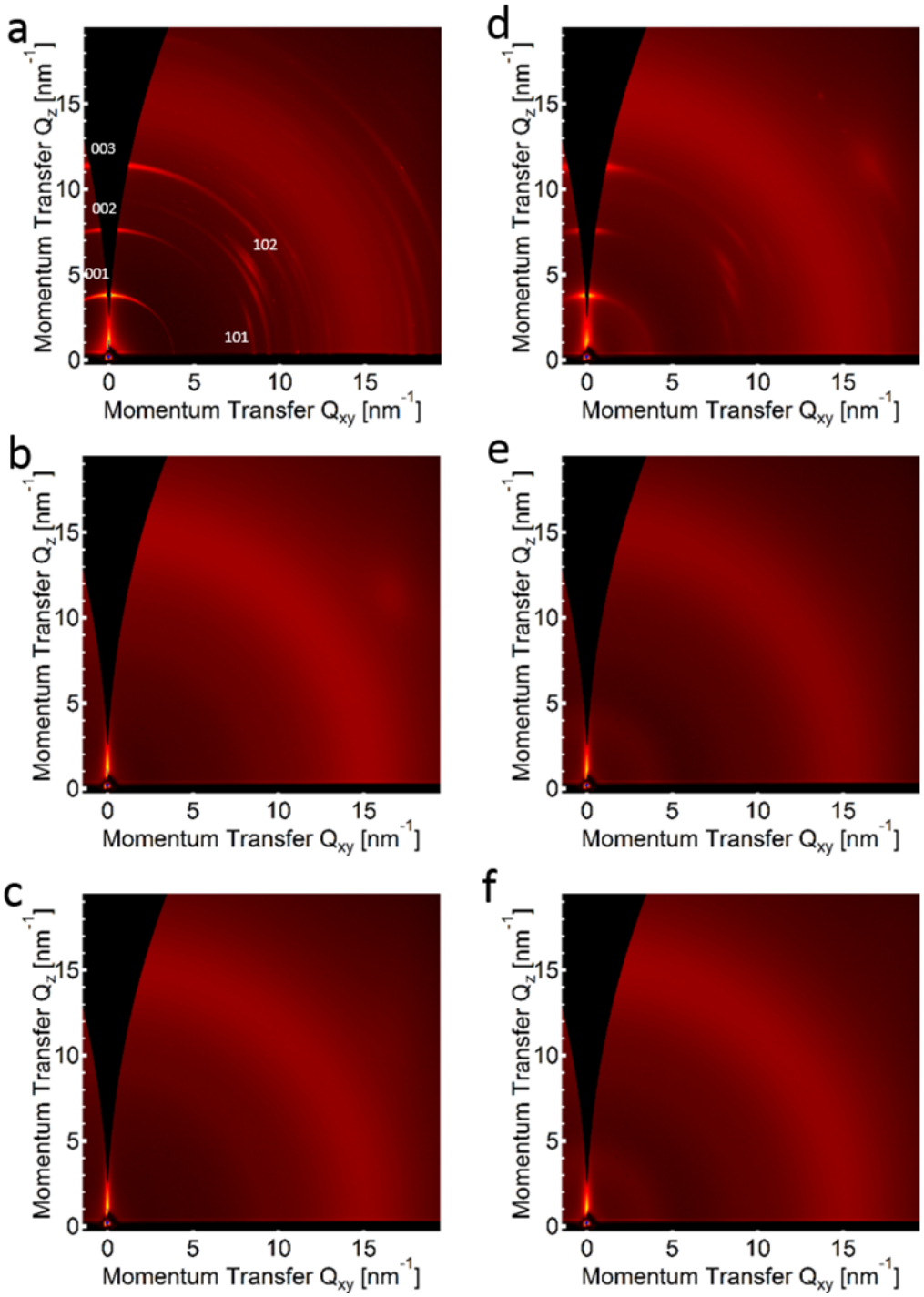

Figure 4.7: GIWAXS measurements on pure films of **(a)** TIPS-TAP, **(b)** TIPS-TAP-1T, and **(c)** TIPS-TAP-2T and on donor acceptor blends of **(d)** PTB7:TIPS-TAP, **(e)** PTB7:TIPS-TAP-1T, and **(f)** PTB7:TIPS-TAP-2T. Reproduced with permission from [20]. Copyright © 2017 WILEY-VCH Verlag GmbH & Co. KGaA, Weinheim.

to bound excitonic states and separated charge carriers, respectively. The substantially larger absorption cross-section of excitons compared to charges and the large overlap of the absorption band of these two in the studied region make the analysis of early charge generation processes very complicated.

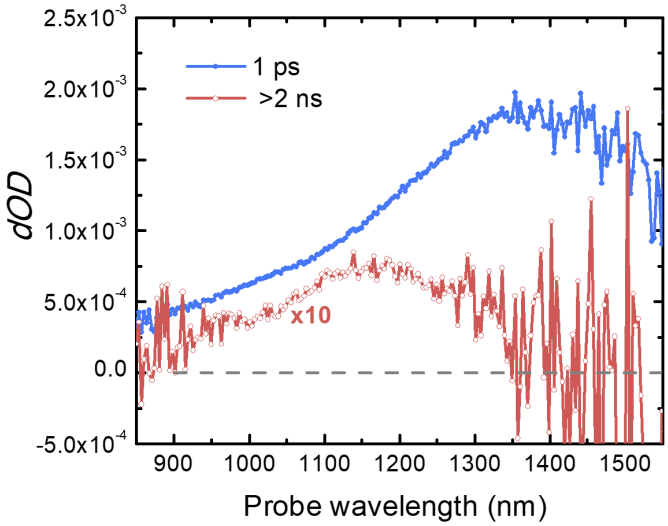

Figure 4.8: TA spectra for a PTB7:TIPS-TAP blend film at short (1 *ps*) and long (> 2 *ns*) delay times. The latter is multiplied by 10 for better visibility. Reproduced with permission from [20]. Copyright © 2017 WILEY-VCH Verlag GmbH & Co. KGaA, Weinheim.

In order to illustrate the entire TA progression, we show transients at 1100 *nm* probe frequency of all PTB7:acceptor films and devices in **Fig. 4.9**, with the x-axis subdivided into short (< 1 *ps*) and long (up to 1 *ns*) delay times. The cross-section of charges at this wavelength is the highest and is almost comparable to exciton absorption. Charge dynamics in films are compared in **Fig. 4.9a**. We associate charge generation within the films with the early, sub-10 *ps* dynamics. We analysed our data with singular value deconvolution (SVD), which confirmed that changes in the excited-state population in these blends occur on the $\sim$ 10 *ps* timescale, in good agreement with the existence of large pure donor and acceptor phases. [284] After their formation, at a $\sim$ 10 *ps* timescale, charge carriers experience a fast and efficient geminate recombination. This stark recombination can explain the poor performance of PTB7:TIPS-TAP devices, however, it cannot explain why the better performing PTB7:TIPS-TAP-1T and PTB7:TIPS-TAP-2T devices show very similar kinetics when measured in films. The recombination time as well as the survival efficiency for charged states in both latter films exceed the values observed for PTB7:TIPS-TAP only by $\sim$ 20 %. In order to investigate whether the kinetics observed in these films is representative for the device operation, we performed further TA measurements on complete, working devices under short-circuit conditions.

TA transients of working devices (**Fig. 4.9b**) show in contrast to measurements of

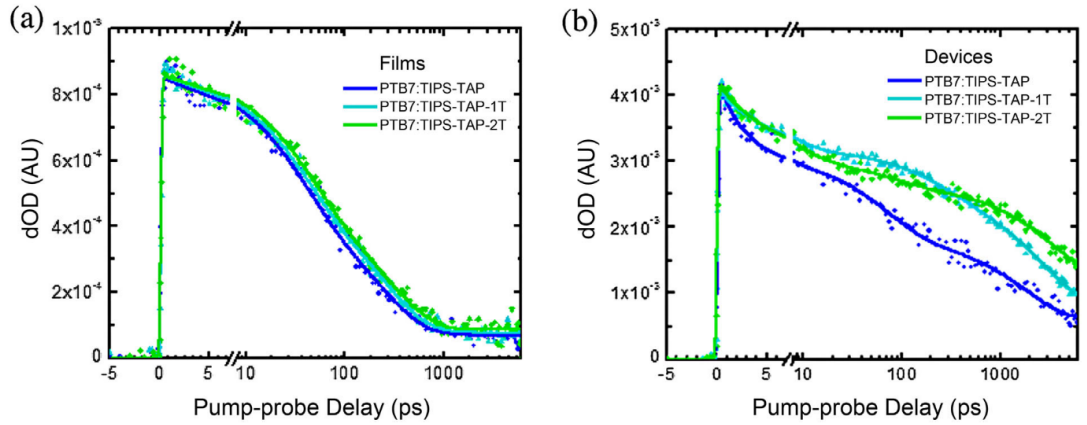

Figure 4.9: TA transients at 1100 *nm* probing wavelength as a function of delay time representing the evolution of charge dynamics in **(a)** films and **(b)** complete solar cells of PTB7:TIPS-TAP (dark blue), PTB7:TIPS-TAP-1T (light blue), and PTB7:TIPS-TAP-2T (green). Dots and lines are representing measurement data and fits, respectively. Reproduced with permission from [20]. Copyright © 2017 WILEY-VCH Verlag GmbH & Co. KGaA, Weinheim.

films (**Fig. 4.9b**) a pronounced material dependency: Charge recombination dynamics within the first nanosecond after generation for PTB7:TIPS-TAP-1T and PTB7:TIPS-TAP-2T is greatly reduced compared to PTB7:TIPS-TAP. While recombination in the latter is quite strong, it is delayed ($\sim$ *ns*) and largely suppressed in the other two derivatives, accounting for a total loss of less than 50 % of charge carriers in PTB7:TIPS-TAP-2T. We note, that these devices are normally operated under one-Sun working conditions, while the photon flux and concentration of the excited states in TA measurements corresponds to a $\sim$ 20 Sun continuous-wave illumination. Hence, a part of the observed decay can be associated with exciton-exciton annihilation and/or bimolecular recombination, which is not present under normal device operation.

4.5.1 Field-Dependent Charge Dynamics

The difference we observed between the charge dynamics in films and devices indicates a strong built-in field-dependence of charge separation and recombination, which is quite surprising. These findings are possibly very specific for the new type of molecular acceptors reported in this study and have been very rarely observed for conventional, polymer:fullerene blends. In the latter, such an external electrical field is not necessary for long-range charge separation, [285] since the electron injection into the delocalized LUMO states of the fullerene acceptor happens without the need for electrons to overcome any free-energy barrier. [286] Furthermore, it has been demonstrated for a variety of polymer:fullerene systems with a comparable driving energy for charge separation, that a highly efficient and ultrafast charge separation and transfer is completely independent on the particular choice of fullerene acceptor or even material morphology. [287] It is thus rational to study the photophysics of thin films of polymer:fullerene systems in thin layers and not in functional devices, [132, 221, 288]

but puts a question mark over existing studies on non-fullerene acceptor systems showing similar photophysics to that of polymer:fullerene systems. [289–291] In our investigated system of non-fullerene *N*-Heteroacenes, charge separation in PTB7:TIPS-TAP-1T and PTB7:TIPS-TAP-2T seemingly occurs through a slow ($\sim$ *ps*) activation, with the external field in the device being essential for achieving high efficiency of this process.

4.5.2 Bimolecular Recombination

While the sub-*ns* dynamics in both PTB7:TIPS-TAP-1T and PTB7:TIPS-TAP-2T are similar, the decay after 1 *ns* is about twice as slow in PTB7:TIPS-TAP-2T. We associate this decay at this timescale with bimolecular recombination. We also believe, that this loss channel is mainly responsible for the clear difference in device performance of PTB7:TIPS-TAP-1T and PTB7:TIPS-TAP-2T. Generally, bimolecular recombination is determined by the availability of states serving as recombination centres and by the charge carrier mobility. In order to further study charge carrier recombination, we carried out steady-state illumination-intensity dependent measurements, shown in **Fig. 4.10** and evaluated as described in **Sec. 2.2.3**. While the photocurrent shows an almost identical behaviour for all investigated acceptor systems, the differences in V_{OC} are significant. We believe, that the dissimilarities in bimolecular recombination observed in the TA transients in **Fig. 4.9** can be associated with a lower density of states and with that a decreased number of low-energy recombination centres at the interface between PTB7 and TIPS-TAP-2T compared to TIPS-TAP-1T. [65] The effect of molecular orientation, specifically that of the *N*-Heteroacene acceptor toward the PTB7 donor is a further interesting and important effect. Recent publications highlight, that the efficiency of charge separation, and thus the overall device performance, in systems with non-fullerene acceptors is strongly dependent on the degree of exposure of the acceptors π-framework to the donor. [292]

We found this unusual photophysics very interesting and investigated this effect in both a further *N*-Heteroacene, [122] and a fullerene ($PC_{70}BM$) system with PffBT4T-2OD as the donor. [123] This topic is, however, not further discussed in this thesis.

4.6 Summary

In this work, we introduced *N*-Heteroacenes as a new class of organic, non-fullerene small molecules, as electron accepting materials in organic solar cells. With the introduction of triptycene units to the original TIPS-TAP molecule we are able to test a class of gradually modified *N*-Heteroacenes and find that these changes can dramatically change the energy level structure of the system, the polymer-acceptor blend morphology, the photophysics of charge carriers and with that the overall OPV device performance. The tested *N*-Heteroacenes show a completely different behaviour com-

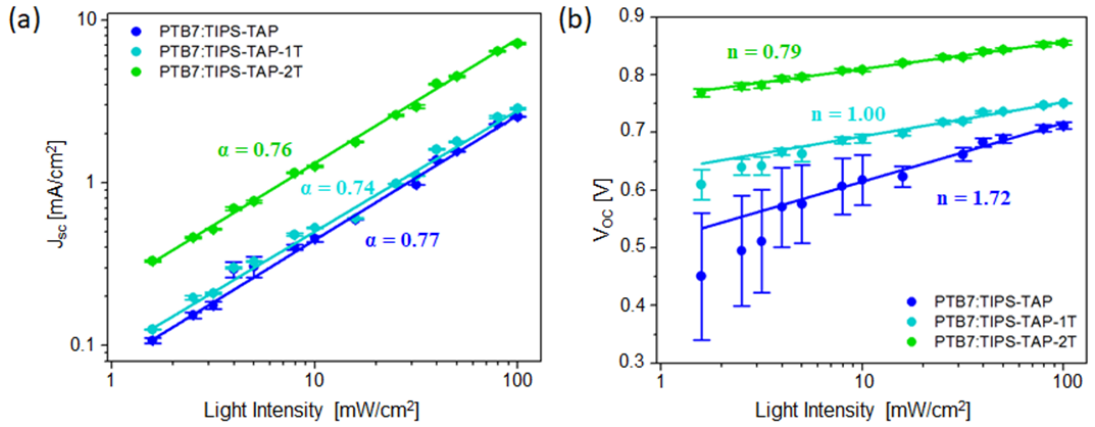

Figure 4.10: Light intensity measurements of the **(a)** J_{sc} and **(b)** V_{OC} for PTB7:TIPS-TAP (dark blue), PTB7:TIPS-TAP-1T (light blue), and PTB7:TIPS-TAP-2T (green). Individual measurements are denoted with dots, including error bars, while corresponding linear fits are shown as lines. Reproduced with permission from [20]. Copyright © 2017 WILEY-VCH Verlag GmbH & Co. KGaA, Weinheim.

pared to conventional fullerene acceptors, especially their photophysics, which shows a strong electric field-dependence and an unusually slow charge generation. When substituting two triptycene units to the tetraazapentacene core molecule, recombination losses, when compared with unsubstituted molecules, are suppressed. The class of *N*-Heteroacenes offers a large versatility of possible chemical structures, [293–295] which could allow in future to tune molecular properties further in order to achieve better electron accepting materials with a further suppressed recombination. Their tendency to crystallize and thus the overall microstructure can also be tuned by choosing different side chains. [296] The overall device performance can be further boosted by an additional optimization of the microstructure, which can be achieved for example by the use of additives during processing, which has already been shown for other non-fullerene acceptors. [297–299] In summary, this new material system of *N*-Heteroacenes shows respectable photovoltaic performance up to 2.5 % without extensive optimization, but only with a variation of substituted side chains, motivating for their further development.

Part II

Damage-Free UPS Depth Profiling

5 | Visualising the Vertical Energetic Landscape in Organic Photovoltaics

This chapter is based on our recent publication in the journal Joule with the title: "Visualising the Vertical Energetic Landscape in Organic Photovoltaics". [34] This project was performed in collaboration with Andreas Weu from our group, Jiangbin Zhang from the group of Prof. Dr. Richard H. Friend (University of Cambridge, UK), Zhuping Fei from the group of Prof. Dr. Martin Heeney (Imperial College London, UK) and Prof. Dr. Yongsheng Chen (Nankai University, China), who performed and supervised the synthesis and layer fabrication for high efficiency photovoltaic materials.

5.1 Introduction

Research on OPV devices resulted in impressive PCEs surpassing 16 % and 17.3 % for single and multi-junction devices, respectively. [12, 300] The efficiency of solar cells depends, as described in **Section 2.1.1**, mainly on their J_{sc}, V_{OC} and FF. Up to date, EQEs exceed 90 %, [301] resulting in J_{sc} as high as 20.20 mA/cm^2, and FFs approach 80 %, [302] being thus as good as other commercialized high efficiency technologies, such as gallium arsenide (GaAs) and c-Si. [303] Up to now, it is mainly the V_{OC} of OPV devices which limits their performance, making them still less efficient than established inorganic photovoltaic technology or perovskite solar cells, and should be optimized further. The V_{OC} is, as introduced earlier, commonly associated with the photovoltaic gap energy (E_g^{PV}) at the D/A interface. [42, 304] An accurate determination of donor and acceptor energy levels, especially at their interface is thus the first important step for V_{OC} optimization and elucidation of energetic losses. The alignment at such organic-organic interfaces is still not fully understood, but it is particularly important for the new range of high-efficiency photovoltaic systems including both fullerenes [305, 306] and NFAs, [15, 18, 247, 248, 307] with low driving energy offsets between donor and acceptor HOMO/LUMO levels, as well as for ternary systems. [308, 309] The real energetic alignment of all these systems remains unclear, because of a lack of techniques offering reliable information: while

a reporting of energy levels is ubiquitous in OPV device studies, [289, 310] energetic values obtained by different techniques, including CV measurements, [311, 312] DFT calculations, [311, 313] Kelvin probe measurement, [313, 314] differential pulsed voltammetry, [313] and PES [20, 311, 315, 316] are often combined, resulting in a large scatter of reported energetics, even for the same material system. [317–319] Additionally, in these reports, polarization, [320] and interfacial effects [171, 320, 321] such as band bending and interface dipoles are not taken into account.

Several studies attempted to obtain the energetic landscape more accurately, including CT luminescence studies, [35, 117, 322, 323] UPS measurements on blend film surfaces with varying donor to acceptor ratios and extrapolating them to a BHJ, [324] simulations, [191, 193, 325, 326] and scanning Kelvin probe microscopy. [327–329] CT state measurements, however, are very sensitive to variations in active layer thickness and device architecture, [330] and ultimately do not provide information about the overall energetics (relative HOMO and LUMO levels) in OPV devices. Simulations strongly depend on reliable input parameters and do not substitute direct experimental measurements. And last but not least, scanning Kelvin probe microscopy is limited by tip size convolution effects and complex sample preparation methods, [331] and additionally does not yield any information on the DOS of the materials. [332]

It is widely accepted that the most accurate and reliable method for determining the energetic levels, including the VL position and DOS, [333] of materials is UPS, which is highly surface sensitive and is thus limited to the top $\sim 2\ nm$ of the investigated sample. [334] Consequently, energetic alignment investigation were limited to thermally evaporable small molecules, accessible by "layer-by-layer" measurements, including consecutive steps of a few *nm* of material deposition followed by spectroscopic characterization *in situ*. [335–337]

Such a "layer-by-layer" approach is not suitable with solution-processed materials, which are deposited in a single step by spin coating. [338, 339] A possible way of obtaining energetic information in these layers would be by depth profiling, e.g. by a succession of etching steps and surface sensitive investigations. The latter, in studies comprising molecular depth profiles, is dominantly performed by XPS or secondary ion mass spectrometry (SIMS), while etching steps are typically make use of monoatomic Ar bombardment. This is done despite the fact, that the latter introduces significant surface damage, especially for organic materials. [340, 341] GCIBs, [30] in which argon gas clusters are formed by a supersonic expansion, resulting in clusters with a tunable cluster size ($100 - 10000\ atoms/cluster$) with a few eV per atom, [29] offer the opportunity of damage free depth profiling, [342–348] as introduced in earlier sections. GCIB etching has already found application with SIMS and XPS, [349, 350] and only in a handful of reports with UPS. [351, 352] The authors show by comparing

"layer-by-layer" measurements with GCIB depth profiles, that the latter results in an essentially damage-free removal of thermally evaporated organic molecules. Solution processed active layers, as in most OPV devices, have not been, however, examined with this technique.

In this chapter, we present the first demonstration of an accurate determination of energetic landscapes in OSCs by a succession of UPS measurements and GCIB etching steps. First, we probe a BHJ and a bilayer of the widely investigated model material system of P3HT and $PC_{60}BM$ and show, that UPS depth profiling not only results in an accurate determination of the vertical energetic landscape, but also in information on the material percentage, with a better resolution than XPS depth profiling. Next, we apply our technique to several high-efficiency systems, namely PffBT4T-2OD:$PC_{70}BM$, PFBDB-T:C8-ITIC, PBDB-T:NCBDT, DRCN5T:$PC_{70}BM$ and PTB7:$PC_{70}BM$ and demonstrate its broad applicability to various material systems including fullerenes, NFAs, polymers and small molecules. Finally, we demonstrate that when comparing the E_g^{PV} measured by UPS depth profiling and by measurements of the individual components of the blend with measured CT state energies for the very same systems, the latter comparison results in a poor, while our technique in a very good agreement. This observation demonstrates that interfacial effects, such as band bending and interfacial dipoles are only present when the donor and acceptor are blended, and that this will also strongly influence their energetic alignment. This observation highlights the need for energetic characterization methods, such as UPS depth profiling, or other approaches that can correctly determine E_g^{PV}, rather than the common characterization of the constituent materials, assuming VL alignment when blended. A more accurate determination of E_g^{PV} would result in a better V_{OC} estimation and also offer additional insights into V_{OC} and consequent PCE losses.

5.2 Method Development

5.2.1 Why Gas Cluster Ion Beams?

The efficacy of UPS depth profiling relies on essentially damage-free etching, such that the electronic structure of the materials stays unaltered, and thus the acquisition of UPS stays meaningful. While monoatomic Ar etching is a well-established, suitable tool for metal and inorganic material removal, the high kinetic energy of the ions results in significant damage to organic materials, [353–356] with the depth of introduced damage being even higher than that of the probing depth of XPS. [357] To overcome this issue, our method makes use of GCIBs, the working principle of which is schematically shown in **Fig. 5.1A**. The formation of Ar clusters, as described in great detail in **Sec. 3.3.2.1**, is based on supersonic gas expansion: high pressure Ar gas flows trough a nozzle into a lower pressure region, resulting in Ar clusters (agglomerates of atoms). Next, they flow through multiple skimmers and get charged by a filament. Magnetic

lenses and multiple electrodes ensure proper size selection and focusing, respectively. Key differences between monoatomic and cluster etching impact on thin films are summarized in **Fig. 5.1B**. While monoatomic etching results in a deep material penetration and a large degree of intermixing, cluster etching results in the formation of a shallow crater with negligible damage. [358, 359] Furthermore, monoatomic etching yield is considerably lower than that of cluster modes for the same beam current, thus, in order to eject a comparable amount of material, the sample would need to be bombarded significantly longer with the former, increasing the degree of damage even further. [360] Molecular dynamic simulations as well as empirical measurements of GCIB based etching show its advantages over monoatomic ion sources. [361, 362] For more clarity, the succession of UPS measurements and cluster etching is schematically drawn in **Fig. 5.1C**.

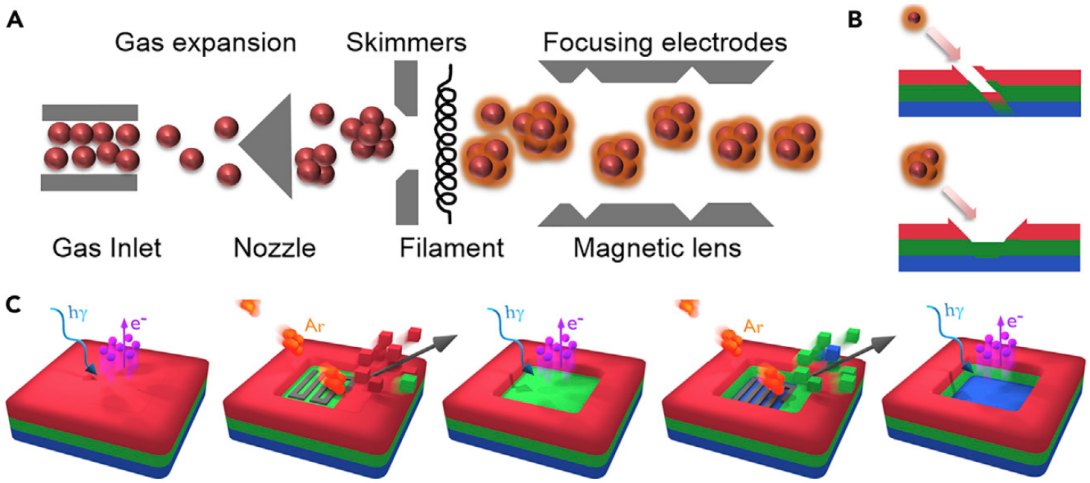

Figure 5.1: (A) Schematics of GCIB formation, where Ar ions from a gas inlet get into a gas expansion region through a nozzle, forming clusters, getting pre-size selected by multiple skimmers and charged by a filament. Afterwards, the charged clusters are size selected by a magnetic lens and are focused onto the substrate by electrodes. **(B)** Schematic representation of monoatomic and GCIB impact differences on a multi-layered thin film. **(C)** Schematic representation of depth profiling, e. g. the succession of surface sensitive investigations with UPS and etching steps with Ar-GCIB. Incident UV photons (blue wavy arrow) and emitted photoelectrons (purple spheres) represent UPS/XPS measurements. Etching is represented with cluster spheres (orange) and a grey line, representing rastering, resulting in material removal (cubes flying away). Reprinted with permission from [34]. Copyright © 2019 Published by Elsevier Inc.

5.2.1.1 Monoatomic vs. Cluster Etching

To further illustrate impact differences between monoatomic and cluster modes, we investigated their effect with XPS as well as UPS on several organic materials (P3HT, $PC_{60}BM$, PffBT4T-2OD, $PC_{70}BM$, PBDB-T, NCBDT, PFBDB-T and C8-ITIC), as shown in **Fig. 5.2**.

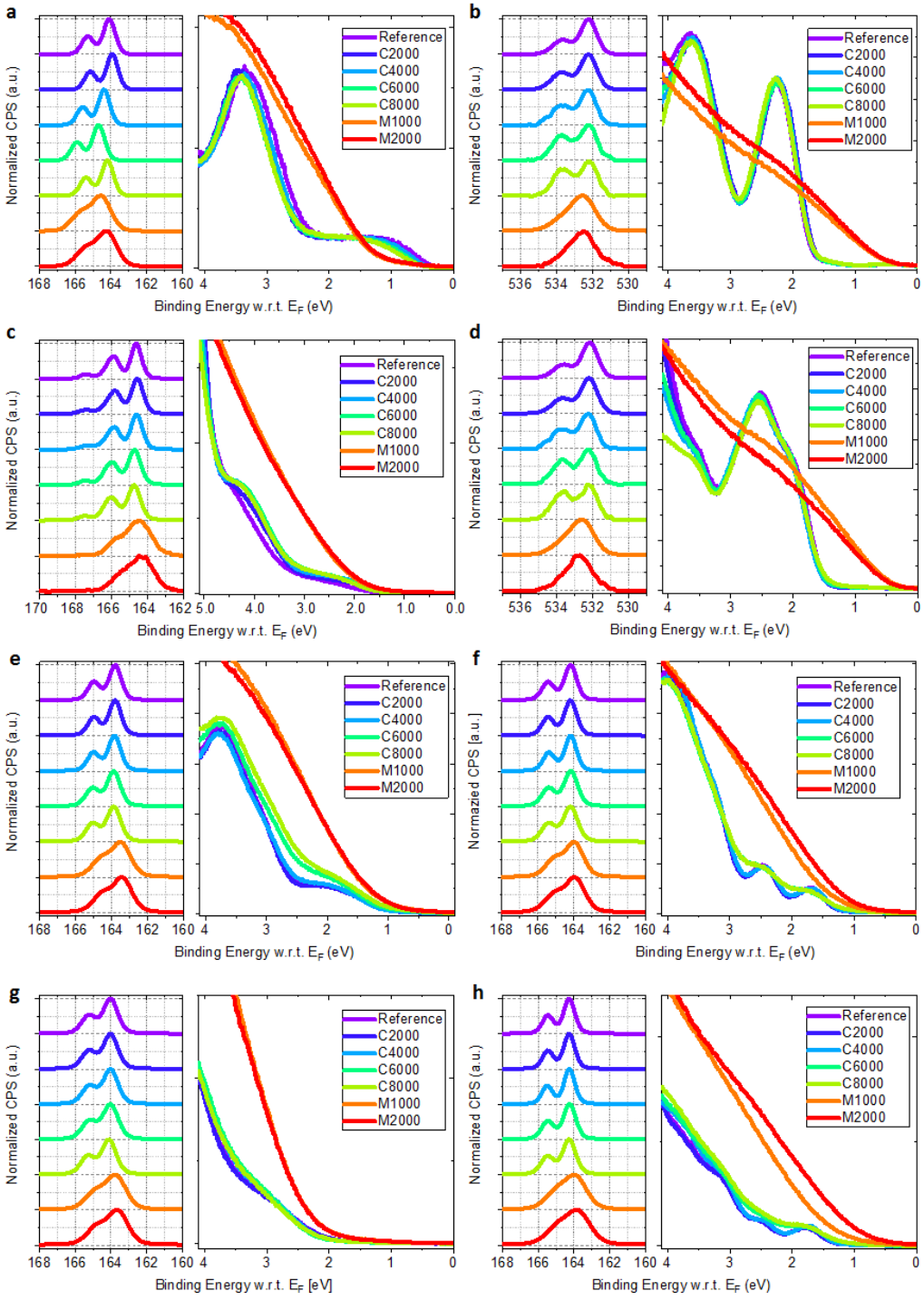

Figure 5.2: Damage comparison by XPS and UPS of a reference measurement (Reference, purple) with 4 different cluster modes with kinetic energies ranging from 2000 *eV* to 8000 *eV* (C2000 (dark blue), C4000 (light blue), C6000 (dark green) and C8000 (light green)) and 2 monoatomic modes with kinetic energies of 1000 *eV* (M1000, orange) and 2000 *eV* (M2000, red) after 15 second of etching. Comparisons by XPS (*S2p* or *O1s* spectra) and UPS (DOS) are shown on left and right panels, respectively, for **(a)** P3HT, **(b)** $PC_{60}BM$, **(c)** PffBT4T-2OD, **(d)** $PC_{70}BM$, **(e)** PBDB-T, **(f)** NCBDT, **(g)** PFBDB-T and **C8-ITIC**. Reprinted with permission from [34]. Copyright © 2019 Published by Elsevier Inc.

Impact differences were tested for four cluster and two monoatomic kinetic energies, ranging from $(2-8)\ keV$ and $(1-2)\ keV$, respectively, and compared with a reference spectrum without the 15 s etching step. UPS measurements are represented with corresponding DOS regions in subgraphs on the right: regardless of ion energy, monoatomic etching results for each investigated material in a complete destruction of the valence band region. At the same time, cluster etching preserves the original form of the DOS for almost all tested kinetic energies, in good agreement with previous investigations. [351] Higher energy cluster etching ($(6-8)\ keV$) introduces for some of the materials minimal changes and smears out some peaks, the effect still not comparable to the complete destruction of monoatomic modes. XPS results are represented with the corresponding *S2p*, or with the *O1s* spectra for the two fullerenes since they do not contain any S. Both are plotted in the left panel in each subgraph. A comparison of the XPS leads us to the same conclusion as the UPS results: while monoatomic etching results in significant broadening of all tested spectra (in average 35 % broader full width half maximum (FWHM) as for the reference spectrum), cluster etching yields no, or only minimal spectral broadening ($<$ 10 % broader FWHMs). We note, that for the *O1s* spectrum case, the change in the signal corresponds to surface contamination removal. For all further depth profiling experiments, cluster etching with a kinetic energy of 4000 eV was chosen to ensure minimal damage and reasonable etch times.

In order to further investigate impact differences between monoatomic and cluster etching, we carried out a UPS depth profile experiment on a thin P3HT:PC_{60}BM BHJ film using the monoatomic Ar ion etching source, a 3D representation of which is shown on the left in **Fig. 5.3**. Both the whole UPS region including the SECO (for binding energies in the range of $\sim (20-0)\ eV$ and the zoomed in valence band region (for binding energies in the range of $\sim (5-0)\ eV$, with the HOMO features, are shown. The latter is shown again in the individual measurement representation, from the top surface down to the underlying ZnO ranging from green to red. This spectrum is also compared with analogous cluster etching results for the very same film. Only after a few etching steps with the monoatomic source, no identifiable valence band structure can be measured due to a strong damage of the organic materials in the blend. On the contrary, GCIB etching preserves the electronic structure throughout the layer, and allows thus for an extraction of meaningful information about composition, as well as electronic structure as a funciton of depth, as we will discuss more in detail below.

5.2.2 UPS Depth Profiling

Measuring both XPS and UPS depth profiles allows for the extraction of compositional as well as energetic landscapes as a function of depth. We note, that our technique only results in a vertical resolution and does not provide lateral resolution, since both UPS and XPS spectra are collected from an area of $\sim 0.7\ mm^2$. On the one hand, depth profiles utilizing XPS allow for an atomic percentage determination of all individual atoms

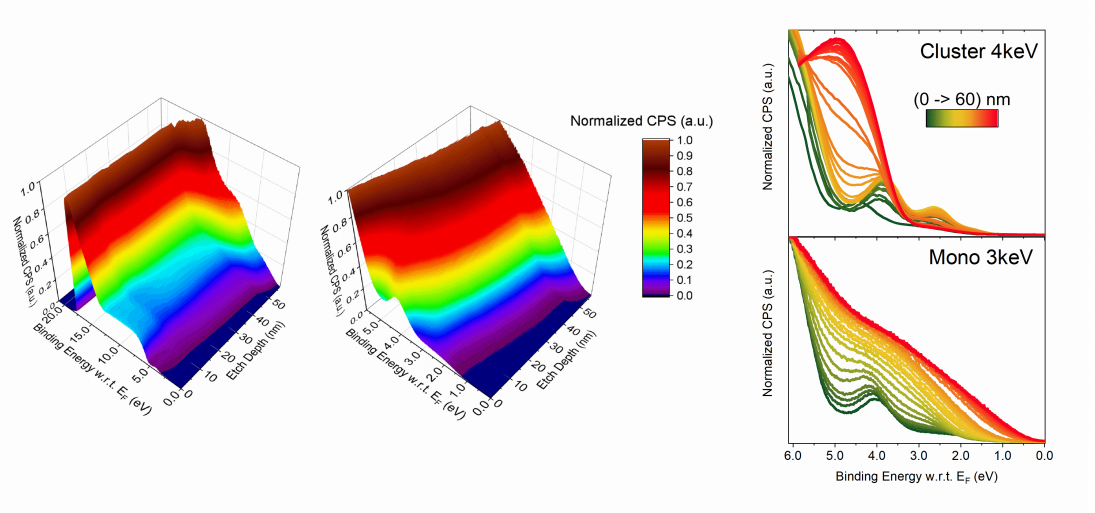

Figure 5.3: UPS depth profile comparison of monoatomic (3 *keV*) and cluster (4 *keV*) etching of a P3HT:PC_{60}BM film. 3D representation of UPS measurements for monoatomic etching are shown both for the entire measured region (left), and a zoomed in version of the DOS region (middle). Electronic structure evolution is also plotted in 2D (bottom right) with colours marking the etch depth from the top surface (green) down to the bottom (red) and compared to etching with a cluster source (top right). Reprinted with permission from [34]. Copyright © 2019 Published by Elsevier Inc.

present in the layer, with a vertical resolution of $\sim 10\ nm$, limited by the XPS probing depth. By knowing the chemical formulas of all constituent materials, atomic percentage values allow for a material percentage determination, as described in **Sec. A.2.2.1**. On the other hand, UPS depth profiles yield valuable information about the vertical energetic landscape, or more specifically the positions of the Fermi level, VL, and IPs for all constituent materials, in the top $\sim (1-2)\ nm$ of the film. Since the HOMO and LUMO terms are ubiquitous in literature to express the IP and EA of materials, we will carry on with this notation. Nevertheless, we want to remind the reader that the former expressions are purely one electron based theoretical constructs, [103] while our measurements represent real films. HOMO level positions are always determined by low binding energy edge fitting of the valence band. [171]

5.2.2.1 Fitting Procedure

In order to extract energy level information for all constituent materials, it is necessary to disentangle their individual relative contributions from the overall measured UPS spectrum. In our study we fit the valence band spectrum by a linear combination of the valence band spectra of the individual constituent materials, as proposed by *Yun et al.* [363] Following this approach, we are able to identify HOMO features of both the donor and the acceptor materials with respect to the Fermi level for all tested material systems. Additionally, we are able to extract the relative contribution of each material from the overall measured UPS spectrum. The whole fitting procedure is explicitly

described in **Sec. A.2.1.3** and is schematically shown for a BHJ of $P3HT : PC_{60}BM$ in **Fig. 5.4**.

5.2.2.2 Depth Profiling of a P3HT:PC_{60}BM Bulk Heterojunction

UPS depth profile measurements of a 60 nm thick P3HT:PC_{60}BM BHJ spin coated on a ZnO substrate are summarized in representative 3D maps in **Fig. 5.5A** and **B** with the whole region and the valence band region (up to 6 eV below the Fermi level), respectively. In order to highlight regions of particular interest, the depth scale is subdivided into three regions: surface ($(0-10)$ nm), bulk ($(10-58)$ nm) and bottom interface (around 60 nm).

Material percentage data representing relative contributions can be compared to the XPS results obtained by S/C atomic ratio measurements, as represented in **Fig. 5.5C** with a solid and a dotted line, respectively. Measurement data and corresponding fits at representative etch depths, denoted with **1** to **7** in this main graph, are shown in panels above and next to the main graph. In each panel, orange circles denote the original UPS measurements, while the fitted contributions of P3HT, PC_{60}BM, and ZnO are shown in blue, red, and green, respectively. The sum of the three, referred to from now on as the overall fit, is shown as a purple line.
UPS measurements show, that the very top surface, at depth point **1** (0 nm), consists only of P3HT, which is in excellent agreement with previous reports. [364, 365] From this point on, the PC_{60}BM contribution gradually increases with depth at points **2** (3 nm) and **3** (7 nm), until it reaches its maximum at depth point **4** (17 nm). Looking deeper into the layer results in a plateau region, represented at depth point **5** (29 nm), until the interface with ZnO is reached, showing DOS contribution from all constituent materials, as in depth point **6** (60 nm), resulting finally in only ZnO signal at depth point **7** (62 nm).
An increasing amount of PC_{60}BM in the top $\sim$ 20 nm layer is in good agreement with previous results obtained by XPS depth profiling utilizing monoatomic etching [364] as well as by angle resolved XPS. [366] Deviations in our UPS and XPS depth profiling material percentage results originate from some key differences between the UPS and XPS techniques, such as their probing depth being $\sim$ 5 times larger for XPS than for UPS. We note, that each data point in **Fig. 5.5** represents a vertical average from the denoted depth on until the probing depth of the corresponding technique. This results in a smearing out effect for the XPS depth profile, resulting in a poorer resolution than provided by UPS depth profiling, visible at regions with fast changes in material contribution: depth points **1** to **4** and near depth point **6**. Additionally, at the very surface, adventitious carbon alters the S/C ratio, which is used for material percentage determination in XPS measurements, introducing a falsely high PC_{60}BM amount. Differences in material composition results determined by UPS fitting and XPS calculation can be attributed to the latter two effects. In summary, using UPS depth profiles to extract compositional information eliminates the effects of adventitious carbon and significantly increases the depth resolution due to the enhanced surface sensitivity of

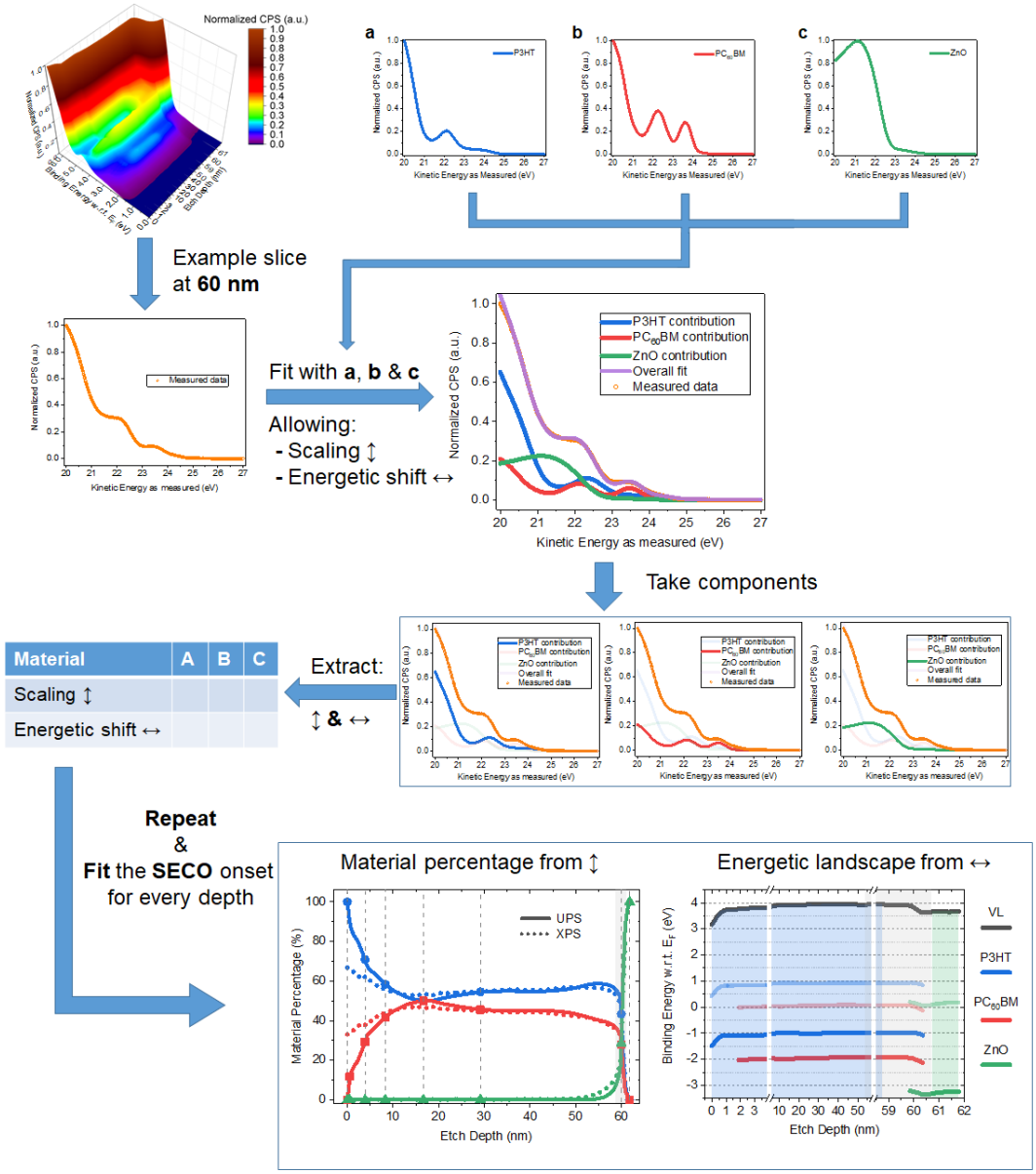

Figure 5.4: Schematic representation of UPS depth profile fitting. The 3D representation of the entire UPS depth profile and UPS measurements of the individual materials constituting the blend are shown in the top left and right corners, respectively. An example slice (at 60 *nm*) of the 3D data is taken for fitting representation: the measured spectrum is fitted by the 3 constituting components by a linear combination allowing an energetic shift and scaling representing band bending/dipole effects and material composition variations, respectively. The original data (orange dots) and the sum of the individual fits, thus the overall fit (purple line) are in an excellent agreement. Components (energetic shift and scaling) for all constituent materials can be now extracted and the whole procedure can be repeated for all measured etch depths. SECO onsets can be simply fitted by a linear fit. With this, both the compositional profile and the energetic landscape can be extracted. Reprinted with permission from [34]. Copyright © 2019 Published by Elsevier Inc.

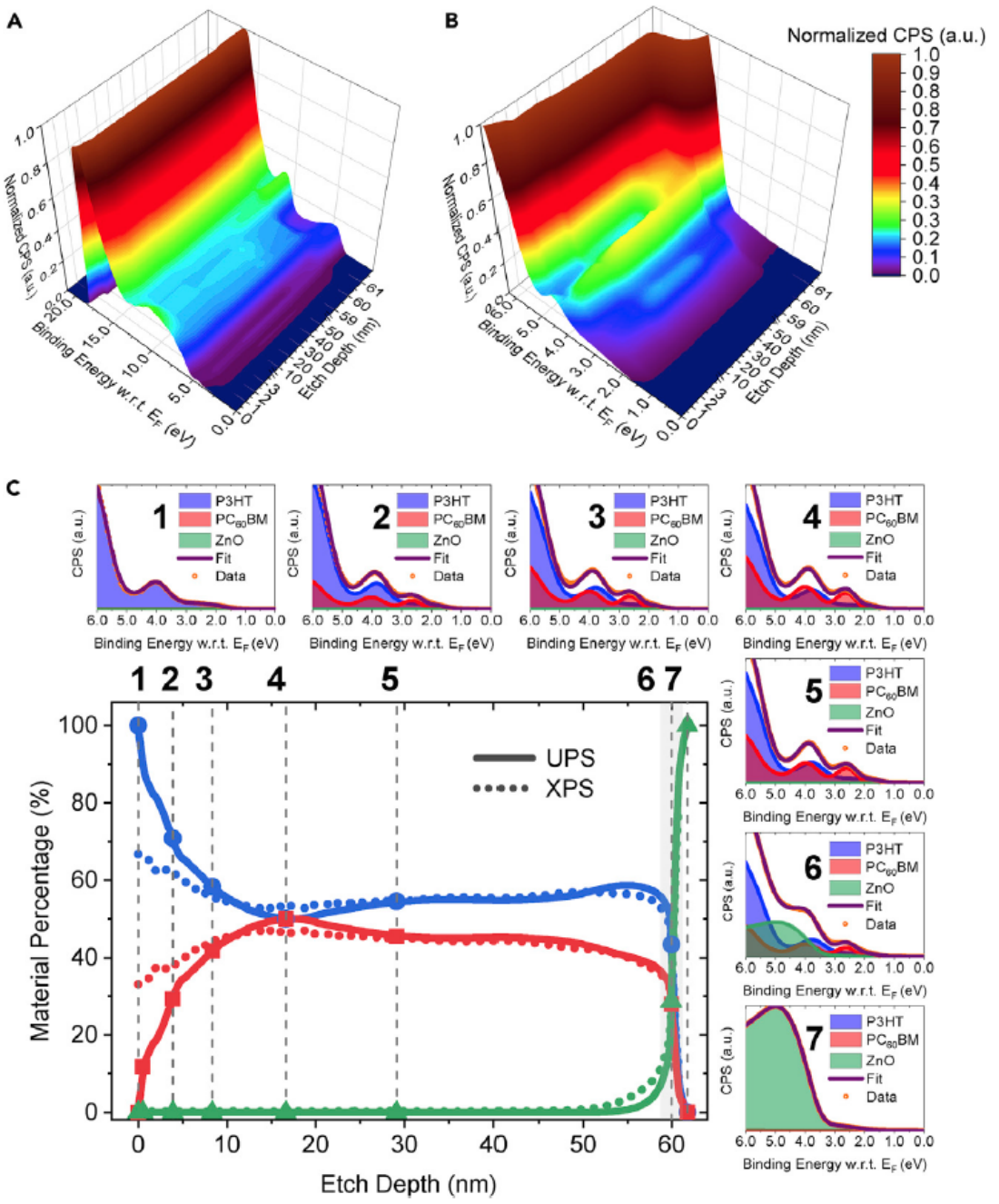

Figure 5.5: **(A)** 3D representation of the measured UPS spectra of a spin coated, 60 *nm* thick P3HT:$PC_{60}BM$ BHJ on ZnO as a function of etch depth. **(B)** Zoomed in version of the latter highlighting the HOMO region throughout the layer. Both are plotted with respect to the Fermi energy (E_F). **(C)** Material percentage data from both UPS depth profile fitting (solid line) and S/C atomic ratios measured by XPS depth profiling (dotted line). Seven representative valence band spectra and corresponding fits are shown on the top and the left of the main graph and correspond to the marked points in the latter. P3HT, $PC_{60}BM$, and ZnO contributions are denoted with blue, red, and green colours, respectively. The sum of these three is denoted with a purple line, while the original measurements with orange dots in the side graphs. Reprinted with permission from [34]. Copyright © 2019 Published by Elsevier Inc.

UPS compared to XPS.

5.2.2.3 Excluding Preferencial Etching

Etching a layer consisting of two materials, or even two different atoms, raises the question of preferential etching, which occurs when one material (atom) is etched faster than the other. This would result in an accumulation of the latter and the measured profile would no longer represent the actual composition. Three observations let us conclude, that no preferencial etching occurs for our measurements:

1. We do not observe any gradual material accumulation, but a plateau region.
2. The existence of such a plateau region occuring both in XPS and UPS measurements shows, that the measured top 2 nm of the surface (typically measured by UPS) represents the somewhat deeper measurement ($\sim$ 10 nm) of composition by XPS not yet affected by etching.
3. Etching results in smooth surfaces throughout the entire sample up until the ZnO interface, as confirmed by AFM measurements, shown in **Fig. 5.6**. Representative microgpraphs of the height and adhesion are shown at the etch depths of 1 nm, 20 nm, and 60 nm in **a**, **b**, and **c**, respectively. Firstly, the surface roughness stays constant at (2.0 ± 0.3) nm throughout the entire bulk, changing to 3.1 nm only upon reaching the ZnO layer. Secondly, the material contrast, represented by the adhesion, shows no correlation with the height in the bulk and shows changes only upon reaching the ZnO interface.

5.2.2.4 Depth Profiling of a P3HT/PC_{60}BM Bi-layer

In order to further test the depth resolution and capabilities of UPS depth profiling, we performed depth profiles on a BL of P3HT/PC_{60}BM. Similarly, as in the previous section, representative 3D maps and resulting material composition of a BL consisting of 55 nm P3HT on top of 110 nm PC_{60}BM spin coated on top of the ZnO substrate is shown in **Fig. 5.7**.

In the case of a P3HT/PC_{60}BM BL we see a similar correlation between UPS and XPS depth profile results regarding material composition shown in **Fig. 5.7**. While the latter are rather smeared out, UPS depth profiles show significantly sharper interfaces. Representative slices are again shown above and left to the main graph with the same colour notation as for the BHJ. While on the very surface (depth point **1**) XPS and UPS results are similar, at the first interface (depth points **2** to **4**) differences arise from the larger probing depth of XPS. In the middle of the underlying PC_{60}BM (depth point **5**), the both spectra show again only the presence of PC_{60}BM, while at the interface to ZnO (depth points from **6** to **7**), material percentage differences are even higher, probably to the 3.1 nm roughness of ZnO. We note, that the lack of an absolutely abrupt interface in this material system is probably caused by the diffusion of PC_{60}BM molecules into the

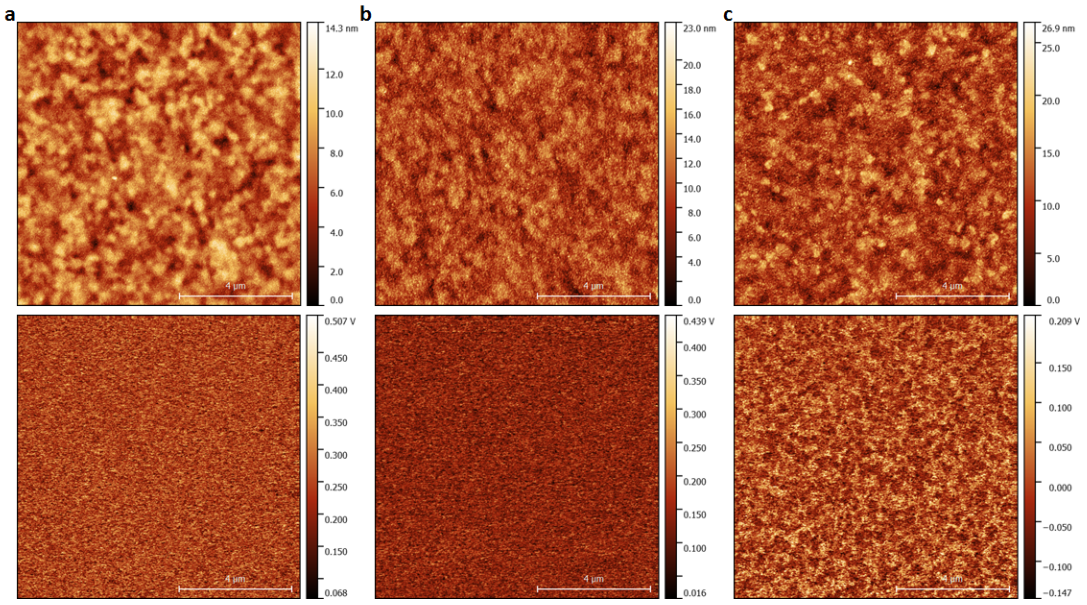

Figure 5.6: Representative height (top row) and adhesion (bottom row) micrographs measured by AFM at etch depths of **(a)** 1 *nm*, **(b)** 20 *nm* and **(c)** 60 *nm* in a BHJ of P3HT:$PC_{60}BM$ with an overall layer thickness of $\sim$ 60 *nm* spin coated on ZnO. Reprinted with permission from [34]. Copyright © 2019 Published by Elsevier Inc.

P3HT layer above, as already reported previously. [367, 368] In summary, these results show, that GCIB etching does not result in any re-deposition or implantation of overlayer material into deeper layers. Furthermore, the electronic structure consistency throughout thick layers of the very same material confirms the damage free character of GCIB etching.

5.2.3 Determining Energetic Landscapes

Apart from the material percentage information, UPS depth profiles also reveal the vertical energetic landscape indicated by changes in the SECO and HOMO onsets. We note, that extracting the LUMO positions directly would require inverse photoemission spectroscopy measurements. These, however, require acquisition at multiple spots and exhibit a large experimental error due to a low signal-to-noise ratio and additionally often induce damage to organic layers. [369, 370] For these reasons we decided to approximate the LUMO levels by subtracting the optical gap of each material from the measured HOMO position. [150] We note that this estimation does not account for the exciton binding energy and the broadening of the optical gap and neglects thus for differences between transport and optical transport levels. [371] Nevertheless, this approximation still results in a good estimate for the photovoltaic gaps as we will discuss later. Optical gaps of all investigated materials are summarized in **Table 5.1**.

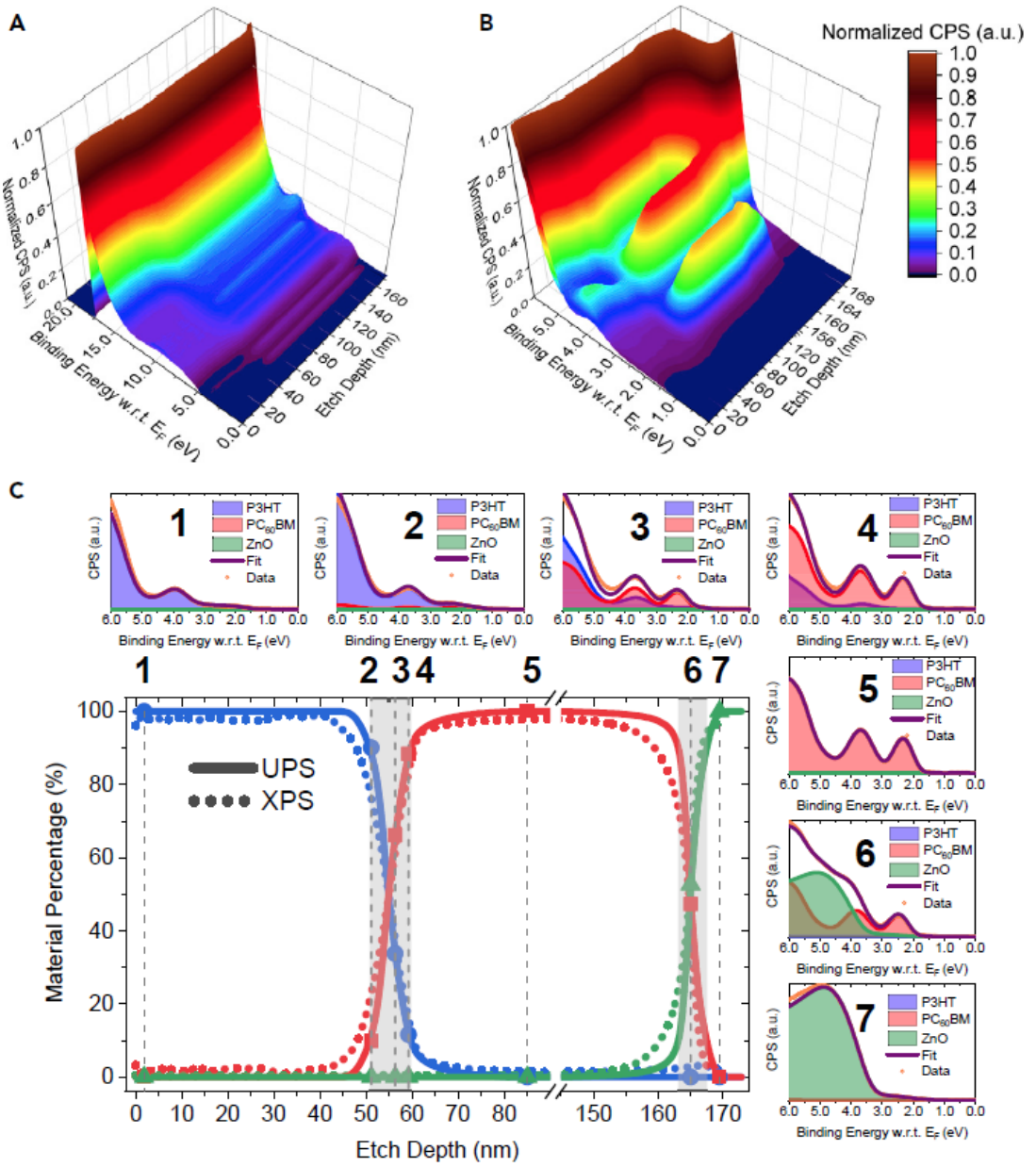

Figure 5.7: **(A)** 3D representation of the measured UPS spectra of a spin coated, 60 *nm* thick P3HT:$PC_{60}BM$ BL on ZnO as a function of etch depth. **(B)** Zoomed in version of the latter highlighting the HOMO region throughout the layer. Both are plotted with respect to the Fermi energy (E_F). **(C)** Material percentage data from both UPS depth profile fitting (solid line) and S/C atomic ratios measured by XPS depth profiling (dotted line). Seven representative valence band spectra and corresponding fits are shown on the top and the left of the main graph and correspond to the marked points in the latter. P3HT, $PC_{60}BM$, and ZnO contributions are denoted with blue, red, and green colours, respectively. The sum of these three is denoted with a purple line, while the original measurements with orange dots in the side graphs. Reprinted with permission from [34]. Copyright © 2019 Published by Elsevier Inc.

Table 5.1: Summary of optical gaps for all investigated materials determined by UV-VIS absorption spectroscopy of thin films with values from the indicated references. Values were estimated by linearly fitting the low energy onset. Adapted from [34]. Copyright © 2019 Published by Elsevier Inc.

Material	Optical Gap (eV)	Material	Optical Gap (eV)
P3HT	1.90 [34]	C8-ITIC	1.72 [248]
$PC_{60}BM$	2.00 [34]	PffBT4T-2OD	1.65 [123]
PBDB-T	2.41 [34]	DRCN5T	1.61 [34]
NCBDT	1.47 [253]	PTB7	1.60 [20]
PFBDB-T	2.01 [248]	$PC_{70}BM$	1.85 [123]

5.2.3.1 Energetic Landscape of P3HT:$PC_{60}BM$ Bulk Heterojunction and P3HT/$PC_{60}BM$ Bi-layer

Resulting energetic landscapes for the BHJ and BL of P3HT and $PC_{60}BM$ are summarized in **Fig. 5.8A** and **B**, respectively.

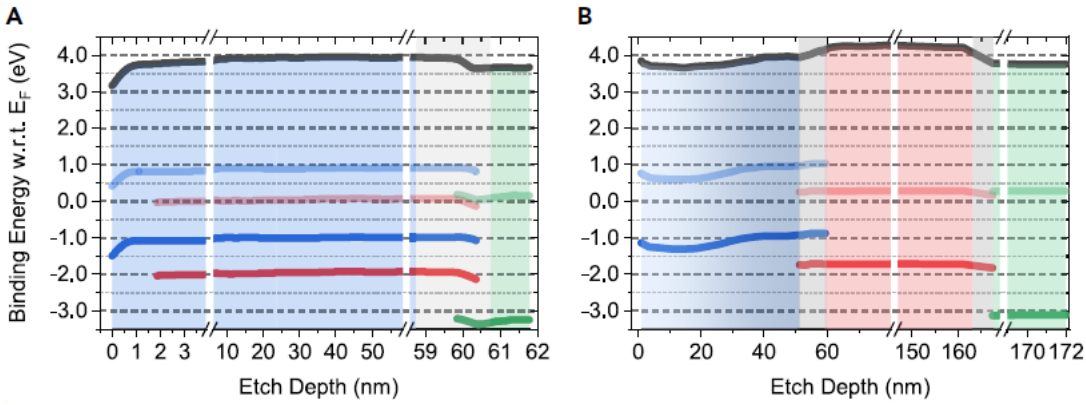

Figure 5.8: Energetic Landscapes including vacuum level positions (black), measured valence and estimated conduction band positions with respect to the Fermi level of the donor (blue), acceptor (red) materials and ZnO (green) for the investigated **(A)** P3HT:$PC_{60}BM$ BHJ and **(B)** P3HT/$PC_{60}BM$ BL. Reprinted with permission from [34]. Copyright © 2019 Published by Elsevier Inc.

The energetic landscape of the P3HT:$PC_{60}BM$ BHJ reveals several interfacial effects. At the $PC_{60}BM$/ZnO interface, a surface dipole can be observed resulting in a work function change from 3.6 eV in the ZnO to 4.0 eV in the $PC_{60}BM$ either due to to polarization effects, [320] or a charge transfer to the $PC_{60}BM$, in good agreement with previous reports. [364, 372] The VL and all other energy levels with respect to E_F stay constant throughout the entire bulk layer. The Φ measured by UPS is generally limited by the higher work function material, [373] and hence, due to the presence of $PC_{60}BM$ in the blend, the work function cannot be below 4.0 eV. In the thin P3HT layer on the surface, the limitation by the higher work function material is lifted, resulting in a bending of the P3HT energy levels at the surface and consequently the

Φ decreases to 3.6 eV. This band bending is in excellent agreement with previous reports of UPS measurements on P3HT:$PC_{60}BM$ with varying donor to acceptor ratio, in which an increasing amount of $PC_{60}BM$ resulted in a Φ shift and an overall band bending on the order of 0.5 eV. [365]

In the case of the P3HT/$PC_{60}BM$ BL, a similar dipole at the ZnO interface can be observed, as in the BHJ case, while a second dipole at the P3HT/$PC_{60}BM$ interface also occurs. The latter can be attributed to a charge transfer from the P3HT into the $PC_{60}BM$, as suggested in previous studies. [374] Such a charge transfer results in gradual band bendings and the region near the interface in P3HT thus exhibits a lower density of electrons and a smaller energetic distance between the Fermi level and the HOMO of P3HT. This energetic distance increases, corresponding to a higher density of electrons, as we move further away from the interface towards the surface. This suggests, that electron transfer takes place only in the interface region. We note, that the opportunity of very small amounts of $PC_{60}BM$ diffusing into the P3HT layer cannot be ruled out, [367, 368] which would also influence the band bending near the P3HT/$PC_{60}BM$ interface. [365] Nevertheless, our measurements reveal a dipole moment of 0.3 eV, in excellent agreement with previous measurements performed on electrospray deposited P3HT/$PC_{60}BM$ BLs measured in situ (0.35 eV dipole), [375] and measurements on P3HT/C60 BLs ($(0.3 - 0.4)$ eV dipole). [376] The small upward bending at the very surface results from the preparation method of the BL film including exposure to water and oxygen during fabrication. [377]

E_g^{PV} for the Systems with P3HT and $PC_{60}BM$

Both BHJ and BL films result in a similar estimated E_g^{PV} of (1.03 ± 0.04) eV and (1.16 ± 0.02) eV, respectively. We want to stress, that these values are approximations due to the estimation of the transport gap with the optical gap and note, that the errors listed above are of statistical nature, resulting from averaging individual measurements collected throughout the entire film thickness. The experimental error of each measurement is approximately $(0.10 - 0.15)$ eV, originating from both measurement and fitting errors. Despite P3HT:$PC_{60}BM$ being the most investigated organic photovoltaic system to date, reported energetic values show large variations, [317–319] resulting thus in E_g^{PV}s in the range of $(0.9 - 1.4)$ eV. [97, 378–380] Our results are in good agreement with previous direct vacuum electrospray deposition measurements (*in situ*) by *Park et al.* [375] resulting in $E_g^{PV} = 0.9$ eV and are also in close agreement with CT state energies measured by luminescence spectroscopy. [210, 330]

5.2.3.2 Energetic Landscapes of Other High-Efficiency Photovoltaic Systems

In order to demonstrate the applicability of our technique beyond the model system of P3HT:$PC_{60}BM$, we chose four high-performance OPV systems, with both

polymer and small molecule donors and both fullerene and non-fullerene acceptors: PffBT4T-2OD:$PC_{70}BM$ with a PCE approaching 11 %, [123, 381] the two non-fullerene systems PBDB-T:NCBDT and PFBDB-T:C8-ITIC resulting in PCEs of 12 % and 13 %, [247, 248] respectively and last but not least the small molecule system DRCN5T:$PC_{70}BM$ with a PCE of $\sim$ 9 %. [382] UPS measurements of these systems summarized in 3D energetic maps are shown in **Fig. 5.9**.

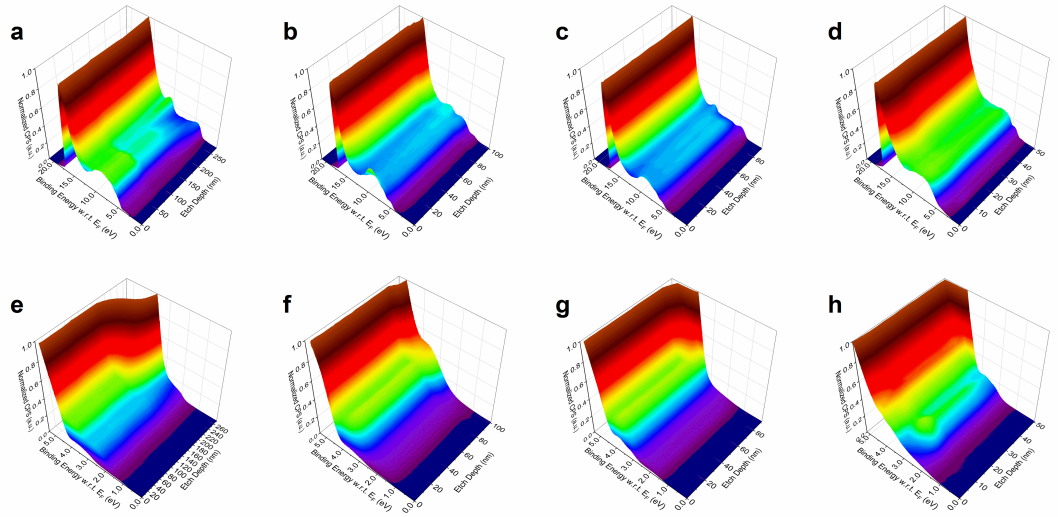

Figure 5.9: 3D energetic maps, representing UPS measurements for different BHJ systems of **(a)** PffBT4T-2OD:$PC_{70}BM$, **(b)** PBDB-T:NCBDT, **(c)** PFBDB-T:C8-ITIC and **(d)** DRCN5T:$PC_{70}BM$ with zoomed in versions of the DOS region on **(e)**, **(f)**, **(g)** and **(h)**, respectively. Reprinted with permission from [34]. Copyright © 2019 Published by Elsevier Inc.

Data fitting as described previously results in compositional profiles and energetic landscapes, whereas we will restrict us here to the energetic profiles including the estimated LUMO levels of the high-efficiency systems, shown in **Fig. 5.10**.

Unlike in the case of P3HT:$PC_{60}BM$, no strong surface segregation of either of the components can be observed. This also leads to rather flat energetic levels, probably resulting in better charge carrier transport in these systems. One can again extract the E_g^{PV} for each of these system resulting in $(1.31 \pm 0.02)\ eV$ for both PffBT4T-2OD:$PC_{70}BM$ and DRCN5T:$PC_{70}BM$, and $(1.48 \pm 0.03)\ eV$ and $(1.61 \pm 0.02)\ eV$ for PBDB-T:NCBDT and PFBDB-T:C8-ITIC, respectively. As mentioned already for the P3HT:$PC_{60}BM$ systems, the listed errors are of statistical nature, demonstrating a highly constant E_g^{PV} with almost no deviation throughout the entire BHJ.

5.2.4 A Comparison of Estimated Photovoltaic Gaps from Different Approaches with Device V_{OC}s

While E_g^{PV} values extracted from our UPS depth profile measurements include uncertainties due to the use of optical gaps, our method allows us an accurate determination

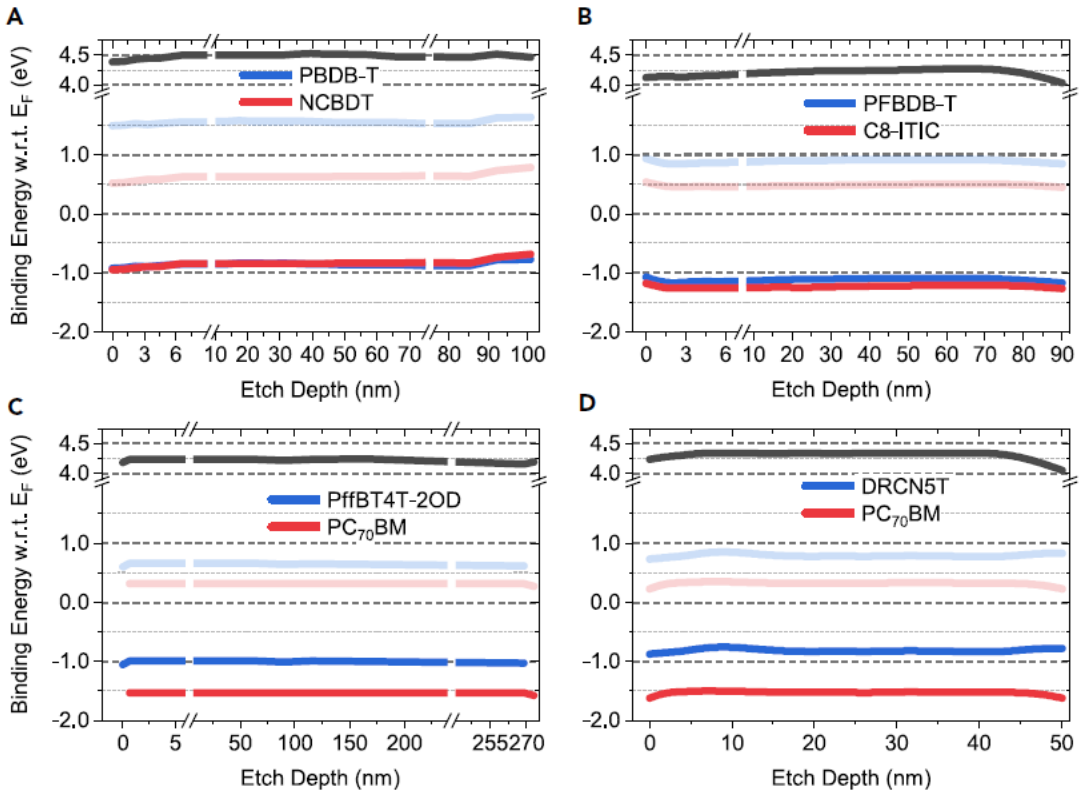

Figure 5.10: Energetic Landscapes including vacuum level positions (black), measured valence and estimated conduction band positions with respect to the Fermi level of the donor (blue), and acceptor (red) materials for the investigated **(A)** PBDB-T:NCBDT, **(B)** PFBDB-T:C8-ITIC, **(C)** PffBT4T-2OD:PC70BM, and **(D)** DRCN5T:PC70BM BHJs. Reprinted with permission from [34]. Copyright © 2019 Published by Elsevier Inc.

of HOMO-HOMO offsets for all investigated material systems. It has been shown recently by *Qian et al.*, [35] that low energetic offsets are one of two prerequisites for low non-radiative voltage losses and thus high PCEs in OSCs. These offsets could be estimated by measurements on each blend component separately, such an approach will omit taking into account interfacial effects, such as band bending and dipoles between these materials and their vertical evolution across the device. Our technique accurately measures HOMO-HOMO offsets throughout the active layer and can thus be applied for new material system characterization, in order to identify promising candidates with a low energetic offset. HOMO-HOMO offsets, E_g^{PV} values and measured device V_{OC}s of all investigated systems and that of PTB7:$PC_{70}BM$, discussed in more detail in **Chapter 6**, are summarized in **Table 5.2**. We observe high HOMO-HOMO offsets for all systems employing fullerenes and remarkable low offsets for the two investigated NFA systems, being probably critical for their high performance.

The practice of calculating E_g^{PV} from energy levels measured for individual blend components and following V_{OC} estimation is excessively common in literature. While these energy levels are frequently extracted from PES measurements, often different

Table 5.2: Estimated E_g^{PV}s, V_{OC}s, and HOMO-HOMO offsets for all investigated BHJ systems including P3HT:$PC_{60}BM$, PffBT4T-2OD:$PC_{70}BM$, DRCN5T:$PC_{70}BM$, PTB7:$PC_{70}BM$, PBDB-T:NCBDT, and PFBDB-T:C8-ITIC. Adapted from [34]. Copyright © 2019 Published by Elsevier Inc.

Acceptor Type	Material System	E_{PV} (eV)	V_{OC} (V)	HOMO-HOMO Offset (eV)
Fullerene	P3HT:$PC_{60}BM$	1.03 ± 0.04	0.60	0.97 ± 0.04
	PffBT4T-2OD:$PC_{70}BM$	1.31 ± 0.02	0.75	0.54 ± 0.04
	DRCN5T:$PC_{70}BM$	1.31 ± 0.04	0.93	0.53 ± 0.04
	PTB7:$PC_{60}BM$	1.17 ± 0.03	0.77	0.68 ± 0.04
Non-fullerene	PBDB-T:NCBDT	1.48 ± 0.03	0.84	0.02 ± 0.02
	PFBDB-T:C8-ITIC	1.61 ± 0.02	0.93	0.12 ± 0.02

methods are used introducing additional errors. In order to check the validity of this approach, we compared E_g^{PV} values calculated from measurements on individual blend components with results obtained from UPS depth profiling on BHJ active layers. Furthermore, we compared these results with corresponding device V_{OC}s and reported CT energy values, as shown in **Fig. 5.11**. Reliable CT energy values measured for the same active layer morphology as measured by UPS depth profiling were only available for 5 out of 6 systems in literature. [210, 248, 253, 383, 384]

The results clearly show that E_g^{PV} values obtained from measuring individual components can be neither correlated to measured device V_{OC}s, nor CT state energies. Furthermore, in some cases the estimated E_g^{PV} is even lower than the device V_{OC}, which would imply negative losses. On the contrary, E_g^{PV} values determined by UPS depth profile measurements are in a good agreement with measured CT energies. Additionally, they can be very well correlated to device V_{OC}s, showing a linear correlation (slope 1) with a certain offset varying for each material system. We note that this offset and thus the difference between E_g^{PV}/E_{CT} and the V_{OC} is not necessarily a constant value and depends on the overall energetic losses including radiative and non-radiative recombination in each particular system. [194] Generally, all OSCs lose voltage both due to radiative and non-radiative recombination, the latter being either geminate or non-geminate including recombination through traps, structural defects, triplet states and many more. [194] Correspondingly, it is not expected that all E_g^{PV} values fall on the same line with a slope of 1, but rather show some variation along, which is in good agreement with our results. We note, that both E_g^{PV} values obtained by UPS depth profile measurements and individual component measurements neglect for exciton binding energy due to the use of the optical gap for the calculation of the appecptor LUMO in each system. Nevertheless, the former method represent a far more accurate picture of the energetic alignment at the D/A interface than results obtained from individual blend component measurements. In summary, we can conclude, that:

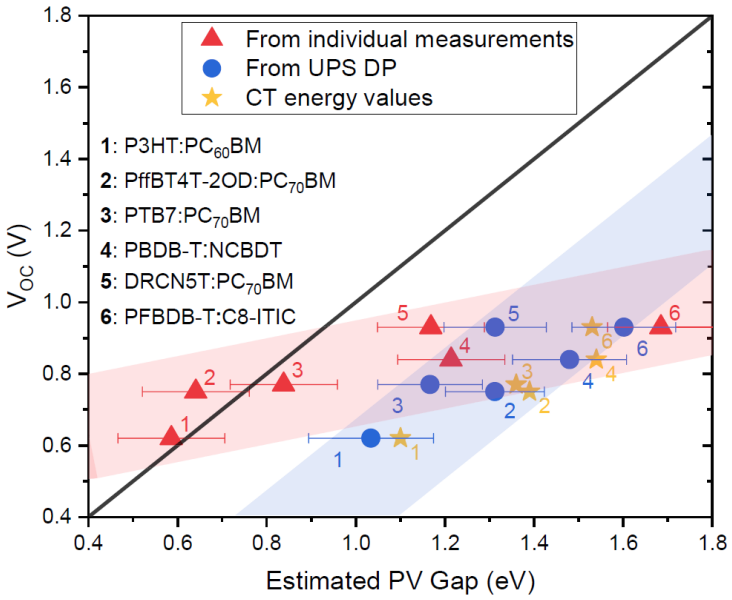

Figure 5.11: Relation between E_g^{PV} values obtained from different approaches and the V_{OC} of corresponding devices for all investigated material systems. The photovoltaic gap was estimated by individual component measurements (red triangles), UPS depth profile evaluations (blue dots) and CT energy values (yellow stars) taken from literature for devices with a similar film morphology, when available. Investigated systems are denoted with numbers from **1** to **6**. Red and blue semitransparent bars with a thickness of $\sim 0.07\ eV$ are guides for the eye and represent fits of the corresponding E_g^{PV}, with a slope of 1 for the latter. E_g^{PV} errors originate from both optical gap estimations and HOMO level determinations from UPS depth profile measurements. Reprinted with permission from [34]. Copyright © 2019 Published by Elsevier Inc.

- The good agreement with CT energy values suggests that the energetic alignment obtained by our technique is representative for the CT exciton energy and is a good measure when investigating new photovoltaic systems.

- UPS depth profiling correctly predicts E_g^{PV} values for a variety of material systems, while the combination of individual component measurements fails. This suggests a significant ground state electronic interaction between the blend components for several systems, such as in the case of the P3HT/PC_{60}BM BL, where a dipole is formed between the two. The nature of this electronic interaction differs largely between the BHJ and BL cases and depends thus not only on the materials of choice but also on their microstructure in the blend. Hence, UPS depth profile measurements and OPV device characterization, including device V_{OC} must be performed on blends of identical microstructure.

5.3 Summary and Outlook

In this chapter we introduced our newly developed UPS depth profiling technique, where UPS or XPS measurements are combined with essentially damage-free GCIB etching, and demonstrated its applicability on a range of photovoltaic material systems. The new methodology accurately determines the energetic landscape, including an accurate determination of HOMO-HOMO offsets and an estimation of E_g^{PV}, of both BHJ and BL systems. Furthermore, the use of UPS as the surface sensitive measurement technique offers compositional profile information on a much higher depth resolution, when compared with XPS depth profiles. The development of this method opens up a vast array of opportunities for the study of OPV systems including energetic landscape determination for any type of multi-layered devices. It could help to better understand the energetic alignment at organic/organic interfaces, specifically the importance of the HOMO-HOMO offset. Finally, our method allows for CT state energy estimation, and with that also potential device V_{OC} prediction.

Since UPS depth profiling can be performed at any point in the device lifetime, it thus also offers valuable insights into the temporal evolution of compositional electronic profiles after device operation. Insights on how environmental degradation affects the energetic landscape of devices, could lead to a development of more stable devices and to find mitigation strategies.

The possibility to extract both high-resolution compositional information and energy-level evolution has fascinating implications. Ternary organic photovoltaic systems have recently drawn attention of the community due to their impressive efficiencies surpassing 11 %. [309] Much remains unknown, however, about their energetic alignment and the vertical compositional distribution of the third material. It has been proposed recently, that a sequential deposition of the third material after film formation of the first two can significantly enhance performance. [385] Alternatively, the possibility of a spontaneous segregation of the third component to the film surface resulting in an improved charge extraction and thus an increased V_{OC} has been also suggested. [386] Applying UPS depth profiling to such ternary systems would allow the accurate determination of both their compositional and energetic profiles. Additionally, sequentially deposited D/A layers, [253] and other novel film structures can be also investigated in great detail with our technique.

The ability to cross organic/organic as well as organic/inorganic interfaces, while accurately determining the energetic alignment at them, makes our methodology of great interest to the study of complete PV or even tandem devices. Recently, organic tandem cells have made a come-back with record efficiencies of 15 % [387] and 17.3 %, [300] published in close succession. UPS depth profiles could be performed on an entire stack of such a device in order to extract the entire vertical energetic

alignment between all interlayers.

Furthermore, we stress, that our methodology is not limited to photovoltaic systems only. Our technique is directly applicable to study energetic landscape progression of any multi-layered device, including light-emitting diodes, photodetectors, doped layers and many more. Solution-processed doping of organic materials has been demonstrated to have remarkable applications in organic field-effect transistors as well as light-emitting diodes. [388] An accurate determination of dopant distribution in the host matrix is, however, very difficult, especially in the case of surface doping. [389] UPS depth profiling would allow the simultaneous determination of depth evolution of doping and its effects on the overall energetic landscape.

Finally, the ability to extract compositional information from electronic structure measurements is intriguing and opens up new opportunities: considering a blended material system with two components comprising the same elements, but a dissimilar electronic structure, UPS depth profiling would be able to successfully distinguish the components, while other methods, such as XPS depth profiling, would struggle or fail entirely.

6 Application of UPS Depth Profiling in Various Systems

In this chapter, the most important applications of our recently developed UPS depth profiling technique, introduced in the previous chapter, are summarized. We utilized our technique to measure a variety of systems in different fields of application, ranging from the investigation of energetic alignment changes upon device degradation, [34] differences in sequentially and conventionally deposited BHJ blends, [43] energetics and injection barriers in spin-injection materials, [45] impact of doping in organic photodetectors, [44] and lastly energetic and compositional profile investigations for complex ternary blends. [390] All these topics will be discussed in this chapter in order to highlight the broad applicability of our recently developed etching technique.

First, UPS depth profiling is applied to pristine and degraded BHJ films consisting of DRCN5T:$PC_{70}BM$ and PTB7:$PC_{70}BM$ in order to probe the evolution of energetic levels upon environmental degradation, which is currently not possible with any other method. We are not only able to determine their energetic landscapes, but also to correlate variations in p-doping behaviour to compositional anomalies. We carry on by visualising small changes in composition between sequentially and conventionally deposited BHJs, which is not possible with standard techniques such as XPS. Next, we introduce our recent investigations of charge carrier injection barriers and energetic levels in both spintronic devices and photodetectors: we study both the impact of side chain variations, and that of molecular doping on device energetics. Finally, we push the envelope of our technique and investigate more complex ternary systems, and show that we are able to measure the smallest PV gaps in these systems and to correlate these to the V_{OC} of corresponding devices. With this we are able to both explain and predict a highly debated topic up to date: the behaviour of device V_{OC} in ternary systems.[401]

6.1 Evolution of BHJ Energetics Upon Degradation in Oxygen and Light

Despite tremendous advances in OPV research in the last decades resulting in a device performance exceeding 16 %, [12] the Achilles heel of OSCs remains their instability

and environmental deterioration. In order to be able to develop practical mitigation strategies, factors affecting environmental degradation need to be addressed and understood in more detail. Currently, there are a variety of different degradation mechanism known including: active material or interface degradation, diffusion of molecular oxygen and water into the device layers, interlayer or electrode diffusion, morphological changes, reaction between electrode and organic material and lastly macroscopic changes such as formation of cracks or delamination. [391] Exposure to air typically results in rapid deterioration of device performance, especially when combined with exposure to light. Specifically, when fullerene based donor-acceptor blends are degraded with oxygen (such as in this section), photo-oxidation of the fullerenes was reported to be the primary degradation mechanism. [392]

In this section we take a closer look at the change in vertical compositional profiles and energetic alignment upon degradation in 20 % oxygen and 1 Sun light illumination. With this, we explore changes in the vertical charge transport behaviour in working devices and investigate possible correlations between composition and energetic changes of the active layer upon environmental degradation.

6.1.1 Evolution of the Energetic Landscape upon Degradation

Changes in the energetic landscape play a crucial role for the device performance, since all fundamental processes such as charge injection, generation, transport and extraction are affected. To demonstrate the versatility of our newly developed method, we studied the evolution of the energetic landscape and the compositional profile of a small molecule:fullerene (DRCN5T:$PC_{70}BM$) and a polymer:fullere (PTB7:$PC_{70}BM$) system upon degradation (exposure to 1 sun illumination and dry air for 12 h), as shown in **Fig. 6.1**.

Looking only at the energetics of pristine (non-degraded) systems, all levels look rather flat without any strong surface or interface effects, similar to other high-performance systems described in the last chapter. In the case of DRCN5T:$PC_{70}BM$, however, significant changes to the energetic landscape can be observed upon degradation. The Fermi level position shifts closer to the HOMO for both DRCN5T and $PC_{70}BM$, suggesting a strong p-doping by oxygen, as already reported in previous studies. [393, 394] These shifts happen, however, in a non-homogeneous way: while the surface values show a relatively minor energy level change, a far stronger change (an *energetic hill/peak*) occurs 10 *nm* below the surface. Interestingly, this seems to correlate with the compositional profile, since at the very same depth an inversion in the donor-acceptor composition occurs: while the surface is donor molecule rich, at a depth of 10 *nm* the fullerene acceptor constitutes the majority ($\sim$ 60 %) of the overall composition (*compositional hill/peak*). These results demonstrate that environmental degradation can result in a non-uniform, but compositional profile dependent, change of the energetic landscape, since we observe an enhanced p-doping by oxygen in $PC_{70}BM$ rich regions.

The energetic landscape in the PTB7:$PC_{70}BM$ system, in which the compositional

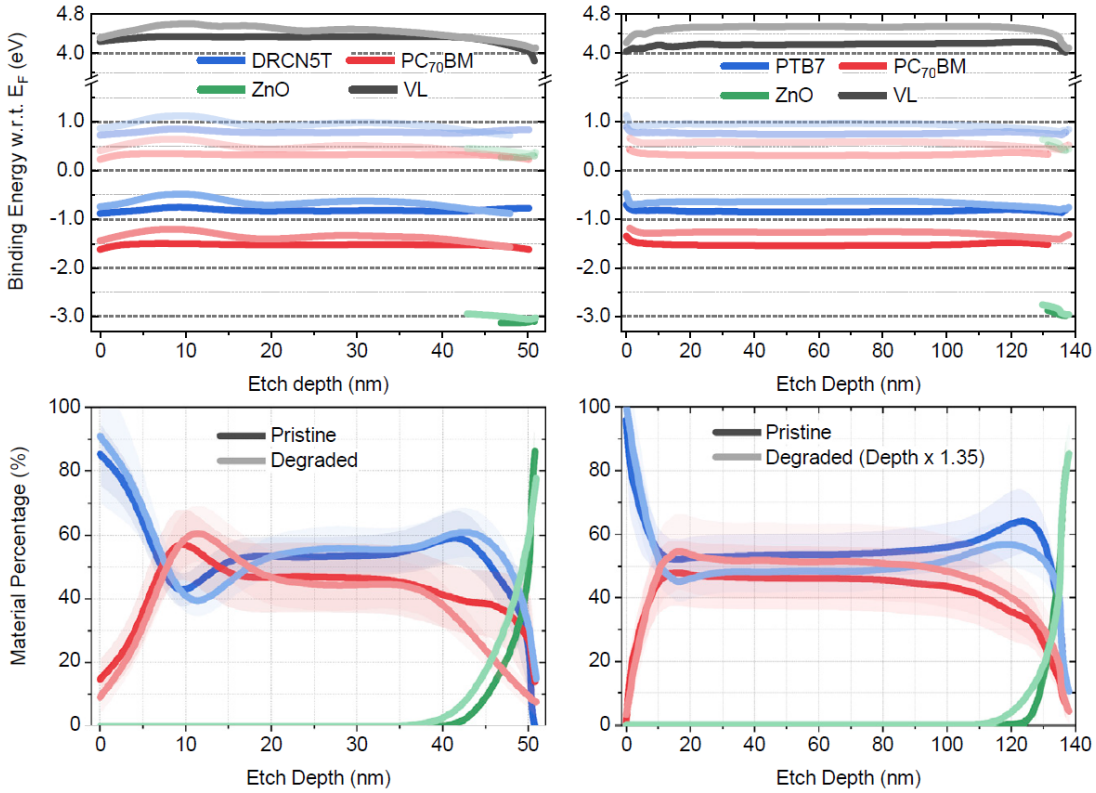

Figure 6.1: Change of the material percentage (bottom) and that of the energetic landscape (top) for the two material systems: DRCN5T:$PC_{70}BM$ (on the left) and PTB7:$PC_{70}BM$ (on the right). Pristine and degraded samples are denoted with darker and lighter colours, while the donor, acceptor and underlying ZnO layer are denoted with blue, red and green colours, respectively. Energetic landscapes are represented with respect to the common Fermi level and include the vacuum level (black), HOMO levels, and estimated LUMO levels (semi-transparent). The latter are estimated from the optical gap of the corresponding materials. Reprinted with permission from [34]. Copyright © 2019 Published by Elsevier Inc.

profile remains constant after a $\sim 10\ nm$ thick PTB7 rich surface layer, shows a uniform p-type doping effect. This is possibly the result of a lacking fullerene rich inversion layer in the compositional profile, in contrast to degraded DRCN5T:$PC_{70}BM$ blends.

Correlating Energetic to Compositional Changes

In order to verify the observed correlation between the energetic and compositional hills, *e. g.* the stronger p-doped energetic region and the fullerene rich inversion layer in the DRCN5T:$PC_{70}BM$ system, we fabricated devices with different donor to acceptor ratios varying from 1:0.5 to 1:1.1, and with different layer thicknesses. With this we were able to fabricate layers with peak positions varying from $\sim 8\ nm$ to $\sim 14\ nm$. Energetic and compositional peak positions of these layers are summarized in **Fig. 6.2**.

While the position of compositional peaks is the same for both donor and acceptor materials, there are slight differences in their energetic peak positions with an offset of

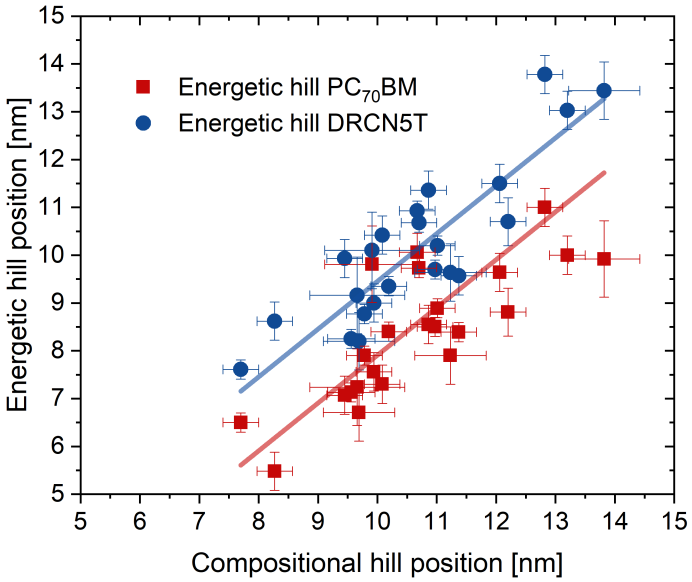

Figure 6.2: Energetic peak position as a function of the compositional peak, e.g. the regions with the maximal p-doping effect and the fullerene rich inversion layer, for DRCN5T (blue) as well as $PC_{70}BM$ (red). While compositional peak positions are the same for both materials, energetic peak positions differ. Semi-transparent lines are included as guides for the eye in corresponding colours.

approximately 1 *nm*. Lines with a slope of 1 of energetic peak positions as a function of the compositional peak for both materials serve as a guide for the eye. Linear fits (**Fig. B.1**) show slopes of 0.97 ± 0.12 and 0.76 ± 0.12 for the donor and acceptor materials, respectively, confirming our previous assumption regarding a correlation between the energetic and compositional peak positions.

This example of substantially different energetic degradation pathways in two similar systems highlights the crucial importance of UPS depth profiling. Such local effects within the active layer cannot be probed by any other technique up to date despite their critical impact on physical processes, such as charge generation and transport.

6.2 Vertical Stratification in Sequentially vs. Conventionally Deposited BHJs

There has been extensive research in finding better performing active layer morphologies than conventional (c) BHJs, sequential (sq) deposition being one of these approaches. [395] The main difference between these two methods is the number of deposition steps: while conventional BHJs are fabricated in one single spin-coating step, sequential blends are deposited by a two-step solution process. Currently, no profound understanding exists, why sq-BHJ devices perform better as their conventional

counterparts. The aim of this section is to explore the small differences in compositional profiles between c-BHJ and sq-BHJ blends. Conventionally and sequentially deposited PBDB-T:NCBDT BHJs were fabricated by Jiangbin Zhang as described in *Zhang et al.* [253]

XPS Depth Profiling Fails Compositional Determination

XPS can be generally applied for atomic percentage determination; furthermore, the additional knowledge of the molecular structure of the investigated materials allows for material percentage profile calculation. This works also the other way around: from knowing the material percentage of the donor (in a blend of donor and acceptor), allows for a theoretical atomic percentage calculation, as shown in **Fig. 6.3a**. Here, the implications of a donor (PBDB-T) variation from 15 % to 65 % are shown for the theoretical values of C, S, O, N, and fluorine (F). This donor variation region was chosen, since in the sq-BHJ case an excess of acceptor material (lower amount of donor material) is expected near the surface, while in the c-BHJ case the donor to acceptor ratio should be 1:1 throughout the film. The expected higher amount of acceptor material in the top sq-BHJ layer would thus imply lower S and O, but higher N, F, and C signals.

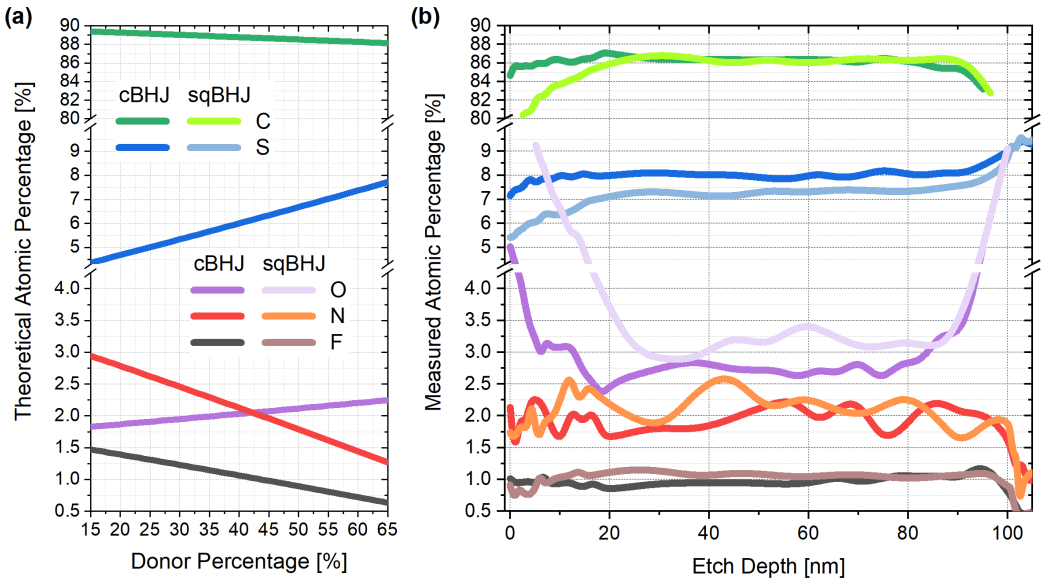

Figure 6.3: (a) Theoretical atomic percentage values for different PBDB-T fractions varied from 15 % to 65 % for a PBDB-T:NCBDT blend. Shown are the elements C (green), S (blue), O (violet), N (red) and F (black). The y axis is subdivided into three regions of interest. **(b)** Atomic percentage values for the same elements measured by XPS depth profiling for a 100 *nm* thick c-BHJ and sq-BHJ, represented with in dark and light colours, respectively.

Measured atomic percentage data of the very same elements for 100 *nm* thick c-BHJ as well as sq-BHJ films is shown in **Fig. 6.3b**. The top 10 *nm* region exhibits very high O values, which can be attributed to surface contamination and possible O diffusion into the top layer during fabrication. A meaningful statement can, however, not be

made by these measurements, partly due to the too-low signal to noise ratio of XPS at such low atomic percentage values, as in the case of N and F. Measurements of the sq-BHJ show, for example, higher O but lower S values at the same time, which are not in agreement with theoretical values. Furthermore, N, F and C values for c-BHJ and sq-BHJ show no clear trend when compared. Hence, in order to study compositional profile differences between the two fabrication methods a more sensitive technique is desired.

Advantages of UPS Depth Profiling

In order to extract compositional information from UPS depth profiling, the measurements are usually calibrated by XPS depth profile data in compositional plateau regions, where the higher probing depth of XPS (10 *nm*, being thus 5 times as high as for UPS) does not influence the measured material percentage. In the case of sequentially deposited layers, however, XPS measurements yield no useful information. Furthermore, the DOS for the two materials of interest (PBDB-T and NCBDT) are very similar, especially after several etching steps as shown in **Fig. B.2**. Hence, a decomposition of these features from the UPS spectra of c-BHJ and sq-BHJ is rather difficult. Decomposition of the DOS would also introduce unnecessary fitting errors and computational time. Instead, we focus on the topic of interest: the possible compositional differences between the two fabrication methods. Thus, in order to highlight differences between c-BHJ and sq-BHJ, we calculate their UPS signal difference ($UPS_c - UPS_{sq}$) for each investigated depth from 0 *nm* up until 100 *nm*, as shown in **Fig. 6.4a**, with a colour scale denoting different etch depths.

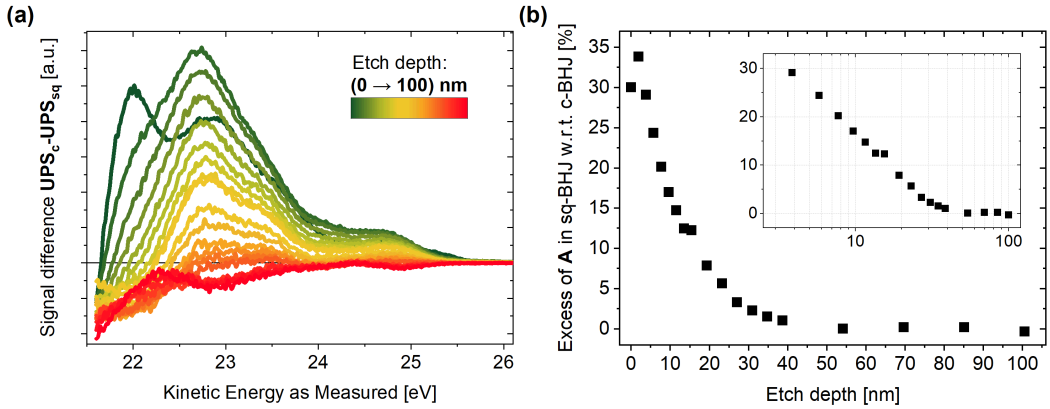

Figure 6.4: **(a)** UPS signal difference of a conventionally and a sequentially deposited PBDB-T:NCBDT BHJ for each measured depth in a UPS depth profile from 0 *nm* (top surface) to 100 *nm* (interface to the underlying PEDOT:PSS layer). **(b)** Excess of acceptor material in the sq-BHJ layer with respect to the c-BHJ layer as a function of etch depth, extracted from the spectra shown in **(a)**. A logarithmic representation is provided in the inset.

Since there are only donor (D) and acceptor (A) in the blend, if the material percentage of A at a given depth is x, then that of D is necessarily $(100 - x)$. We can assume

that the percentage of A is x and y in the c-BHJ and sq-BHJ blends, respectively, and with that:

$$\begin{aligned} \mathrm{UPS}_c &= x \cdot \mathrm{UPS}_A + (100 - x) \cdot \mathrm{UPS}_D \\ \mathrm{UPS}_{sq} &= y \cdot \mathrm{UPS}_A + (100 - y) \cdot \mathrm{UPS}_D \end{aligned} \tag{6.1}$$

where UPS_A and UPS_D are the individual UPS spectra for the acceptor and donor material, respectively. The difference spectrum can be thus written as:

$$\mathrm{UPS}_c - \mathrm{UPS}_{sq} = (\mathrm{UPS}_A - \mathrm{UPS}_D) \cdot (x - y) \tag{6.2}$$

The difference spectrum is thus directly proportional to $(UPS_A - UPS_D)$ and $(x - y)$. We note that this is only true if the two UPS spectra are not shifted in energy. This indeed holds for our measurements, as the shape of the difference spectrum remains almost the same for each depth (**Fig. 6.4a**), except for small differences in the very first spectrum originating, most probably, from slightly different energetics at the surface. Consequently, we fitted the c-BHJ and sq-BHJ spectra only at the very surface, as shown in **Fig. B.3**, and assumed that the c-BHJ has a vertically homogeneous and constant D:A ratio of 1:1, which should hold according to the fabrication parameters and was also confirmed by energy dispersive x-ray (EDX) results. [43] With this, we show that there is a ~ 35 % excess of acceptor material in the sq-BHJ with respect to the c-BHJ at the very surface, supporting the idea of an NCBDT rich top layer. According to **Eq. 6.2**, integrating up all individual spectra yields the excess of acceptor material for each measured depth, as summarized in **Fig. 6.4b**. The inset has a logarithmic scale and shows that the amount of NCBDT exponentially decreases, until it reaches zero at around 40 nm. From this depth on, UPS spectra of the c-BHJ and sq-BHJ are indistinguishable, their spectral difference approaches thus zero and consequently both form a uniform BHJ with a D:A ratio of 1:1. With this we have shown, that the top layer of sequentially deposited samples is acceptor rich, leading to better performing devices.

6.3 Additional Material Systems

In this section we show that UPS depth profiling can be also applied for a variety of organic material systems: apart from OPV devices, we investigated the material properties of organic semiconductors for spintronic applications and that of molecular doping in photodetectors. In addition to vertical energetic level progression profiles we also determined charge injection barriers.

6.3.1 Change in Energetics in a Spintronic System

In the filed of spin-based information processing, where instead of electrical charge, pure spin currents are needed, materials with long spin relaxation times and long spin diffusion lengths are desired. [396, 397] Spin currents can than be injected from ferromagnetic substrates into non-magnetic materials, such as DNTT or its derivatives. In

this section, we investigate the change in electronic structure of 40 *nm* thick organic layers of three DNTT derivatives, fabricated by Angela Wittmann, [45] with a focus on the hole injection barrier at the organic layer interface with the underlying Py substrate. HOMO positions for all investigated components with respect to the Fermi level E_F as a function of etch depth (reverse film thickness) are shown in **Fig. 6.5a**. Corresponding UPS spectrum fits for the very surface and at the organic/Py interface are shown in **Fig. B.4**. No significant band bending can be observed for neither DNTT nor diPh-DNTT, while for the C8-DNTT derivative a strong variation in the HOMO level with respect to E_F near the interface with Permalloy can be observed. At the same time, the vacuum level positions for all three derivatives stay rather flat. These, and other findings presented by *Wittmann et al.* [45] suggest a uniform spin diffusion into the bulk of DNTT and diPh-DNTT, and a significantly lower spin concentration in the bulk than at the interface for C8-DNTT.

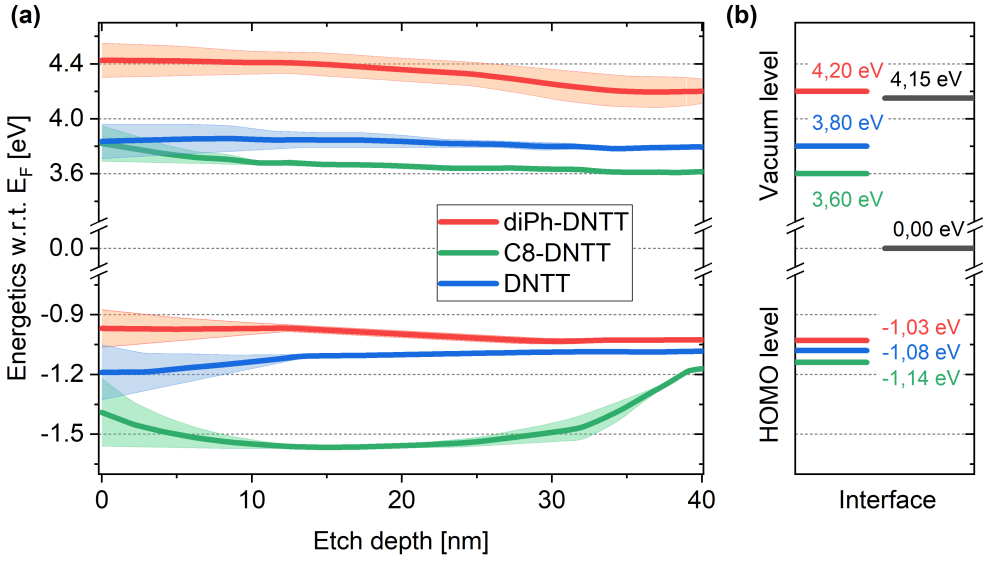

Figure 6.5: (a) Vertical energetic level progression for thin layers of DNTT (blue), diPh-DNTT (orange) and C8-DNTT (green) on top of a Py substrate. Shown are corresponding HOMO and vacuum level positions with respect to E_F. Semi-transparent regions denote the error determined by two consecutive depth profile measurements. **(b)** Energetic values directly at the Py interface, with HOMO levels representing hole injection barriers.

Interface values, including the work function and the Fermi level of Py, are summarized in **Fig. 6.5b**. All three molecules are slightly p-doped at the the interface with Py and have similar injection barriers of $\sim 1.1\ eV$ with only small differences observed on the order of the accuracy of the UPS technique (50 meV). There is, however, an increasing trend for the three components, diPh-DNTT having the smallest, while C8-DNTT the largest injection barrier for holes.

6.3.2 Change in Energetics Upon Interlayer Doping

Thin layers (80 *nm*) of both doped and undoped $PC_{60}BM$ were deposited on TiN with an additionally 50 *nm* thick C_{70} on top, deposited by Himanshu Shekhar. [44] In doped $PC_{60}BM$ layers, N-DMBI served as the dopant. In order to investigate the differences in energy level alignment, UPS depth profiles were carried out on an undoped (0 %), and both a 1 % and 5 % doped $PC_{60}BM$ layer. Since in this material system, we were only interested in charge carrier transport, we restrict the results here to the resulting HOMO levels with respect to E_F, as shown in **Fig. 6.6**. The HOMO level of the undoped $PC_{60}BM$ layer is about 1.3 *eV* below the Fermi level of TiN and stays rather constant across the entire $PC_{60}BM$ layer, except a small upward bending at the interface with C_{70}. The HOMO level of the latter stays again flat, except for the very top surface resulting from vacuum effects. Interestingly, doping of the $PC_{60}BM$ layer does not only introduce a tremendous n-doping of this layer, but also that of the C_{70} overlayer and thus an advantageous interfacial alignment between $PC_{60}BM$ and C_{70} in both doped and undoped cases is observed. Furthermore, a small dopant amount of 1 % already has a significant n-doping effect, while increasing to 5 % overall doping does not introduce any further strong n-type doping.

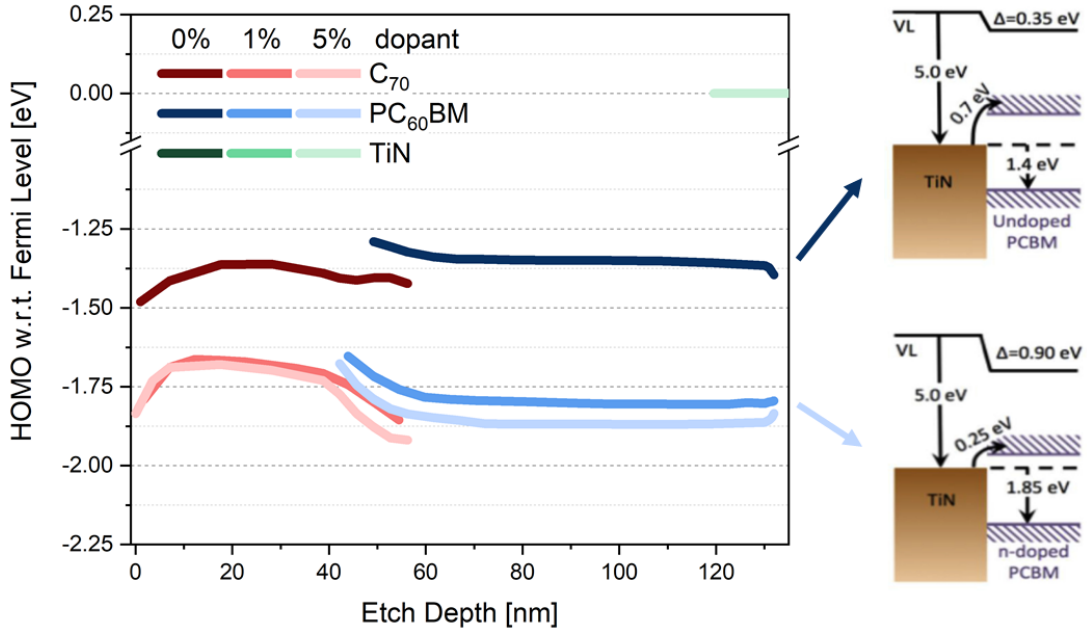

Figure 6.6: HOMO level alignment of a stack of $C_{70}/PC_{60}BM/TiN$ for 0 %, 1 %, and 5 % molecular doping levels of $PC_{60}BM$ with N-DMBI as dopant on the left. C_{70}, $PC_{60}BM$, and TiN are denoted with red, blue, and green colours respectively. Corresponding schematics of the $PC_{60}BM$/TiN interface energetics for the undoped and 5 % n-doped cases on the left. Adapted with permission from [44] and changed. Copyright © 2019 Elsevier B.V. All rights reserved.

Taking a closer look at the $PC_{60}BM$/Py interface results in further insights regarding electron injection into the $PC_{60}BM$ layer, as summarized on the right side in

Fig. 6.6. The deposition of undoped $PC_{60}BM$ on TiN results in an interfacial dipole $\Delta_{0\ \%} = 0.35\ eV$, and thus a reduction of the TiN work function from 5.0 eV to 4.65 eV. At the same time, the hole injection barrier reduces to 1.4 eV, resulting in an overall ionization potential of 6.05 eV, being in excellent agreement with previous reports. [364] We estimate the LUMO level position of $PC_{60}BM$ by subtracting its electronic bandgap of 2.1 eV, [398] yielding the corresponding electron injection barrier of 0.7 eV. In the case of 5 % doping, both the dipole and the hole injection barrier at the Py interface increases to $\Delta_{5\ \%} = 0.90\ eV$ and 1.85 eV, respectively. Consequently, the electron injection barrier reduces to 0.25 eV, which should yield efficient charge injection into doped layers.

In summary, we have successfully applied UPS depth profiling to to measure energetic alignment and charge carrier injection in a spintronic system with different side chains, as well as in a photodetector with an either doped or undoped $PC_{60}BM$ interlayer. These results confirm that our UPS depth profiling technique can be successfully applied to a wide variety of organic thin film layers.

6.4 Origin of Open-Circuit Voltage Tuning in Ternary Organic Solar Cells

Numerous optimization strategies, including novel device structures have been proposed in recent years in order to overcome limitations in OSC performance. One possibility is an enhancement of the amount of absorbed light achieved in, for example, tandem devices with multiple active sub-layers ensuring complementary light absorption. [300, 399, 400] Fabrication of such stacked architectures, however, is quite challenging. [401] Another possible device structure yielding a broad absorption window is achieved by TSCs, constructed by an active layer consisting of three materials, of which two are either donors or acceptors. [215, 308, 402–405] An increase in the number of absorbing materials can enhance the absorption window as well as charge mobility and thus increase both J_{sc} [309, 402, 406] and FF of the OPV device, respectively. [253, 403, 407] In addition, non-radiative loss channels can be minimized by profitable material mixing ratios, resulting in both enhanced FFs and V_{OC}s. [408] Finally, a careful component selection allows for a further boost in device V_{OC}, resulting in record TSC efficiencies exceeding 14 %. [409] The possibility of the simultaneous enhancement of all important device parameters is intriguing and has thus drawn the latest research interests to ternary blends.

Aspects governing TSC performance, such as the location of the third component in the blend, recombination dynamics and energetic alignment, or the reason for the continuous tunability of the V_{OC} by changing the ratio of the two donor (D) or two acceptor (A) materials, however, are still not entirely understood. [37, 242, 308, 410–413] Several models have been developed in order to predict device V_{OC}, such as the parallel junction, [414] energy cascade, [415, 416] alloy, [410, 417] and the Gaussian disorder model. [404, 405] In the parallel junction model, the active layer is treated as two

independent and isolated sub-systems of both D:A combinations. While this model predicts a theoretical V_{OC} between the values of the corresponding binary blends, the energy cascade model predicts values close to that of the binary device with the lowest V_{OC}. Both the alloy and the Gaussian disorder model are highly dependent on material miscibility, and successfully anticipate the tunability of V_{OC} in ternary devices. While the former predicts the device V_{OC} from the interface band gap, the latter takes the quasi Fermi level splitting, including broadened HOMO and LUMO levels due to disorder, into account. When compared with experimental results, however, the alloy model fails to explain the V_{OC} evolution for fullerene based devices, [418, 419] while the Gaussian disorder model successfully predicts changes in experimental values. [404, 405] In their recent review, Gasparini et al. [401] suggest that the V_{OC} is predominantly determined by the lowest CT state energy in the active layer. The authors argue that other, higher energy CT states first migrate to the lowest energy CT state prior to separation.

Herein, we apply our recently developed depth profiling technique, [34] in order to probe the vertical energetic landscape in two TSC systems with either two fullerene derivatives or a fullerene and a NFA as the acceptor materials. We find an excellent agreement between the V_{OC} of fabricated photovoltaic devices and the smaller estimated PV gap, which is also a measure for the CT state energy. With that we conclude that a correct estimation of energetic values within a blend is of crucial importance when predicting device properties. Furthermore, we investigate vertical compositional profiles and show that we are able to get reasonable results even in the case of two fullerene acceptors with highly similar compositional structures.

6.4.1 PBDB-T-2Cl:ITIC-2F:$PC_{70}BM$

In order to show the applicability of our technique, we first investigate a fullerene/NFA system with $PC_{70}BM$ and ITIC-2F as acceptor molecules and PBDB-T-2Cl as donor. For this reason, OPV devices were fabricated and UPS and XPS depth profiles were carried out on the same layers. The acceptor to fullerene ratio was varied from acceptor only to fullerene only, with main results shown in this section.

6.4.1.1 Device Performance

Inverted architecture OPV devices were fabricated with varying acceptor to fullerene weight ratios, while keeping a constant donor mass ratio of 50 %. In particular, the NFA weight ratio was varied from 0 % (NFA only) to 100 % (fullerene only). Hero IV curves, their corresponding EQE curves and averaged device parameters are shown in **Fig. 6.7** and summarized in **Table 6.1**.

While moving from fullerene only (green) to NFA only (red) devices, the short circuit current is strongly enhanced due to the additional absorption provided by the NFA, as also confirmed by the change in the EQE spectrum from 700 *nm* to 800 *nm*. This enhancement is accompanied by a rise in the FF, but also by a decrease in V_{OC}.

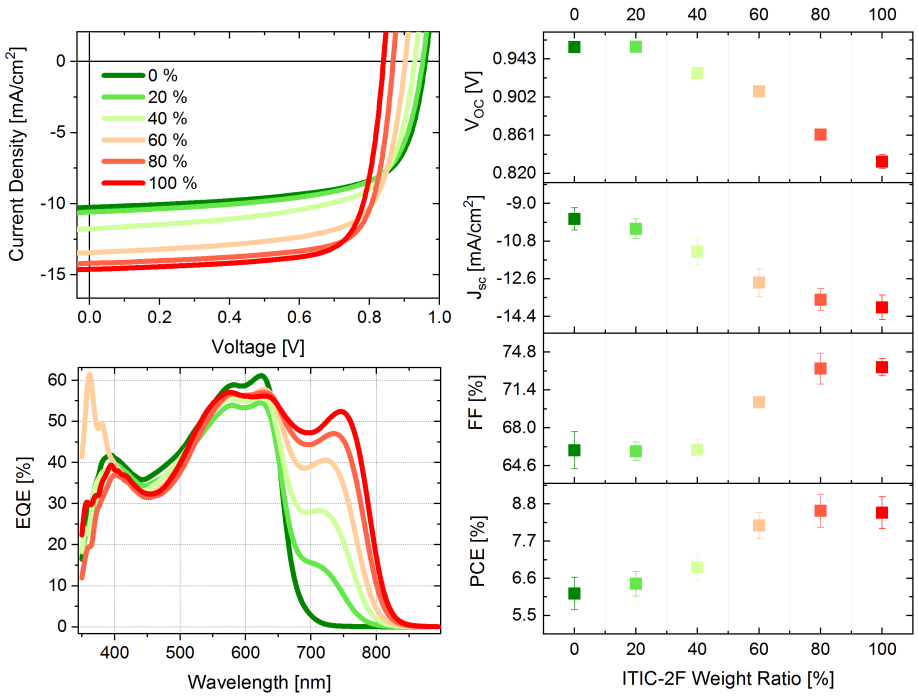

Figure 6.7: Hero IV and corresponding EQE curves on the left for varying ITIC-2F:$PC_{70}BM$ ratios (from 0 % (green) to 100 % (red) ITIC-2F) and a constant PBDB-T-2Cl mass ratio of 50 %. Averaged device parameter values including V_{OC}, J_{sc}, FF and PCE on the right.

All in all, this leads to an overall increase in performance from 6.74 % to 9.22 % device efficiency, with hero device values of 9.30 % for an ITIC-2F weight ratio of 80 %.

Table 6.1: Summary of the photovoltaic parameters V_{OC}, J_{sc}, FF and PCE for different donor/acceptor/fullerene mixing ratios for 16 devices each. Hero pixel PCE values are shown in brackets.

ITIC-2F Weight Ratio	V_{OC} (V)	$J_{sc}(mA/cm^2)$	FF (%)	PCE (%)
0 %	0.96 ± 0.01	-9.7 ± 0.6	66 ± 2	6.15 ± 0.49 (6.74)
20 %	0.96 ± 0.01	-10.2 ± 0.5	66 ± 1	6.44 ± 0.37 (6.76)
40 %	0.93 ± 0.01	-11.3 ± 0.6	66 ± 1	6.92 ± 0.41 (7.25)
60 %	0.91 ± 0.01	-12.8 ± 0.7	70 ± 1	8.16 ± 0.38 (8.55)
80 %	0.86 ± 0.01	-13.6 ± 0.5	73 ± 2	8.60 ± 0.49 (9.30)
100 %	0.83 ± 0.01	-14.0 ± 0.6	73 ± 1	8.54 ± 0.47 (9.22)

6.4.1.2 XPS Depth Profiling: Compositional Profiles

XPS depth profiles carried out on the same films resulted in vertically resolved compositional information, as summarized in **Fig. 6.8**. Donor, acceptor, and fullerene con-

tributions are plotted separately for clarity, while all graphs also contain the ZnO (substrate) contribution.

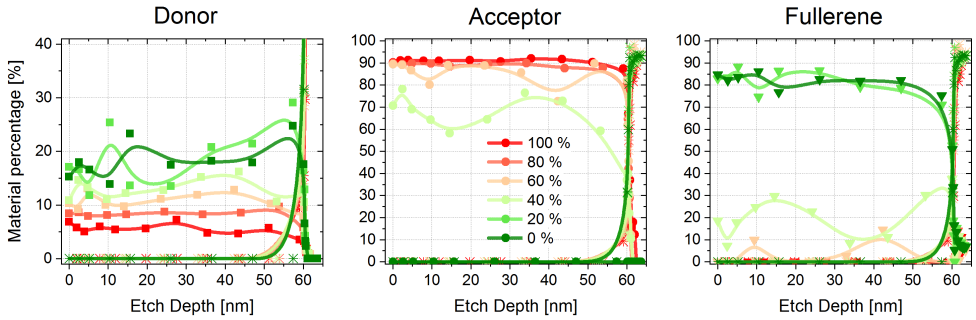

Figure 6.8: Material percentage values as a function of etch depth for the donor, acceptor, and fullerene materials from the left to the right for an ITIC-2F weight ratio varied from 0 % (green) to 100 % (red).

Interestingly, increasing the fullerene ratio from 0 % to 20 % during fabrication results in virtually no change in the acceptor and fullerene material percentages in the resulting films. A further increase to 40 % results only in minor, local changes at the etch depths of 10 nm and $\sim$ 42 nm, resulting probably from random variations during fabrication. The first remarkable changes in film composition appear at a fullerene ratio of 60 %, resulting in an alternating material percentage between the acceptor and the fullerene. Finally, for both 80 % and 100 % fullerene ratios, there is barely any acceptor material left in the films. Interestingly, the material percentage of the donor material increases with increasing fullerene contribution; the overall film thickness, however, shows no correlation with mixing ratio, as shown in **Fig. B.5**.

6.4.1.3 UPS Depth Profiling: Correlation between V_{OC} and E_g^{PV}

UPS depth profiling results, in addition to compositional profiles in a vertical energetic level alignment with a high resolution. This enables a PV gap estimation for each measured depth. In ternary blends, two PV gaps can be determined: the difference between the HOMO of the donor and the LUMO of (i) the non-fullerene and (ii) the fullerene acceptor. It has been suggested by *Gasparini et al.* [401], that the V_{OC} is predominantly determined by the lowest CT state energy in the active layer and thus by the smaller of the two PV gaps. In order to investigate this claim, averaged values for both the V_{OC} and the energy of the smallest PV gap are shown in **Fig. 6.9**.

We note that the two y-axes are shifted relative to each other, but still have the same scaling, making their slopes comparable. V_{OC} and the PV gap values estimated by UPS depth profiling are in good agreement. Photovoltaic gaps determined by measuring IP values for the individual materials, often used for device energetics estimation, are shown as a dashed line for comparison. The V_{OC} as a function of the estimated PV gap is shown in **Fig. B.6** and shows a slope of $(1.16 \pm 0.12)\ eV/V$ and an intersection

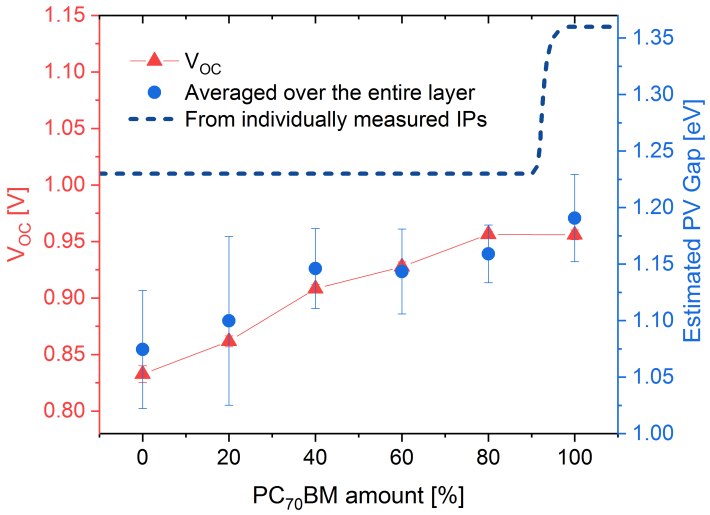

Figure 6.9: Device V_{OC} and estimated PV gap values, for the smaller PV gap system, averaged over the entire measured active layer as a function of the amount of $PC_{70}BM$. Minimum PV gap values calculated from individual IP measurements are shown as a dashed line for more clarity.

with the x-axis at $(0.35 \pm 0.12)\ eV$ when linearly fitted. Such a good V_{OC} to PV gap correlation (a slope of nearly 1) suggests that the sum of radiative and non-radiative recombination losses does not change significantly by changing the mixing ratio of ITIC-2F and $PC_{70}BM$. Furthermore, the sum of losses (represented by the x-axis interception in average) is very low, compared with other state-of-the-art systems. [34]

6.4.2 PTB7:$PC_{70}BM$:ICBA

In order to further confirm the validity and wide applicability of our method, we investigated a system incorporating two fullerene derivatives as acceptors: ICBA and $PC_{70}BM$. PTB7 serves as the donor material in this study. It has been shown recently, that this material combination fabricated in a standard architecture yields reasonable device PCEs. [420] We are particularly interested in this system due to the large similarity in chemical composition of the fullerene derivatives, which makes a determination of a compositional profile especially challenging. Similar to the previous study, we investigated changes in photovoltaic performance and the energetic alignment in devices with varying ICBA:$PC_{70}BM$ ratios. **Fig. 6.10** summarizes the photovoltaic performance for a series of devices (16 pixels each) with an ICBA weight ratio from 0 % to 30 %. Averaged values and hero pixel PCEs are summarized in **Table 6.2**.

Changes in EQE spectrum are less pronounced, than for the previously studied material system: an increased ICBA (and thus decreased $PC_{70}BM$) ratio results in a slight decrease in conversion efficiency of photoelectrons in the wide range of wavelengths from 400 nm to 700 nm, resulting in a decrease in device J_{sc}. Concurrently, an

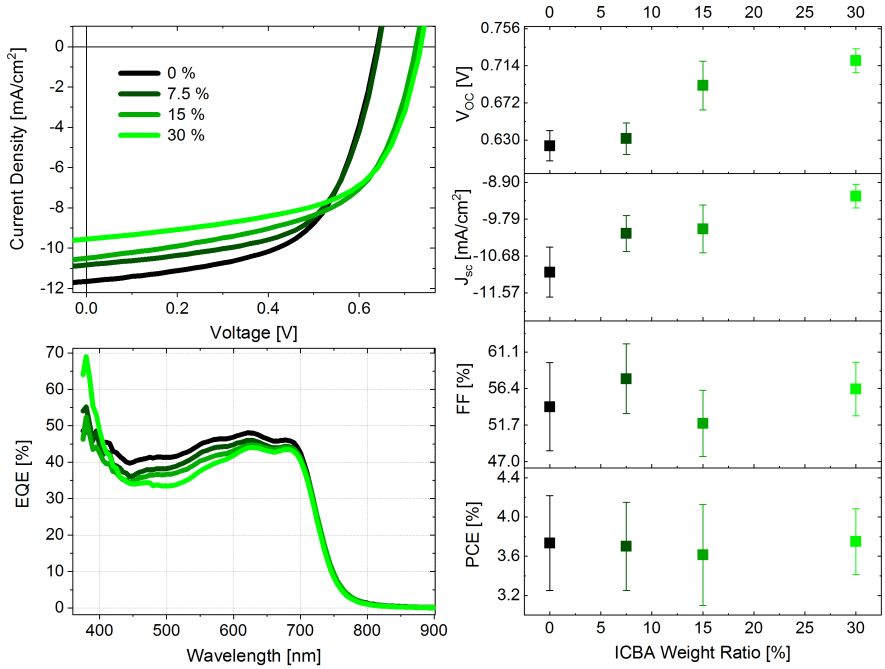

Figure 6.10: Hero IV and corresponding EQE curves on the left for varying ICBA:$PC_{70}BM$ ratios (ICBA weight ratio form 0 % (dark green) to 30 % (light green)) and a constant PTB7 mass ratio of 50 %. Averaged device parameter values including V_{OC}, J_{sc}, FF and PCE are shown on the right. IV measurements were performed by Yvonne Hofstetter.

Table 6.2: Summary of the photovoltaic parameters V_{OC}, J_{sc}, FF and PCE for different material mixing ratios and an ICBA weight ratio ranging from 0 % to 30 %. Hero pixel PCE values are shown in brackets.

ICBA Weight Ratio	V_{OC} (V)	$J_{sc}(mA/cm^2)$	FF (%)	PCE (%)
0 %	0.62 ± 0.02	-11.1 ± 0.6	54 ± 6	3.73 ± 0.48 (4.41)
7.5 %	0.63 ± 0.02	-10.1 ± 0.4	58 ± 4	3.70 ± 0.45 (4.25)
15 %	0.69 ± 0.03	-10.0 ± 0.6	52 ± 4	3.61 ± 0.51 (4.33)
30 %	0.72 ± 0.01	-9.2 ± 0.3	56 ± 3	3.75 ± 0.34 (4.17)

increase in V_{OC} can be observed, while no significant changes in FF occur. A constant FF confirms an equal quality of extraction layers, while the reason for changes in V_{OC} can be further investigated by UPS depth profiling. All in all, the overall device PCE stays rather constant over the whole investigated mixing ratio range.

6.4.2.1 UPS Depth Profiling: Correlation between V_{OC} and E_g^{PV}

Next, we investigate the vertical energetic landscape and estimate the PV gap in these films at each measured depth. PV gaps and corresponding device V_{OC}s, are plotted as

a function of ICBA weight ratio in **Fig. 6.11**.

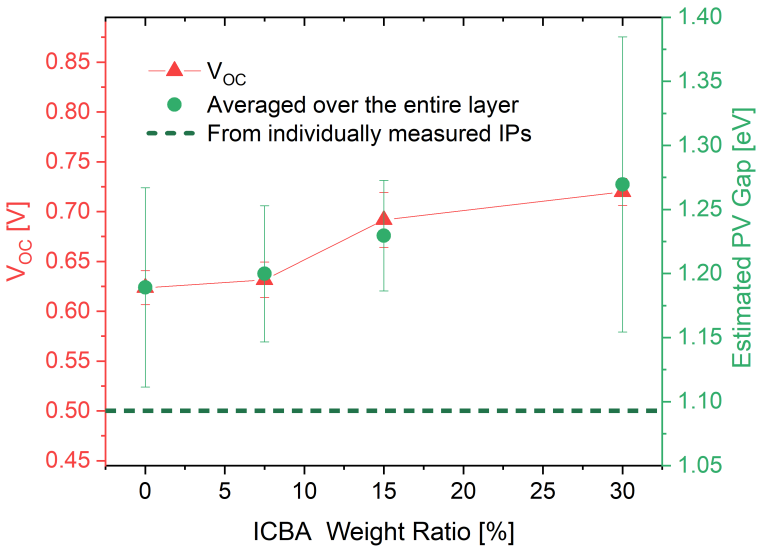

Figure 6.11: Device V_{OC} and estimated PV gap values for the smaller PV gap system, averaged over the entire measured active layer as a function of the amount of ICBA. Minimum PV gap values calculated from individual IP measurements are shown as a dashed line for comparison.

PV gap values were averaged over the entire measured device thickness, and the resulting E_g^{PV} is determined by the smaller value, representing also the CT state energy. PV gap values calculated from individually measured IP values are shown as a dashed line for comparison. Similarly to the previously reported ternary system, the correlation between device V_{OC} and smallest PV gap values implies a constant sum of radiative and non-radiative losses. A linear fit of V_{OC} and smallest estimated PV gap values can be found in **Fig. B.7** and shows a slope of $(1.22 \pm 0.13)\ eV/V$ and an interception with the x-axis at $(0.68 \pm 0.06)\ eV$. We again stress, that individually measured IP values do not yield any correlation and can thus not predict the change in V_{OC} for fullerne:fullerene mixing.

6.4.2.2 The Superiority of UPS over XPS Depth Profiling: Compositional Profiles

A comparison of material composition progression resulting from XPS and UPS depth profiles is shown in **Fig. 6.12**. These measurements highlight the superiority of UPS over XPS depth profiling for a system where the chemical structure of two materials is very similar, such as is the case for ICBA ($C_{78}H_{16}$) and $PC_{70}BM$ ($C_{82}H_{14}O_2$).

When varying the fabrication conditions, necessarily the ratio of the two fullerenes also should change. While XPS depth profiling fails entirely in resolving these differences between fullerne:fullerene mixing ratios, UPS depth profiling provides excellent results due to differences in the DOS of ICBA and $PC_{70}BM$. For all mixing ratios, there

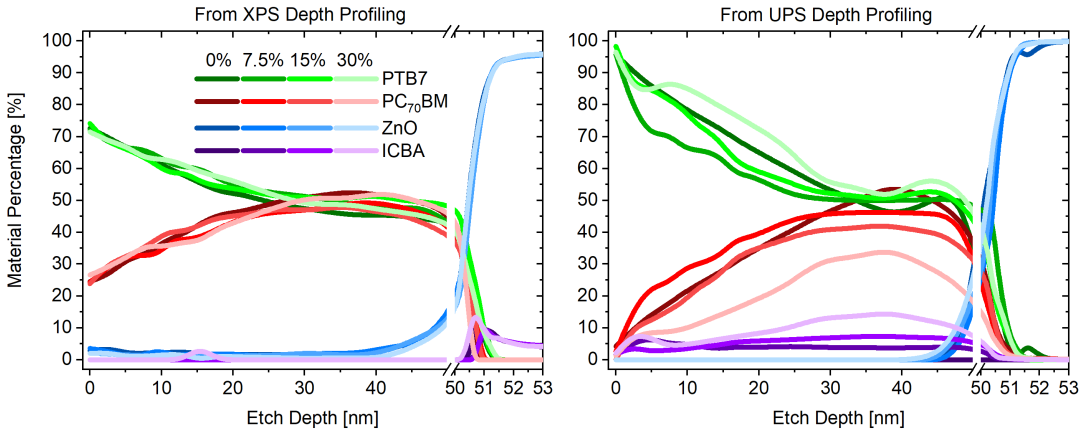

Figure 6.12: Compositional percentage values calculated from XPS and UPS depth profiling for different ICBA mass ratios. PTB7, $PC_{70}BM$, ZnO, and ICBA are denoted with green, red, blue, and purple colours, respectively.

is a rather large gradually changing region from a donor-rich top surface to a more mixed plateau region, first appearing at an etch depth of $\sim$ 30 *nm* for an overall film thickness of 50 *nm*.

6.5 Summary

In this chapter, several examples from the wide range of applications of our recently introduced UPS depth profiling technique are given. Particularly, we tested the effects of environmental degradation of the vertical energetic alignment in two OPV systems. While pristine energetics for both were very similar, degradation in oxygen and light introduced composition dependent p-doping, strengthening the importance of correct determination of energetic values governing device physics. Next, we investigated sequentially and conventionally deposited BHJ layers and confirmed an excess of the acceptor material in the top surface in sequentially deposited samples by UPS depth profiling. We also successfully studied the change in energetic alignment and charge carrier injection barriers for spintronic and doped photodetector systems resulting from layer doping and side chain variation. Finally, our results for two investigated highly complex ternary systems show an excellent agreement between estimated PV values and device V_{OC}, highlighting the strength of our UPS depth profiling method and suggesting that the sum of radiative and non-radiative energetic losses in ternary systems is independent on material mixing ratio. Furthermore, we have also shown the superiority of UPS over XPS depth profiling. A possible application of this technique, when compositional profiles for material combinations with very similar chemical structures are desired, is fascinating and will allow to study compositional profiles of systems which cannot be probed by any other technique.

In summary, we have applied our UPS depth profiling technique for a variety of

material systems, and explored their vertical energetic and compositional profiles, charge carrier injection barriers and correlated the device V_{OC} with the physically more fundamental PV gap. We emphasise that a fundamental understanding of energetic landscape progression is of crucial importance when interpreting device parameters, such as the J_{sc}, V_{OC} and with that the overall PCE. We believe that our method will help to better understand these processes, the energetic alignment and coherences between compositional and energetic distributions in more detail, and therefore help to find mitigation strategies regarding environmental degradation.

7 | Conclusions and Outlook

The aim of this thesis was to provide a correct determination of the energetic alignment in OSCs. Its importance cannot be understated when a deeper understanding of OPV device operation and accompanying device parameters, such as the V_{OC}, is desired. **Chapter 2** introduced the reader to the full complexity of light-to-electricity conversion in OSC devices, and covered the general physics of solar cells, the current understanding of excitons, recombination, energetic alignment, and the causes of V_{OC} loss. Next, all materials as well as experimental and analytical methods, with special focus on UPS and GCIB etching, were presented in **Chapter 3**.

Non-Fullerene Acceptors in Organic Photovoltaic Devices

In the first part of this thesis (**Chapter 4**) a new class of NFAs, *N*-Heteroacenes, was introduced. We investigated how side chain variations (with triptycene units) of a TIPS-TAP molecule affect the energy level structure, active layer morphology, photophysics and the overall OPV device performance. We discovered that the substitution of triptycene units suppresses recombination and lowers the tendency for the molecules to crystallize. Most interestingly, the photophysics of all three tested derivatives shows completely different behaviour than that of conventional fullerene acceptors: charge separation is unusually slow in these systems and has an additional, strong electric field-dependence. With side chain variations alone, we were able to boost the device performance by up to 2.5 %. The large versatility of possible *N*-Heteroacenes makes them excellent candidates for future electron accepting materials and allows for further optimization. The overall device PCE could thus be tuned by other side chains and additionally boosted by microstructure optimization during processing. In summary, we investigated a new class of NFAs and showed possible optimization pathways for this molecular system.

Visualisation of the Energetic Landscape in Organic Photovoltaic Devices

The second part of this thesis, starting with **Chapter 5**, introduced our recently developed depth profiling technique based on a succession of surface-sensitive measurements and essentially damage-free etching steps. The former is achieved by either UPS or XPS, while etching is performed by Ar GCIB sputtering. This method allows for an

accurate determination of vertical energetic and compositional landscapes with a high spatial resolution, limited only by the surface-sensitive investigation technique, which is $\sim$ 2 *nm* for UPS and $\sim$ 10 *nm* for XPS. Probing the energetic landscape yields an accurate determination of the vacuum level, HOMO levels of all constituent materials and an estimation of corresponding LUMO levels. The new methodology thus allows for accurate HOMO-HOMO level measurements and an estimation of the E_g^{PV}, both being extremely important for a more profound understanding of device physics, energetic alignment at organic/organic interfaces, and for developing photovoltaic improvement strategies. We employed our methodology on BHJ as well as BL devices including a wide range of high-performance photovoltaic material systems. E_g^{PV} of such devices is commonly determined in literature by energy level measurements on individual layers when the materials of interest are not blended. Our investigations showed that such an approach results in no correlation with corresponding device V_{OC}s, predicting sometimes even impossible negative energetic losses. On the other hand, E_g^{PV}s estimated by our newly developed method not only correlate with device V_{OC}, but also with corresponding CT state energies. These results show that the energetic alignment in organic/organic layers is non-trivial, and that interfacial effects such as dipole formation and band bending cannot be neglected.

Our depth profiling technique is not limited to OSCs only, but also allows for the investigation of any type of multi-layered structure and at any point in device lifetime, as shown for several example systems in **Chapter 6**. First, we investigated the temporal evolution of compositional and energetic profiles after device operation for both a polymer (PTB7) and a small molecule (DRCN5T) blended with a fullerene ($PC_{70}BM$). Both pristine (non-degraded) material systems show flat energetic levels throughout the entire layer and are thus rather similar; however, this no longer holds true after environmental degradation. While deterioration upon oxygen and light exposure introduces a strong p-doping for both systems, the resulting energetics heavily depends on the corresponding compositional profile throughout the active layer: the extent of p-doping is even higher in regions with enhanced amounts of the fullerene acceptor. Hence, in the PTB7:$PC_{70}BM$ system, where the compositional profile is uniform, so is the amount of p-doping. In the DRCN5T:$PC_{70}BM$ system, however, a $PC_{70}BM$ rich region (*compositional hill*) at an etch depth of $\sim$ 10 *nm* occurs and results in an enhanced p-doping of the energetic levels (*energetic hill*). Investigation of multiple layers with varied film thicknesses and donor to acceptor ratios showed different compositional peak positions and a clear correlation to energetic peak positions. Future work will allow further insights on the impact of environmental degradation on the energetic landscape of devices and will lead to better mitigation strategies and, ultimately, to a development of more stable solar cells.

Next, we showed that UPS depth profiling enables the comparison of compositionally similar samples of sequentially and conventionally deposited BHJs, whereas XPS depth profiling fails. We were able to prove that our methodology is not limited to photovoltaic systems only: it is directly applicable to the study of energetic landscape

progression of any multi-layered device, including photodetectors, spintronic systems and the effect of interlayer doping. The versatility of UPS depth profiling was further demonstrated by successful investigation of energetic landscapes and charge carrier injection barriers at metal interfaces in both doped photodetectors and spintronic layers with varied side chains.

Finally, we analysed complex ternary systems to address their still highly debated energetic alignment and the vertical compositional mixing of the third material. In particular, we studied two ternary systems with two acceptor materials each including NFAs and fullerenes, and estimated the PV gap for varying acceptor to acceptor mixing ratios. An excellent correlation of E_g^{PV} with corresponding device V_{OC} suggests that the sum of radiative and non-radiative energetic losses in both investigated ternary systems is independent of the mixing ratio. Furthermore, a comparison with PV gap values determined by energetic measurements on individual, not blended materials did not correlate to measured V_{OC} values at all. Additionally, we showed that while XPS depth profiling yields a vertical compositional profile for the first investigated ternary system, it fails for the second one because of the almost identical chemical composition of the two fullerene derivatives serving as acceptors. This issue can be overcome by utilizing UPS depth profiling, resulting in reasonable compositional profiles with a high depth resolution. UPS depth profiling can thus be applied for blended material systems with components comprising the same chemical elements, but a dissimilar electronic structure, not possible with any other technique up to date.

In summary, we introduced a new class of NFA acceptors and developed a depth profiling technique, allowing for vertical energetic and compositional profile measurements at any point in device lifetime. With this, estimated E_g^{PV} are correlated to the CT state energy and device V_{OC}s. Our results suggest that an accurate energy level determination in OPV devices is of crucial importance. The developed method is applicable for a wide range of organic multi-layered modules, as demonstrated for photodetectors, spintronic devices and TSCs.

Our developed technique is of great importance for the organic photovoltaic community, since it allows to measure properties of layers previously not accessible, and therefore opens up the way for a deeper understanding of device physics, including the V_{OC}. The ability to cross organic/organic as well as organic/inorganic interfaces makes our methodology of great interest for complete devices. Future work could include an accurate determination of compositional and energetic alignment in novel tandem devices or complete solar cells, including electron and hole transport layers. This could be conducted not just on organic only solar cells, but could also be expanded to hybrid perovskite devices as well as quantum dot based solar cells. All in all, the method developed in this work yields a new tool to probe previously hidden material properties and will help to develop new materials and to find optimal material combinations in photovoltaic devices.

Part III

Appendix

A The Fitting Program *LaFit*

In order to extract information from depth profile measurements, all data needs to be fitted in a proper way. We implemented a fitting program written in *Matlab 2018b* using *App Designer* to automatize and standardize data fitting, referred to from now on as *"LaFit"*. In this chapter, the latter program is described in great detail.
First, all requirements for data import are described. Next, an overview of the main functions of *LaFit* is given, followed by a detailed description of these. Finally, example files and the most important *MatLab* codes are provided. The entire program can be downloaded from HERE.

A.1 File Requirements for Data Import

In the following, file requirements for data input are described. Note, that in each case the number of empty lines in the import files is crucial.

- Atomic percentage files extracted from XPS depth profiles can be directly imported to *LaFit*. They need to be simply copied into a *.txt* file. An example file structure is given in **Section A.3.1**.
- Single UPS spectra are also imported by copying the spectrum into a *.txt* file. For an automatized import, the file name needs to have the following form:

  X_20eV_IP.txt

  with **X** being the materials name. An example file structure is given in **Section A.3.1**. The energy range of each individual material spectrum should be from 20 eV until 27 eV, however all contributing spectra needs to have the same kinetic energy range and needs to start with a lower value than the depth profile data described above.
- UPS depth profile data is imported from *.txt* files generated in *Avantage* by the data exporter tool. For material percentage and HOMO level fitting, *LaFit* needs one depth profile measured in the HOMO region (preferably from 20 eV until 27 eV). However, for a SECO fit a second depth profile file, including UPS measurements of the whole kinetic energy range is needed. For automatized data

import, the files need to be in the same containing folder and have the very same name, except the ending, which needs to be 'HOMO' and 'SECO', respectively. An example file structure is given in **Section A.3.1**.

A.2 Main Functions

The main window of the fitting program is shown on **Figure A.1** with coloured rectangles serving clarity: Red denotes material properties and percentage, green UPS fitting parameters, light blue energetic properties and dark blue data saving and loading.

Figure A.1: Overview of the fitting program used to extract information from UPS and XPS depth profiles. The program is subdivided into smaller parts which are marked with coloured rectangles for more clarity: material input and material percentage calculation buttons (red), UPS data fitting (green), energetic alignment(blue) and data saving and loading (dark blue).

Upon starting *LaFit*, the program directory is updated and saved under the **"Extra input data"** tab automatically. However, this should be double-checked and edited manually if necessary. At any stage of data evaluation, *LaFit* offers the opportunity to save or re-load any pre-evaluated data by clicking the corresponding buttons marked in the dark blue rectangle. Data fitting can be generally done in the following way:

Material Percentage from XPS Depth Profiles

- First, the number of materials existent in the layer needs to be given in the **"# Mat"** field. This will be automatically fixed, as soon as material information is obtained later on. The materials will be denoted from now on as **D**, **A**, **B** and **F**.

- Next, material properties need to be loaded. These are saved in a separate *Excel* file including *the materials name* and corresponding *chemical composition*, *molecular weight*, *optical band gap* and *etch rate* for different etching modes. Most of these properties will be later on needed for material percentage calculations. In order to access these properties, one first needs to choose all materials the layers of interest are made of (standard values are $P3HT$, $PC_{60}BM$, ZnO and $PC_{70}BM$) and the elements which should be used later on for molecular percentage calculation (standard elements are S, C, Zn and C) and finally push the **"Get Material Information"** button. All necessary information is now loaded into tables in the **"Data"** tab. *LaFit* also offers the opportunity to indicate the etching mode, or whether the samples were annealed or not. Changing the latter will change the materials name, for which it will be searched in the corresponding Excel table to the original name plus the *"annealed"* extension. During import, estimated etch velocities are loaded for the given etching mode from the corresponding column. To change these latter two parameters in only important, however, in case some of the material informations from the Excel file mentioned above would be affected by this information.

- As the next step, material percentage from XPS depth profiles can be calculated. After pushing the **"Load atomic percentage file"** button, the *.txt* file with atomic percentage data - saved as described in **Section A.1** - can be selected and loaded. The desired material percentage can then be calculated as described in **Section A.2.2.1** and plotted on the left axes under the **"Material percentage"** tab by pushing the **"Show material percentage"** button. *LaFit* offers the opportunity to calculate these percentages either analytically or numerically. This is, however, only the case if the program is used for 3 materials in the layer. For 2 or 4 materials, the analytical or the numerical solution, respectively will be used automatically.

Fitting of UPS Depth Profiles

- Firstly, individual UPS spectra of the consisting materials of the whole layer need to be loaded. If these are saved as described in **Section A.1**, **"Load All standard"** can be chosen and all spectra can be simply loaded by clicking the **"Load"** button. It is important here to chose the same energy range as in the saved data name. Otherwise, all spectra can be also loaded individually. All spectra are now visualized in the **"UPS_HOMO"** tab including automatized HOMO onset fittings, as described in **Section A.2.1.1** in more detail.
  Next, the whole depth profile can be loaded by clicking **"Load BHJ"**. In case one selects the **"No SECO"** check box, only the HOMO region depth profile will be loaded.

In order to fit this data with the individual UPS spectra, the kinetic energy range of all spectra needs to be the same. In case, the depth profile data does not fulfil this criteria, the spectrum can be "filled up" with data taken from the SECO measurements by using the **"Fill up until"** check-box. This is however only possible if the **"No SECO"** check-bos is deactivated.
Prior to fitting, numerous parameters can be adjusted, which are described in **Section A.2.1.3** in more detail.

- From the resulting fit parameters of a UPS depth profile, one can calculate material percentage, as described below in **Section A.2.2.2**. For this, one needs to select a D:A:F ratio, which should hold at the selected plateau etch step and click the **"Show material percentage"** button. The calculated data is now also plotted in the left axes in the **"Material percentage"** tab. Please note, that such a practice will normalize all data and all results gathered this way will only give information about curve shapes but not amplitudes.

- The resulting fit parameters also reveal the vertical energetic profile of the measured film. This can be visualized on the **"Energetics"** tab by clicking **"Show energetic diagram"**. The energetics is automatically plotted for the whole measurement region, however some of the materials are not present in the entire film. For a better visualization, several rulers allow the user to change the plot region of each material. If one wants to plot less materials, then measured, *LaFit* allows for de-selecting materials in an arbitrary way.

A.2.1 UPS Data Fitting

A.2.1.1 HOMO Onset Fitting

In order to be able to reconstruct the energetic alignment in a depth profile, the valence band (VB) needs to be fitted, resulting in the HOMO onset. A proper way would be to measure angle resolved UPS, plot every spectrum logarithmically and fit the onsets. This would give a complete representation of the VB progression in k-space. In community however, the HOMO level is commonly determined by one of the following ways:

- One can fit the whole DOS with Gauss curves, each representing an electronic state. The HOMO level can be then attributed to the highest kinetic energy Gauss curves tail.

- Alternatively, one can fit the onset of the DOS linearly, whereby the DOS can be plotted either logarithmically or linearly.

In this work, and thus in the MatLab Fitting Program, we use the latter approximation and fit the low binding energy edge of the linearly plotted DOS as described by *Kahn et. al.*.[171] For this, an automatized MatLab code has been written, shown in

Section A.3.2.
This program works the following way:

1. A function is fitted to the measured data points, after they got normalized.
2. Since, the data is now represented as a continuous function, it can be differentiated yielding in peaks with each having a certain position p, width w and height h.
3. Now, noise needs to be separated from data and thus, the right peak needs to be selected, which represents the sought onset. Generally one finds the desired peak, when h is higher than 5 % $\cdot \frac{1}{s}$ of the highest peak, with the introduced parameter s being the sensitivity. Its pre-defined value is 1, but can be also changed in case the corresponding HOMO onset is very shallow.
4. Once the right peak is selected, limits for fitting are set from $p - \frac{w}{3}$ to $p + \frac{2w}{3}$, and the HOMO onset can be fitted linearly.

LaFit alternatively offers a manual fit of the HOMO region, in case the automatic fitting would fail entirely. Manual values can be entered manually under the **"Extra input data"** tab.

A.2.1.2 SECO Onset Fitting

The SECO onset is determined by a linear fit of the high binding energy edge of the DOS spectrum.

A.2.1.3 Fitting of UPS Depth Profiles

Fitting of UPS depth profiles is shown schematically on **Fig. 5.4**. The measured spectrum F is fitted by a linear combination of the UPS spectra of the individual consisting materials f_i, by allowing for every material a *scaling* $\boldsymbol{s_i}$ and an *energetic shift* $\boldsymbol{e_i}$ as parameters and with n denoting the number of materials:

$$F(x, s_1, s_2, ..., e_1, e_2, ...) = \sum_{i=1}^{n} s_i \cdot f_i(x - e_i) \tag{A.1}$$

Since the sensitivity of the UPS measurements for different materials is slightly varying, all individual UPS spectrum measurements got normalized, as described in **Section A.2**. This implies, that they cannot be directly compared, hence each depth profile measurement gets normalized prior to fitting. F and all f_i in **Eq. A.1** are representing thus normalized spectra. This implies, that the resulting *scalings* $\boldsymbol{s_i}$ are describing the shape of material percentage correctly, but not its exact values, but more to this later in Sec. A.2.2.2.
Prior to fitting, different parameters, among others the limits for s_i and e_i can be adjusted:

- Start values for the energetic shift parameters e_i can be given by the **"Allowed shifts in E"** edit fields **D**, **A**, **B** and **F**, with a tolerance given in the fields below the corresponding materials.

- Start values for the scaling parameters s_i can be given by the **"Allowed scaling parameters"** edit fields for **D**, **A**, **B** and **F**, with allowed minimum and maximum values given in the corresponding edit fields.

- An optional **"D Quenching"** checkbox gives the opportunity to "quench" the original **D** UPS spectrum, which can be of use for some polymer materials, where the DOS gets broader or shallower with (etch) time, changing the form of the corresponding fitting term to:
$$s_D \cdot f_i(q_D x - e_D) \tag{A.2}$$
with q_D being the quenching parameter.

- In order to find peaks in a spectrum, one needs to find its derivative, which is only possible for continuous functions. All loaded single UPS spectra are, however, non-continuous, since they represent measurements of individual data points. Thus, in order to be able to make fits to this data, the spectrum needs to be replaced by a continuous function. This *"functionalizing"* can be described by the adjustable sensitivity parameter **"SP"**, with a standard value of 0.999. A change of this parameter makes only sense, if for some material systems the corresponding UPS spectrum would change very rapidly.

- Fitting of the SECO is done simlutaniously to the HOMO region depth profile fitting. This is done as described in **Sec. A.2.1.2**. The limits for this trivial fit can be adjusted by the corresponding **"Fitting range for SECO fit"** fields. These are given in %, ranging from 0% to 100%.

- It is often the case, that the **B** material, which is normally the base on which the other materials are deposited is not present in the first several spectra. In order to gain some computational time, the contribution of **B** can be set automatically to 0 until a certain etch level by the **"Base fit start at the following value"** field.

- In many cases, secondary electrons already play a role in the measured near E_F DOS. This can be overcome by not fitting the entire loaded HOMO region spectra, but only a part of it. This region can be chosen by the corresponding **"Fitting range"** fields.

After all these fields are adjusted properly, fitting can be done by simply pushing the **"Fit BHJ curves"** button. The corresponding script for less than 4 and for 4 materials is given in **Sec. A.3.2** and **A.3.2**, respectively.

A.2.2 Material Percentage Determination

A.2.2.1 Material Percentage from an XPS Depth Profile

In general, the atomic percentage of an individual element x_1 in a certain mixture of i materials $M_1, M_2 \dots M_i$ is given by:

$$\%x_1 = \frac{\sum_i [\%M_i \cdot \frac{N_A}{M_W^{M_i}} \cdot \#{x_1}^{M_i}]}{\sum_i [\%M_i \cdot \frac{N_A}{M_W^{M_i}} \cdot (\sum_k \#{x_k}^{M_i})]} \tag{A.3}$$

with N_A the Avogadro number, $M_W^{M_i}$ the molecular weight of the material M_i, $\#{x_k}^{M_i}$ the number of x_k atoms in the material M_i and $\%M_i$ the material percentage of M_i in the mixture of all materials. Furthermore, the sum of all materials M_i needs to be unity:

$$\sum_i \%M_i = 100\ \% \tag{A.4}$$

The atomic percentage for all x_j atoms is analogue and in case of two materials D and A, with the corresponding atoms of interest x_D and x_A, this problem is analytically solvable yielding the following material ratio:

$$\frac{\%D}{\%A} = \frac{M_W^D}{M_W^A} \cdot \frac{\#x_A^A \%x_D - \#x_D^A \%x_A}{\#x_D^D \%x_A - \#x_A^D \%x_D} \tag{A.5}$$

The error of this quantity can be estimated by propagation of error and is given by:

$$\triangle \frac{\%D}{\%A} = \frac{M_W^D}{M_W^A} \cdot \frac{|\#x_A^A \#x_D^D - \#x_D^A \#x_A^D|}{(\#x_D^D - \#x_A^D \frac{\%x_D}{\%x_A})^2} \cdot \frac{\%x_D}{\%x_A} \cdot \sqrt{\delta(\%x_A)^2 + \delta(\%x_D)^2} \tag{A.6}$$

where $\delta(\%x_i) = \frac{\triangle \%x_i}{\%x_i}$ is denoting the relative error of the corresponding atomic percentage. Since there are only two materials in this system, the sum of $\%D$ and $\%A$ is 100 %.

In case of more than two materials, this equation system still can be solved analytically, if there are no intermixing atomic terms in **Eq. A.3**, e.g.

$$\#{x_i}^{M_k} = 0, \forall i \neq k \tag{A.7}$$

Otherwise the solution can be only approximated numerically by for example the *lsqcurvefit* function in *Matlab*. Alternatively, one can ignore data, and calculate D/A and D/B from **Eq. A.3** and set the sum of D, A and B to one. This method offers an alternative to the numerical approximation described above, in case, some of the values would be very off, and the fit function would not come to a solution. One can switch between the analytical and numerical solutions described here with the *"Analytical*

solution" button, applicable only for less than 4 materials. For 4 materials only the numerical solution makes sense. Corresponding *MatLab* codes for 2, 3 and 4 materials are given in **Sections A.3.2**, **A.3.2** and **A.3.2**, respectively.

A.2.2.2 Material Percentage from a UPS Depth Profile

In order to determine exact material percentage values from UPS depth profile results, one needs to re-scale the resulting scaling parameters s_i manually and calibrate them to an arbitrary value. This can be done by entering the desired ratio (represented by the *D:A:F* field) at a certain etch time (given by the *plateau* field). A good option to choose these values is from a corresponding XPS depth profile, determined by as in **Sec. A.2.2.1**, optimally at a plateau region, where XPS depth profiling should provide exact values even due to its higher probing depth. The *MatLab* code for re-scaling is shown in **Sec. A.3.2**.

A.2.3 Energetic Diagram

A vertically resolved energetic alignment diagram can be plotted by clicking the **"Show energetic diagram"** button, which plot the corresponding graph under the **"Energetics"** tab. HOMO levels of corresponding materials are calculated from the original UPS spectrum fit described in **Sec. A.2.1.1** and the energetic shift e_i determined by UPS depth profile fitting described in **Sec. A.2.1.3**. Adding up these two values will result in the real position of the HOMO level at a certain etch position of the corresponding material. This can thus vary throughout the entire film. LUMO levels are also plotted in the resulting graph as estimates. They are estimated from optical gap measurements, by adding the optical gap value to the determined HOMO level. [150] This is only an approximation, since it does not account for the exciton binding energy, as described in **Sec. 2.3.2.2**. Nevertheless, it yields in a good approximation and allows for a visualisation of the LUMO level. Finally, the VL is also plotted, determined by SECO fitting, as described in **Sec. A.2.1.2**. We note, that this always represents the higher Φ material in the mixture as shown by *Schultz et. al.* [373]

A.3 Example Files and *MatLab* Codes

A.3.1 Example Files for Data Import

XPS Depth Profiles

```
1  ?
2  Axis     Peaks    Elements=        5
3  Axis     Etch Time        Elements=        43
4  Axis     Etch Level       Elements=        43
5
6  C:\Users\engineer\AppData\Local\Temp\VGD{F5486BAC-A73C-4E8B-AEF7-FC905E75F05F}.vgd
7
8
9
10                  Peaks (P)\Peaks N1s Scan A       F1s Scan A       S2p      C1s      O1s

11 Etch Time (EtchTime)     Etch Level (EtchLevel)
12 s                Atomic % (%)     Atomic % (%)     Atomic % (%)     Atomic % (%)     Atomic
       % (%)
13 0.000000         0.000000         1.73855  0.915809         5.41707  78.1108  13.8177
14 15.0000          1.00000          1.63296  0.676689         5.45963  79.3005  12.9302
15 30.0020          2.00000          1.79553  0.868576         5.72676  79.3115  12.2976
16 ...              ...              ...      ...              ...      ...      ...
```

Single UPS Spectra

```
1  ?
2  Axis     Energy   Elements=        701
3
4  C:\2015-16\VincentLami\2019-MM-DD - XYZ.VGD
5
6
7
8
9
10 Kinetic Energy (E)
11 eV               Counts / s
12 20.0000          1.47778e+006
13 20.0100          1.47211e+006
14 ...              ...
15 26.9900          15.4247
16 27.0000          16.1458
```

UPS Depth Profiles

```
1  ;========================================================================
2  ;Dump of DataSpace 'C:\2015-16\VincentLami\2019-MM-DD - XYZ.VGD'
3  ; on DD/MM/2019 at 13:50:04
4  ;========================================================================
5
6
7  ;[Note that this file can be reloaded only if certain syntax rules are NOT broken]
8
9  $FORMAT=4
10
11 ;DataSpace has 2 data axes as follows:
12 ;   #=      start,     end,       numSpaceAxes
```

```
$DATAAXES=2,#empty#
    0=         0,       700,          1
    1=         0,        43,          2

;=========================================================================

;DataSpace has 3 space axes as follows:
;   #=       start,         width,       numPoints,  axisType,   linear,  symbol,
    unit,      label
$SPACEAXES=3
    0=      20.000000,       0.010000,       701,  ENERGY,   LINEAR,  'E',   'eV',    '
        Energy'
    1=       0.000000,      85.128930,        44,  ETCHTIME,   NON-LINEAR,  'EtchTime',
           's',    'Etch Time'
    2=       0.000000,       1.000000,        44,  ETCHLEVEL,   LINEAR,  'EtchLevel',
          '',    'Etch Level'

;=========================================================================

;Values on axis 0 where axis 1 = 0;
$AXISVALUE= DATAAXIS=1 SPACEAXIS=1 LABEL='Etch Time' POINT=0 VALUE=0.000000;
$AXISVALUE= DATAAXIS=1 SPACEAXIS=2 LABEL='Etch Level' POINT=0 VALUE=0.000000;
$DATA=*,0
LIST@    0=    125605.026000,    124904.836000,    123495.380000,    122437.860000
LIST@    4=    120389.122000,    119599.920000,    119356.564000,    118062.148000
...    ...=    ...           ,    ...           ,    ...           ,    ...
LIST@ 696=         1.860000,         1.870000,         2.996000,         5.080000
LIST@ 700=         2.740000
;Values on axis 0 where axis 1 = 1;
$AXISVALUE= DATAAXIS=1 SPACEAXIS=1 LABEL='Etch Time' POINT=1 VALUE=15.010000;
$AXISVALUE= DATAAXIS=1 SPACEAXIS=2 LABEL='Etch Level' POINT=1 VALUE=1.000000;
$DATA=*,1
LIST@    0=    116016.914000,    115280.588000,    115049.150000,    114283.392000
...    ...=    ...           ,    ...           ,    ...           ,    ...
```

A.3.2 Important *MatLab* Codes

LaFit is provided on the Cloud, however the most important code fragments are listed below.

MatLab Code for Material Percentage Calculation for Two Materials

```
function [x,x_error] = XPS_atomic_2materials(method, nSD, nSA,  nCD, nCA, prS_all,
    prC_all, MWD,MWA)

if strcmp(method,'On')==1
        prC=prC_all; prS=prS_all;
        y=MWD./MWA.*((nCA.*prS-nSA.*prC)./(nSD.*prC-nCD.*prS));
        DonorP=100.*y./(1+y);
        dy = abs(prS./prC.*sqrt(2*0.1.^2).*MWD./MWA.*(nCA.*nSD-nSA.*nCD)./((nSD-nCD.*(
            prS./prC)).^2));
        DonorError = abs(100.*dy./((1+y).^2));
        x=[DonorP/100,(100-DonorP)/100]; x_error=[DonorError/100,DonorError/100];

elseif strcmp(method,'Off')==1
    x=zeros(length(prS_all),2); x_error=zeros(length(prS_all),2);
    vS=[nSD/MWD,nSA/MWA]; vC=[nCD/MWD,nCA/MWA];
    ossz=[(nSD+nCD)/MWD,(nSA+nCA)/MWA];
```

```
    for i=1:length(prS_all)
        prS=prS_all(i)/(prS_all(i)+prC_all(i)); prC=prC_all(i)/(prS_all(i)+prC_all(i))
            ;
        xdata=horzcat(vS,vC,ossz,prS,prC);
        fun = @(d,xdata) horzcat(10000.*([xdata(1),xdata(2)]*[d(1);d(2)]-xdata(7).*[
            xdata(5),xdata(6)]*[d(1);d(2)]),...
                                 10000.*([xdata(3),xdata(4)]*[d(1);d(2)]-xdata(8).*[
                                     xdata(5),xdata(6)]*[d(1);d(2)]),...
                                 1.*(d(1)+d(2)));
        d0 = [0.5,0.5]; lb = [0,0]; ub = [1,1]; ydata=[0,0,1];
        options = optimoptions('lsqcurvefit','Algorithm','trust-region-reflective','
            FunctionTolerance',1e-8,'OptimalityTolerance',1e-9);
        [d,~,residual,~,~,~,jacobian] = lsqcurvefit(fun,d0,xdata,ydata,lb,ub,options);
        x(i,:)=d(:)/sum(d(:));
        ci = nlparci(d,residual,'jacobian',jacobian,'alpha',0.32); % alpha=0.32 means
            1 sigma variance; nlparci gives back d(:)-1sigma and d(:)+1sigma in case
            alpha is 0.32
        ci2=abs(ci(:,1)-ci(:,2))./2; %ci2 is now 1 sigma
        x_error(i,:)=ci2(:)+abs(d(:).*0.1)+0.01; % Fitting error + 10 % error + 1% in
            every case
    end
end
end
```

MatLab Code for Material Percentage Calculation for Three Materials

```
function [x,x_error] = XPS_atomic_3materials(method, nSD, nSA, nSB, nCD, nCA, nCB,
    nZnD, nZnA, nZnB, prS_all, prC_all, prZn_all,MWD,MWA,MWB)

if strcmp(method,'On')==1
    x=zeros(length(prS_all),3);
    x_error=zeros(length(prS_all),3);
    for i=1:length(prS_all)
        prS=prS_all(i); prC=prC_all(i); prZn=prZn_all(i);
        % In order to prevent dividing with 0
        if prC==0
            prC=0.001;
        end
        if prS==0
            prS=0.001;
        end
        if prZn==0
            prZn=0.001;
        end
        % Calculate y = D/A and z = D/B
        y=MWD./MWA.*((nCA.*prS-nSA.*prC)./(nSD.*prC-nCD.*prS));
        dy = abs(prS./prC.*sqrt(2*0.1.^2).*MWD./MWA.*(nCA.*nSD-nSA.*nCD)./((nSD-nCD.*(
            prS./prC)).^2));
        y2=1/y; dy2=dy/y^2;
        z=MWD./MWB.*((nZnB.*prS-nSB.*prZn)./(nSD.*prZn-nZnD.*prS));
        dz = abs(prS./prZn.*sqrt(2*0.1.^2).*MWD./MWB.*(nZnB.*nSD-nSB.*nZnD)./((nSD-
            nZnD.*(prS./prZn)).^2));
        z2=1/z; dz2=dz/z^2;
        x(i,:)=[1./(1+y2+z2);y2./(1+y2+z2);z2./(1+y2+z2)];
        x_error(i,:)=[1./((1+y2+z2).^2).*sqrt((dy2).^2+(dz2).^2);1./((1+y2+z2).^2).*
            sqrt(((1+z2).*dy2).^2+(dz2).^2);1./((1+y2+z2).^2).*sqrt((dy2).^2+((1+y2).*
            dz2).^2)];
    end
elseif strcmp(method,'Grr')==1

```

```
30 A=[nSD/MWD-nSB/MWB, nSA/MWA-nSB/MWB;nCD/MWD-nCB/MWB,nCA/MWA-nCB/MWB;nZnD/MWD-nZnB/MWB,
       nZnA/MWA-nZnB/MWB];
31 v1=[(nSD+nCD+nZnD)/MWD-(nSB+nCB+nZnB)/MWB;(nSA+nCA+nZnA)/MWA-(nSB+nCB+nZnB)/MWB];
32 v2=[nSB/MWB;nCB/MWB;nZnB/MWB]; v3=((nSB+nCB+nZnB)/MWB);
33
34 x0=[1/2;1/2]; lb=[0;0]; ub=[1;1];
35 x=zeros(length(prS_all),3);
36 x_error=zeros(length(prS_all),3);
37 for i=1:length(prS_all)
38     prS=prS_all(i); prC=prC_all(i);
39     if (prZn_all(i)<0.005)
40         y=MWD./MWA.*((nCA.*prS-nSA.*prC)./(nSD.*prC-nCD.*prS));
41         dy = abs(prS./prC.*sqrt(2*0.1.^2).*MWD./MWA.*(nCA.*nSD-nSA.*nCD)./((nSD-nCD.*(
               prS./prC)).^2));
42         x(i,:)=[y./(1+y);1-y./(1+y);0];
43         x_error(i,:)=[dy/(1+y)^2;dy/(1+y)^2;0];
44     else
45         prZn=prZn_all(i);
46         vP=[prS;prC;prZn]; % Numbers between 0 and 1, sum is 1
47         fun = @(y) 100.*(A*y-((v1'*y+v3).*vP-v2));
48         %options = optimoptions('lsqnonlin','FunctionTolerance',1e-14,'Algorithm','
               trust-region-reflective','OptimalityTolerance',1e-14,'StepTolerance',1e
               -21,'MaxFunctionEvaluations',10000,'MaxIterations',2000);
49         [y,~,residual,~,~,~,jacobian] = lsqnonlin(fun,x0,lb,ub);%,options);
50         x(i,:)=[y(1);y(2);abs(1-y(1)-y(2))];
51         ci = nlparci(y,residual,'jacobian',jacobian,'alpha',0.32); % alpha=0.32 means
               1 sigma variance
52         ci2=abs(ci(:,1)-ci(:,2))./2;
53         x_error(i,:)=[ci2(1)+y(1)*0.1+0.01;ci2(2)+y(2)*0.1+0.01;0.01+sqrt(ci2(1)^2+ci2
               (2)^2)+abs(1-y(1)-y(2))*0.1];
54     end
55 end
56 elseif strcmp(method,'Off')==1
57     x=zeros(length(prS_all),3);
58     x_error=zeros(length(prS_all),3);
59     vS=[nSD/MWD,nSA/MWA,nSB/MWB]; vC=[nCD/MWD,nCA/MWA,nCB/MWB]; vZn=[nZnD/MWD,nZnA/MWA
           ,nZnB/MWB];
60     ossz=[(nSD+nCD+nZnD)/MWD,(nSA+nCA+nZnA)/MWA,(nSB+nCB+nZnB)/MWB];
61     for i=1:length(prS_all)
62         prS=prS_all(i)/(prS_all(i)+prC_all(i)+prZn_all(i)); prC=prC_all(i)/(prS_all(i)
               +prC_all(i)+prZn_all(i)); prZn=prZn_all(i)/(prS_all(i)+prC_all(i)+prZn_all
               (i));
63         xdata=horzcat(vS,vC,vZn,ossz,prS,prC,prZn);
64         fun = @(d,xdata) horzcat(10000.*([xdata(1),xdata(2),xdata(3)]*[d(1);d(2);d(3)
               ]-xdata(13).*[xdata(10),xdata(11),xdata(12)]*[d(1);d(2);d(3)]),...
65                                  10000.*([xdata(4),xdata(5),xdata(6)]*[d(1);d(2);d(3)
                                        ]-xdata(14).*[xdata(10),xdata(11),xdata(12)]*[d
                                        (1);d(2);d(3)]),...
66                                  10000.*([xdata(7),xdata(8),xdata(9)]*[d(1);d(2);d(3)
                                        ]-xdata(15).*[xdata(10),xdata(11),xdata(12)]*[d
                                        (1);d(2);d(3)]),...
67                                  1.*(d(1)+d(2)+d(3)));
68         d0 = [0.55,0.35,0.1]; lb = [0,0,0]; ub = [1,1,1]; ydata=[0,0,0,1];
69         options = optimoptions('lsqcurvefit','Algorithm','trust-region-reflective','
               FunctionTolerance',1e-8,'OptimalityTolerance',1e-9);
70         [d,~,residual,~,~,~,jacobian] = lsqcurvefit(fun,d0,xdata,ydata,lb,ub,options);
71         x(i,:)=d(:)/sum(d(:));
72         ci = nlparci(d,residual,'jacobian',jacobian,'alpha',0.32); % alpha=0.32 means
               1 sigma variance; nlparci gives back d(:)-1sigma and d(:)+1sigma in case
               alpha is 0.32
```

```
        ci2=abs(ci(:,1)-ci(:,2))./2; %ci2 is now 1 sigma
        x_error(i,:)=ci2(:)+abs(d(:).*0.1)+0.01; % Fitting error + 10 % error + 1% in every case
    end
end
end
```

MatLab Code for Material Percentage Calculation for Four Materials

```
function [x,x_error] = XPS_atomic_4materials(nSD,nSA,nSB,nSF, nCD,nCA,nCB,nCF, nZnD, nZnA,nZnB,nZnF, nFmD,nFmA,nFmB,nFmF, prS_all,prC_all,prZn_all,prFm_all, MWD,MWA, MWB,MWF)

    x=zeros(length(prS_all),4); x_error=zeros(length(prS_all),4); %Saving computational time
    vS=[nSD/MWD,nSA/MWA,nSB/MWB,nSF/MWF]; vC=[nCD/MWD,nCA/MWA,nCB/MWB,nCF/MWF]; vZn=[nZnD/MWD,nZnA/MWA,nZnB/MWB,nZnF/MWF]; vFm=[nFmD/MWD,nFmA/MWA,nFmB/MWB,nFmF/MWF];
    ossz=[(nSD+nCD+nZnD+nFmD)/MWD,(nSA+nCA+nZnA+nFmA)/MWA,(nSB+nCB+nZnB+nFmB)/MWB,(nSF+nCF+nZnF+nFmF)/MWF];
    for i=1:length(prS_all)
        prS=prS_all(i)/(prS_all(i)+prC_all(i)+prZn_all(i)+prFm_all(i)); prC=prC_all(i)/(prS_all(i)+prC_all(i)+prZn_all(i)+prFm_all(i)); prZn=prZn_all(i)/(prS_all(i)+prC_all(i)+prZn_all(i)+prFm_all(i)); prFm=prFm_all(i)/(prS_all(i)+prC_all(i)+prZn_all(i)+prFm_all(i));
        xdata=horzcat(vS,vC,vZn,vFm,ossz,prS,prC,prZn,prFm);
        fun = @(d,xdata) horzcat(10000.*([xdata(1),xdata(2),xdata(3),xdata(4)]*[d(1);d(2);d(3);d(4)]-xdata(21).*[xdata(17),xdata(18),xdata(19),xdata(20)]*[d(1);d(2);d(3);d(4)]),...
                                 10000.*([xdata(5),xdata(6),xdata(7),xdata(8)]*[d(1);d(2);d(3);d(4)]-xdata(22).*[xdata(17),xdata(18),xdata(19),xdata(20)]*[d(1);d(2);d(3);d(4)]),...
                                 10000.*([xdata(9),xdata(10),xdata(11),xdata(12)]*[d(1);d(2);d(3);d(4)]-xdata(23).*[xdata(17),xdata(18),xdata(19),xdata(20)]*[d(1);d(2);d(3);d(4)]),...
                                 10000.*([xdata(13),xdata(14),xdata(15),xdata(16)]*[d(1);d(2);d(3);d(4)]-xdata(24).*[xdata(17),xdata(18),xdata(19),xdata(20)]*[d(1);d(2);d(3);d(4)]),...
                                 1.*(d(1)+d(2)+d(3)+d(4)));
        d0 = [0.3,0.3,0.3,0.1]; lb = [0,0,0,0]; ub = [1,1,1,1]; ydata=[0,0,0,1]; % Desired results
        options = optimoptions('lsqcurvefit','Algorithm','trust-region-reflective','FunctionTolerance',1e-8,'OptimalityTolerance',1e-9);
        [d,~,residual,~,~,~,jacobian] = lsqcurvefit(fun,d0,xdata,ydata,lb,ub,options);
        x(i,:)=d(:)/sum(d(:));
        ci = nlparci(d,residual,'jacobian',jacobian,'alpha',0.32); % alpha=0.32 means 1 sigma variance; nlparci gives back d(:)-1sigma and d(:)+1sigma in case alpha is 0.32
        ci2=abs(ci(:,1)-ci(:,2))./2; %ci2 is now 1 sigma
        x_error(i,:)=ci2(:)+abs(d(:).*0.1)+0.01; % Fitting error + 10 % error + 1% in every case
    end
end
```

Automatized HOMO Onset Fitting

```
function [x0,eleje,vege,P] = fitUPS_HOMO(Datab,x,e,v,sensitivity) % Here e and v are given as indexes and not as energy
```

```
    % The higher the sensitivity, the smaller peaks will be already fitted
    SmoothingParameter=0.99;
    Data=normalize_vert(Datab);
    [f,~,~] = fit( x(:), Data(:), 'smoothingspline', 'SmoothingParam',
        SmoothingParameter);
    Data2(:) = f(x(:));
    df=abs(diff(Data2));
    [pks,locs,w,p] = findpeaks(df);
    Eb1=x(1); % Eb is given in eV's
    step=x(2)-x(1);
    if (e==0) && (v==0)
    for i=length(pks):(-1):1
        if (p(i)>(0.0005/sensitivity))
            eleje=floor(locs(i)-w(i)/3);
            vege=ceil(locs(i)+2*w(i)/3);
            break;
        else
            eleje=1; vege=50;
        end
    end
    else
        eleje=e; vege=v;
    end
    P = polyfit(x(eleje:vege),Data(eleje:vege),1);
    x0=-P(2)/P(1);
end
```

Fitting of a BHJ with Individual Spectra for less than 4 Materials

```
function [y,dy,f_D,f_A,f_B] = BHJfit(Time,EnergyD,Energy,Data_D,Data_A,Data_B,Data_BHJ
    ,SmoothingParameter,Min_for_Base,x0_D, x0_A,x_Donor,quenchingP,bS,Dshift,Ashift,
    min_start,max_start,Bshift,x0_B,Dmin,Dmax,Amin,Amax,Bmin,Bmax,shiftD,shiftA,shiftB
    )

% n_A -> Procentage of the Acceptor UPS spectrum in the BHJ
% n_D -> Procentage of the Donor UPS spectrum in the BHJ
% n_B -> Procentage of the Base UPS spectrum in the BHJ
% q_D -> Quenching of the Donor UPS spectrum due to crystallinity of donor polymer
% v_A -> Shift of the Acceptor UPS spectrum w.r.t the original measured kE spectrum
% v_D -> Shift of the Donor UPS spectrum w.r.t the original measured kE spectrum

Data_Dn=normalize_vert(Data_D); Data_An=normalize_vert(Data_A);
Data_Bn=normalize_vert(Data_B); Data_BHJn=normalize_vert(Data_BHJ);

for i=1:length(Time) % To fit for all depths
    % To have the measurement points as continuous functions
    [f_D,~,~] = fit( EnergyD(i,:)', Data_Dn(i,:)', 'smoothingspline', 'SmoothingParam'
        , SmoothingParameter);
    [f_A,~,~] = fit( EnergyD(i,:)', Data_An(i,:)', 'smoothingspline', 'SmoothingParam'
        , SmoothingParameter);
    [f_B,~,~] = fit( EnergyD(i,:)', Data_Bn(i,:)', 'smoothingspline', 'SmoothingParam'
        , SmoothingParameter);

      F = @(x,xdata) x(1)*(f_D(x(6)*(xdata-x_Donor)+x_Donor-x(4))) + x(2)*(f_A(xdata-
          x(5))) + x(3)*(f_B(xdata-x(7)));
      % This is the function, where the parameter are to be estimated
      x0 = [x0_D, x0_A, x0_B, shiftD, shiftA, 1, shiftB]; % Starting parameters
      % If quenching is allowed, the donor spectra can be quenched
      if (quenchingP==1)
          qL=0.8; qU=1.2;
```

```
        else
            qL=0.99999; qU=1.00001;
        end
        % If base shift is allowed, the base spetrum can be also shifted in energy
        if (bS==1)
            bL=shiftB-Bshift; bU=shiftB+Bshift;
        else
            bL=0; bU=0;
        end
        % Testing whether we need to fit the base or not
        if (i>Min_for_Base)
             lb = [Dmin,Amin,Bmin,shiftD-Dshift,shiftA-Ashift,qL,bL];
             ub = [Dmax,Amax,Bmax,shiftD+Dshift,shiftA+Ashift,qU,bU];
        else
             lb = [Dmin,Amin,0,shiftD-Dshift,shiftA-Ashift,qL,bL];
             ub = [Dmax,Amax,0,shiftD+Dshift,shiftA+Ashift,qU,bU];
        end
        % Fitting
        options = optimoptions('lsqcurvefit','FiniteDifferenceType','central');
        [x,~,residual,~,~,~,jacobian] = lsqcurvefit(F,x0,Energy(i,min_start:max_start)
            ',Data_BHJn(i,min_start:max_start)',lb,ub,options);
         dx=zeros(7,1);
         ci = nlparci(x,residual,'jacobian',jacobian,'alpha',0.01);
         dx(:)=abs(ci(:,1)-ci(:,2))./2;
         if (x(2)<0.005)
             x(5)=0;
         end
         y(i,:)=x(:); dy(i,:)=dx(:)+0.05;
end
end
```

Fitting of a BHJ with Individual Spectra for 4 Materials

```
function [y,dy,f_D,f_A,f_B,f_F] = BHJfit_for4(Time,EnergyD,Energy,Data_D,Data_A,Data_B
    ,Data_BHJ,SmoothingParameter,Min_for_Base,x0_D, x0_A,x_Donor,quenchingP,bS,Dshift,
    Ashift,min_start,max_start,Bshift,x0_B,Dmin,Dmax,Amin,Amax,Bmin,Bmax,shiftD,shiftA
    ,shiftB,Data_F,x0_F,shiftF,Fshift,Fmin,Fmax)

% n_A -> Procentage of the Acceptor UPS spectrum in the BHJ
% n_D -> Procentage of the Donor UPS spectrum in the BHJ
% n_B -> Procentage of the Base UPS spectrum in the BHJ
% q_D -> Quenching of the Donor UPS spectrum due to crystallinity of donor polymer
% v_A -> Shift of the Acceptor UPS spectrum w.r.t the original measured kE spectrum
% v_D -> Shift of the Donor UPS spectrum w.r.t the original measured kE spectrum

Data_Dn=normalize_vert(Data_D); Data_An=normalize_vert(Data_A);
Data_Bn=normalize_vert(Data_B); Data_Fn=normalize_vert(Data_F);
Data_BHJn=normalize_vert(Data_BHJ);

for i=1:length(Time) % To fit for all depths
    % To have the measurement points as continuous functions
    [f_D,~,~] = fit( EnergyD(i,:)', Data_Dn(i,:)', 'smoothingspline', 'SmoothingParam'
        , SmoothingParameter);
    [f_A,~,~] = fit( EnergyD(i,:)', Data_An(i,:)', 'smoothingspline', 'SmoothingParam'
        , SmoothingParameter);
    [f_B,~,~] = fit( EnergyD(i,:)', Data_Bn(i,:)', 'smoothingspline', 'SmoothingParam'
        , SmoothingParameter);
    [f_F,~,~] = fit( EnergyD(i,:)', Data_Fn(i,:)', 'smoothingspline', 'SmoothingParam'
        , SmoothingParameter);

```

```
21          F = @(x,xdata) x(1)*(f_D(x(6)*(xdata-x_Donor)+x_Donor-x(4))) + x(2)*(f_A(xdata-
                x(5))) + x(3)*(f_B(xdata-x(7))) + x(8)*(f_F(xdata-x(9)));
22          % This is the function, where the parameter are to be estimated
23          x0 = [x0_D, x0_A, x0_B, shiftD, shiftA, 1, shiftB, x0_F, shiftF]; % Starting
                parameters
24          % If quenching is allowed, the donor spectra can be quenched
25          if (quenchingP==1)
26              qL=0.8; qU=1.2;
27          else
28              qL=0.99999; qU=1.00001;
29          end
30          % If base shift is allowed, the base spetrum can be also shifted in
31          % energy
32          if (bS==1)
33              bL=shiftB-Bshift; bU=shiftB+Bshift;
34          else
35              bL=0; bU=0;
36          end
37          % Testing whether we need to fit the base or not
38          if (i>Min_for_Base)
39                lb = [Dmin,Amin,Bmin,shiftD-Dshift,shiftA-Ashift,qL,bL,Fmin,shiftF-Fshift
                      ];
40                ub = [Dmax,Amax,Bmax,shiftD+Dshift,shiftA+Ashift,qU,bU,Fmax,shiftF+Fshift
                      ];
41          else
42                lb = [Dmin,Amin,0,shiftD-Dshift,shiftA-Ashift,qL,bL,Fmin,shiftF-Fshift];
43                ub = [Dmax,Amax,0,shiftD+Dshift,shiftA+Ashift,qU,bU,Fmax,shiftF+Fshift];
44          end
45          % Fitting
46          options = optimoptions('lsqcurvefit','FiniteDifferenceType','central');
47          [x,~,residual,~,~,~,jacobian] = lsqcurvefit(F,x0,Energy(i,min_start:max_start)
                ',Data_BHJn(i,min_start:max_start)',lb,ub,options);
48           dx=zeros(9,1);
49           ci = nlparci(x,residual,'jacobian',jacobian,'alpha',0.01);
50           dx(:)=abs(ci(:,1)-ci(:,2))./2;
51           if (x(2)<0.005)
52               x(5)=0;
53           end
54           y(i,:)=x(:); dy(i,:)=dx(:)+0.05;
55  end
56  end
```

MatLab Code for UPS Depth Profile Material Percentage Re-Scaling

```
1   function [rat_D,rat_A,rat_B,rat_F] = rescaling(Time, Data, PlateauValue,D, A, F,
        NumberOfMaterials)
2
3   szam=size(Data(1,:)); sz=szam(2)/2; const1=length(Time);
4   k=PlateauValue; err=0; err2=0;
5
6   if k<length(Data(:,1))
7       const3=length(Data(:,1));
8       if (D.*A.*F==0)
9           msgbox('Please choose a data point, where all 3 materials are present, OR fit
                with two materials only.'); err=1;
10      else
11          if NumberOfMaterials<4
12              DAF=D/(D+A); DAF2=A/(D+A);
13          elseif NumberOfMaterials==4
14              DAF=D/(D+A+F); DAF2=A/(D+A+F); DAF3=F/(D+A+F);
```

```
15            dK=Data(k,1)./DAF; aK=Data(k,2)./DAF2; szorzo=dK*aK;
16        end
17        if NumberOfMaterials==3
18            bK=0.1*max(Data(:,3));
19            if bK==0
20                err2=1;
21            end
22        elseif NumberOfMaterials==4
23            bK=0.1*max(Data(:,3));
24            if bK==0
25                err2=1;
26            end
27            fK=Data(k,8)./DAF3; szorzo=szorzo*fK;
28        end
29        if szorzo==0
30            msgbox('Please choose a data point, where all materials are present!'); err
                  =1;
31        end
32     end
33    if err==0
34      rD=zeros(1,length(Data(:,1))); rA=zeros(1,length(Data(:,1))); drD=zeros(1,length(
            Data(:,1))); drA=zeros(1,length(Data(:,1)));
35      rB=zeros(1,length(Data(:,1))); rF=zeros(1,length(Data(:,1))); drB=zeros(1,length(
            Data(:,1))); drF=zeros(1,length(Data(:,1)));
36      rat_D=zeros(1,length(Data(:,1))); rat_A=zeros(1,length(Data(:,1))); drat_D=zeros
            (1,length(Data(:,1))); drat_A=zeros(1,length(Data(:,1)));
37      rat_B=zeros(1,length(Data(:,1))); rat_F=zeros(1,length(Data(:,1))); drat_B=zeros
            (1,length(Data(:,1))); drat_F=zeros(1,length(Data(:,1)));
38      for i=1:length(Data(:,1))
39        rD(i)=Data(i,1)./dK; rA(i)=Data(i,2)./aK; osszeg=rD(i)+rA(i);
40        drD(i)=rD(i)*sqrt((Data(i,sz+1)./Data(i,1)).^2+0.1.^2);
41        drA(i)=rA(i)*sqrt((Data(i,sz+2)./Data(i,2)).^2+0.1.^2);
42        if NumberOfMaterials==3
43          if err2==0
44            rB(i)=Data(i,3)./bK; drB(i)=rB(i)*sqrt((Data(i,sz+3)./Data(i,3)).^2+0.1.^2)
                  ;
45          else
46            rB(i)=Data(i,3); drB(i)=rB(i)*sqrt((Data(i,sz+3)./Data(i,3)).^2+0.1.^2);
47          end
48          osszeg=osszeg+rB(i);
49        elseif NumberOfMaterials==4
50          if err2==0
51            rB(i)=Data(i,3)./bK; drB(i)=rB(i)*sqrt((Data(i,sz+3)./Data(i,3)).^2+0.1.^2)
                  ;
52          else
53            rB(i)=Data(i,3); drB(i)=rB(i)*sqrt((Data(i,sz+3)./Data(i,3)).^2+0.1.^2);
54          end
55          rF(i)=Data(i,8)./fK; osszeg=osszeg+rB(i)+rF(i); drF(i)=rF(i)*sqrt((Data(i,sz
                +8)./Data(i,8)).^2+0.1.^2);
56        end
57        rat_D(i)=rD(i)/osszeg; rat_A(i)=rA(i)/osszeg; drat_D(i)=drD(i)/osszeg; drat_A(i
              )=drA(i)/osszeg;
58        if NumberOfMaterials==3
59          rat_B(i)=rB(i)/osszeg; drat_B(i)=drB(i)/osszeg;
60        elseif NumberOfMaterials==4
61          rat_B(i)=rB(i)/osszeg; drat_B(i)=drB(i)/osszeg; rat_F(i)=rF(i)/osszeg; drat_F
                (i)=drF(i)/osszeg;
62        end
63      end
64    end
```

```
65 else
66     msgbox('Please choose a plateau, which is within the measured data range.');
67 end
```

B | Supplementary Figures

Supplementary Figures for Chapter 6

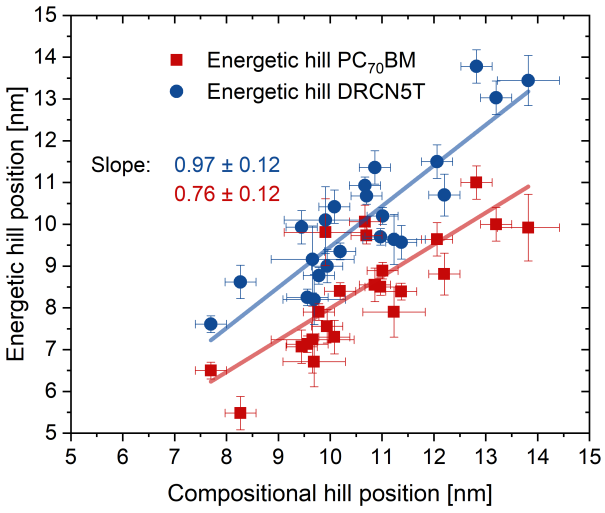

Figure B.1: Energetic peak position as a function of the compositional peak, e.g. the regions with the maximal p-doping effect and the fullerene rich inversion layer, for DRCN5T (blue) as well as $PC_{70}BM$ (red). Linear fits are included in corresponding colours.

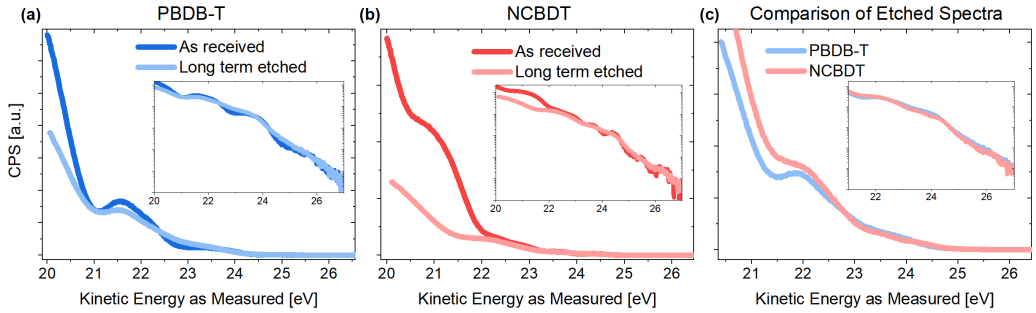

Figure B.2: UPS measurements of **(a)** PBDB-T and **(b)** NCBDT for fresh (as received) and etched (500 s with a 4 keV kinetic energy cluster source) in dark and light colours, respectively. **(c)** Comparison of the etched UPS spectra showing great similarities between the two.

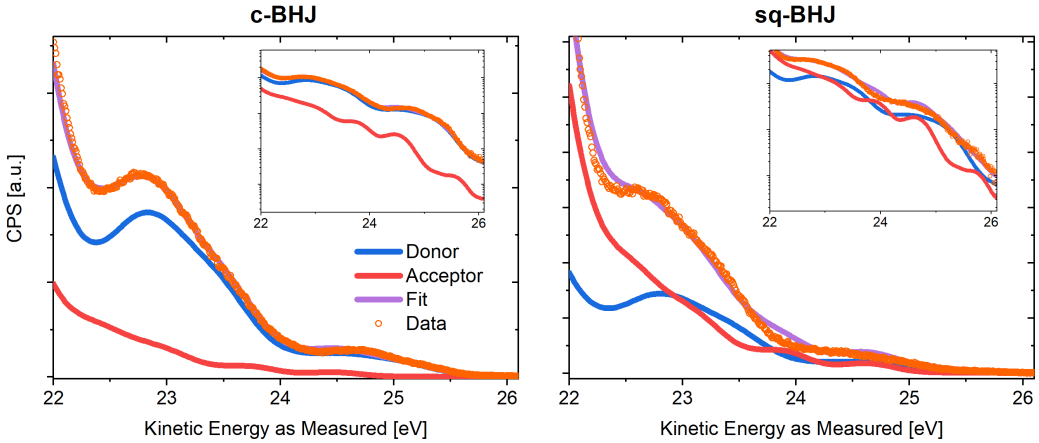

Figure B.3: Top surface UPS measurements for a c-BHJ (left) and an sq-BHJ (right) blend denoted with orange circles and corresponding fits with as received donor and acceptor UPS spectra. Resulting donor and acceptor contributions are denoted with blue and red colours, while their sum, the overall fit, is shown as a purple line.

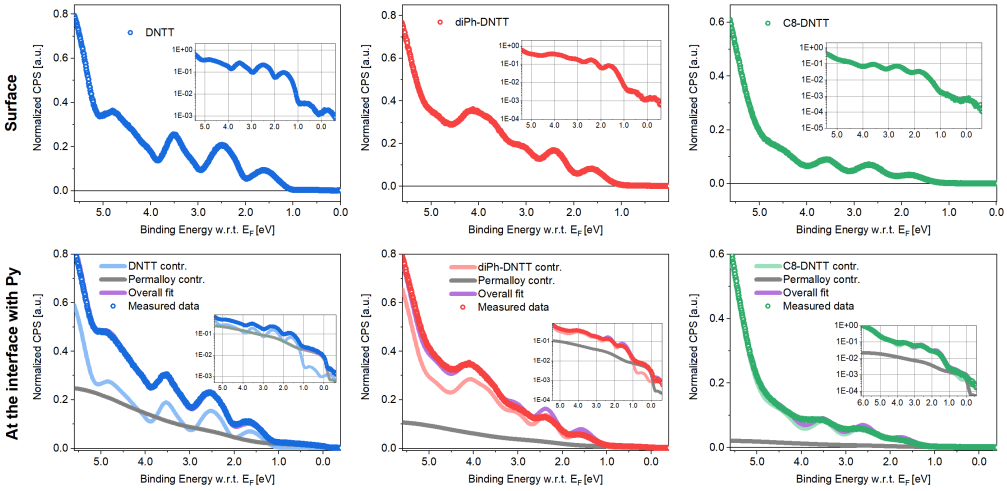

Figure B.4: Fitted UPS spectra with the individual DNTT derivative component (from left to the right: DNTT, diPh-DNTT and C8-DNTT) at the surface (top) and at the interface with permalloy (bottom). Logarithmic scale representations are included in the insets.

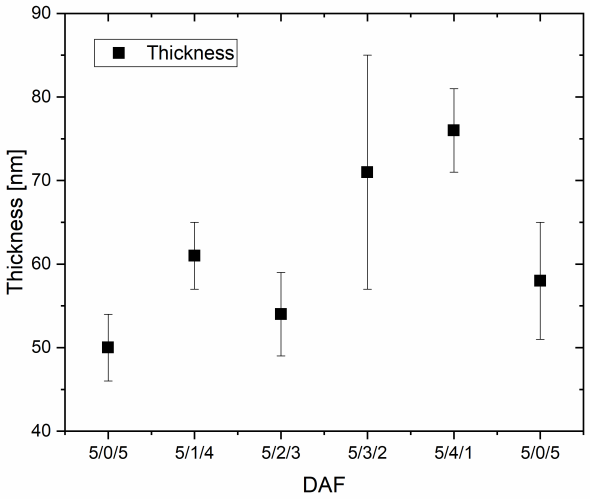

Figure B.5: Thickness measurements for PBDB-T-2Cl (D) / ITIC-2F (A) / $PC_{70}BM$ (F) ternary blends with varying D/A/F ratio. Measured by Julian Frigyes Butcher.

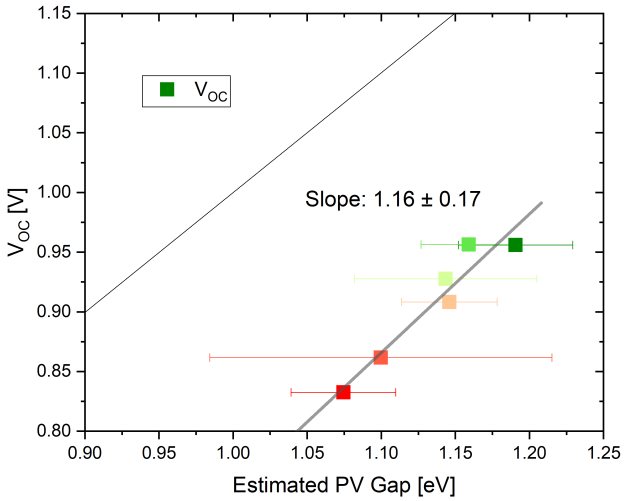

Figure B.6: Device V_{OC} plotted as a function of the smaller estimated PV gap value for a PBDB-T-2Cl:ITIC-2F:$PC_{70}BM$ ternary system with varying ITIC-2F:$PC_{70}BM$ ratio (With the same colour code as in **Fig. 6.9**). PV gap values were averaged over the entire measured active layer. A think black line represents the case where V_{OC} is equal to the estimated PV gap.

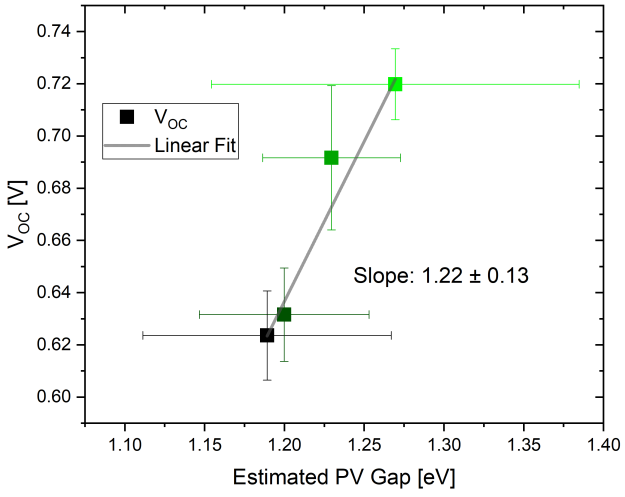

Figure B.7: Device V_{OC} plotted as a function of the smaller estimated PV gap value for a PTB7:$PC_{70}BM$:ICBA ternary system with varying $PC_{70}BM$:ICBA ratio (With the same colour code as in **Fig. 6.11**). PV gap values were averaged over the entire measured active layer.

Bibliography

[1] Peter Hoffmann. *Tomorrow's Energy: Hydrogen, Fuel Cells, and the Prospects for a Cleaner Planet*. MIT Press, Cambridge, Massachusetts, 2012. ISBN 9780262516952.

[2] Earth System Research Laboratory. Trends in Atmospheric Carbon Dioxide, 2019. URL https://www.esrl.noaa.gov/gmd/ccgg/trends/full.html.

[3] NASA. GISS Surface Temperature Analysis, 2019. URL https://data.giss.nasa.gov/gistemp/graphs/.

[4] United Nations Climate Change. The Paris Agreement, 2015. URL https://unfccc.int/process-and-meetings/the-paris-agreement/the-paris-agreement.

[5] Fraunhofer Institute for Solar Energy Systems ISE. Net public electricity generation in Germany, 2019. URL https://www.energy-charts.de/energy.htm?source=all-sources&period=annual&year=all.

[6] BP. Statistical Review of World Energy (68th edition), 2019. URL https://www.bp.com/content/dam/bp/business-sites/en/global/corporate/pdfs/energy-economics/statistical-review/bp-stats-review-2019-electricity.pdf.

[7] United Nations Framework Convention on Climate Change. World Energy System Not On Track to Meet Paris Agreement Goals, 2019. URL https://unfccc.int/news/world-energy-system-not-on-track-to-meet-paris-agreement-goals.

[8] Seth B. Darling and Fengqi You. The case for organic photovoltaics. *RSC Adv.*, 3(39):17633, sep 2013. ISSN 2046-2069. doi: 10.1039/c3ra42989j. URL http://xlink.rsc.org/?DOI=c3ra42989j.

[9] Solar Power Europe. Global Market Outlook For Solar Power / 2018 - 2022, 2018. URL http://www.solarpowereurope.org/wp-content/uploads/2018/09/Global-Market-Outlook-2018-2022.pdf.

[10] International Renewable Energy Agency. Global Energy Transformation, 2018. URL https://www.irena.org/-/media/Files/IRENA/Agency/Publication/2018/Apr/IRENA_Report_GET_2018.pdf.

[11] Naveen Kumar Elumalai and Ashraf Uddin. Open circuit voltage of organic solar cells: an in-depth review. *Energy Environ. Sci.*, 9(2):391–410, 2016. ISSN 1754-5692. doi: 10.1039/C5EE02871J. URL http://xlink.rsc.org/?DOI=C5EE02871J.

[12] Yong Cui, Huifeng Yao, Jianqi Zhang, Tao Zhang, Yuming Wang, Ling Hong, Kaihu Xian, Bowei Xu, Shaoqing Zhang, Jing Peng, Zhixiang Wei, Feng Gao, and Jianhui Hou. Over 16chlorinated acceptor with increased open-circuit voltages. *Nat. Commun.*, 10(1):2515, dec 2019. ISSN 2041-1723. doi: 10.1038/s41467-019-10351-5. URL https://doi.org/10.1038/s41467-019-10351-5http://www.nature.com/articles/s41467-019-10351-5.

[13] National Renewable Energy Laboratory. Best Research-Cell Efficiency Chart, 2019. URL https://www.nrel.gov/pv/cell-efficiency.html.

[14] Christopher M. Proctor, Martijn Kuik, and Thuc Quyen Nguyen. Charge carrier recombination in organic solar cells. *Prog. Polym. Sci.*, 38(12):1941–1960, 2013. ISSN 00796700. doi: 10.1016/j.progpolymsci.2013.08.008. URL http://dx.doi.org/10.1016/j.progpolymsci.2013.08.008.

[15] Cenqi Yan, Stephen Barlow, Zhaohui Wang, He Yan, Alex K.-Y. Jen, Seth R. Marder, and Xiaowei Zhan. Non-fullerene acceptors for organic solar cells. *Nat. Rev. Mater.*, 3(3):18003, feb 2018. ISSN 2058-8437. doi: 10.1038/natrevmats.2018.3. URL http://www.nature.com/articles/natrevmats20183.

[16] Xiaoyan Du, Thomas Heumueller, Wolfgang Gruber, Andrej Classen, Tobias Unruh, Ning Li, and Christoph J. Brabec. Efficient Polymer Solar Cells Based on Non-fullerene Acceptors with Potential Device Lifetime Approaching 10 Years. *Joule*, 3(1):215–226, 2019. ISSN 25424351. doi: 10.1016/j.joule.2018.09.001. URL https://doi.org/10.1016/j.joule.2018.09.001.

[17] Yun Liu, Lijian Zuo, Xueliang Shi, Alex K.-Y. Jen, and David S Ginger. Unexpectedly Slow Yet Efficient Picosecond to Nanosecond Photoinduced Hole-Transfer Occurs in a Polymer/Nonfullerene Acceptor Organic Photovoltaic Blend. *ACS Energy Lett.*, 3(10):2396–2403, oct 2018. ISSN 2380-8195. doi: 10.1021/acsenergylett.8b01416. URL https://pubs.acs.org/doi/10.1021/acsenergylett.8b01416.http://pubs.acs.org/doi/10.1021/acsenergylett.8b01416.

[18] Pei Cheng, Gang Li, Xiaowei Zhan, and Yang Yang. Next-generation organic photovoltaics based on non-fullerene acceptors. *Nat. Photonics*, 12(3):131–142, mar 2018. ISSN 1749-4885. doi: 10.1038/s41566-018-0104-9. URL http://www.nature.com/articles/s41566-018-0104-9.

[19] Yuze Lin and Xiaowei Zhan. Non-fullerene acceptors for organic photovoltaics: an emerging horizon. *Mater. Horizons*, 1(5):470–488, 2014. ISSN 2051-6347. doi: 10.1039/c4mh00042k. URL http://xlink.rsc.org/?DOI=c4mh00042k.

[20] Vincent Lami, David Leibold, Paul Fassl, Yvonne J Hofstetter, David Becker-Koch, Philipp Biegger, Fabian Paulus, Paul E Hopkinson, Michael Adams, Uwe H F Bunz, Sven Huettner, Ian Howard, Artem A Bakulin, and Yana Vaynzof. N -Heteroacenes as a New Class of Non-Fullerene Electron Acceptors for Organic Bulk-Heterojunction Photovoltaic Devices. *Sol. RRL*, 1(6):1700053, jun 2017. ISSN 2367198X. doi: 10.1002/solr.201700053. URL http://doi.wiley.com/10.1002/solr.201700053.

[21] Andreas Distler, Tobias Sauermann, Hans-Joachim Egelhaaf, Sheila Rodman, Dave Waller, Kap-Soo Cheon, Mike Lee, and Dirk M. Guldi. The Effect of PCBM Dimerization on the Performance of Bulk Heterojunction Solar Cells. *Adv. Energy Mater.*, 4(1):1300693, jan 2014. ISSN 16146832. doi: 10.1002/aenm.201300693. URL http://doi.wiley.com/10.1002/aenm.201300693.

[22] Yuze Lin, Jiayu Wang, Zhi-Guo Zhang, Huitao Bai, Yongfang Li, Daoben Zhu, and Xiaowei Zhan. An Electron Acceptor Challenging Fullerenes for Efficient Polymer Solar Cells. *Adv. Mater.*, 27(7):1170–1174, feb 2015. ISSN 09359648. doi: 10.1002/adma.201404317. URL http://doi.wiley.com/10.1002/adma.201404317.

[23] Guangrui He, Zhi Li, Xiangjian Wan, Jiaoyan Zhou, Guankui Long, Shuzhong Zhang, Mingtao Zhang, and Yongsheng Chen. Efficient small molecule bulk heterojunction solar cells with high fill factors via introduction of π-stacking moieties as end group. *J. Mater. Chem. A*, 1(5):1801–1809, jan 2013. ISSN 2050-7488. doi: 10.1039/C2TA00496H. URL http://xlink.rsc.org/?DOI=C2TA00496H.

[24] Yong Zhang, Jingyu Zou, Hin-Lap Yip, Kung-Shih Chen, David F. Zeigler, Ying Sun, and Alex K.-Y. Jen. Indacenodithiophene and Quinoxaline-Based Conjugated Polymers for Highly Efficient Polymer Solar Cells. *Chem. Mater.*, 23 (9):2289–2291, may 2011. ISSN 0897-4756. doi: 10.1021/cm200316s. URL https://pubs.acs.org/doi/10.1021/cm200316s.

[25] Christian B Nielsen, Sarah Holliday, Hung-yang Chen, Samuel J Cryer, and Iain McCulloch. Non-Fullerene Electron Acceptors for Use in Organic Solar Cells. *Acc. Chem. Res.*, 48(11):2803–2812, nov 2015. ISSN 0001-4842. doi: 10.1021/acs.accounts.5b00199. URL http://pubs.acs.org/doi/10.1021/acs.accounts.5b00199.

[26] Ruifa Jin, Fengxin Wang, Ruijie Guan, Xiaomin Zheng, and Tao Zhang. Design of perylene-diimides-based small-molecules semiconductors for organic solar cells. *Mol. Phys.*, 115(14):1591–1597, jul 2017. ISSN 0026-8976. doi: 10.1080/00268976.2017.1308028. URL https://www.tandfonline.com/doi/full/10.1080/00268976.2017.1308028.

[27] Feng Liu, Zichun Zhou, Cheng Zhang, Jianyun Zhang, Qin Hu, Thomas Vergote, Feng Liu, Thomas P. Russell, and Xiaozhang Zhu. Efficient Semitransparent Solar Cells with High NIR Responsiveness Enabled by a Small-Bandgap Electron

Acceptor. *Adv. Mater.*, 29(21):1606574, jun 2017. ISSN 09359648. doi: 10.1002/adma.201606574. URL http://doi.wiley.com/10.1002/adma.201606574.

[28] J. J. Dittmer, E. A. Marseglia, and R. H. Friend. Electron Trapping in Dye/Polymer Blend Photovoltaic Cells. *Adv. Mater.*, 12(17):1270–1274, sep 2000. ISSN 0935-9648. doi: 10.1002/1521-4095(200009)12:17<1270::AID-ADMA1270>3.0.CO;2-8. URL http://doi.wiley.com/10.1002/1521-4095%28200009%2912%3A17%3C1270%3A%3AAID-ADMA1270%3E3.0.CO%3B2-8.

[29] Isao Yamada, Jiro Matsuo, Noriaki Toyoda, and Allen Kirkpatrick. Materials processing by gas cluster ion beams. *Mater. Sci. Eng. R*, 34:231–295, 2001. URL https://www.sciencedirect.com/science/article/pii/S0168583X07001085.

[30] Jiro Matsuo, Chihiro Okubo, Toshio Seki, Takaaki Aoki, Noriaki Toyoda, and Isao Yamada. A new secondary ion mass spectrometry (SIMS) system with high-intensity cluster ion source. *Nucl. Instruments Methods Phys. Res. Sect. B Beam Interact. with Mater. Atoms*, 219-220:463–467, jun 2004. ISSN 0168-583X. doi: 10.1016/J.NIMB.2004.01.103. URL http://www.sciencedirect.com/science/article/pii/S0168583X04001314.

[31] Isao Yamada. Cluster ion beam process technology – 20 years of R&D history. *Nucl. Instruments Methods Phys. Res. B*, 257:632–638, 2007. doi: 10.1016/j.nimb.2007.01.124. URL www.elsevier.com/locate/nimb.

[32] Noriaki Toyoda and Isao Yamada. Gas Cluster Ion Beam Equipment and Applications for Surface Processing. *IEEE Trans. Plasma Sci.*, 36(4):1471–1488, aug 2008. ISSN 0093-3813. doi: 10.1109/TPS.2008.927266. URL http://ieeexplore.ieee.org/document/4599119/.

[33] I. Yamada, J. Matsuo, N. Toyoda, T. Aoki, and T. Seki. Progress and applications of cluster ion beam technology. *Curr. Opin. Solid State Mater. Sci.*, 19(1):12–18, feb 2015. ISSN 1359-0286. doi: 10.1016/J.COSSMS.2014.11.002. URL https://www.sciencedirect.com/science/article/pii/S1359028614000850.

[34] Vincent Lami, Andreas Weu, Jiangbin Zhang, Yongsheng Chen, Zhuping Fei, Martin Heeney, Richard H. Friend, and Yana Vaynzof. Visualising the Vertical Energetic Landscape in Organic Photovoltaics. *Joule*, 2019. doi: 10.1016/j.joule.2019.06.018. URL https://www.sciencedirect.com/science/article/abs/pii/S2542435119303095.

[35] Deping Qian, Zilong Zheng, Huifeng Yao, Wolfgang Tress, Thomas R Hopper, Shula Chen, Sunsun Li, Jing Liu, Shangshang Chen, Jiangbin Zhang, Xiao-Ke Liu, Bowei Gao, Liangqi Ouyang, Yingzhi Jin, Galia Pozina, Irina A Buyanova, Weimin M Chen, Olle Inganäs, Veaceslav Coropceanu, Jean-Luc Bredas, He Yan, Jianhui Hou, Fengling Zhang, Artem A Bakulin, and Feng Gao. Design rules for minimizing voltage losses in high-efficiency organic solar cells. *Nat. Mater.*, 17(8):703–709, aug 2018. ISSN 1476-1122. doi: 10.1038/s41563-018-0128-z. URL https://doi.org/10.1038/s41563-018-0128-z.

[36] C. J. Brabec, A. Cravino, D. Meissner, N. S. Sariciftci, T. Fromherz, M. T. Rispens, L. Sanchez, and J. C. Hummelen. Origin of the Open Circuit Voltage of Plastic Solar Cells. *Adv. Funct. Mater.*, 11(5):374–380, oct 2001. ISSN 1616-301X. doi: 10.1002/1616-3028(200110)11:5<374::AID-ADFM374>3.0.CO;2-W. URL http://doi.wiley.com/10.1002/1616-3028%28200110%2911%3A5%3C374%3A%3AAID-ADFM374%3E3.0.CO%3B2-W.

[37] Markus C. Scharber, David Mühlbacher, Markus Koppe, Patrick Denk, Christoph Waldauf, Alan J. Heeger, and Christoph J. Brabec. Design rules for donors in bulk-heterojunction solar cells - Towards 10 % energy-conversion efficiency. *Adv. Mater.*, 18(502783):789–794, 2006. ISSN 09359648. doi: 10.1002/adma.200501717. URL https://onlinelibrary.wiley.com/doi/10.1002/adma.200501717.

[38] Dirk Veldman, Stefan C J Meskers, and René A J Janssen. The Energy of Charge-Transfer States in Electron Donor–Acceptor Blends: Insight into the Energy Losses in Organic Solar Cells. *Adv. Funct. Mater.*, 19(12):1939–1948, jun 2009. ISSN 1616-301X. doi: 10.1002/adfm.200900090. URL https://onlinelibrary.wiley.com/doi/abs/10.1002/adfm.200900090.

[39] V. D. Mihailetchi, P. W. M. Blom, J. C. Hummelen, and M. T. Rispens. Cathode dependence of the open-circuit voltage of polymer:fullerene bulk heterojunction solar cells. *J. Appl. Phys.*, 94(10):6849–6854, nov 2003. ISSN 0021-8979. doi: 10.1063/1.1620683. URL http://aip.scitation.org/doi/10.1063/1.1620683.

[40] Vincent Lemaur, Michelle Steel, David Beljonne, Jean-Luc Brédas, and Jérôme Cornil. Photoinduced Charge Generation and Recombination Dynamics in Model Donor/Acceptor Pairs for Organic Solar Cell Applications: A Full Quantum-Chemical Treatment. *J. Am. Chem. Soc.*, 127(16):6077–6086, apr 2005. ISSN 0002-7863. doi: 10.1021/ja042390l. URL https://pubs.acs.org/doi/abs/10.1021/ja042390l.

[41] Gilles Dennler, Markus C. Scharber, and Christoph J. Brabec. Polymer-fullerene bulk-heterojunction solar cells. *Adv. Mater.*, 21(13):1323–1338, 2009. ISSN 09359648. doi: 10.1002/adma.200801283. URL http://doi.wiley.com/10.1002/adma.200801283.

[42] M.C. Scharber and N.S. Sariciftci. Efficiency of bulk-heterojunction organic solar cells. *Prog. Polym. Sci.*, 38(12):1929–1940, dec 2013. ISSN 00796700. doi: 10.1016/j.progpolymsci.2013.05.001. URL http://dx.doi.org/10.1016/j.progpolymsci.2013.05.001.

[43] J. Zhang, M. H. Futscher, V. Lami, F. U. Kosasih, C. Cho, Q. Gu, A. Sadhanala, A. J. Pearson, B. Kan, G. Divitini, X. Wan, D. Credgington, N. C. Greenham, Y. Chen, C. Ducati, B. Ehrler, Y. Vaynzof, R. H. Friend, and A. A. Bakulin. Sequentially Deposited versus Conventional Nonfullerene Organic Solar Cells: Interfacial Trap States, Charge-Transfer States, and Vertical Stratification. in review, 2019.

[44] Himanshu Shekhar, Vincent Lami, Olga Solomeshch, Amos Fenigstein, Leitner Tomer, Lavi Becky, Yana Vaynzof, and Nir Tessler. Doping induced performance enhancement in inverted small molecule organic photodiodes operating below 1V reverse bias - Towards compatibility with CMOS for imaging applications. *Org. Electron.*, 67:1–9, apr 2019. ISSN 15661199. doi: 10.1016/j.orgel.2019.01.002. URL https://www.sciencedirect.com/science/article/pii/S1566119919300023.

[45] A. Wittmann, G. Schweicher, K. Broch, J. Novak, V. Lami, Y. Vaynzof, E. McNellis, J. Sinova, K. Takimiya, S. Watanabe, J. Takeya, and H. Sirringhaus. Tuning Spin Current Injection at Ferromagnet/Non-Magnet Interfaces by Molecular Design. in review, 2019.

[46] Juan Bisquert. *The Physics of Solar Cells*. CRC Press, 2018. ISBN 9781138305243.

[47] W. Shockley. The Theory of p-n Junctions in Semiconductors and p-n Junction Transistors. *Bell Syst. Tech. J.*, 28(3):435–489, jul 1949. ISSN 00058580. doi: 10.1002/j.1538-7305.1949.tb03645.x. URL http://ieeexplore.ieee.org/lpdocs/epic03/wrapper.htm?arnumber=6773080.

[48] Peter Würfel and Uli Würfel. *Physics of Solar Cells: From Basic Principles to Advanced Concepts*. Wiley-VCH Verlag GmbH & Co., Weinheim, 3rd editio edition, 2016. ISBN 978-3-527-41312-6.

[49] W J Potscavage, S Yoo, and B Kippelen. Origin of the open-circuit voltage in multilayer heterojunction organic solar cells. *Appl. Phys. Lett.*, 93(19):193308, nov 2008. ISSN 0003-6951. doi: 10.1063/1.3027061. URL https://aip.scitation.org/doi/pdf/10.1063/1.3027061?class=pdf.

[50] David Leibold. *New Acceptor Molecules for Bulk Heterojunction Organic Solar Cells (M. Sc. Thesis) Heidelberg University*. 2017.

[51] ASTM Reference Spectra. URL http://rredc.nrel.gov/solar/spectra/am1.5/ASTMG173/ASTMG173.html.

[52] William Shockley and Hans J. Queisser. Detailed Balance Limit of Efficiency of p-n Junction Solar Cells. *J. Appl. Phys.*, 32(3):510, jun 1961. ISSN 00218979. doi: 10.1063/1.1736034. URL http://scitation.aip.org/content/aip/journal/jap/32/3/10.1063/1.1736034.

[53] Robert T. Ross. Thermodynamic Limitations on the Conversion of Radiant Energy into Work. *J. Chem. Phys.*, 45(1):1–7, jul 1966. ISSN 0021-9606. doi: 10.1063/1.1727289. URL http://aip.scitation.org/doi/10.1063/1.1727289.

[54] Mary D. Archer and James R. Bolton. Requirements for ideal performance of photochemical and photovoltaic solar energy converters. *J. Phys. Chem.*, 94(21):8028–8036, oct 1990. ISSN 0022-3654. doi: 10.1021/j100384a011. URL http://pubs.acs.org/doi/abs/10.1021/j100384a011.

[55] T. Markvart and P.T. Landsberg. Thermodynamics and reciprocity of solar energy conversion. *Phys. E Low-dimensional Syst. Nanostructures*, 14(1-2):71–77, apr 2002. ISSN 13869477. doi: 10.1016/S1386-9477(02)00352-1. URL https://www.sciencedirect.com/science/article/pii/S1386947702003521.

[56] W. Ruppel and P. Wurfel. Upper limit for the conversion of solar energy. *IEEE Trans. Electron Devices*, 27(4):877–882, apr 1980. ISSN 0018-9383. doi: 10.1109/T-ED.1980.19950. URL http://ieeexplore.ieee.org/document/1480743/.

[57] Martin A. Green, Jianhua Zhao, Aihua Wang, Peter J. Reece, and Michael Gal. Efficient silicon light-emitting diodes. *Nature*, 412(6849):805–808, aug 2001. ISSN 0028-0836. doi: 10.1038/35090539. URL http://www.nature.com/articles/35090539.

[58] Martin A. Green. Radiative efficiency of state-of-the-art photovoltaic cells. *Prog. Photovolt Res. Appl.*, 20:472–476, 2012. ISSN 10627995. doi: 10.1002/pip. URL http://dx.doi.org/10.1002/pip.1160.

[59] Carsten Deibel and Vladimir Dyakonov. Polymer–fullerene bulk heterojunction solar cells. *Reports Prog. Phys.*, 73(9):096401, sep 2010. ISSN 0034-4885. doi: 10.1088/0034-4885/73/9/096401. URL http://stacks.iop.org/0034-4885/73/i=9/a=096401?key=crossref.69cccd41d2f369f354d75f5beb6c4812.

[60] Song Chen, Sai Wing Tsang, Tzung Han Lai, John R. Reynolds, and Franky So. Dielectric effect on the photovoltage loss in organic photovoltaic cells. *Adv. Mater.*, 26(35):6125–6131, 2014. ISSN 15214095. doi: 10.1002/adma.201401987. URL http://doi.wiley.com/10.1002/adma.201400431.

[61] Michael P. Hughes, Katie D. Rosenthal, Niva A. Ran, Martin Seifrid, Guillermo C. Bazan, and Thuc-Quyen Nguyen. Determining the Dielectric Constants of Organic Photovoltaic Materials Using Impedance Spectroscopy. *Adv. Funct. Mater.*, 28(32):1801542, aug 2018. ISSN 1616301X. doi: 10.1002/adfm.201801542. URL http://doi.wiley.com/10.1002/adfm.201801542.

[62] David R. Lide. *Handbook of Chemistry ans Physics 84th Edition*. CRC Press LLC, 2004. URL http://doi.wiley.com/10.1002/adfm.201801542.

[63] Namchul Cho, Cody W. Schlenker, Kristina M. Knesting, Patrick Koelsch, Hin-Lap Yip, David S. Ginger, and Alex K.Y. Jen. High-Dielectric Constant Side-Chain Polymers Show Reduced Non-Geminate Recombination in Heterojunction Solar Cells. *Adv. Energy Mater.*, 4(10):1301857, jul 2014. ISSN 16146832. doi: 10.1002/aenm.201301857. URL http://doi.wiley.com/10.1002/aenm.201301857.

[64] Viktor V. Brus, Christopher M. Proctor, Niva A. Ran, and Thuc-Quyen Nguyen. Capacitance Spectroscopy for Quantifying Recombination Losses in Non-fullerene Small-Molecule Bulk Heterojunction Solar Cells. *Adv. Energy Mater.*,

6(11):1502250, jun 2016. ISSN 16146832. doi: 10.1002/aenm.201502250. URL http://doi.wiley.com/10.1002/aenm.201502250.

[65] Samuel D. Collins, Christopher M. Proctor, Niva A. Ran, and Thuc-Quyen Nguyen. Understanding Open-Circuit Voltage Loss through the Density of States in Organic Bulk Heterojunction Solar Cells. *Adv. Energy Mater.*, 6(4): 1501721, feb 2016. ISSN 16146832. doi: 10.1002/aenm.201501721. URL http://doi.wiley.com/10.1002/aenm.201501721.

[66] Guglielmo Lanzani. *The Photophysics behind Photovoltaics and Photonics*. John Wiley & Sons, 2012. ISBN 978-3-527-41054-5.

[67] M. Hoffmann, K. Schmidt, T. Fritz, T. Hasche, V.M. Agranovich, and K. Leo. The lowest energy Frenkel and charge-transfer excitons in quasi-one-dimensional structures: application to MePTCDI and PTCDA crystals. *Chem. Phys.*, 258(1): 73–96, aug 2000. ISSN 0301-0104. doi: 10.1016/S0301-0104(00)00157-9. URL https://www.sciencedirect.com/science/article/pii/S0301010400001579.

[68] M. Fahlman and W.R. Salaneck. Surfaces and interfaces in polymer-based electronics. *Surf. Sci.*, 500(1-3):904–922, mar 2002. ISSN 00396028. doi: 10.1016/S0039-6028(01)01554-0. URL https://www.sciencedirect.com/science/article/pii/S0039602801015540.

[69] Slawomir Braun, William R. Salaneck, and Mats Fahlman. Energy-Level Alignment at Organic/Metal and Organic/Organic Interfaces. *Adv. Mater.*, 21(14-15):1450–1472, apr 2009. ISSN 09359648. doi: 10.1002/adma.200802893. URL http://doi.wiley.com/10.1002/adma.200802893.

[70] Wolfgang Tress. *Device Physics of Organic Solar Cells*. PhD thesis, Technische Universität Dresden, 2011.

[71] T Koopmans. Über die Zuordnung von Wellenfunktionen und Eigenwerten zu den Einzelnen Elektronen Eines Atoms. *Physica*, 1(1-6):104–113, jan 1934. ISSN 00318914. doi: 10.1016/S0031-8914(34)90011-2. URL https://www.sciencedirect.com/science/article/pii/S0031891434900112.

[72] N S Sariciftci, L Smilowitz, A. J. Heeger, and F Wudl. Photoinduced Electron Transfer from a Conducting Polymer to Buckminsterfullerene. *Science*, 258(5087): 1474–1476, nov 1992. ISSN 0036-8075. doi: 10.1126/science.258.5087.1474. URL http://www.ncbi.nlm.nih.gov/pubmed/17755110.

[73] Steffan Cook, Ruyzi Katoh, and Akihiro Furube. Ultrafast Studies of Charge Generation in PCBM:P3HT Blend Films following Excitation of the Fullerene PCBM. *J. Phys. Chem. C*, 113(6):2547–2552, feb 2009. ISSN 1932-7447. doi: 10.1021/jp8050774. URL https://pubs.acs.org/doi/10.1021/jp8050774.

[74] Vincent Lami. *New acceptor and donor molecules in bulk heterojunction organic solar cells (M. Sc. Thesis) Heidelberg University*. 2016.

[75] Ching W. Tang. Two-layer organic photovoltaic cell. *Appl. Phys. Lett.*, 48(2):183–185, jan 1986. ISSN 0003-6951. doi: 10.1063/1.96937. URL http://link.aip.org/link/APPLAB/v48/i2/p183/s1&Agg=doi.

[76] P. W. M. Blom, V. D. Mihailetchi, L. J. A. Koster, and D. E. Markov. Device Physics of Polymer:Fullerene Bulk Heterojunction Solar Cells. *Adv. Mater.*, 19 (12):1551–1566, jun 2007. ISSN 09359648. doi: 10.1002/adma.200601093. URL http://doi.wiley.com/10.1002/adma.200601093.

[77] G. Yu, J. Gao, J. C. Hummelen, F. Wudl, and A. J. Heeger. Polymer Photovoltaic Cells: Enhanced Efficiencies via a Network of Internal Donor-Acceptor Heterojunctions. *Science*, 270(5243):1789–1791, dec 1995. ISSN 0036-8075. doi: 10.1126/science.270.5243.1789. URL http://www.sciencemag.org/cgi/doi/10.1126/science.270.5243.1789.

[78] J. J. M. Halls, C. A. Walsh, N. C. Greenham, E. A. Marseglia, R. H. Friend, S. C. Moratti, and A. B. Holmes. Efficient photodiodes from interpenetrating polymer networks. *Nature*, 376(6540):498–500, aug 1995. ISSN 0028-0836. doi: 10.1038/376498a0. URL http://www.nature.com/articles/376498a0.

[79] Kevin M. Coakley and Michael D. McGehee. Conjugated Polymer Photovoltaic Cells. *Chem. Mater.*, 16(23):4533–4542, nov 2004. ISSN 0897-4756. doi: 10.1021/cm049654n. URL https://pubs.acs.org/doi/10.1021/cm049654n.

[80] Peter K. Watkins, Alison B. Walker, and Geraldine L B Verschoor. Dynamical Monte Carlo Modelling of Organic Solar Cells: The Dependence of Internal Quantum Efficiency on Morphology. *Nano Lett.*, 5(9):1814–1818, sep 2005. ISSN 1530-6984. doi: 10.1021/nl051098o. URL https://pubs.acs.org/doi/10.1021/nl051098o.

[81] Gregory D Scholes. Long-Range Resonance Energy Transfer in Molecular Systems. *Annu. Rev. Phys. Chem.*, 54(1):57–87, oct 2003. ISSN 0066-426X. doi: 10.1146/annurev.physchem.54.011002.103746. URL http://www.annualreviews.org/doi/10.1146/annurev.physchem.54.011002.103746.

[82] R Koeppe and N S Sariciftci. Photoinduced charge and energy transfer involving fullerene derivatives. *Photochem. Photobiol. Sci.*, 5(12):1122, 2006. ISSN 1474-905X. doi: 10.1039/b612933c. URL www.rsc.org/ppshttp://xlink.rsc.org/?DOI=b612933c.

[83] Wade A. Luhman and Russell J. Holmes. Investigation of Energy Transfer in Organic Photovoltaic Cells and Impact on Exciton Diffusion Length Measurements. *Adv. Funct. Mater.*, 21(4):764–771, feb 2011. ISSN 1616301X. doi: 10.1002/adfm.201001928. URL http://doi.wiley.com/10.1002/adfm.201001928.

[84] U Lemmer, A Ochse, M Deussen, R.F. Mahrt, E.O. Göbel, H Bassler, P Haring Bolivar, G Wegmann, and H Kurz. Energy transfer in molecularly doped conjugated polymers. *Synth. Met.*, 78(3):289–293, apr 1996. ISSN 03796779.

doi: 10.1016/0379-6779(96)80152-4. URL http://linkinghub.elsevier.com/retrieve/pii/0379677996801524.

[85] Vicki Cleave, Goghan Yahioglu, Pierre Le Barny, Richard H. Friend, and Nir Tessler. Harvesting Singlet and Triplet Energy in Polymer LEDs. *Adv. Mater.*, 11(4):285–288, mar 1999. ISSN 0935-9648. doi: 10.1002/(SICI)1521-4095(199903)11:4<285::AID-ADMA285>3.0.CO;2-N. URL http://doi.wiley.com/10.1002/%28SICI%291521-4095%28199903%2911%3A4%3C285%3A%3AAID-ADMA285%3E3.0.CO%3B2-N.

[86] Anna Köhler and H. Bässler. Triplet states in organic semiconductors. *Mater. Sci. Eng. R Reports*, 66(4-6):71–109, nov 2009. ISSN 0927796X. doi: 10.1016/j.mser.2009.09.001. URL https://linkinghub.elsevier.com/retrieve/pii/S0927796X09000886.

[87] D L Dexter. A Theory of Sensitized Luminescence in Solids. *J. Chem. Phys.*, 21 (5):836–850, may 1953. ISSN 0021-9606. doi: 10.1063/1.1699044. URL https://doi.org/10.1063/1.1699044.

[88] Oleksandr V Mikhnenko, Paul W M Blom, and Thuc-Quyen Nguyen. Exciton diffusion in organic semiconductors. *Energy Environ. Sci.*, 8(7):1867–1888, 2015. ISSN 1754-5692. doi: 10.1039/C5EE00925A. URL www.rsc.org/eeshttp://xlink.rsc.org/?DOI=C5EE00925A.

[89] Martin Pope. Electronic Processes in Organic Crystals and Polymers, 1999.

[90] M. Scheidler, U. Lemmer, R. Kersting, S. Karg, W. Riess, B. Cleve, R. F. Mahrt, H. Kurz, H. Bässler, E. O. Göbel, and P. Thomas. Monte Carlo study of picosecond exciton relaxation and dissociation in poly(phenylenevinylene). *Phys. Rev. B*, 54(8):5536–5544, aug 1996. ISSN 0163-1829. doi: 10.1103/PhysRevB.54.5536. URL https://link.aps.org/doi/10.1103/PhysRevB.54.5536.

[91] Alice Ruini, Marilia J. Caldas, Giovanni Bussi, and Elisa Molinari. Solid State Effects on Exciton States and Optical Properties of PPV. *Phys. Rev. Lett.*, 88(20): 206403, may 2002. ISSN 0031-9007. doi: 10.1103/PhysRevLett.88.206403. URL https://link.aps.org/doi/10.1103/PhysRevLett.88.206403.

[92] Jean-Luc Brédas, David Beljonne, Veaceslav Coropceanu, and Jérôme Cornil. Charge-Transfer and Energy-Transfer Processes in π-Conjugated Oligomers and Polymers: A Molecular Picture. *Chem. Rev.*, 104(11):4971–5004, nov 2004. ISSN 0009-2665. doi: 10.1021/cr040084k. URL https://pubs.acs.org/doi/abs/10.1021/cr040084k.

[93] Millicent B. Smith and Josef Michl. Singlet Fission. *Chem. Rev.*, 110(11):6891–6936, nov 2010. ISSN 0009-2665. doi: 10.1021/cr1002613. URL http://pubs.acs.org/doi/abs/10.1021/cr1002613.

[94] Peter Peumans, Aharon Yakimov, and Stephen R. Forrest. Small molecular weight organic thin-film photodetectors and solar cells. *J. Appl. Phys.*, 93(7): 3693–3723, apr 2003. ISSN 0021-8979. doi: 10.1063/1.1534621. URL http://aip.scitation.org/doi/10.1063/1.1534621.

[95] K. Hasharoni, M. Keshavarz-K., A. Sastre, R. González, C. Bellavia-Lund, Y. Greenwald, T. Swager, F. Wudl, and A. J. Heeger. Near IR photoluminescence in mixed films of conjugated polymers and fullerenes. *J. Chem. Phys.*, 107(7):2308–2312, aug 1997. ISSN 0021-9606. doi: 10.1063/1.474607. URL http://aip.scitation.org/doi/10.1063/1.474607.

[96] Maria Antoniemi Loi, Stefano Toffanin, Michele Muccini, Michael Forster, Ulrich Scherf, and Markus Scharber. Charge transfer excitons in bulk heterojunctions of a polyfluorene copolymer and a fullerene derivative. *Adv. Funct. Mater.*, 17 (13):2111–2116, 2007. ISSN 1616301X. doi: 10.1002/adfm.200601098. URL http://doi.wiley.com/10.1002/adfm.200601098.

[97] Koen Vandewal, Abay Gadisa, Wibren D. Oosterbaan, Sabine Bertho, Fateme Banishoeib, Ineke Van Severen, Laurence Lutsen, Thomas J. Cleij, Dirk Vanderzande, and Jean V. Manca. The Relation Between Open-Circuit Voltage and the Onset of Photocurrent Generation by Charge-Transfer Absorption in Polymer : Fullerene Bulk Heterojunction Solar Cells. *Adv. Funct. Mater.*, 18 (14):2064–2070, jul 2008. ISSN 1616301X. doi: 10.1002/adfm.200800056. URL http://doi.wiley.com/10.1002/adfm.200800056.

[98] Christoph J Brabec, Gerald Zerza, Giulio Cerullo, Sandro De Silvestri, Silvia Luzzati, Jan C Hummelen, and Serdar Sariciftci. Tracing photoinduced electron transfer process in conjugated polymer/fullerene bulk heterojunctions in real time. *Chem. Phys. Lett.*, 340(3-4):232–236, jun 2001. ISSN 00092614. doi: 10.1016/S0009-2614(01)00431-6. URL https://linkinghub.elsevier.com/retrieve/pii/S0009261401004316.

[99] Artem A. Bakulin, Jan C. Hummelen, Maxim S. Pshenichnikov, and Paul H. M. van Loosdrecht. Ultrafast Hole-Transfer Dynamics in Polymer/PCBM Bulk Heterojunctions. *Adv. Funct. Mater.*, 20(10):1653–1660, may 2010. ISSN 1616301X. doi: 10.1002/adfm.200902099. URL http://doi.wiley.com/10.1002/adfm.200902099.

[100] Sarah R. Cowan, Natalie Banerji, Wei Lin Leong, and Alan J. Heeger. Charge Formation, Recombination, and Sweep-Out Dynamics in Organic Solar Cells. *Adv. Funct. Mater.*, 22(6):1116–1128, mar 2012. ISSN 1616301X. doi: 10.1002/adfm.201101632. URL http://doi.wiley.com/10.1002/adfm.201101632.

[101] Loren G. Kaake, Jacek J. Jasieniak, Ronald C. Bakus, Gregory C. Welch, Daniel Moses, Guillermo C. Bazan, and Alan J. Heeger. Photoinduced Charge Generation in a Molecular Bulk Heterojunction Material. *J. Am. Chem. Soc.*, 134

(48):19828–19838, dec 2012. ISSN 0002-7863. doi: 10.1021/ja308949m. URL http://pubs.acs.org/doi/10.1021/ja308949m.

[102] Koen Vandewal, Kristofer Tvingstedt, Abay Gadisa, Olle Inganäs, and Jean V Manca. On the origin of the open-circuit voltage of polymer–fullerene solar cells. *Nat. Mater.*, 8(11):904–909, nov 2009. ISSN 1476-1122. doi: 10.1038/nmat2548. URL http://dx.doi.org/10.1038/nmat2548.

[103] Jean-Luc Brédas, Joseph E Norton, Jérôme Cornil, and Veaceslav Coropceanu. Molecular Understanding of Organic Solar Cells: The Challenges. *Acc. Chem. Res.*, 42(11):1691–1699, nov 2009. ISSN 0001-4842. doi: 10.1021/ar900099h. URL https://pubs.acs.org/doi/10.1021/ar900099h.

[104] Carsten Deibel, Thomas Strobel, and Vladimir Dyakonov. Role of the Charge Transfer State in Organic Donor-Acceptor Solar Cells. *Adv. Mater.*, 22(37):4097–4111, aug 2010. ISSN 09359648. doi: 10.1002/adma.201000376. URL http://doi.wiley.com/10.1002/adma.201000376.

[105] Tracey M. Clarke and James R. Durrant. Charge Photogeneration in Organic Solar Cells. *Chem. Rev.*, 110(11):6736–6767, nov 2010. ISSN 0009-2665. doi: 10.1021/cr900271s. URL https://pubs.acs.org/doi/10.1021/cr900271s.

[106] Artem A. Bakulin, Stoichko D. Dimitrov, Akshay Rao, Philip C. Y. Chow, Christian B. Nielsen, Bob C. Schroeder, Iain McCulloch, Huib J. Bakker, James R. Durrant, and Richard H. Friend. Charge-Transfer State Dynamics Following Hole and Electron Transfer in Organic Photovoltaic Devices. *J. Phys. Chem. Lett.*, 4(1):209–215, jan 2013. ISSN 1948-7185. doi: 10.1021/jz301883y. URL http://pubs.acs.org/doi/10.1021/jz301883y.

[107] Eric T. Hoke, Koen Vandewal, Jonathan A. Bartelt, William R. Mateker, Jessica D. Douglas, Rodrigo Noriega, Kenneth R. Graham, Jean M. J. Fréchet, Alberto Salleo, and Michael D. McGehee. Recombination in Polymer:Fullerene Solar Cells with Open-Circuit Voltages Approaching and Exceeding 1.0 V. *Adv. Energy Mater.*, 3(2):220–230, feb 2013. ISSN 16146832. doi: 10.1002/aenm.201200474. URL http://doi.wiley.com/10.1002/aenm.201200474.

[108] Chris Groves. Suppression of geminate charge recombination in organic photovoltaic devices with a cascaded energy heterojunction. *Energy Environ. Sci.*, 6(5):1546, apr 2013. ISSN 1754-5692. doi: 10.1039/c3ee24455e. URL http://xlink.rsc.org/?DOI=c3ee24455e.

[109] Brian A. Gregg. Charged defects in soft semiconductors and their influence on organic photovoltaics. *Soft Matter*, 5(16):2985, aug 2009. ISSN 1744-683X. doi: 10.1039/b905722f. URL http://xlink.rsc.org/?DOI=b905722f.

[110] Brian A. Gregg. Entropy of Charge Separation in Organic Photovoltaic Cells: The Benefit of Higher Dimensionality. *J. Phys. Chem. Lett.*, 2(24):3013–3015, dec

2011. ISSN 1948-7185. doi: 10.1021/jz2012403. URL https://pubs.acs.org/doi/10.1021/jz2012403.

[111] A. A. Bakulin, A. Rao, V. G. Pavelyev, P. H. M. van Loosdrecht, M. S. Pshenichnikov, D. Niedzialek, J. Cornil, D. Beljonne, and R. H. Friend. The Role of Driving Energy and Delocalized States for Charge Separation in Organic Semiconductors. *Science*, 335(6074):1340–1344, mar 2012. ISSN 0036-8075. doi: 10.1126/science.1217745. URL http://www.sciencemag.org/cgi/doi/10.1126/science.1217745.

[112] Askat E. Jailaubekov, Adam P. Willard, John R. Tritsch, Wai-Lun Chan, Na Sai, Raluca Gearba, Loren G. Kaake, Kenrick J. Williams, Kevin Leung, Peter J. Rossky, and X-Y. Zhu. Hot charge-transfer excitons set the time limit for charge separation at donor/acceptor interfaces in organic photovoltaics. *Nat. Mater.*, 12(1):66–73, jan 2013. ISSN 1476-1122. doi: 10.1038/nmat3500. URL http://www.nature.com/articles/nmat3500.

[113] G. Grancini, M. Maiuri, D. Fazzi, A. Petrozza, H-J. Egelhaaf, D. Brida, G. Cerullo, and G. Lanzani. Hot exciton dissociation in polymer solar cells. *Nat. Mater.*, 12 (1):29–33, jan 2013. ISSN 1476-1122. doi: 10.1038/nmat3502. URL http://www.nature.com/articles/nmat3502.

[114] Yi Zhou, Kristofer Tvingstedt, Fengling Zhang, Chunxia Du, Wei-Xin Ni, Mats R. Andersson, and Olle Inganas. Observation of a Charge Transfer State in Low-Bandgap Polymer/Fullerene Blend Systems by Photoluminescence and Electroluminescence Studies. *Adv. Funct. Mater.*, 19(20):3293–3299, oct 2009. ISSN 1616301X. doi: 10.1002/adfm.200900702. URL http://doi.wiley.com/10.1002/adfm.200900702.

[115] Jiye Lee, Koen Vandewal, Shane R. Yost, Matthias E. Bahlke, Ludwig Goris, Marc A. Baldo, Jean V. Manca, and Troy Van Voorhis. Charge Transfer State Versus Hot Exciton Dissociation in Polymer-Fullerene Blended Solar Cells. *J. Am. Chem. Soc.*, 132(34):11878–11880, sep 2010. ISSN 0002-7863. doi: 10.1021/ja1045742. URL https://pubs.acs.org/doi/10.1021/ja1045742.

[116] Tom G. J. van der Hofstad, Daniele Di Nuzzo, Mauricio van den Berg, René A. J. Janssen, and Stefan C. J. Meskers. Influence of Photon Excess Energy on Charge Carrier Dynamics in a Polymer-Fullerene Solar Cell. *Adv. Energy Mater.*, 2(9):1095–1099, sep 2012. ISSN 16146832. doi: 10.1002/aenm.201200030. URL http://doi.wiley.com/10.1002/aenm.201200030.

[117] Koen Vandewal, Steve Albrecht, Eric T Hoke, Kenneth R Graham, Johannes Widmer, Jessica D Douglas, Marcel Schubert, William R Mateker, Jason T Bloking, George F Burkhard, Alan Sellinger, Jean M. J. Fréchet, Aram Amassian, Moritz K Riede, Michael D McGehee, Dieter Neher, and Alberto Salleo. Efficient charge generation by relaxed charge-transfer states at organic interfaces.

Nat. Mater., 13(1):63–68, jan 2014. ISSN 1476-1122. doi: 10.1038/nmat3807. URL http://www.nature.com/articles/nmat3807.

[118] Tao Liu and Alessandro Troisi. What Makes Fullerene Acceptors Special as Electron Acceptors in Organic Solar Cells and How to Replace Them. *Adv. Mater.*, 25(7):1038–1041, feb 2013. ISSN 09359648. doi: 10.1002/adma.201203486. URL http://doi.wiley.com/10.1002/adma.201203486.

[119] Antti Ojala, Andreas Petersen, Andreas Fuchs, Robert Lovrincic, Carl Pölking, Jens Trollmann, Jaehyung Hwang, Christian Lennartz, Helmut Reichelt, Hans Wolfgang Höffken, Annemarie Pucci, Peter Erk, Thomas Kirchartz, and Frank Würthner. Merocyanine/C60 Planar Heterojunction Solar Cells: Effect of Dye Orientation on Exciton Dissociation and Solar Cell Performance. *Adv. Funct. Mater.*, 22(1):86–96, jan 2012. ISSN 1616301X. doi: 10.1002/adfm.201101697. URL http://doi.wiley.com/10.1002/adfm.201101697.

[120] Steve Albrecht, Silvia Janietz, Wolfram Schindler, Johannes Frisch, Jona Kurpiers, Juliane Kniepert, Sahika Inal, Patrick Pingel, Konstantinos Fostiropoulos, Norbert Koch, and Dieter Neher. Fluorinated Copolymer PCPDTBT with Enhanced Open-Circuit Voltage and Reduced Recombination for Highly Efficient Polymer Solar Cells. *J. Am. Chem. Soc.*, 134(36):14932–14944, sep 2012. ISSN 0002-7863. doi: 10.1021/ja305039j. URL http://pubs.acs.org/doi/10.1021/ja305039j.

[121] Yuan Zhang, Jianhua Liu, and Thuc-Quyen Nguyen. Photoresponse of Donor/Acceptor Blends in Organic Transistors: A Tool for Understanding Field-Assisted Charge Separation in Small Molecule Bulk Heterojunction Solar Cells. *ACS Appl. Mater. Interfaces*, 5(7):2347–2353, apr 2013. ISSN 1944-8244. doi: 10.1021/am302833j. URL http://pubs.acs.org/doi/10.1021/am302833j.

[122] David Leibold, Vincent Lami, Yvonne J Hofstetter, David Becker, Andreas Weu, Philipp Biegger, Fabian Paulus, Uwe H F Bunz, Paul E Hopkinson, and Artem A Bakulin. Triptycenyl - phenazino - thiadiazole as acceptor in organic bulk- heterojunction solar cells. *Org. Electron.*, 57(March):285–291, 2018. ISSN 1566-1199. doi: 10.1016/j.orgel.2018.03.001. URL https://doi.org/10.1016/j.orgel.2018.03.001.

[123] Andreas Weu, Thomas R. Hopper, Vincent Lami, Joshua A. Kreß, Artem A. Bakulin, and Yana Vaynzof. Field-Assisted Exciton Dissociation in Highly Efficient PffBT4T-2OD:Fullerene Organic Solar Cells. *Chem. Mater.*, 30(8):2660–2667, apr 2018. ISSN 0897-4756. doi: 10.1021/acs.chemmater.8b00094. URL http://pubs.acs.org/doi/10.1021/acs.chemmater.8b00094.

[124] Girish Lakhwani, Akshay Rao, and Richard H Friend. Bimolecular Recombination in Organic Photovoltaics. *Annu. Rev. Phys. Chem.*, 65(1):557–581, apr 2014. ISSN 0066-426X. doi: 10.1146/annurev-physchem-040513-103615. URL http://www.annualreviews.org/doi/10.1146/annurev-physchem-040513-103615.

[125] P.W.M. Blom and M.J.M. De Jong. Device operation of polymer light-emitting diodes. *Philips J. Res.*, 51(4):479–494, jan 1998. ISSN 01655817. doi: 10.1016/S0165-5817(98)00019-9. URL https://linkinghub.elsevier.com/retrieve/pii/S0165581798000199.

[126] Bright Walker, Arnold B. Tamayo, Xuan-Dung Dang, Peter Zalar, Jung Hwa Seo, Andres Garcia, Mananya Tantiwiwat, and Thuc-Quyen Nguyen. Nanoscale Phase Separation and High Photovoltaic Efficiency in Solution-Processed, Small-Molecule Bulk Heterojunction Solar Cells. *Adv. Funct. Mater.*, 19(19):3063–3069, oct 2009. ISSN 1616301X. doi: 10.1002/adfm.200900832. URL http://doi.wiley.com/10.1002/adfm.200900832.

[127] Carsten Deibel, Alexander Wagenpfahl, and Vladimir Dyakonov. Influence of charge carrier mobility on the performance of organic solar cells. *Phys. status solidi - Rapid Res. Lett.*, 2(4):175–177, jun 2008. ISSN 18626254. doi: 10.1002/pssr.200802110. URL http://doi.wiley.com/10.1002/pssr.200802110.

[128] L. J. A. Koster, V. D. Mihailetchi, and P. W. M. Blom. Bimolecular recombination in polymer/fullerene bulk heterojunction solar cells. *Appl. Phys. Lett.*, 88(5):052104, jan 2006. ISSN 0003-6951. doi: 10.1063/1.2170424. URL http://aip.scitation.org/doi/10.1063/1.2170424.

[129] A. Pivrikas, N. S. Sariciftci, G. Juška, and R. Österbacka. A review of charge transport and recombination in polymer/fullerene organic solar cells. *Prog. Photovoltaics Res. Appl.*, 15(8):677–696, dec 2007. ISSN 10627995. doi: 10.1002/pip.791. URL http://doi.wiley.com/10.1002/pip.791.

[130] C. Deibel, A. Baumann, and V. Dyakonov. Polaron recombination in pristine and annealed bulk heterojunction solar cells. *Appl. Phys. Lett.*, 93(16):163303, oct 2008. ISSN 0003-6951. doi: 10.1063/1.3005593. URL http://aip.scitation.org/doi/10.1063/1.3005593.

[131] A. Baumann, J. Lorrmann, D. Rauh, C. Deibel, and V. Dyakonov. A New Approach for Probing the Mobility and Lifetime of Photogenerated Charge Carriers in Organic Solar Cells Under Real Operating Conditions. *Adv. Mater.*, 24 (32):4381–4386, aug 2012. ISSN 09359648. doi: 10.1002/adma.201200874. URL http://doi.wiley.com/10.1002/adma.201200874.

[132] Ian A. Howard, Ralf Mauer, Michael Meister, and Frederic Laquai. Effect of Morphology on Ultrafast Free Carrier Generation in Polythiophene:Fullerene Organic Solar Cells. *J. Am. Chem. Soc.*, 132(42):14866–14876, oct 2010. ISSN 0002-7863. doi: 10.1021/ja105260d. URL https://pubs.acs.org/doi/10.1021/ja105260d.

[133] C. Deibel, A. Wagenpfahl, and V. Dyakonov. Origin of reduced polaron recombination in organic semiconductor devices. *Phys. Rev. B*, 80(7):075203, aug 2009. ISSN 1098-0121. doi: 10.1103/PhysRevB.80.075203. URL https://link.aps.org/doi/10.1103/PhysRevB.80.075203.

[134] L. J. A. Koster, E. C. P. Smits, V. D. Mihailetchi, and P. W. M. Blom. Device model for the operation of polymer/fullerene bulk heterojunction solar cells. *Phys. Rev. B*, 72(8):085205, aug 2005. ISSN 1098-0121. doi: 10.1103/PhysRevB.72.085205. URL https://link.aps.org/doi/10.1103/PhysRevB.72.085205.

[135] David P. McMahon, David L. Cheung, and Alessandro Troisi. Why Holes and Electrons Separate So Well in Polymer/Fullerene Photovoltaic Cells. *J. Phys. Chem. Lett.*, 2(21):2737–2741, nov 2011. ISSN 1948-7185. doi: 10.1021/jz201325g. URL https://pubs.acs.org/doi/10.1021/jz201325g.

[136] W. Shockley and W. T. Read. Statistics of the Recombinations of Holes and Electrons. *Phys. Rev.*, 87(5):835–842, sep 1952. ISSN 0031-899X. doi: 10.1103/PhysRev.87.835. URL https://link.aps.org/doi/10.1103/PhysRev.87.835.

[137] M. Kuik, L. J. A. Koster, G. A. H. Wetzelaer, and P. W. M. Blom. Trap-Assisted Recombination in Disordered Organic Semiconductors. *Phys. Rev. Lett.*, 107(25): 256805, dec 2011. ISSN 0031-9007. doi: 10.1103/PhysRevLett.107.256805. URL https://link.aps.org/doi/10.1103/PhysRevLett.107.256805.

[138] V I Klimov. Optical Gain and Stimulated Emission in Nanocrystal Quantum Dots. *Science*, 290(5490):314–317, oct 2000. ISSN 00368075. doi: 10.1126/science.290.5490.314. URL http://www.sciencemag.org/cgi/doi/10.1126/science.290.5490.314.

[139] Sarah R. Cowan, Anshuman Roy, and Alan J. Heeger. Recombination in polymer-fullerene bulk heterojunction solar cells. *Phys. Rev. B*, 82(24):245207, dec 2010. ISSN 1098-0121. doi: 10.1103/PhysRevB.82.245207. URL https://link.aps.org/doi/10.1103/PhysRevB.82.245207.

[140] Davide Bartesaghi, Irene del Carmen Pérez, Juliane Kniepert, Steffen Roland, Mathieu Turbiez, Dieter Neher, and L. Jan Anton Koster. Competition between recombination and extraction of free charges determines the fill factor of organic solar cells. *Nat. Commun.*, 6(1):7083, nov 2015. ISSN 2041-1723. doi: 10.1038/ncomms8083. URL http://www.nature.com/articles/ncomms8083.

[141] George F. A. Dibb, Thomas Kirchartz, Dan Credgington, James R. Durrant, and Jenny Nelson. Analysis of the Relationship between Linearity of Corrected Photocurrent and the Order of Recombination in Organic Solar Cells. *J. Phys. Chem. Lett.*, 2(19):2407–2411, oct 2011. ISSN 1948-7185. doi: 10.1021/jz201104d. URL https://pubs.acs.org/doi/10.1021/jz201104d.

[142] L. J. A. Koster, V. D. Mihailetchi, H. Xie, and P. W. M. Blom. Origin of the light intensity dependence of the short-circuit current of polymer/fullerene solar cells. *Appl. Phys. Lett.*, 87(20):203502, nov 2005. ISSN 0003-6951. doi: 10.1063/1.2130396. URL http://aip.scitation.org/doi/10.1063/1.2130396.

[143] A. Rose. *Concepts in photoconductivity and allied problems*. Interscience publishers, 1963.

[144] E. A. Katz, D. Faiman, S. M. Tuladhar, J. M. Kroon, M. M. Wienk, T. Fromherz, F. Padinger, C. J. Brabec, and N. S. Sariciftci. Temperature dependence for the photovoltaic device parameters of polymer-fullerene solar cells under operating conditions. *J. Appl. Phys.*, 90(10):5343–5350, nov 2001. ISSN 0021-8979. doi: 10.1063/1.1412270. URL http://aip.scitation.org/doi/10.1063/1.1412270.

[145] D. Chirvase, Z. Chiguvare, M. Knipper, J. Parisi, V. Dyakonov, and J. C. Hummelen. Temperature dependent characteristics of poly(3 hexylthiophene)-fullerene based heterojunction organic solar cells. *J. Appl. Phys.*, 93(6):3376–3383, mar 2003. ISSN 0021-8979. doi: 10.1063/1.1545162. URL http://aip.scitation.org/doi/10.1063/1.1545162.

[146] Andres Cuevas. The Recombination Parameter J0. *Energy Procedia*, 55:53–62, jan 2014. ISSN 18766102. doi: 10.1016/j.egypro.2014.08.073. URL https://linkinghub.elsevier.com/retrieve/pii/S1876610214012971.

[147] L. J. A. Koster, V. D. Mihailetchi, R. Ramaker, and P. W. M. Blom. Light intensity dependence of open-circuit voltage of polymer:fullerene solar cells. *Appl. Phys. Lett.*, 86(12):123509, mar 2005. ISSN 0003-6951. doi: 10.1063/1.1889240. URL http://aip.scitation.org/doi/10.1063/1.1889240.

[148] D. A. da Silva Filho, E.-G. Kim, and J.-L. Brédas. Transport Properties in the Rubrene Crystal: Electronic Coupling and Vibrational Reorganization Energy. *Adv. Mater.*, 17(8):1072–1076, apr 2005. ISSN 09359648. doi: 10.1002/adma.200401866. URL http://doi.wiley.com/10.1002/adma.200401866.

[149] Norbert Koch, Nobuo Ueno, and Andrew T.S. Wee. The Molecule—Metal Interface: Energy Levels at Molecule – Metal Interfaces. In *Mol. interface*, chapter 8. WI LEY-VCH Verlag GmbH & Co. KGaA, 2013.

[150] Hisao Ishii, Kiyoshi Sugiyama, Eisuke Ito, and Kazuhiko Seki. Energy Level Alignment and Interfacial Electronic Structures at Organic/Metal and Organic/Organic Interfaces. *Adv. Mater.*, 11(8):605–625, jun 1999. ISSN 0935-9648. doi: 10.1002/(SICI)1521-4095(199906)11:8<605::AID-ADMA605>3.0.CO;2-Q. URL http://doi.wiley.com/10.1002/%28SICI%291521-4095%28199906%2911%3A8%3C605%3A%3AAID-ADMA605%3E3.0.CO%3B2-Q.

[151] Kazuhiko Seki, Naoki Hayashi, Hiroshi Oji, Eisuke Ito, Yukio Ouchi, and Hisao Ishii. Electronic structure of organic/metal interfaces. *Thin Solid Films*, 393(1-2):298–303, aug 2001. ISSN 00406090. doi: 10.1016/S0040-6090(01)01094-X. URL https://linkinghub.elsevier.com/retrieve/pii/S004060900101094X.

[152] S. K. M. Jönsson, W. R. Salaneck, and M. Fahlman. X-ray photoelectron spectroscopy study of the metal/polymer contacts involving aluminum and poly(3,4-ethylenedioxythiophene)-poly(styrenesulfonic acid) derivatives. *J. Mater. Res.*, 18(5):1219–1226, may 2003. ISSN 0884-2914. doi: 10.1557/JMR.2003.0167. URL https://www.cambridge.org/core/product/identifier/S0884291400063615/type/journal_article.

[153] M Fahlman, A Crispin, X Crispin, S K M Henze, M P de Jong, W Osikowicz, C Tengstedt, and W R Salaneck. Electronic structure of hybrid interfaces for polymer-based electronics. *J. Phys. Condens. Matter*, 19(18): 183202, may 2007. ISSN 0953-8984. doi: 10.1088/0953-8984/19/18/183202. URL http://stacks.iop.org/0953-8984/19/i=18/a=183202?key=crossref.74a41e2e7b2d9311305d8ed12e2f0683.

[154] Slawomir Braun, Michel P. de Jong, Wojciech Osikowicz, and William R. Salaneck. Influence of the electrode work function on the energy level alignment at organic-organic interfaces. *Appl. Phys. Lett.*, 91(20):202108, nov 2007. ISSN 0003-6951. doi: 10.1063/1.2806938. URL http://aip.scitation.org/doi/10.1063/1.2806938.

[155] Naoki Sato, Kazuhiko Seki, and Hiroo Inokuchi. Polarization energies of organic solids determined by ultraviolet photoelectron spectroscopy. *J. Chem. Soc. Faraday Trans. 2*, 77(9):1621, jan 1981. ISSN 0300-9238. doi: 10.1039/f29817701621. URL http://xlink.rsc.org/?DOI=f29817701621.

[156] I.G. Hill, A. Kahn, Z.G. Soos, and R.A. Pascal, Jr. Charge-separation energy in films of π-conjugated organic molecules. *Chem. Phys. Lett.*, 327(3-4):181–188, sep 2000. ISSN 00092614. doi: 10.1016/S0009-2614(00)00882-4. URL https://linkinghub.elsevier.com/retrieve/pii/S0009261400008824.

[157] E.V. Tsiper, Z.G. Soos, W. Gao, and A. Kahn. Electronic polarization at surfaces and thin films of organic molecular crystals: PTCDA. *Chem. Phys. Lett.*, 360(1-2):47–52, jul 2002. ISSN 00092614. doi: 10.1016/S0009-2614(02)00774-1. URL https://linkinghub.elsevier.com/retrieve/pii/S0009261402007741.

[158] S Krause, M B Casu, A Schöll, and E Umbach. Determination of transport levels of organic semiconductors by UPS and IPS. *New J. Phys.*, 10(8):085001, aug 2008. ISSN 1367-2630. doi: 10.1088/1367-2630/10/8/085001. URL http://stacks.iop.org/1367-2630/10/i=8/a=085001?key=crossref.31d6872606814b3ad0779a3fd06868ec.

[159] Y. Hirose, W. Chen, E. I. Haskal, S. R. Forrest, and A. Kahn. Band lineup at an organic-inorganic semiconductor heterointerface: perylenetetracarboxylic dianhydride/GaAs(100). *Appl. Phys. Lett.*, 64(25):3482–3484, jun 1994. ISSN 0003-6951. doi: 10.1063/1.111247. URL http://aip.scitation.org/doi/10.1063/1.111247.

[160] C.I. Wu, Y. Hirose, H. Sirringhaus, and A. Kahn. Electron-hole interaction energy in the organic molecular semiconductor PTCDA. *Chem. Phys. Lett.*, 272(1-2):43–47, jun 1997. ISSN 00092614. doi: 10.1016/S0009-2614(97)00481-8. URL https://linkinghub.elsevier.com/retrieve/pii/S0009261497004818.

[161] T. Takahashi, S. Suzuki, T. Morikawa, H. Katayama-Yoshida, S. Hasegawa, H. Inokuchi, K. Seki, K. Kikuchi, S. Suzuki, K. Ikemoto, and Y. Achiba. Pseudo-

gap at the Fermi level in K3C60 observed by photoemission and inverse photoemission. *Phys. Rev. Lett.*, 68(8):1232–1235, feb 1992. ISSN 0031-9007. doi: 10.1103/PhysRevLett.68.1232. URL https://link.aps.org/doi/10.1103/PhysRevLett.68.1232.

[162] Winfried Mönch. *Semiconductor Surfaces and Interfaces*, volume 26 of *Springer Series in Surface Sciences*. Springer Berlin Heidelberg, Berlin, Heidelberg, 3rd, rev. edition, 2001. ISBN 978-3-642-08748-6. doi: 10.1007/978-3-662-04459-9. URL http://link.springer.com/10.1007/978-3-662-04459-9.

[163] A WAN, J HWANG, F AMY, and A KAHN. Impact of electrode contamination on the α-NPD/Au hole injection barrier. *Org. Electron.*, 6(1):47–54, feb 2005. ISSN 15661199. doi: 10.1016/j.orgel.2005.02.003. URL https://linkinghub.elsevier.com/retrieve/pii/S1566119905000066.

[164] Annica Crispin, Xavier Crispin, Mats Fahlman, Magnus Berggren, and William R Salaneck. Transition between energy level alignment regimes at a low band gap polymer-electrode interfaces. *Appl. Phys. Lett.*, 89(21):213503, nov 2006. ISSN 0003-6951. doi: 10.1063/1.2396899. URL https://doi.org/10.1063/1.2396899.

[165] G Greczynski, Th Kugler, and W R Salaneck. Energy level alignment in organic-based three-layer structures studied by photoelectron spectroscopy. *J. Appl. Phys.*, 88(12):7187–7191, dec 2000. ISSN 0021-8979. doi: 10.1063/1.1328059. URL https://doi.org/10.1063/1.1328059.

[166] Hyeunseok Cheun, Canek Fuentes-Hernandez, Yinhua Zhou, William J Potscavage, Sung-Jin Kim, Jaewon Shim, Amir Dindar, and Bernard Kippelen. Electrical and Optical Properties of ZnO Processed by Atomic Layer Deposition in Inverted Polymer Solar Cells. *J. Phys. Chem. C*, 114(48):20713–20718, dec 2010. ISSN 1932-7447. doi: 10.1021/jp106641j. URL https://pubs.acs.org/doi/10.1021/jp106641j.

[167] H. Moormann, D. Kohl, and G. Heiland. Work function and band bending on clean cleaved zinc oxide surfaces. *Surf. Sci.*, 80:261–264, feb 1979. ISSN 00396028. doi: 10.1016/0039-6028(79)90685-X. URL https://linkinghub.elsevier.com/retrieve/pii/003960287990685X.

[168] Yinhua Zhou, Canek Fuentes-Hernandez, Jaewon Shim, Jens Meyer, Anthony J Giordano, Hong Li, Paul Winget, Theodoros Papadopoulos, Hyeunseok Cheun, Jungbae Kim, Mathieu Fenoll, Amir Dindar, Wojciech Haske, Ehsan Najafabadi, Talha M Khan, Hossein Sojoudi, Stephen Barlow, Samuel Graham, J.-L. Bredas, Seth R Marder, Antoine Kahn, and Bernard Kippelen. A Universal Method to Produce Low-Work Function Electrodes for Organic Electronics. *Science*, 336 (6079):327–332, apr 2012. ISSN 0036-8075. doi: 10.1126/science.1218829. URL http://www.sciencemag.org/cgi/doi/10.1126/science.1218829.

[169] Raphael Schlesinger, Yong Xu, Oliver T. Hofmann, Stefanie Winkler, Johannes Frisch, Jens Niederhausen, Antje Vollmer, Sylke Blumstengel, Fritz Henneberger, Patrick Rinke, Matthias Scheffler, and Norbert Koch. Controlling the work function of ZnO and the energy-level alignment at the interface to organic semiconductors with a molecular electron acceptor. *Phys. Rev. B*, 87(15):155311, apr 2013. ISSN 1098-0121. doi: 10.1103/PhysRevB.87.155311. URL https://link.aps.org/doi/10.1103/PhysRevB.87.155311.

[170] Xavier Crispin, Victor Geskin, Annica Crispin, Jérôme Cornil, Roberto Lazzaroni, William R Salaneck, and Jean-Luc Brédas. Characterization of the Interface Dipole at Organic/ Metal Interfaces. *J. Am. Chem. Soc.*, 124(27):8131–8141, jul 2002. ISSN 0002-7863. doi: 10.1021/ja025673r. URL https://pubs.acs.org/doi/10.1021/ja025673r.

[171] Antoine Kahn, Norbert Koch, and Weiying Gao. Electronic structure and electrical properties of interfaces between metals and ?-conjugated molecular films. *J. Polym. Sci. Part B Polym. Phys.*, 41(21):2529–2548, nov 2003. ISSN 0887-6266. doi: 10.1002/polb.10642. URL http://doi.wiley.com/10.1002/polb.10642.

[172] Jaehyung Hwang, Alan Wan, and Antoine Kahn. Energetics of metal–organic interfaces: New experiments and assessment of the field. *Mater. Sci. Eng. R Reports*, 64(1-2):1–31, mar 2009. ISSN 0927-796X. doi: 10.1016/J.MSER.2008.12.001. URL https://www.sciencedirect.com/science/article/pii/S0927796X08001228.

[173] Steven G. Louie and Marvin L. Cohen. Electronic structure of a metal-semiconductor interface. *Phys. Rev. B*, 13(6):2461–2469, mar 1976. ISSN 0556-2805. doi: 10.1103/PhysRevB.13.2461. URL https://link.aps.org/doi/10.1103/PhysRevB.13.2461.

[174] Winfried Mönch. Metal-semiconductor contacts: electronic properties. *Surf. Sci.*, 299-300:928–944, jan 1994. ISSN 00396028. doi: 10.1016/0039-6028(94)90707-2. URL https://linkinghub.elsevier.com/retrieve/pii/0039602894907072.

[175] H Vázquez, F Flores, R Oszwaldowski, J Ortega, R Pérez, and A Kahn. Barrier formation at metal–organic interfaces: dipole formation and the charge neutrality level. *Appl. Surf. Sci.*, 234(1-4):107–112, jul 2004. ISSN 01694332. doi: 10.1016/j.apsusc.2004.05.084. URL https://linkinghub.elsevier.com/retrieve/pii/S0169433204007275.

[176] H. Vázquez, Y. J. Dappe, J. Ortega, and F. Flores. Energy level alignment at metal/organic semiconductor interfaces: "Pillow" effect, induced density of interface states, and charge neutrality level. *J. Chem. Phys.*, 126(14):144703, apr 2007. ISSN 0021-9606. doi: 10.1063/1.2717165. URL http://aip.scitation.org/doi/10.1063/1.2717165.

[177] Robert L. Wells and Tomlinson Fort. Adsorption of water on clean gold by measurement of work function changes. *Surf. Sci.*, 32(3):554–560, sep 1972.

ISSN 00396028. doi: 10.1016/0039-6028(72)90182-3. URL https://linkinghub.elsevier.com/retrieve/pii/0039602872901823.

[178] W.M.H. Sachtler, G.J.H. Dorgelo, and A.A. Holscher. The work function of gold. *Surf. Sci.*, 5(2):221–229, oct 1966. ISSN 00396028. doi: 10.1016/0039-6028(66)90083-5. URL https://linkinghub.elsevier.com/retrieve/pii/0039602866900835.

[179] W. Osikowicz, M. P. de Jong, S. Braun, C. Tengstedt, M. Fahlman, and W. R. Salaneck. Energetics at Au top and bottom contacts on conjugated polymers. *Appl. Phys. Lett.*, 88(19):193504, may 2006. ISSN 0003-6951. doi: 10.1063/1.2201627. URL http://aip.scitation.org/doi/10.1063/1.2201627.

[180] William E Ford, Deqing Gao, Nikolaus Knorr, Rene Wirtz, Frank Scholz, Zoi Karipidou, Kodo Ogasawara, Silvia Rosselli, Vadim Rodin, Gabriele Nelles, and Florian von Wrochem. Organic Dipole Layers for Ultralow Work Function Electrodes. *ACS Nano*, 8(9):9173–9180, sep 2014. ISSN 1936-0851. doi: 10.1021/nn502794z. URL http://pubs.acs.org/doi/10.1021/nn502794z.

[181] Lorenz Romaner, Georg Heimel, Claudia Ambrosch-Draxl, and Egbert Zojer. The Dielectric Constant of Self-Assembled Monolayers. *Adv. Funct. Mater.*, 18 (24):3999–4006, dec 2008. ISSN 1616301X. doi: 10.1002/adfm.200800876. URL http://doi.wiley.com/10.1002/adfm.200800876.

[182] Robert G Parr and Ralph G Pearson. Absolute hardness: companion parameter to absolute electronegativity. *J. Am. Chem. Soc.*, 105(26):7512–7516, dec 1983. ISSN 0002-7863. doi: 10.1021/ja00364a005. URL http://pubs.acs.org/doi/abs/10.1021/ja00364a005.

[183] H. Ishii, N. Hayashi, E. Ito, Y. Washizu, K. Sugi, Y. Kimura, M. Niwano, Y. Ouchi, and K. Seki. Kelvin probe study of band bending at organic semiconductor/metal interfaces: examination of Fermi level alignment. *Phys. status solidi*, 201(6):1075–1094, may 2004. ISSN 0031-8965. doi: 10.1002/pssa.200404346. URL http://doi.wiley.com/10.1002/pssa.200404346.

[184] Toshio Nishi, Kaname Kanai, Yukio Ouchi, Martin R. Willis, and Kazuhiko Seki. Evidence for the atmospheric p-type doping of titanyl phthalocyanine thin film by oxygen observed as the change of interfacial electronic structure. *Chem. Phys. Lett.*, 414(4-6):479–482, oct 2005. ISSN 00092614. doi: 10.1016/j.cplett.2005.08.113. URL https://linkinghub.elsevier.com/retrieve/pii/S0009261405012972.

[185] Carl Tengstedt, Wojciech Osikowicz, William R. Salaneck, Ian D. Parker, Che-H. Hsu, and Mats Fahlman. Fermi-level pinning at conjugated polymer interfaces. *Appl. Phys. Lett.*, 88(5):053502, jan 2006. ISSN 0003-6951. doi: 10.1063/1.2168515. URL http://aip.scitation.org/doi/10.1063/1.2168515.

[186] O. Tal, Y. Rosenwaks, Y. Preezant, N. Tessler, C. K. Chan, and A. Kahn. Direct Determination of the Hole Density of States in Undoped and Doped Amorphous Organic Films with High Lateral Resolution. *Phys. Rev. Lett.*, 95(25):256405, dec 2005. ISSN 0031-9007. doi: 10.1103/PhysRevLett.95.256405. URL https://link.aps.org/doi/10.1103/PhysRevLett.95.256405.

[187] K. Celebi, P. J. Jadhav, K. M. Milaninia, M. Bora, and M. A. Baldo. The density of states in thin film copper phthalocyanine measured by Kelvin probe force microscopy. *Appl. Phys. Lett.*, 93(8):083308, aug 2008. ISSN 0003-6951. doi: 10.1063/1.2976634. URL http://aip.scitation.org/doi/10.1063/1.2976634.

[188] Hong Ying Mao, Fabio Bussolotti, Dong-Chen Qi, Rui Wang, Satoshi Kera, Nobuo Ueno, Andrew Thye Shen Wee, and Wei Chen. Mechanism of the Fermi level pinning at organic donor–acceptor heterojunction interfaces. *Org. Electron.*, 12(3):534–540, mar 2011. ISSN 15661199. doi: 10.1016/j.orgel.2011.01.003. URL https://linkinghub.elsevier.com/retrieve/pii/S1566119911000127.

[189] J Campbell Scott. Metal–organic interface and charge injection in organic electronic devices. *J. Vac. Sci. Technol. A Vacuum, Surfaces, Film.*, 21(3):521–531, may 2003. ISSN 0734-2101. doi: 10.1116/1.1559919. URL http://avs.scitation.org/doi/10.1116/1.1559919.

[190] Yongli Gao. Surface analytical studies of interfaces in organic semiconductor devices. *Mater. Sci. Eng. R Reports*, 68(3):39–87, apr 2010. ISSN 0927796X. doi: 10.1016/j.mser.2010.01.001. URL https://linkinghub.elsevier.com/retrieve/pii/S0927796X10000136.

[191] Martin Oehzelt, Kouki Akaike, Norbert Koch, and Georg Heimel. Energy-level alignment at organic heterointerfaces. *Sci. Adv.*, 1(10):e1501127, nov 2015. ISSN 2375-2548. doi: 10.1126/sciadv.1501127. URL http://advances.sciencemag.org/lookup/doi/10.1126/sciadv.1501127.

[192] James C Blakesley and Neil C Greenham. Charge transfer at polymer-electrode interfaces: The effect of energetic disorder and thermal injection on band bending and open-circuit voltage. *J. Appl. Phys.*, 106(3):034507, aug 2009. ISSN 0021-8979. doi: 10.1063/1.3187787. URL http://aip.scitation.org/doi/10.1063/1.3187787.

[193] Martin Oehzelt, Norbert Koch, and Georg Heimel. Organic semiconductor density of states controls the energy level alignment at electrode interfaces. *Nat. Commun.*, 5, 2014. doi: 10.1038/ncomms5174. URL https://www.nature.com/articles/ncomms5174.pdf.

[194] S. Matthew Menke, Niva A. Ran, Guillermo C. Bazan, and Richard H. Friend. Understanding Energy Loss in Organic Solar Cells: Toward a New Efficiency Regime. *Joule*, 2(1):25–35, jan 2018. ISSN 25424351. doi: 10.1016/j.joule.2017.09.020. URL https://linkinghub.elsevier.com/retrieve/pii/S2542435117300946.

[195] James C. Blakesley and Dieter Neher. Relationship between energetic disorder and open-circuit voltage in bulk heterojunction organic solar cells. *Phys. Rev. B*, 84(7):075210, aug 2011. ISSN 1098-0121. doi: 10.1103/PhysRevB.84.075210. URL https://link.aps.org/doi/10.1103/PhysRevB.84.075210.

[196] Erin L. Ratcliff, Andres Garcia, Sergio A. Paniagua, Sarah R. Cowan, Anthony J. Giordano, David S. Ginley, Seth R. Marder, Joseph J. Berry, and Dana C. Olson. Investigating the Influence of Interfacial Contact Properties on Open Circuit Voltages in Organic Photovoltaic Performance: Work Function Versus Selectivity. *Adv. Energy Mater.*, 3(5):647–656, may 2013. ISSN 16146832. doi: 10.1002/aenm.201200669. URL http://doi.wiley.com/10.1002/aenm.201200669.

[197] Andrea Zampetti, Amir Hossein Fallahpour, Martina Dianetti, Luigi Salamandra, Francesco Santoni, Alessio Gagliardi, Matthias Auf der Maur, Francesca Brunetti, Andrea Reale, Thomas M. Brown, and Aldo Di Carlo. Influence of the interface material layers and semiconductor energetic disorder on the open circuit voltage in polymer solar cells. *J. Polym. Sci. Part B Polym. Phys.*, 53(10):690–699, may 2015. ISSN 08876266. doi: 10.1002/polb.23685. URL http://doi.wiley.com/10.1002/polb.23685.

[198] J. Liu, Y. Shi, and Y. Yang. Solvation-Induced Morphology Effects on the Performance of Polymer-Based Photovoltaic Devices. *Adv. Funct. Mater.*, 11(6):420, dec 2001. ISSN 1616301X. doi: 10.1002/1616-3028(200112)11:6<420::AID-ADFM420>3.0.CO;2-K. URL http://doi.wiley.com/10.1002/1616-3028%28200112%2911%3A6%3C420%3A%3AAID-ADFM420%3E3.0.CO%3B2-K.

[199] K. Schick, E. Daub, S. Finkbeiner, and P. Würfel. Verification of a generalized Planck law for luminescence radiation from silicon solar cells. *Appl. Phys. A Solids Surfaces*, 54(2):109–114, feb 1992. ISSN 0721-7250. doi: 10.1007/BF00323895. URL http://link.springer.com/10.1007/BF00323895.

[200] Germà Garcia-Belmonte and Juan Bisquert. Open-circuit voltage limit caused by recombination through tail states in bulk heterojunction polymer-fullerene solar cells. *Appl. Phys. Lett.*, 96(11):113301, mar 2010. ISSN 0003-6951. doi: 10.1063/1.3358121. URL https://doi.org/10.1063/1.3358121.

[201] Nir Tessler and Yohai Roichman. Amorphous organic molecule/polymer diodes and transistors—Comparison between predictions based on Gaussian or exponential density of states. *Org. Electron.*, 6(5-6):200–210, dec 2005. ISSN 15661199. doi: 10.1016/j.orgel.2005.06.006. URL https://linkinghub.elsevier.com/retrieve/pii/S1566119905000534.

[202] Thomas Heumueller, Timothy M. Burke, William R. Mateker, Isaac T. Sachs-Quintana, Koen Vandewal, Christoph J. Brabec, and Michael D. McGehee. Disorder-Induced Open-Circuit Voltage Losses in Organic Solar Cells During Photoinduced Burn-In. *Adv. Energy Mater.*, 5(14):1500111, jul 2015. ISSN

16146832. doi: 10.1002/aenm.201500111. URL http://doi.wiley.com/10.1002/aenm.201500111.

[203] Germà Garcia-Belmonte, Pablo P. Boix, Juan Bisquert, Martijn Lenes, Henk J. Bolink, Andrea La Rosa, Salvatore Filippone, and Nazario Martín. Influence of the Intermediate Density-of-States Occupancy on Open-Circuit Voltage of Bulk Heterojunction Solar Cells with Different Fullerene Acceptors. *J. Phys. Chem. Lett.*, 1(17):2566–2571, sep 2010. ISSN 1948-7185. doi: 10.1021/jz100956d. URL https://pubs.acs.org/doi/10.1021/jz100956d.

[204] Germà Garcia-Belmonte, Pablo P. Boix, Juan Bisquert, Michele Sessolo, and Henk J. Bolink. Simultaneous determination of carrier lifetime and electron density-of-states in P3HT:PCBM organic solar cells under illumination by impedance spectroscopy. *Sol. Energy Mater. Sol. Cells*, 94(2):366–375, feb 2010. ISSN 09270248. doi: 10.1016/j.solmat.2009.10.015. URL https://linkinghub.elsevier.com/retrieve/pii/S0927024809003705.

[205] Koen Vandewal. Interfacial Charge Transfer States in Condensed Phase Systems. *Annu. Rev. Phys. Chem.*, 67(1):113–133, may 2016. ISSN 0066-426X. doi: 10.1146/annurev-physchem-040215-112144. URL http://www.annualreviews.org/doi/10.1146/annurev-physchem-040215-112144.

[206] Robert S Mulliken. Molecular Compounds and their Spectra. III. The Interaction of Electron Donors and Acceptors. *J. Phys. Chem.*, 56(7):801–822, jul 1952. ISSN 0022-3654. doi: 10.1021/j150499a001. URL http://pubs.acs.org/doi/abs/10.1021/j150499a001.

[207] I.-W. Hwang, C. Soci, D. Moses, Z. Zhu, D. Waller, R. Gaudiana, C. J. Brabec, and A. J. Heeger. Ultrafast Electron Transfer and Decay Dynamics in a Small Band Gap Bulk Heterojunction Material. *Adv. Mater.*, 19(17):2307–2312, sep 2007. ISSN 09359648. doi: 10.1002/adma.200602437. URL http://doi.wiley.com/10.1002/adma.200602437.

[208] Hideo Ohkita, Steffan Cook, Yeni Astuti, Warren Duffy, Steve Tierney, Weimin Zhang, Martin Heeney, Iain McCulloch, Jenny Nelson, Donal D. C. Bradley, and James R. Durrant. Charge Carrier Formation in Polythiophene/Fullerene Blend Films Studied by Transient Absorption Spectroscopy. *J. Am. Chem. Soc.*, 130(10):3030–3042, mar 2008. ISSN 0002-7863. doi: 10.1021/ja076568q. URL https://pubs.acs.org/doi/abs/10.1021/ja076568q.

[209] Priyadarshi Panda, Dirk Veldman, Jörgen Sweelssen, Jolanda J. A. M. Bastiaansen, Bea M. W. Langeveld-Voss, and Stefan C. J. Meskers. Charge Transfer Absorption for π-Conjugated Polymers and Oligomers Mixed with Electron Acceptors. *J. Phys. Chem. B*, 111(19):5076–5081, may 2007. ISSN 1520-6106. doi: 10.1021/jp070796p. URL http://pubs.acs.org/doi/abs/10.1021/jp070796p.

[210] Koen Vandewal, Wibren D. Oosterbaan, Sabine Bertho, Veerle Vrindts, Abay Gadisa, Laurence Lutsen, Dirk Vanderzande, and Jean V. Manca. Varying polymer crystallinity in nanofiber poly(3-alkylthiophene): PCBM solar cells: Influence on charge-transfer state energy and open-circuit voltage. *Appl. Phys. Lett.*, 95(12):123303, sep 2009. ISSN 0003-6951. doi: 10.1063/1.3232242. URL http://aip.scitation.org/doi/10.1063/1.3232242.

[211] L. Goris, K. Haenen, M. Nesládek, P. Wagner, D. Vanderzande, L. De Schepper, J. D'haen, L. Lutsen, and J. V. Manca. Absorption phenomena in organic thin films for solar cell applications investigated by photothermal deflection spectroscopy. *J. Mater. Sci.*, 40(6):1413–1418, mar 2005. ISSN 0022-2461. doi: 10.1007/s10853-005-0576-0. URL http://link.springer.com/10.1007/s10853-005-0576-0.

[212] M. A. Loi, S. Toffanin, M. Muccini, M. Forster, U. Scherf, and M. Scharber. Charge Transfer Excitons in Bulk Heterojunctions of a Polyfluorene Copolymer and a Fullerene Derivative. *Adv. Funct. Mater.*, 17(13):2111–2116, sep 2007. ISSN 1616301X. doi: 10.1002/adfm.200601098. URL http://doi.wiley.com/10.1002/adfm.200601098.

[213] Kristofer Tvingstedt, Koen Vandewal, Abay Gadisa, Fengling Zhang, Jean Manca, and Olle Inganas. Electroluminescence from Charge Transfer States in Polymer Solar Cells. *J. Am. Chem. Soc.*, 131(33):11819–11824, aug 2009. ISSN 0002-7863. doi: 10.1021/ja903100p. URL https://pubs.acs.org/doi/10.1021/ja903100p.

[214] Koen Vandewal, Kristofer Tvingstedt, Abay Gadisa, Olle Inganäs, and Jean V. Manca. Relating the open-circuit voltage to interface molecular properties of donor:acceptor bulk heterojunction solar cells. *Phys. Rev. B*, 81(12):125204, mar 2010. ISSN 1098-0121. doi: 10.1103/PhysRevB.81.125204. URL https://link.aps.org/doi/10.1103/PhysRevB.81.125204.

[215] Baobing Fan, Xiaoyan Du, Feng Liu, Wenkai Zhong, Lei Ying, Ruihao Xie, Xiaofeng Tang, Kang An, Jingming Xin, Ning Li, Wei Ma, Christoph J. Brabec, Fei Huang, and Yong Cao. Fine-tuning of the chemical structure of photoactive materials for highly efficient organic photovoltaics. *Nat. Energy*, 3(12):1051–1058, dec 2018. ISSN 2058-7546. doi: 10.1038/s41560-018-0263-4. URL http://dx.doi.org/10.1038/s41560-018-0263-4http://www.nature.com/articles/s41560-018-0263-4.

[216] R A Marcus. Relation between charge transfer absorption and fluorescence spectra and the inverted region. *J. Phys. Chem.*, 93(8):3078–3086, apr 1989. ISSN 0022-3654. doi: 10.1021/j100345a040. URL http://pubs.acs.org/doi/abs/10.1021/j100345a040.

[217] R. A. Street, K. W. Song, J. E. Northrup, and S. Cowan. Photoconductivity measurements of the electronic structure of organic solar cells. *Phys. Rev. B*, 83(16):

165207, apr 2011. ISSN 1098-0121. doi: 10.1103/PhysRevB.83.165207. URL https://link.aps.org/doi/10.1103/PhysRevB.83.165207.

[218] Timothy M. Burke, Sean Sweetnam, Koen Vandewal, and Michael D. McGehee. Beyond Langevin Recombination: How Equilibrium Between Free Carriers and Charge Transfer States Determines the Open-Circuit Voltage of Organic Solar Cells. *Adv. Energy Mater.*, 5(11):1500123, jun 2015. ISSN 16146832. doi: 10.1002/aenm.201500123. URL http://doi.wiley.com/10.1002/aenm.201500123.

[219] David C. Coffey, Bryon W. Larson, Alexander W. Hains, James B. Whitaker, Nikos Kopidakis, Olga V. Boltalina, Steven H. Strauss, and Garry Rumbles. An Optimal Driving Force for Converting Excitons into Free Carriers in Excitonic Solar Cells. *J. Phys. Chem. C*, 116(16):8916–8923, apr 2012. ISSN 1932-7447. doi: 10.1021/jp302275z. URL http://pubs.acs.org/doi/10.1021/jp302275z.

[220] Alexander J. Ward, Arvydas Ruseckas, Mohanad Mousa Kareem, Bernd Ebenhoch, Luis A. Serrano, Manal Al-Eid, Brian Fitzpatrick, Vincent M. Rotello, Graeme Cooke, and Ifor D. W. Samuel. The Impact of Driving Force on Electron Transfer Rates in Photovoltaic Donor-Acceptor Blends. *Adv. Mater.*, 27 (15):2496–2500, apr 2015. ISSN 09359648. doi: 10.1002/adma.201405623. URL http://doi.wiley.com/10.1002/adma.201405623.

[221] Françoise Provencher, Nicolas Bérubé, Anthony W. Parker, Gregory M. Greetham, Michael Towrie, Christoph Hellmann, Michel Côté, Natalie Stingelin, Carlos Silva, and Sophia C. Hayes. Direct observation of ultrafast long-range charge separation at polymer–fullerene heterojunctions. *Nat. Commun.*, 5(1):4288, sep 2014. ISSN 2041-1723. doi: 10.1038/ncomms5288. URL http://www.nature.com/articles/ncomms5288.

[222] S. M. Falke, C. A. Rozzi, D. Brida, M. Maiuri, M. Amato, E. Sommer, A. De Sio, A. Rubio, G. Cerullo, E. Molinari, and C. Lienau. Coherent ultrafast charge transfer in an organic photovoltaic blend. *Science*, 344(6187):1001–1005, may 2014. ISSN 0036-8075. doi: 10.1126/science.1249771. URL http://www.sciencemag.org/cgi/doi/10.1126/science.1249771.

[223] Koen Vandewal, Zaifei Ma, Jonas Bergqvist, Zheng Tang, Ergang Wang, Patrik Henriksson, Kristofer Tvingstedt, Mats R. Andersson, Fengling Zhang, and Olle Inganäs. Quantification of Quantum Efficiency and Energy Losses in Low Bandgap Polymer:Fullerene Solar Cells with High Open-Circuit Voltage. *Adv. Funct. Mater.*, 22(16):3480–3490, aug 2012. ISSN 1616301X. doi: 10.1002/adfm.201200608. URL http://doi.wiley.com/10.1002/adfm.201200608.

[224] Arun Aby Paraecattil and Natalie Banerji. Charge Separation Pathways in a Highly Efficient Polymer: Fullerene Solar Cell Material. *J. Am. Chem. Soc.*, 136 (4):1472–1482, jan 2014. ISSN 0002-7863. doi: 10.1021/ja410340g. URL http://pubs.acs.org/doi/10.1021/ja410340g.

[225] J. J. Benson-Smith, L. Goris, K. Vandewal, K. Haenen, J. V. Manca, D. Vanderzande, D. D. C. Bradley, and J. Nelson. Formation of a Ground-State Charge-Transfer Complex in Polyfluorene//[6,6]-Phenyl-C61 Butyric Acid Methyl Ester (PCBM) Blend Films and Its Role in the Function of Polymer/PCBM Solar Cells. *Adv. Funct. Mater.*, 17(3):451–457, feb 2007. ISSN 1616301X. doi: 10.1002/adfm.200600484. URL http://doi.wiley.com/10.1002/adfm.200600484.

[226] Mark A Faist, Thomas Kirchartz, Wei Gong, Raja Shahid Ashraf, Iain McCulloch, John C de Mello, Nicholas J Ekins-Daukes, Donal D. C. Bradley, and Jenny Nelson. Competition between the Charge Transfer State and the Singlet States of Donor or Acceptor Limiting the Efficiency in Polymer:Fullerene Solar Cells. *J. Am. Chem. Soc.*, 134(1):685–692, jan 2012. ISSN 0002-7863. doi: 10.1021/ja210029w. URL http://pubs.acs.org/doi/10.1021/ja210029w.

[227] Sebastian Westenhoff, Ian A. Howard, Justin M. Hodgkiss, Kiril R. Kirov, Hugo A. Bronstein, Charlotte K. Williams, Neil C. Greenham, and Richard H. Friend. Charge Recombination in Organic Photovoltaic Devices with High Open-Circuit Voltages. *J. Am. Chem. Soc.*, 130(41):13653–13658, oct 2008. ISSN 0002-7863. doi: 10.1021/ja803054g. URL https://pubs.acs.org/doi/10.1021/ja803054g.

[228] David C. Coffey, Bryon W. Larson, Alexander W. Hains, James B. Whitaker, Nikos Kopidakis, Olga V. Boltalina, Steven H. Strauss, and Garry Rumbles. An Optimal Driving Force for Converting Excitons into Free Carriers in Excitonic Solar Cells. *J. Phys. Chem. C*, 116(16):8916–8923, apr 2012. ISSN 1932-7447. doi: 10.1021/jp302275z. URL http://pubs.acs.org/doi/10.1021/ja306110bhttp://pubs.acs.org/doi/10.1021/jp302275z.

[229] Wendi Chang, Daniel N. Congreve, Eric Hontz, Matthias E. Bahlke, David P. McMahon, Sebastian Reineke, Tony C. Wu, Vladimir Bulović, Troy Van Voorhis, and Marc A. Baldo. Spin-dependent charge transfer state design rules in organic photovoltaics. *Nat. Commun.*, 6(1):6415, may 2015. ISSN 2041-1723. doi: 10.1038/ncomms7415. URL http://www.nature.com/articles/ncomms7415.

[230] David Braun. Electronic injection and conduction processes for polymer devices. *J. Polym. Sci. Part B Polym. Phys.*, 41(21):2622–2629, nov 2003. ISSN 0887-6266. doi: 10.1002/polb.10654. URL http://doi.wiley.com/10.1002/polb.10654.

[231] P Wurfel. The chemical potential of radiation. *J. Phys. C Solid State Phys.*, 15(18):3967–3985, jun 1982. ISSN 0022-3719. doi: 10.1088/0022-3719/15/18/012. URL http://stacks.iop.org/0022-3719/15/i=18/a=012?key=crossref.f7e08aa4381a98aeb0bb4154ce38ad96.

[232] Uwe Rau. Reciprocity relation between photovoltaic quantum efficiency and electroluminescent emission of solar cells. *Phys. Rev. B*, 76(8):085303, aug 2007. ISSN 1098-0121. doi: 10.1103/PhysRevB.76.085303. URL https://link.aps.org/doi/10.1103/PhysRevB.76.085303.

[233] Koen Vandewal, Kristofer Tvingstedt, and Olle Inganäs. Charge Transfer States in Organic Donor–Acceptor Solar Cells. In *Semicond. Semimetals*, volume 85, pages 261–295. 2011. ISBN 9780123910608. doi: 10.1016/B978-0-12-391060-8.00008-3. URL https://linkinghub.elsevier.com/retrieve/pii/B9780123910608000083.

[234] Uli Würfel, Dieter Neher, Annika Spies, and Steve Albrecht. Impact of charge transport on current-voltage characteristics and power-conversion efficiency of organic solar cells. *Nat. Commun.*, 6:1–9, 2015. ISSN 20411723. doi: 10.1038/ncomms7951. URL http://www.nature.com/ncomms/2015/150424/ncomms7951/full/ncomms7951.html.

[235] Koen Vandewal, Johannes Widmer, Thomas Heumueller, Christoph J. Brabec, Michael D. McGehee, Karl Leo, Moritz Riede, and Alberto Salleo. Increased Open-Circuit Voltage of Organic Solar Cells by Reduced Donor-Acceptor Interface Area. *Adv. Mater.*, 26(23):3839–3843, jun 2014. ISSN 09359648. doi: 10.1002/adma.201400114. URL http://doi.wiley.com/10.1002/adma.201400114.

[236] Kenneth R. Graham, Patrick Erwin, Dennis Nordlund, Koen Vandewal, Ruipeng Li, Guy O. Ngongang Ndjawa, Eric T. Hoke, Alberto Salleo, Mark E. Thompson, Michael D. McGehee, and Aram Amassian. Re-evaluating the Role of Sterics and Electronic Coupling in Determining the Open-Circuit Voltage of Organic Solar Cells. *Adv. Mater.*, 25(42):6076–6082, nov 2013. ISSN 09359648. doi: 10.1002/adma.201301319. URL http://doi.wiley.com/10.1002/adma.201301319.

[237] Dana B. Sulas, Kai Yao, Jeremy J. Intemann, Spencer T. Williams, Chang-Zhi Li, Chu-Chen Chueh, Jeffrey J. Richards, Yuyin Xi, Lilo D. Pozzo, Cody W. Schlenker, Alex K.-Y. Jen, and David S. Ginger. Open-Circuit Voltage Losses in Selenium-Substituted Organic Photovoltaic Devices from Increased Density of Charge-Transfer States. *Chem. Mater.*, 27(19):6583–6591, oct 2015. ISSN 0897-4756. doi: 10.1021/acs.chemmater.5b02133. URL http://pubs.acs.org/doi/10.1021/acs.chemmater.5b02133.

[238] Xian-Kai Chen and Jean-Luc Brédas. Voltage Losses in Organic Solar Cells: Understanding the Contributions of Intramolecular Vibrations to Nonradiative Recombinations. *Adv. Energy Mater.*, 8(9):1702227, mar 2018. ISSN 16146832. doi: 10.1002/aenm.201702227. URL http://doi.wiley.com/10.1002/aenm.201702227.

[239] Andrew N. Bartynski, Mark Gruber, Saptaparna Das, Sylvie Rangan, Sonya Mollinger, Cong Trinh, Stephen E Bradforth, Koen Vandewal, Alberto Salleo, Robert A Bartynski, Wolfgang Bruetting, and Mark E Thompson. Symmetry-Breaking Charge Transfer in a Zinc Chlorodipyrrin Acceptor for High Open Circuit Voltage Organic Photovoltaics. *J. Am. Chem. Soc.*, 137(16):5397–5405, apr 2015. ISSN 0002-7863. doi: 10.1021/jacs.5b00146. URL http://pubs.acs.org/doi/10.1021/jacs.5b00146.

[240] Hiroo Inokuchi. Photoconductivity of the Condensed Polynuclear Aromatic Compounds. *Bull. Chem. Soc. Jpn.*, 27(1):22–27, jan 1954. ISSN 0009-2673. doi: 10.1246/bcsj.27.22. URL http://www.journal.csj.jp/doi/10.1246/bcsj.27.22.

[241] Norbert Koch, Nobuo Ueno, and Andrew T.S. Wee. The Molecule—Metal Interface: Introduction to the Molecule – Metal Interface. In *Mol. interface*, chapter 1. WI LEY-VCH Verlag GmbH & Co. KGaA, 2013.

[242] Wenchao Zhao, Sunsun Li, Huifeng Yao, Shaoqing Zhang, Yun Zhang, Bei Yang, and Jianhui Hou. Molecular Optimization Enables over 13Cells. *J. Am. Chem. Soc.*, 139:7148–7151, 2017. doi: 10.1021/jacs.7b02677. URL https://pubs.acs.org/sharingguidelines.

[243] Jianhui Hou, Olle Inganäs, Richard H. Friend, and Feng Gao. Organic solar cells based on non-fullerene acceptors. *Nat. Mater.*, 17(2):119–128, feb 2018. ISSN 1476-1122. doi: 10.1038/nmat5063. URL http://www.nature.com/articles/nmat5063.

[244] D. Baran, T. Kirchartz, S. Wheeler, S. Dimitrov, M. Abdelsamie, J. Gorman, R. S. Ashraf, S. Holliday, A. Wadsworth, N. Gasparini, P. Kaienburg, H. Yan, A. Amassian, C. J. Brabec, J. R. Durrant, and I. McCulloch. Reduced voltage losses yield 10solar cells with >1 V open circuit voltages. *Energy Environ. Sci.*, 9(12):3783–3793, 2016. ISSN 1754-5692. doi: 10.1039/C6EE02598F. URL http://xlink.rsc.org/?DOI=C6EE02598F.

[245] Jing Liu, Shangshang Chen, Deping Qian, Bhoj Gautam, Guofang Yang, Jingbo Zhao, Jonas Bergqvist, Fengling Zhang, Wei Ma, Harald Ade, Olle Inganäs, Kenan Gundogdu, Feng Gao, and He Yan. Fast charge separation in a non-fullerene organic solar cell with a small driving force. *Nat. Energy*, 1(7):16089, jul 2016. ISSN 2058-7546. doi: 10.1038/nenergy.2016.89. URL http://www.nature.com/articles/nenergy201689.

[246] Mark E. Ziffer, Sae Byeok Jo, Hongliang Zhong, Long Ye, Hongbin Liu, Francis Lin, Jie Zhang, Xiaosong Li, Harald W. Ade, Alex K.-Y. Jen, and David S. Ginger. Long-Lived, Non-Geminate, Radiative Recombination of Photogenerated Charges in a Polymer/Small-Molecule Acceptor Photovoltaic Blend. *J. Am. Chem. Soc.*, 140(31):9996–10008, aug 2018. ISSN 0002-7863. doi: 10.1021/jacs.8b05834. URL http://pubs.acs.org/doi/10.1021/jacs.8b05834.

[247] Bin Kan, Jiangbin Zhang, Feng Liu, Xiangjian Wan, Chenxi Li, Xin Ke, Yunchuang Wang, Huanran Feng, Yamin Zhang, Guankui Long, Richard H. Friend, Artem A. Bakulin, and Yongsheng Chen. Fine-Tuning the Energy Levels of a Nonfullerene Small-Molecule Acceptor to Achieve a High Short-Circuit Current and a Power Conversion Efficiency over 12 *Adv. Mater.*, 30 (3):1704904, jan 2018. ISSN 09359648. doi: 10.1002/adma.201704904. URL http://doi.wiley.com/10.1002/adma.201704904.

[248] Zhuping Fei, Flurin D. Eisner, Xuechen Jiao, Mohammed Azzouzi, Jason A. Röhr, Yang Han, Munazza Shahid, Anthony S. R. Chesman, Christopher D. Easton, Christopher R. McNeill, Thomas D. Anthopoulos, Jenny Nelson, and Martin Heeney. An Alkylated Indacenodithieno[3,2- b]thiophene-Based Nonfullerene Acceptor with High Crystallinity Exhibiting Single Junction Solar Cell Efficiencies Greater than 13 *Adv. Mater.*, 30(8):1705209, feb 2018. ISSN 09359648. doi: 10.1002/adma.201705209. URL http://doi.wiley.com/10.1002/adma.201705209.

[249] Philipp Biegger, Manuel Schaffroth, Kerstin Brödner, Olena Tverskoy, Frank Rominger, and Uwe H. F. Bunz. Bisalkynylated 3,6-diiminocyclohexa-1,4-diene-1,4-diamine. *Chem. Commun.*, 51(80):14844–14847, 2015. ISSN 1359-7345. doi: 10.1039/C5CC05427C. URL http://xlink.rsc.org/?DOI=C5CC05427C.

[250] N. Koch, A. Vollmer, and A. Elschner. Influence of water on the work function of conducting poly(3,4-ethylenedioxythiophene)/poly(styrenesulfonate). *Appl. Phys. Lett.*, 90(4):043512, jan 2007. ISSN 0003-6951. doi: 10.1063/1.2435350. URL http://aip.scitation.org/doi/10.1063/1.2435350.

[251] Lamia Znaidi. Sol–gel-deposited ZnO thin films: A review. *Mater. Sci. Eng. B*, 174(1-3):18–30, oct 2010. ISSN 09215107. doi: 10.1016/j.mseb.2010.07.001. URL https://linkinghub.elsevier.com/retrieve/pii/S0921510710004630.

[252] Seungchul Kwon, Kyung-Geun Lim, Myungsun Shim, Hong Chul Moon, Jicheol Park, Gumhye Jeon, Jihyun Shin, Kilwon Cho, Tae-Woo Lee, and Jin Kon Kim. Air-stable inverted structure of hybrid solar cells using a cesium-doped ZnO electron transport layer prepared by a sol–gel process. *J. Mater. Chem. A*, 1(38): 11802, 2013. ISSN 2050-7488. doi: 10.1039/c3ta12425h. URL http://xlink.rsc.org/?DOI=c3ta12425h.

[253] Jiangbin Zhang, Bin Kan, Andrew J Pearson, Andrew J Parnell, Joshaniel F K Cooper, Xiao-ke Liu, Patrick J Conaghan, Thomas R. Hopper, Yutian Wu, Xiangjian Wan, Feng Gao, Neil C. Greenham, Artem A. Bakulin, Yongsheng Chen, and Richard H Friend. Efficient non-fullerene organic solar cells employing sequentially deposited donor–acceptor layers. *J. Mater. Chem. A*, 6 (37):18225–18233, 2018. ISSN 2050-7488. doi: 10.1039/C8TA06860G. URL http://xlink.rsc.org/?DOI=C8TA06860G.

[254] E. W. Becker, K. Bier, and W. Henkes. Strahlen aus kondensierten Atomen und Molekeln im Hochvakuum. Technical report, 1956. URL https://link.springer.com/content/pdf/10.1007%2FBF01330428.pdf.

[255] O F Hagena and W Obert. Cluster Formation in Expanding Supersonic Jets: Effect of Pressure, Temperature, Nozzle Size, and Test Gas. *J. Chem. Phys.*, 56 (5):1793–1802, 1972. doi: 10.1063/1.1694827. URL http://aip.scitation.org/toc/jcp/56/5.

[256] William Thomson. On the Equilibrium of Vapour at a Curved Surface of Liquid. *Proc. R. Soc. Edinburgh*, 7:63–68, 1872. doi: 10.1017/S0370164600041729. URL http://www.journals.cambridge.org/abstract_S0370164600041729.

[257] Otto F Hagena. Nucleation and growth of clusters in expanding nozzle flows. *Surf. Sci.*, 106(1-3):101–116, may 1981. ISSN 00396028. doi: 10.1016/0039-6028(81)90187-4. URL https://linkinghub.elsevier.com/retrieve/pii/0039602881901874.

[258] O F Hagena. Condensation in Free Jets: Comparison of Rare Gases and Metals. Technical report, 1987. URL https://link.springer.com/content/pdf/10.1007%2FBF01436638.pdf.

[259] Otto F Hagena. Cluster ion sources (invited). *Rev. Sci. Instrum.*, 63(106):2374–2838, 1992. doi: 10.1063/1.3204974. URL https://doi.org/10.1063/1.1142933.

[260] Vladimir N Popok, Ingo Barke, Eleanor E.B. Campbell, and Karl-Heinz Meiwes-Broer. Cluster–surface interaction: From soft landing to implantation. *Surf. Sci. Rep.*, 66(10):347–377, oct 2011. ISSN 01675729. doi: 10.1016/j.surfrep.2011.05.002. URL https://linkinghub.elsevier.com/retrieve/pii/S0167572911000318.

[261] D. B. Fenner, R. P. Torti, L. P. Allen, N. Toyoda, A. R. Kirkpatrick, J. A. Greer, V. Difilippo, and J. Hautala. Etching and Surface Smoothing with Gas-Cluster Ion Beams. *MRS Proc.*, 585:27, jan 1999. ISSN 1946-4274. doi: 10.1557/PROC-585-27. URL http://journals.cambridge.org/abstract_S1946427400182703.

[262] J.A Greer, D.B Fenner, J. Hautala, L.P Allen, V. DiFilippo, N. Toyoda, I. Yamada, J. Matsuo, E. Minami, and H. Katsumata. Etching, smoothing, and deposition with gas-cluster ion beam technology. *Surf. Coatings Technol.*, 133-134:273–282, nov 2000. ISSN 02578972. doi: 10.1016/S0257-8972(00)00876-8. URL https://linkinghub.elsevier.com/retrieve/pii/S0257897200008768.

[263] Takaaki Aoki, Toshio Seki, and Jiro Matsuo. Molecular dynamics simulations for gas cluster ion beam processes. *Vacuum*, 84(8):994–998, mar 2010. ISSN 0042207X. doi: 10.1016/j.vacuum.2009.11.018. URL https://linkinghub.elsevier.com/retrieve/pii/S0042207X09005697.

[264] Takaaki Aoki. Molecular dynamics simulations of cluster impacts on solid targets: implantation, surface modification, and sputtering. *J. Comput. Electron.*, 13 (1):108–121, mar 2014. ISSN 1569-8025. doi: 10.1007/s10825-013-0504-5. URL http://link.springer.com/10.1007/s10825-013-0504-5.

[265] Isao Yamada. Investigation of ionized cluster beam bombardment and its applications for materials modification. *Radiat. Eff. Defects Solids*, 124(1):69–80, mar 1992. ISSN 1042-0150. doi: 10.1080/10420159208219829. URL http://www.tandfonline.com/doi/abs/10.1080/10420159208219829.

[266] Isao Yamada. Low-energy cluster ion beam modification of surfaces. *Nucl. Instruments Methods Phys. Res. Sect. B Beam Interact. with Mater. Atoms*, 148(1-4): 1–11, jan 1999. ISSN 0168583X. doi: 10.1016/S0168-583X(98)00875-1. URL https://linkinghub.elsevier.com/retrieve/pii/S0168583X98008751.

[267] Yunus Sevinchan. *Analysis of the Effects of Caesium Doping on the Properties of Zinc Oxide Layers and Inverted Hybrid Photovoltaic Devices (B. Sc. Thesis) Heidelberg University*. 2014.

[268] Sophie Negele. *Photoluminescence Quantum Efficiency of Organic-Inorganic Lead Halide Perovskite under Different Environmental Influence (B. Sc. Thesis) Heidelberg University*. 2016.

[269] John C. de Mello, H. Felix Wittmann, and Richard H. Friend. An improved experimental determination of external photoluminescence quantum efficiency. *Adv. Mater.*, 9(3):230–232, mar 1997. ISSN 0935-9648. doi: 10.1002/adma.19970090308. URL http://doi.wiley.com/10.1002/adma.19970090308.

[270] Alexandra Maria Bausch. *Department of Physics and Astronomy*. PhD thesis, Heidelberg University, 2017.

[271] David Becker-Koch. *Exploring sub-bandgap states in organic and hybrid photovoltaic materials using photothermal deflection spectroscopy*. PhD thesis, Heidelberg University, 2016.

[272] Newport Corp. Technical Note: Simulation of Solar Irradiation, 2019. URL https://www.newport.com/n/simulation-of-solar-irradiation.

[273] Clay H. Seaman. Calibration of solar cells by the reference cell method—The spectral mismatch problem. *Sol. Energy*, 29(4):291–298, jan 1982. ISSN 0038092X. doi: 10.1016/0038-092X(82)90244-4. URL https://linkinghub.elsevier.com/retrieve/pii/0038092X82902444.

[274] Vishal Shrotriya, Gang Li, Yan Yao, Tom Moriarty, Keith Emery, and Yang Yang. Accurate Measurement and Characterization of Organic Solar Cells. *Adv. Funct. Mater.*, 16(15):2016–2023, oct 2006. ISSN 1616-301X. doi: 10.1002/adfm.200600489. URL http://doi.wiley.com/10.1002/adfm.200600489.

[275] Andreas Weu. *Identifying Degradation Mechanisms in P3HT:PCBM Organic Solar Cells (M. Sc. Thesis) Heidelberg University*. 2016.

[276] Paul Faßl. *Exploration of Properties, Stability and Reproducibility of Perovskite Solar Cells*. PhD thesis, Heidelberg University, 2018.

[277] Xiangyue Meng, Guangyao Zhao, Qi Xu, Zhan'Ao Tan, Zhuxia Zhang, Li Jiang, Chunying Shu, Chunru Wang, and Yongfang Li. Effects of Fullerene Bisadduct Regioisomers on Photovoltaic Performance. *Adv. Funct. Mater.*, 24(1):158–163, jan 2014. ISSN 1616301X. doi: 10.1002/adfm.201301411. URL http://doi.wiley.com/10.1002/adfm.201301411.

[278] Chengyuan Wang, Takuya Okabe, Guankui Long, Daiki Kuzuhara, Yang Zhao, Naoki Aratani, Hiroko Yamada, and Qichun Zhang. A novel D– π –A small molecule with N -heteroacene as acceptor moiety for photovoltaic application. *Dye. Pigment.*, 122:231–237, nov 2015. ISSN 01437208. doi: 10.1016/j.dyepig.2015.06.029. URL https://linkinghub.elsevier.com/retrieve/pii/S0143720815002478.

[279] Shaobin Miao, Anthony L. Appleton, Nancy Berger, Stephen Barlow, Seth R. Marder, Kenneth I. Hardcastle, and Uwe H. F. Bunz. 6,13-Diethynyl-5,7,12,14-tetraazapentacene. *Chem. - A Eur. J.*, 15(20):4990–4993, may 2009. ISSN 09476539. doi: 10.1002/chem.200900324. URL http://doi.wiley.com/10.1002/chem.200900324.

[280] Zhixiong Liang, Qin Tang, Jianbin Xu, and Qian Miao. Soluble and Stable N-Heteropentacenes with High Field-Effect Mobility. *Adv. Mater.*, 23(13):1535–1539, apr 2011. ISSN 09359648. doi: 10.1002/adma.201004325. URL http://doi.wiley.com/10.1002/adma.201004325.

[281] Guobiao Xue, Jiake Wu, Congcheng Fan, Shuang Liu, Zhuoting Huang, Yujing Liu, Bowen Shan, Huolin L. Xin, Qian Miao, Hongzheng Chen, and Hanying Li. Boosting the electron mobility of solution-grown organic single crystals via reducing the amount of polar solvent residues. *Mater. Horizons*, 3(2):119–123, feb 2016. ISSN 2051-6347. doi: 10.1039/C5MH00190K. URL http://xlink.rsc.org/?DOI=C5MH00190K.

[282] Fabian Paulus, Jens U. Engelhart, Paul E. Hopkinson, Christian Schimpf, Andreas Leineweber, Henning Sirringhaus, Yana Vaynzof, and Uwe H. F. Bunz. The effect of tuning the microstructure of TIPS-tetraazapentacene on the performance of solution processed thin film transistors. *J. Mater. Chem. C*, 4(6):1194–1200, 2016. ISSN 2050-7526. doi: 10.1039/C5TC03326H. URL http://xlink.rsc.org/?DOI=C5TC03326H.

[283] Philipp Biegger, Olena Tverskoy, Frank Rominger, and Uwe H. F. Bunz. Synthesis of Triptycene-Substituted Azapentacene and Azahexacene Derivatives. *Chem. - A Eur. J.*, 22(45):16315–16322, nov 2016. ISSN 09476539. doi: 10.1002/chem.201603360. URL http://doi.wiley.com/10.1002/chem.201603360.

[284] Sebastian Westenhoff, Ian A. Howard, and Richard H. Friend. Probing the Morphology and Energy Landscape of Blends of Conjugated Polymers with Sub-10 nm Resolution. *Phys. Rev. Lett.*, 101(1):016102, jul 2008. ISSN 0031-9007. doi: 10.1103/PhysRevLett.101.016102. URL https://link.aps.org/doi/10.1103/PhysRevLett.101.016102.

[285] Brett M. Savoie, Akshay Rao, Artem A. Bakulin, Simon Gelinas, Bijan Movaghar, Richard H. Friend, Tobin J. Marks, and Mark A. Ratner. Unequal Partnership: Asymmetric Roles of Polymeric Donor and Fullerene Acceptor in Generating

Free Charge. *J. Am. Chem. Soc.*, 136(7):2876–2884, feb 2014. ISSN 0002-7863. doi: 10.1021/ja411859m. URL http://pubs.acs.org/doi/10.1021/ja411859m.

[286] S. Gelinas, Akshay Rao, Abhishek Kumar, Samuel L Smith, Alex W Chin, Jenny Clark, Tom S van der Poll, Guillermo C Bazan, and Richard H Friend. Ultrafast Long-Range Charge Separation in Organic Semiconductor Photovoltaic Diodes. *Science*, 343(6170):512–516, jan 2014. ISSN 0036-8075. doi: 10.1126/science.1246249. URL http://www.sciencemag.org/cgi/doi/10.1126/science.1246249.

[287] Andreas C. Jakowetz, Marcus L. Böhm, Jiangbin Zhang, Aditya Sadhanala, Sven Huettner, Artem A. Bakulin, Akshay Rao, and Richard H. Friend. What Controls the Rate of Ultrafast Charge Transfer and Charge Separation Efficiency in Organic Photovoltaic Blends. *J. Am. Chem. Soc.*, 138(36):11672–11679, sep 2016. ISSN 0002-7863. doi: 10.1021/jacs.6b05131. URL http://pubs.acs.org/doi/10.1021/jacs.6b05131.

[288] Joseph K. Gallaher, Shyamal K. K. Prasad, Mohammad A. Uddin, Taehyo Kim, Jin Young Kim, Han Young Woo, and Justin M. Hodgkiss. Spectroscopically tracking charge separation in polymer : fullerene blends with a three-phase morphology. *Energy Environ. Sci.*, 8(9):2713–2724, aug 2015. ISSN 1754-5692. doi: 10.1039/C5EE01713K. URL http://xlink.rsc.org/?DOI=C5EE01713K.

[289] Sarah Holliday, Raja Shahid Ashraf, Andrew Wadsworth, Derya Baran, Syeda Amber Yousaf, Christian B. Nielsen, Ching-Hong Tan, Stoichko D. Dimitrov, Zhengrong Shang, Nicola Gasparini, Maha Alamoudi, Frédéric Laquai, Christoph J. Brabec, Alberto Salleo, James R. Durrant, and Iain McCulloch. High-efficiency and air-stable P3HT-based polymer solar cells with a new non-fullerene acceptor. *Nat. Commun.*, 7(1):11585, sep 2016. ISSN 2041-1723. doi: 10.1038/ncomms11585. URL http://www.nature.com/articles/ncomms11585.

[290] Paul E. Shaw, Pascal Wolfer, Benjamin Langley, Paul L. Burn, and Paul Meredith. Impact of Acceptor Crystallinity on the Photophysics of Nonfullerene Blends for Organic Solar Cells. *J. Phys. Chem. C*, 118(25):13460–13466, jun 2014. ISSN 1932-7447. doi: 10.1021/jp503150u. URL http://pubs.acs.org/doi/10.1021/jp503150u.

[291] Safa Shoaee, Florent Deledalle, Pabitra Shakya Tuladhar, Ravichandran Shivanna, Sridhar Rajaram, K. S. Narayan, and James R. Durrant. A Comparison of Charge Separation Dynamics in Organic Blend Films Employing Fullerene and Perylene Diimide Electron Acceptors. *J. Phys. Chem. Lett.*, 6(1):201–205, jan 2015. ISSN 1948-7185. doi: 10.1021/jz502385n. URL http://pubs.acs.org/doi/10.1021/jz502385n.

[292] Seihou Jinnai, Yutaka Ie, Yuki Kashimoto, Hiroyuki Yoshida, Makoto Karakawa, and Yoshio Aso. Three-dimensional π-conjugated compounds as non-fullerene acceptors in organic photovoltaics: the influence of acceptor unit orientation at

phase interfaces on photocurrent generation efficiency. *J. Mater. Chem. A*, 5(8): 3932–3938, feb 2017. ISSN 2050-7488. doi: 10.1039/C6TA10608K. URL http://xlink.rsc.org/?DOI=C6TA10608K.

[293] Uwe H. F. Bunz. The Larger Linear N-Heteroacenes. *Acc. Chem. Res.*, 48(6): 1676–1686, jun 2015. ISSN 0001-4842. doi: 10.1021/acs.accounts.5b00118. URL http://pubs.acs.org/doi/10.1021/acs.accounts.5b00118.

[294] Christoph Wetzel, Amaresh Mishra, Elena Mena-Osteritz, Andreas Liess, Matthias Stolte, Frank Würthner, and Peter Bäuerle. Synthesis and Structural Analysis of Thiophene-Pyrrole-Based S , N -Heteroacenes. *Org. Lett.*, 16(2):362–365, jan 2014. ISSN 1523-7060. doi: 10.1021/ol403153z. URL http://pubs.acs.org/doi/10.1021/ol403153z.

[295] Shuaijun Yang, Bowen Shan, Xiaomin Xu, and Qian Miao. Extension of N-Heteroacenes through a Four-Membered Ring. *Chem. - A Eur. J.*, 22(19):6637–6642, may 2016. ISSN 09476539. doi: 10.1002/chem.201600918. URL http://doi.wiley.com/10.1002/chem.201600918.

[296] Fabian Paulus, Michael Porz, Manuel Schaffroth, Frank Rominger, Andreas Leineweber, Yana Vaynzof, and Uwe H.F. Bunz. Side-group engineering: The influence of norbornadienyl substituents on the properties of ethynylated pentacene and tetraazapentacene. *Org. Electron.*, 33:102–109, jun 2016. ISSN 15661199. doi: 10.1016/j.orgel.2016.02.042. URL https://linkinghub.elsevier.com/retrieve/pii/S1566119916300878.

[297] Yuxia Chen, Xin Zhang, Chuanlang Zhan, and Jiannian Yao. Origin of Effects of Additive Solvent on Film-Morphology in Solution-Processed Nonfullerene Solar Cells. *ACS Appl. Mater. Interfaces*, 7(12):6462–6471, apr 2015. ISSN 1944-8244. doi: 10.1021/am507581w. URL http://pubs.acs.org/doi/10.1021/am507581w.

[298] Mingguang Li, Qiuju Liang, Qiaoqiao Zhao, Ke Zhou, Xinhong Yu, Zhiyuan Xie, Jiangang Liu, and Yanchun Han. A bi-continuous network structure of p-DTS(FBTTh 2) 2 /EP-PDI via selective solvent vapor annealing. *J. Mater. Chem. C*, 4(42):10095–10104, oct 2016. ISSN 2050-7526. doi: 10.1039/C6TC03061K. URL http://xlink.rsc.org/?DOI=C6TC03061K.

[299] Andrew Namepetra, Elizabeth Kitching, Ala'a F. Eftaiha, Ian G. Hill, and Gregory C. Welch. Understanding the morphology of solution processed fullerene-free small molecule bulk heterojunction blends. *Phys. Chem. Chem. Phys.*, 18 (18):12476–12485, may 2016. ISSN 1463-9076. doi: 10.1039/C6CP01269H. URL http://xlink.rsc.org/?DOI=C6CP01269H.

[300] Lingxian Meng, Yamin Zhang, Xiangjian Wan, Chenxi Li, Xin Zhang, Yanbo Wang, Xin Ke, Zuo Xiao, Liming Ding, Ruoxi Xia, Hin-Lap Yip, Yong Cao, and Yongsheng Chen. Organic and solution-processed tandem solar cells with 17.3efficiency. *Science*, 361(6407):1094–1098, sep 2018. ISSN 0036-8075. doi:

10.1126/science.aat2612. URL http://www.sciencemag.org/lookup/doi/10.1126/science.aat2612.

[301] Derya Baran, Nicola Gasparini, Andrew Wadsworth, Ching Hong Tan, Nimer Wehbe, Xin Song, Zeinab Hamid, Weimin Zhang, Marios Neophytou, Thomas Kirchartz, Christoph J. Brabec, James R. Durrant, and Iain McCulloch. Robust nonfullerene solar cells approaching unity external quantum efficiency enabled by suppression of geminate recombination. *Nat. Commun.*, 9(1):1–9, 2018. ISSN 20411723. doi: 10.1038/s41467-018-04502-3. URL http://dx.doi.org/10.1038/s41467-018-04502-3.

[302] Kai Zhang, Zhicheng Hu, Chen Sun, Zhihong Wu, Fei Huang, and Yong Cao. Toward Solution-Processed High-Performance Polymer Solar Cells: from Material Design to Device Engineering. *Chem. Mater.*, 29(1):141–148, jan 2017. ISSN 0897-4756. doi: 10.1021/acs.chemmater.6b02802. URL http://pubs.acs.org/doi/10.1021/acs.chemmater.6b02802.

[303] K. Vandewal, J. Benduhn, and V. C. Nikolis. How to determine optical gaps and voltage losses in organic photovoltaic materials. *Sustain. Energy & Fuels*, 2(3):538–544, 2018. ISSN 2398-4902. doi: 10.1039/C7SE00601B. URL http://xlink.rsc.org/?DOI=C7SE00601B.

[304] Akira Tada, Yanfang Geng, Qingshuo Wei, Kazuhito Hashimoto, and Keisuke Tajima. Tailoring organic heterojunction interfaces in bilayer polymer photovoltaic devices. *Nat. Mater.*, 10(6):450–455, jun 2011. ISSN 1476-1122. doi: 10.1038/nmat3026. URL http://www.nature.com/articles/nmat3026.

[305] Ming Wang, Hengbin Wang, Takamichi Yokoyama, Xiaofeng Liu, Ye Huang, Yuan Zhang, Thuc-Quyen Nguyen, Shinji Aramaki, and Guillermo C. Bazan. High Open Circuit Voltage in Regioregular Narrow Band Gap Polymer Solar Cells. *J. Am. Chem. Soc.*, 136(36):12576–12579, sep 2014. ISSN 0002-7863. doi: 10.1021/ja506785w. URL http://pubs.acs.org/doi/10.1021/ja506785w.

[306] Kazuaki Kawashima, Yasunari Tamai, Hideo Ohkita, Itaru Osaka, and Kazuo Takimiya. High-efficiency polymer solar cells with small photon energy loss. *Nat. Commun.*, 6(1):10085, dec 2015. ISSN 2041-1723. doi: 10.1038/ncomms10085. URL http://www.nature.com/articles/ncomms10085.

[307] Jianquan Zhang, Huei Shuan Tan, Xugang Guo, Antonio Facchetti, and He Yan. Material insights and challenges for non-fullerene organic solar cells based on small molecular acceptors. *Nat. Energy*, 3(9):720–731, sep 2018. ISSN 2058-7546. doi: 10.1038/s41560-018-0181-5. URL http://www.nature.com/articles/s41560-018-0181-5.

[308] Derya Baran, Raja Shahid Ashraf, David A. Hanifi, Maged Abdelsamie, Nicola Gasparini, Jason A. Röhr, Sarah Holliday, Andrew Wadsworth, Sarah Lockett, Marios Neophytou, Christopher J. M. Emmott, Jenny Nelson, Christoph J.

Brabec, Aram Amassian, Alberto Salleo, Thomas Kirchartz, James R. Durrant, and Iain McCulloch. Reducing the efficiency–stability–cost gap of organic photovoltaics with highly efficient and stable small molecule acceptor ternary solar cells. *Nat. Mater.*, 16(3):363–369, mar 2017. ISSN 1476-1122. doi: 10.1038/nmat4797. URL http://www.nature.com/articles/nmat4797.

[309] Nicola Gasparini, Luca Lucera, Michael Salvador, Mario Prosa, George D. Spyropoulos, Peter Kubis, Hans-Joachim Egelhaaf, Christoph J. Brabec, and Tayebeh Ameri. High-performance ternary organic solar cells with thick active layer exceeding 11 *Energy Environ. Sci.*, 10(4):885–892, apr 2017. ISSN 1754-5692. doi: 10.1039/C6EE03599J. URL http://xlink.rsc.org/?DOI=C6EE03599J.

[310] Kuan Sun, Zeyun Xiao, Shirong Lu, Wojciech Zajaczkowski, Wojciech Pisula, Eric Hanssen, Jonathan M. White, Rachel M. Williamson, Jegadesan Subbiah, Jianyong Ouyang, Andrew B. Holmes, Wallace W.H. Wong, and David J. Jones. A molecular nematic liquid crystalline material for high-performance organic photovoltaics. *Nat. Commun.*, 6(1):6013, dec 2015. ISSN 2041-1723. doi: 10.1038/ncomms7013. URL http://www.nature.com/articles/ncomms7013.

[311] Elisabeth H. Menke, Vincent Lami, Yana Vaynzof, and Michael Mastalerz. Pi-Extended rigid triptycene-trisaroylenimidazoles as electron acceptors. *Chem. Commun.*, 52(5):1048–1051, 2016. ISSN 1359-7345. doi: 10.1039/C5CC07238G. URL http://xlink.rsc.org/?DOI=C5CC07238G.

[312] Yongfang Li. Molecular Design of Photovoltaic Materials for Polymer Solar Cells: Toward Suitable Electronic Energy Levels and Broad Absorption. *Acc. Chem. Res.*, 45(5):723–733, may 2012. ISSN 0001-4842. doi: 10.1021/ar2002446. URL http://pubs.acs.org/doi/10.1021/ar2002446.

[313] Jarvist Moore Frost, Mark Anton Faist, and Jenny Nelson. Energetic Disorder in Higher Fullerene Adducts: A Quantum Chemical and Voltammetric Study. *Adv. Mater.*, 22(43):4881–4884, nov 2010. ISSN 09359648. doi: 10.1002/adma.201002189. URL http://doi.wiley.com/10.1002/adma.201002189.

[314] Evan J. Spadafora, Renaud Demadrille, Bernard Ratier, and Benjamin Grevin. Imaging the Carrier Photogeneration in Nanoscale Phase Segregated Organic Heterojunctions by Kelvin Probe Force Microscopy. *Nano Lett.*, 10(9):3337–3342, sep 2010. ISSN 1530-6984. doi: 10.1021/nl101001d. URL http://pubs.acs.org/doi/abs/10.1021/nl101001d.

[315] Hisao Ishii and Kazuhiko Seki. Energy level alignment at organic/metal interfaces studied by UV photoemission: breakdown of traditional assumption of a common vacuum level at the interface. *IEEE Trans. Electron Devices*, 44 (8):1295–1301, 1997. ISSN 00189383. doi: 10.1109/16.605471. URL http://ieeexplore.ieee.org/document/605471/.

[316] Wing C. Tsoi, Steve J. Spencer, Li Yang, Amy M. Ballantyne, Patrick G. Nicholson, Alan Turnbull, Alex G. Shard, Craig E. Murphy, Donal D. C. Bradley,

Jenny Nelson, and Ji-Seon Kim. Effect of Crystallization on the Electronic Energy Levels and Thin Film Morphology of P3HT:PCBM Blends. *Macromolecules*, 44(8):2944–2952, apr 2011. ISSN 0024-9297. doi: 10.1021/ma102841e. URL http://pubs.acs.org/doi/abs/10.1021/ma102841e.

[317] Yu-Jui Huang, Wei-Chun Lo, Shun-Wei Liu, Chao-Han Cheng, Chin-Ti Chen, and Juen-Kai Wang. Unified assay of adverse effects from the varied nanoparticle hybrid in polymer–fullerene organic photovoltaics. *Sol. Energy Mater. Sol. Cells*, 116:153–170, sep 2013. ISSN 0927-0248. doi: 10.1016/J.SOLMAT.2013.03.031. URL https://www.sciencedirect.com/science/article/pii/S092702481300144X.

[318] Tayebeh Ameri, Jie Min, Ning Li, Florian Machui, Derya Baran, Michael Forster, Kristina J. Schottler, Daniel Dolfen, Ullrich Scherf, and Christoph J. Brabec. Performance Enhancement of the P3HT/PCBM Solar Cells through NIR Sensitization Using a Small-Bandgap Polymer. *Adv. Energy Mater.*, 2(10):1198–1202, oct 2012. ISSN 16146832. doi: 10.1002/aenm.201200219. URL http://doi.wiley.com/10.1002/aenm.201200219.

[319] Sayantan Das and T. L. Alford. Improved efficiency of P3HT:PCBM solar cells by incorporation of silver oxide interfacial layer. *J. Appl. Phys.*, 116(4):044905, jul 2014. ISSN 0021-8979. doi: 10.1063/1.4891246. URL http://aip.scitation.org/doi/10.1063/1.4891246.

[320] Steffen Duhm, Georg Heimel, Ingo Salzmann, Hendrik Glowatzki, Robert L Johnson, Antje Vollmer, Jürgen P. Rabe, and Norbert Koch. Orientation-dependent ionization energies and interface dipoles in ordered molecular assemblies. *Nat. Mater.*, 7(4):326–332, apr 2008. ISSN 1476-1122. doi: 10.1038/nmat2119. URL http://www.nature.com/articles/nmat2119.

[321] David Cahen and Antoine Kahn. Electron Energetics at Surfaces and Interfaces: Concepts and Experiments. *Adv. Mater.*, 15(4):271–277, feb 2003. ISSN 09359648. doi: 10.1002/adma.200390065. URL http://doi.wiley.com/10.1002/adma.200390065.

[322] Johannes Benduhn, Kristofer Tvingstedt, Fortunato Piersimoni, Sascha Ullbrich, Yeli Fan, Manuel Tropiano, Kathryn A. McGarry, Olaf Zeika, Moritz K. Riede, Christopher J. Douglas, Stephen Barlow, Seth R. Marder, Dieter Neher, Donato Spoltore, and Koen Vandewal. Intrinsic non-radiative voltage losses in fullerene-based organic solar cells. *Nat. Energy*, 2(6):17053, apr 2017. ISSN 2058-7546. doi: 10.1038/nenergy.2017.53. URL http://www.nature.com/articles/nenergy201753.

[323] Flurin D Eisner, Mohammed Azzouzi, Zhuping Fei, Xueyan Hou, Thomas D Anthopoulos, T. John S. Dennis, Martin Heeney, and Jenny Nelson. Hybridization of Local Exciton and Charge-Transfer States Reduces Nonradiative Voltage Losses in Organic Solar Cells. *J. Am. Chem. Soc.*, 141(15):6362–6374, apr 2019.

ISSN 0002-7863. doi: 10.1021/jacs.9b01465. URL http://pubs.acs.org/doi/10.1021/jacs.9b01465.

[324] Qing-Dan Yang, Ho-Wa Li, Yuanhang Cheng, Zhiqiang Guan, Taili Liu, Tsz-Wai Ng, Chun-Sing Lee, and Sai-Wing Tsang. Probing the Energy Level Alignment and the Correlation with Open-Circuit Voltage in Solution-Processed Polymeric Bulk Heterojunction Photovoltaic Devices. *ACS Appl. Mater. Interfaces*, 8 (11):7283–7290, mar 2016. ISSN 1944-8244. doi: 10.1021/acsami.5b11395. URL http://pubs.acs.org/doi/10.1021/acsami.5b11395.

[325] Lothar Ley, Yaou Smets, Christopher I. Pakes, and Jürgen Ristein. Calculating the Universal Energy-Level Alignment of Organic Molecules on Metal Oxides. *Adv. Funct. Mater.*, 23(7):794–805, feb 2013. ISSN 1616301X. doi: 10.1002/adfm.201201412. URL http://doi.wiley.com/10.1002/adfm.201201412.

[326] Nir Tessler and Yana Vaynzof. Preventing Hysteresis in Perovskite Solar Cells by Undoped Charge Blocking Layers. *ACS Appl. Energy Mater.*, 1(2):676–683, feb 2018. ISSN 2574-0962. doi: 10.1021/acsaem.7b00176. URL http://pubs.acs.org/doi/10.1021/acsaem.7b00176.

[327] Qi Chen, Lin Mao, Yaowen Li, Tao Kong, Na Wu, Changqi Ma, Sai Bai, Yizheng Jin, Dan Wu, Wei Lu, Bing Wang, and Liwei Chen. Quantitative o perando visualization of the energy band depth profile in solar cells. *Nat. Commun.*, 6 (1):7745, nov 2015. ISSN 2041-1723. doi: 10.1038/ncomms8745. URL http://www.nature.com/articles/ncomms8745.

[328] Zequn Cui, Jianxia Sun, Dominik Landerer, Christian Sprau, Richard Thelen, Alexander Colsmann, Hendrik Hölscher, Wanli Ma, and Lifeng Chi. Seeing Down to the Bottom: Nondestructive Inspection of All-Polymer Solar Cells by Kelvin Probe Force Microscopy. *Adv. Mater. Interfaces*, 3(18):1600446, sep 2016. ISSN 21967350. doi: 10.1002/admi.201600446. URL http://doi.wiley.com/10.1002/admi.201600446.

[329] Qi Chen, Fengye Ye, Junqi Lai, Pan Dai, Shulong Lu, Changqi Ma, Yanfei Zhao, and Yi Xie. Energy band alignment in operando inverted structure P3HT:PCBM organic solar cells. *Nano Energy*, 40(July):454–461, 2017. ISSN 2211-2855. doi: 10.1016/j.nanoen.2017.08.050. URL http://dx.doi.org/10.1016/j.nanoen.2017.08.050.

[330] Mathias List, Tanmoy Sarkar, Pavlo Perkhun, Jörg Ackermann, Chieh Luo, and Uli Würfel. Correct determination of charge transfer state energy from luminescence spectra in organic solar cells. *Nat. Commun.*, 9(1):3631, dec 2018. ISSN 2041-1723. doi: 10.1038/s41467-018-05987-8. URL http://www.nature.com/articles/s41467-018-05987-8.

[331] F Krok, K Sajewicz, J Konior, M Goryl, P Piatkowski, and M Szymonski. Lateral resolution and potential sensitivity in Kelvin probe force microscopy: Towards

understanding of the sub-nanometer resolution. *Phys. Rev. B*, 77(23):235427, jun 2008. ISSN 1098-0121. doi: 10.1103/PhysRevB.77.235427. URL https://link.aps.org/doi/10.1103/PhysRevB.77.235427.

[332] Sascha Sadewasser and Thilo Glatzel. *Kelvin Probe Force Microscopy*, volume 65 of *Springer Series in Surface Sciences*. Springer International Publishing, Cham, 2018. ISBN 978-3-319-75686-8. doi: 10.1007/978-3-319-75687-5. URL http://link.springer.com/10.1007/978-3-319-75687-5.

[333] Nobuo Ueno, Satoshi Kera, and Kaname Kanai. Fundamental Electronic Structure of Organic Solids and Their Interfaces by Photoemission Spectroscopy and Related Methods. In Norbert Koch, Nobuo Ueno, and Andrew T.S. Wee, editors, *Mol. Interface*, chapter 7, pages 173–217. Wiley-VCH Verlag GmbH & Co. KGaA, Weinheim, Germany, mar 2013. ISBN 9783527653171. doi: 10.1002/9783527653171.ch7. URL http://doi.wiley.com/10.1002/9783527653171.ch7.

[334] L. Ley, M. Cardona, and R. A. Pollak. Photoemission in semiconductors. pages 11–172. Springer, Berlin, Heidelberg, 1979. doi: 10.1007/3-540-09202-1_2. URL http://link.springer.com/10.1007/3-540-09202-1_2.

[335] S. Olthof, R. Meerheim, M. Schober, and K. Leo. Energy level alignment at the interfaces in a multilayer organic light-emitting diode structure. *Phys. Rev. B*, 79 (24):245308, jun 2009. ISSN 1098-0121. doi: 10.1103/PhysRevB.79.245308. URL https://link.aps.org/doi/10.1103/PhysRevB.79.245308.

[336] K. Akaike, N. Koch, and M. Oehzelt. Fermi level pinning induced electrostatic fields and band bending at organic heterojunctions. *Appl. Phys. Lett.*, 105(22): 223303, dec 2014. ISSN 0003-6951. doi: 10.1063/1.4903360. URL http://aip.scitation.org/doi/10.1063/1.4903360.

[337] Selina Olthof and Klaus Meerholz. Substrate-dependent electronic structure and film formation of MAPbI3 perovskites. *Sci. Rep.*, 7(1):40267, dec 2017. ISSN 2045-2322. doi: 10.1038/srep40267. URL http://www.nature.com/articles/srep40267.

[338] David B. Hall, Patrick Underhill, and John M. Torkelson. Spin coating of thin and ultrathin polymer films. *Polym. Eng. Sci.*, 38(12):2039–2045, dec 1998. ISSN 0032-3888. doi: 10.1002/pen.10373. URL http://doi.wiley.com/10.1002/pen.10373.

[339] Serap Günes, Helmut Neugebauer, and Niyazi Serdar Sariciftci. Conjugated Polymer-Based Organic Solar Cells. *Chem. Rev.*, 107(4):1324–1338, apr 2007. ISSN 0009-2665. doi: 10.1021/cr050149z. URL https://pubs.acs.org/doi/10.1021/cr050149z.

[340] D Karpuzov, K L Kostov, E Venkova, P Kirova, I Katardjiev, and G Carter. Xps Study Of Ion Beam Irradiation Effects In Polyimide Layers. *Nucl. Instruments Methods Phys. Res. B3Y*, pages 787–791, 1989. URL https:

//ac.els-cdn.com/0168583X89908975/1-s2.0-0168583X89908975-main.pdf?_tid=fa47b004-10cd-11e8-9ec7-00000aacb35d&acdnat=1518533929_93584290877924bfc501d0ed4f26aa75.

[341] A De Bonis, A Bearzotti, and G Marletta. Structural modifications and electrical properties in ion-irradiated polyimide. *Nucl. Instruments Methods Phys. Res. B*, 151:101–108, 1999. URL https://ac.els-cdn.com/S0168583X99001354/1-s2.0-S0168583X99001354-main.pdf?_tid=db541204-10ce-11e8-8108-00000aacb35e&acdnat=1518534323_ffeb77147557d0e61ef32b53d63d3fc1.

[342] J. L S Lee, S. Ninomiya, J. Matsuo, I. S. Gilmore, M. P. Seah, and A. G. Shard. Organic Depth Profiling of a Nanostructured Delta Layer Reference Material Using Large Argon Cluster Ions. *Anal. Chem.*, 82(1):98–105, jan 2010. ISSN 0003-2700. doi: 10.1021/ac901045q. URL https://pubs.acs.org/doi/10.1021/ac901045q.

[343] Alexander G. Shard, Rasmus Havelund, Martin P. Seah, Steve J. Spencer, Ian S. Gilmore, Nicholas Winograd, Dan Mao, Takuya Miyayama, Ewald Niehuis, Derk Rading, and Rudolf Moellers. Argon Cluster Ion Beams for Organic Depth Profiling: Results from a VAMAS Interlaboratory Study. *Anal. Chem.*, 84(18):7865–7873, sep 2012. ISSN 0003-2700. doi: 10.1021/ac301567t. URL http://pubs.acs.org/doi/10.1021/ac301567t.

[344] Alexander G. Shard, Rasmus Havelund, Steve J. Spencer, Ian S. Gilmore, Morgan R. Alexander, Tina B. Angerer, Satoka Aoyagi, Jean-Paul Barnes, Anass Benayad, Andrzej Bernasik, Giacomo Ceccone, Jonathan D. P. Counsell, Christopher Deeks, John S. Fletcher, Daniel J. Graham, Christian Heuser, Tae Geol Lee, Camille Marie, Mateusz M. Marzec, Gautam Mishra, Derk Rading, Olivier Renault, David J. Scurr, Hyun Kyong Shon, Valentina Spampinato, Hua Tian, Fuyi Wang, Nicholas Winograd, Kui Wu, Andreas Wucher, Yufan Zhou, and Zihua Zhu. Measuring Compositions in Organic Depth Profiling: Results from a VAMAS Interlaboratory Study. *J. Phys. Chem. B*, 119(33):10784–10797, aug 2015. ISSN 1520-6106. doi: 10.1021/acs.jpcb.5b05625. URL http://pubs.acs.org/doi/10.1021/acs.jpcb.5b05625.

[345] D.-J. Yun, C. Jung, H.-I. Lee, K.-H. Kim, Y. K. Kyoung, A. Benayad, and J. Chung. Damage-Free Photoemission Study of Conducting Carbon Composite Electrode Using Ar Gas Cluster Ion Beam Sputtering Process. *J. Electrochem. Soc.*, 159(7): H626–H632, 2012. ISSN 0013-4651. doi: 10.1149/2.011207jes. URL http://jes.ecsdl.org/cgi/doi/10.1149/2.011207jes.

[346] Kan Shen, Andreas Wucher, and Nicholas Winograd. Molecular Depth Profiling with Argon Gas Cluster Ion Beams. *J. Phys. Chem. C*, 119(27):15316–15324, jul 2015. ISSN 1932-7447. doi: 10.1021/acs.jpcc.5b03482. URL http://pubs.acs.org/doi/10.1021/acs.jpcc.5b03482.

[347] T Terlier, G Zappala, C Marie, D Leonard, J-p Barnes, and A Licciardello. ToF-SIMS Depth Profiling of PS-b-PMMA Block Copolymers Using Arn +, C60 ++, and Cs+ Sputtering Ions. *Anal. Chem.*, 89:6984–6991, 2017. doi: 10.1021/acs.analchem.7b00279. URL http://pubs.acs.org/doi/pdf/10.1021/acs.analchem.7b00279.

[348] Satoshi Ninomiya, Kazuya Ichiki, Hideaki Yamada, Yoshihiko Nakata, Toshio Seki, Takaaki Aoki, and Jiro Matsuo. Molecular depth profiling of multilayer structures of organic semiconductor materials by secondary ion mass spectrometry with large argon cluster ion beams. *Rapid Commun. Mass Spectrom.*, 23 (20):3264–3268, oct 2009. ISSN 09514198. doi: 10.1002/rcm.4250. URL http://doi.wiley.com/10.1002/rcm.4250.

[349] Motohiro Tanaka, Kousuke Moritani, Tomokazu Hirota, Noriaki Toyoda, Isao Yamada, Norio Inui, and Kozo Mochiji. Enhanced surface sensitivity in secondary ion mass spectrometric analysis of organic thin films using size-selected Ar gas-cluster ion projectiles. *Rapid Commun. Mass Spectrom.*, 24(10):1405–1410, may 2010. ISSN 09514198. doi: 10.1002/rcm.4529. URL http://doi.wiley.com/10.1002/rcm.4529.

[350] T. Terlier, R. Tiron, A. Gharbi, X. Chevalier, M. Veillerot, E. Martinez, and J.-P. Barnes. Investigation of block depth distribution in PS- b-PMMA block copolymer using ultra-low-energy cesium sputtering in ToF-SIMS. *Surf. Interface Anal.*, 46(2):83–91, feb 2014. doi: 10.1002/sia.5353. URL http://doi.wiley.com/10.1002/sia.5353.

[351] Dong-Jin Yun, Jaegwan Chung, Changhoon Jung, Ki-Hong Kim, Woonjoong Baek, Hyouksoo Han, Benayad Anass, Gyeong-Su Park, and Sung-Hoon Park. An electronic structure reinterpretation of the organic semiconductor/electrode interface based on argon gas cluster ion beam sputtering investigations. *J. Appl. Phys.*, 114(1):013703, jul 2013. ISSN 0021-8979. doi: 10.1063/1.4812582. URL http://aip.scitation.org/doi/10.1063/1.4812582.

[352] Dong-Jin Yun, JaeGwan Chung, Yongsu Kim, Sung-Hoon Park, Seong-Heon Kim, and Sung Heo. Direct comparative study on the energy level alignments in unoccupied/occupied states of organic semiconductor/electrode interface by constructing in-situ photoemission spectroscopy and Ar gas cluster ion beam sputtering integrated analysis system. *J. Appl. Phys.*, 116(15):153702, oct 2014. ISSN 0021-8979. doi: 10.1063/1.4897517. URL http://aip.scitation.org/doi/10.1063/1.4897517.

[353] Takuya Miyayama, Noriaki Sanada, Scott R. Bryan, John S. Hammond, and Mineharu Suzuki. Removal of Ar+ beam-induced damaged layers from polyimide surfaces with argon gas cluster ion beams. *Surf. Interface Anal.*, 42(9):1453–1457, jul 2010. ISSN 01422421. doi: 10.1002/sia.3675. URL http://doi.wiley.com/10.1002/sia.3675.

[354] Rossana Grilli, Robin Simpson, Christopher F Mallinson, and Mark A Baker. Comparison of Ar + Monoatomic and Cluster Ion Sputtering of Ta 2 O 5 at Different Ion Energies, by XPS: Part 2 - Cluster Ions. *Surf. Sci. Spectra*, 21 (1):68–83, dec 2014. ISSN 1055-5269. doi: 10.1116/11.20140702. URL http://avs.scitation.org/doi/10.1116/11.20140702.

[355] R. Steinberger, J. Walter, T. Greunz, J. Duchoslav, M. Arndt, S. Molodtsov, D. C. Meyer, and D. Stifter. XPS study of the effects of long-term Ar⁺ ion and Ar cluster sputtering on the chemical degradation of hydrozincite and iron oxide. *Corros. Sci.*, 99:66–75, 2015. ISSN 0010938X. doi: 10.1016/j.corsci.2015.06.019. URL http://dx.doi.org/10.1016/j.corsci.2015.06.019.

[356] Robin Simpson, Richard G. White, John F. Watts, and Mark A. Baker. XPS investigation of monatomic and cluster argon ion sputtering of tantalum pentoxide. *Appl. Surf. Sci.*, 405:79–87, may 2017. ISSN 0169-4332. doi: 10.1016/J.APSUSC.2017.02.006. URL https://www.sciencedirect.com/science/article/pii/S0169433217303574.

[357] Yvonne J Hofstetter and Yana Vaynzof. Quantifying the Damage Induced by X-ray Photoelectron Spectroscopy Depth Profiling of Organic Conjugated Polymers. *ACS Appl. Polym. Mater.*, page acsapm.9b00148, may 2019. ISSN 2637-6105. doi: 10.1021/acsapm.9b00148. URL http://pubs.acs.org/doi/10.1021/acsapm.9b00148.

[358] Satoshi Ninomiya, Kazuya Ichiki, Hideaki Yamada, Yoshihiko Nakata, Toshio Seki, Takaaki Aoki, and Jiro Matsuo. The effect of incident energy on molecular depth profiling of polymers with large Ar cluster ion beams. *Surf. Interface Anal.*, 43(1-2):221–224, jan 2011. doi: 10.1002/sia.3656. URL http://doi.wiley.com/10.1002/sia.3656.

[359] Satoka Aoyagi, Kousuke Moritani, and Kozo Mochiji. Evaluation of immobilized polypeptides with different C-terminal residues using argon gas-cluster SIMS. *Surf. Interface Anal.*, 43(1-2):344–349, jan 2011. ISSN 01422421. doi: 10.1002/sia.3554. URL http://doi.wiley.com/10.1002/sia.3554.

[360] John C. Vickerman and David Briggs. *ToF-SIMS: Materials Analysis by Mass Spectrometry - 2nd Edition*. IM Publications, 2nd edition, 2013.

[361] Zbigniew Postawa, Bartlomiej Czerwinski, Marek Szewczyk, Edward J. Smiley, Nicholas Winograd, and Barbara J. Garrison. Enhancement of Sputtering Yields Due to C60 versus Ga Bombardment of Ag111 As Explored by Molecular Dynamics Simulations. *Anal. Chem.*, 75(17):4402–4407, 2003. doi: 10.1021/AC034387A. URL https://pubs.acs.org/doi/abs/10.1021/ac034387a.

[362] Zbigniew Postawa, Bartlomiej Czerwinski, Nicholas Winograd, and Barbara J. Garrison. Microscopic Insights into the Sputtering of Thin Organic Films on

Ag111 Induced by C60 and Ga Bombardment. *J. Phys. Chem. B*, 109(24):11973–11979, 2005. doi: 10.1021/JP050821W. URL https://pubs.acs.org/doi/abs/10.1021/jp050821w.

[363] Dong Jin Yun, Weon Ho Shin, Xavier Bulliard, Jong Hwan Park, Seyun Kim, Jae Gwan Chung, Yongsu Kim, Sung Heo, and Seong Heon Kim. Direct characterization of the energy level alignments and molecular components in an organic hetero-junction by integrated photoemission spectroscopy and reflection electron energy loss spectroscopy analysis. *Nanotechnology*, 27(34):1–11, 2016. ISSN 13616528. doi: 10.1088/0957-4484/27/34/345704. URL http://dx.doi.org/10.1088/0957-4484/27/34/345704.

[364] Yana Vaynzof, Dinesh Kabra, Lihong Zhao, Lay Lay Chua, Ullrich Steiner, and Richard H Friend. Surface-Directed Spinodal Decomposition in Poly[3-hexylthiophene] and C 61 -Butyric Acid Methyl Ester Blends. *ACS Nano*, 5 (1):329–336, jan 2011. ISSN 1936-0851. doi: 10.1021/nn102899g. URL http://pubs.acs.org/doi/10.1021/nn102899g.

[365] Zheng Xu, Li-Min Chen, Mei-Hsin Chen, Gang Li, and Yang Yang. Energy level alignment of poly(3-hexylthiophene): [6,6]-phenyl C61 butyric acid methyl ester bulk heterojunction. *Appl. Phys. Lett.*, 95(1):013301, jul 2009. ISSN 0003-6951. doi: 10.1063/1.3163056. URL http://aip.scitation.org/doi/10.1063/1.3163056.

[366] Zheng Xu, Li-Min Chen, Guanwen Yang, Chun-Hao Huang, Jianhui Hou, Yue Wu, Gang Li, Chain-Shu Hsu, and Yang Yang. Vertical Phase Separation in Poly(3-hexylthiophene): Fullerene Derivative Blends and its Advantage for Inverted Structure Solar Cells. *Adv. Funct. Mater.*, 19(8):1227–1234, apr 2009. ISSN 1616301X. doi: 10.1002/adfm.200801286. URL http://doi.wiley.com/10.1002/adfm.200801286.

[367] Xiaoxi He, Brian A. Collins, Benjamin Watts, Harald Ade, and Christopher R. McNeill. Studying Polymer/Fullerene Intermixing and Miscibility in Laterally Patterned Films with X-Ray Spectromicroscopy. *Small*, 8(12):1920–1927, jun 2012. doi: 10.1002/smll.201102382. URL http://doi.wiley.com/10.1002/smll.201102382.

[368] Neil D. Treat, Michael A. Brady, Gordon Smith, Michael F. Toney, Edward J. Kramer, Craig J. Hawker, and Michael L. Chabinyc. Interdiffusion of PCBM and P3HT Reveals Miscibility in a Photovoltaically Active Blend. *Adv. Energy Mater.*, 1(1):82–89, jan 2011. ISSN 16146832. doi: 10.1002/aenm.201000023. URL http://doi.wiley.com/10.1002/aenm.201000023.

[369] J. B. Pendry. New Probe for Unoccupied Bands at Surfaces. *Phys. Rev. Lett.*, 45 (16):1356–1358, oct 1980. ISSN 0031-9007. doi: 10.1103/PhysRevLett.45.1356. URL https://link.aps.org/doi/10.1103/PhysRevLett.45.1356.

[370] Hiroyuki Yoshida. Near-ultraviolet inverse photoemission spectroscopy using ultra-low energy electrons. *Chem. Phys. Lett.*, 539-540:180–185, 2012. doi: 10.

1016/j.cplett.2012.04.058. URL http://dx.doi.org/10.1016/j.cplett.2012.04.058.

[371] S Matthew Menke, Alexandre Cheminal, Patrick Conaghan, Niva A Ran, Neil C Greehnam, Guillermo C Bazan, Thuc-Quyen Nguyen, Akshay Rao, and Richard H Friend. Order enables efficient electron-hole separation at an organic heterojunction with a small energy loss. *Nat. Commun.*, 9(1):277, dec 2018. ISSN 2041-1723. doi: 10.1038/s41467-017-02457-5. URL http://www.nature.com/articles/s41467-017-02457-5.

[372] Yvonne J Hofstetter, Paul E Hopkinson, Artem A Bakulin, and Yana Vaynzof. Simultaneous enhancement in open circuit voltage and short circuit current of hybrid organic–inorganic photovoltaics by inorganic interfacial modification. *J. Mater. Chem. C*, 4(4):1111–1116, 2016. doi: 10.1039/c5tc03206g. URL http://pubs.rsc.org/en/content/articlepdf/2016/TC/C5TC03206G.

[373] Thorsten Schultz, Thomas Lenz, Naresh Kotadiya, Georg Heimel, Gunnar Glasser, Rüdiger Berger, Paul W. M. Blom, Patrick Amsalem, Dago M. de Leeuw, and Norbert Koch. Reliable Work Function Determination of Multicomponent Surfaces and Interfaces: The Role of Electrostatic Potentials in Ultraviolet Photoelectron Spectroscopy. *Adv. Mater. Interfaces*, 4(19):1700324, oct 2017. ISSN 21967350. doi: 10.1002/admi.201700324. URL http://doi.wiley.com/10.1002/admi.201700324.

[374] Harri Aarnio, Parisa Sehati, Slawomir Braun, Mathias Nyman, Michel P. de Jong, Mats Fahlman, and Ronald Österbacka. Spontaneous Charge Transfer and Dipole Formation at the Interface Between P3HT and PCBM. *Adv. Energy Mater.*, 1(5):792–797, oct 2011. ISSN 16146832. doi: 10.1002/aenm.201100074. URL http://doi.wiley.com/10.1002/aenm.201100074.

[375] Soohyung Park, Junkyeong Jeong, Gyeongho Hyun, Minju Kim, Hyunbok Lee, and Yeonjin Yi. The origin of high PCE in PTB7 based photovoltaics: proper charge neutrality level and free energy of charge separation at PTB7/PC71BM interface. *Sci. Rep.*, 6(1):35262, dec 2016. ISSN 2045-2322. doi: 10.1038/srep35262. URL http://www.nature.com/articles/srep35262.

[376] Ze-Lei Guan, Jong Bok Kim, Yueh-Lin Loo, and Antoine Kahn. Electronic structure of the poly(3-hexylthiophene):indene-C60 bisadduct bulk heterojunction. *J. Appl. Phys.*, 110(4):043719, aug 2011. doi: 10.1063/1.3626938. URL http://aip.scitation.org/doi/10.1063/1.3626938.

[377] Umut Aygül, Holger Hintz, Hans-Joachim Egelhaaf, Andreas Distler, Sabine Abb, Heiko Peisert, and Thomas Chassé. Energy Level Alignment of a P3HT/Fullerene Blend during the Initial Steps of Degradation. *J. Phys. Chem. C*, 117(10):4992–4998, mar 2013. ISSN 1932-7447. doi: 10.1021/jp4004642. URL http://pubs.acs.org/doi/10.1021/jp4004642.

[378] Daniel Rauh, Alexander Wagenpfahl, Carsten Deibel, and Vladimir Dyakonov. Relation of open circuit voltage to charge carrier density in organic bulk heterojunction solar cells. *Appl. Phys. Lett.*, 98(13):133301, mar 2011. ISSN 0003-6951. doi: 10.1063/1.3566979. URL http://aip.scitation.org/doi/10.1063/1.3566979.

[379] Ze-Lei Guan, Jong Bok Kim, He Wang, Cherno Jaye, Daniel A. Fischer, Yueh-Lin Loo, and Antoine Kahn. Direct determination of the electronic structure of the poly(3-hexylthiophene):phenyl-[6,6]-C61 butyric acid methyl ester blend. *Org. Electron.*, 11(11):1779–1785, nov 2010. ISSN 1566-1199. doi: 10.1016/J.ORGEL.2010.07.023. URL https://www.sciencedirect.com/science/article/pii/S1566119910002533.

[380] A. Foertig, J. Rauh, V. Dyakonov, and C. Deibel. Shockley equation parameters of P3HT:PCBM solar cells determined by transient techniques. *Phys. Rev. B*, 86 (11):115302, sep 2012. ISSN 1098-0121. doi: 10.1103/PhysRevB.86.115302. URL https://link.aps.org/doi/10.1103/PhysRevB.86.115302.

[381] Wei Ma, Guofang Yang, Kui Jiang, Joshua H. Carpenter, Yang Wu, Xiangyi Meng, Terry McAfee, Jingbo Zhao, Chenhui Zhu, Cheng Wang, Harald Ade, and He Yan. Influence of Processing Parameters and Molecular Weight on the Morphology and Properties of High-Performance PffBT4T-2OD:PC71BM Organic Solar Cells. *Adv. Energy Mater.*, 5(23):1501400, dec 2015. doi: 10.1002/aenm.201501400. URL http://doi.wiley.com/10.1002/aenm.201501400.

[382] Jie Min, Xuechen Jiao, Vito Sgobba, Bin Kan, Thomas Heumüller, Stefanie Rechberger, Erdmann Spiecker, Dirk M. Guldi, Xiangjian Wan, Yongsheng Chen, Harald Ade, and Christoph J. Brabec. High efficiency and stability small molecule solar cells developed by bulk microstructure fine-tuning. *Nano Energy*, 28:241–249, oct 2016. ISSN 2211-2855. doi: 10.1016/J.NANOEN.2016.08.047. URL https://www.sciencedirect.com/science/article/pii/S2211285516303354.

[383] Ning Li, José Darío Perea, Thaer Kassar, Moses Richter, Thomas Heumueller, Gebhard J Matt, Yi Hou, Nusret S Güldal, Haiwei Chen, Shi Chen, Stefan Langner, Marvin Berlinghof, Tobias Unruh, and Christoph J Brabec. Abnormal strong burn-in degradation of highly efficient polymer solar cells caused by spinodal donor-acceptor demixing. *Nat. Commun.*, 8:14541, feb 2017. ISSN 2041-1723. doi: 10.1038/ncomms14541. URL http://www.nature.com/doifinder/10.1038/ncomms14541.

[384] Nakul Jain, Naresh Chandrasekaran, Aditya Sadhanala, Richard H Friend, Christopher R. McNeill, and Dinesh Kabra. Interfacial disorder in efficient polymer solar cells: the impact of donor molecular structure and solvent additives. *J. Mater. Chem. A*, 5(47):24749–24757, 2017. ISSN 2050-7488. doi: 10.1039/C7TA07924A. URL http://xlink.rsc.org/?DOI=C7TA07924A.

[385] Pei Cheng, Rui Wang, Jingshuai Zhu, Wenchao Huang, Sheng-Yung Chang, Lei Meng, Pengyu Sun, Hao-Wen Cheng, Meng Qin, Chenhui Zhu, Xiaowei Zhan, and Yang Yang. Ternary System with Controlled Structure: A New Strategy toward Efficient Organic Photovoltaics. *Adv. Mater.*, 30(8):1705243, feb 2018. ISSN 09359648. doi: 10.1002/adma.201705243. URL http://doi.wiley.com/10.1002/adma.201705243.

[386] Diana Galli, Nicola Gasparini, Michael Forster, Anika Eckert, Christian Widling, Manuela S. Killian, Apostolos Avgeropoulos, Vasilis G. Gregoriou, Ullrich Scherf, Christos L. Chochos, Christoph J. Brabec, and Tayebeh Ameri. Suppressing the Surface Recombination and Tuning the Open-Circuit Voltage of Polymer/Fullerene Solar Cells by Implementing an Aggregative Ternary Compound. *ACS Appl. Mater. Interfaces*, page acsami.8b09174, aug 2018. ISSN 1944-8244. doi: 10.1021/acsami.8b09174. URL http://pubs.acs.org/doi/10.1021/acsami.8b09174.

[387] Xiaozhou Che, Yongxi Li, Yue Qu, and Stephen R. Forrest. High fabrication yield organic tandem photovoltaics combining vacuum- and solution-processed subcells with 15 *Nat. Energy*, 3(5):422–427, may 2018. ISSN 2058-7546. doi: 10.1038/s41560-018-0134-z. URL http://www.nature.com/articles/s41560-018-0134-z.

[388] Björn Lüssem, Chang-Min Keum, Daniel Kasemann, Ben Naab, Zhenan Bao, and Karl Leo. Doped Organic Transistors. *Chem. Rev.*, 116(22):13714–13751, nov 2016. ISSN 0009-2665. doi: 10.1021/acs.chemrev.6b00329. URL http://pubs.acs.org/doi/10.1021/acs.chemrev.6b00329.

[389] Ryo Fujimoto, Yu Yamashita, Shohei Kumagai, Junto Tsurumi, Alexander Hinderhofer, Katharina Broch, Frank Schreiber, Shun Watanabe, and Jun Takeya. Molecular doping in organic semiconductors: fully solution-processed, vacuum-free doping with metal–organic complexes in an orthogonal solvent. *J. Mater. Chem. C*, 5(46):12023–12030, nov 2017. ISSN 2050-7526. doi: 10.1039/C7TC03905K. URL http://xlink.rsc.org/?DOI=C7TC03905K.

[390] Vincent Lami, Yvonne J. Hofstetter, Julian Butscher, and Yana Vaynzof. Origin of open-circuit voltage tuning in ternary organic solar cells. *Prep.*, 2019.

[391] Kion Norrman, Morten V Madsen, Suren A Gevorgyan, and Frederik C Krebs. Degradation Patterns in Water and Oxygen of an Inverted Polymer Solar Cell. *J. Am. Chem. Soc.*, 132(47):16883–16892, dec 2010. ISSN 0002-7863. doi: 10.1021/ja106299g. URL http://pubs.acs.org/doi/abs/10.1021/ja106299g.

[392] Harrison Ka Hin Lee, Andrew M Telford, Jason A. Röhr, Mark F Wyatt, Beth Rice, Jiaying Wu, Alexandre de Castro Maciel, Sachetan M Tuladhar, Emily Speller, James McGettrick, Justin R Searle, Sebastian Pont, Trystan Watson, Thomas Kirchartz, James R Durrant, Wing C Tsoi, Jenny Nelson, and Zhe Li.

The role of fullerenes in the environmental stability of polymer:fullerene solar cells. *Energy & Environ. Sci.*, 11(2):417–428, 2018. ISSN 1754-5692. doi: 10.1039/C7EE02983G. URL http://xlink.rsc.org/?DOI=C7EE02983G.

[393] Julia Schafferhans, Andreas Baumann, Alexander Wagenpfahl, Carsten Deibel, and Vladimir Dyakonov. Oxygen doping of P3HT:PCBM blends: Influence on trap states, charge carrier mobility and solar cell performance. *Org. Electron.*, 11 (10):1693–1700, oct 2010. ISSN 15661199. doi: 10.1016/j.orgel.2010.07.016. URL https://linkinghub.elsevier.com/retrieve/pii/S1566119910002466.

[394] Andreas Weu, Joshua A. Kress, Fabian Paulus, David Becker-Koch, Vincent Lami, Artem A. Bakulin, and Yana Vaynzof. Oxygen-Induced Doping as a Degradation Mechanism in Highly Efficient Organic Solar Cells. *ACS Appl. Energy Mater.*, 2(3):1943–1950, mar 2019. ISSN 2574-0962. doi: 10.1021/acsaem.8b02049. URL http://pubs.acs.org/doi/10.1021/acsaem.8b02049.

[395] Pei Cheng, Cenqi Yan, Yang Wu, Shuixing Dai, Wei Ma, and Xiaowei Zhan. Efficient and stable organic solar cells via a sequential process. *J. Mater. Chem. C*, 4(34):8086–8093, 2016. ISSN 2050-7526. doi: 10.1039/C6TC02338J. URL http://xlink.rsc.org/?DOI=C6TC02338J.

[396] Shun Watanabe, Kazuya Ando, Keehoon Kang, Sebastian Mooser, Yana Vaynzof, Hidekazu Kurebayashi, Eiji Saitoh, and Henning Sirringhaus. Polaron spin current transport in organic semiconductors. *Nat. Phys.*, 10(4):308–313, apr 2014. ISSN 1745-2473. doi: 10.1038/nphys2901. URL http://www.nature.com/articles/nphys2901.

[397] Shu-Jen Wang, Deepak Venkateshvaran, M. R. Mahani, Uday Chopra, Erik R. McNellis, Riccardo Di Pietro, Sam Schott, Angela Wittmann, Guillaume Schweicher, Murat Cubukcu, Keehoon Kang, Remington Carey, Thomas J. Wagner, Janis N. M. Siebrecht, Daniel P. G. H. Wong, Ian E. Jacobs, Razan O. Aboljadayel, Adrian Ionescu, Sergei A. Egorov, Sebastian Mueller, Olga Zadvorna, Piotr Skalski, Cameron Jellett, Mark Little, Adam Marks, Iain McCulloch, Joerg Wunderlich, Jairo Sinova, and Henning Sirringhaus. Long spin diffusion lengths in doped conjugated polymers due to enhanced exchange coupling. *Nat. Electron.*, 2(3):98–107, mar 2019. ISSN 2520-1131. doi: 10.1038/s41928-019-0222-5. URL http://www.nature.com/articles/s41928-019-0222-5.

[398] Rie Nakanishi, Ayumi Nogimura, Ritsuko Eguchi, and Kaname Kanai. Electronic structure of fullerene derivatives in organic photovoltaics. *Org. Electron.*, 15(11):2912–2921, nov 2014. ISSN 15661199. doi: 10.1016/j.orgel.2014.08.013. URL https://linkinghub.elsevier.com/retrieve/pii/S1566119914003310.

[399] Jianyu Yuan, Michael J. Ford, Yalong Xu, Yannan Zhang, Guillermo C. Bazan, and Wanli Ma. Improved Tandem All-Polymer Solar Cells Performance by Using Spectrally Matched Subcells. *Adv. Energy Mater.*, 8(14):1703291, may 2018.

ISSN 16146832. doi: 10.1002/aenm.201703291. URL http://doi.wiley.com/10.1002/aenm.201703291.

[400] Fei Guo, Ning Li, Frank W. Fecher, Nicola Gasparini, Cesar Omar Ramirez Quiroz, Carina Bronnbauer, Yi Hou, Vuk V. Radmilović, Velimir R. Radmilović, Erdmann Spiecker, Karen Forberich, and Christoph J. Brabec. A generic concept to overcome bandgap limitations for designing highly efficient multi-junction photovoltaic cells. *Nat. Commun.*, 6(1):7730, nov 2015. ISSN 2041-1723. doi: 10.1038/ncomms8730. URL http://www.nature.com/articles/ncomms8730.

[401] Nicola Gasparini, Alberto Salleo, Iain McCulloch, and Derya Baran. The role of the third component in ternary organic solar cells. *Nat. Rev. Mater.*, 4(4):229–242, 2019. ISSN 20588437. doi: 10.1038/s41578-019-0093-4. URL http://dx.doi.org/10.1038/s41578-019-0093-4.

[402] Tayebeh Ameri, Parisa Khoram, Jie Min, and Christoph J. Brabec. Organic Ternary Solar Cells: A Review. *Adv. Mater.*, 25(31):4245–4266, aug 2013. ISSN 09359648. doi: 10.1002/adma.201300623. URL http://doi.wiley.com/10.1002/adma.201300623.

[403] Nicola Gasparini, Xuechen Jiao, Thomas Heumueller, Derya Baran, Gebhard J. Matt, Stefanie Fladischer, Erdmann Spiecker, Harald Ade, Christoph J. Brabec, and Tayebeh Ameri. Designing ternary blend bulk heterojunction solar cells with reduced carrier recombination and a fill factor of 77 *Nat. Energy*, 1(9):16118, sep 2016. ISSN 2058-7546. doi: 10.1038/nenergy.2016.118. URL http://www.nature.com/articles/nenergy2016118.

[404] N. Felekidis, E. Wang, and M. Kemerink. Open circuit voltage and efficiency in ternary organic photovoltaic blends. *Energy Environ. Sci.*, 9(1):257–266, jan 2016. ISSN 1754-5692. doi: 10.1039/C5EE03095A. URL http://xlink.rsc.org/?DOI=C5EE03095A.

[405] Nikolaos Felekidis, Armantas Melianas, and Martijn Kemerink. Design Rule for Improved Open-Circuit Voltage in Binary and Ternary Organic Solar Cells. *ACS Appl. Mater. & Interfaces*, 9(42):37070–37077, oct 2017. ISSN 1944-8244. doi: 10.1021/acsami.7b08276. URL http://pubs.acs.org/doi/10.1021/acsami.7b08276.

[406] Xiaoling Ma, Yang Mi, Fujun Zhang, Qiaoshi An, Miao Zhang, Zhenghao Hu, Xinfeng Liu, Jian Zhang, and Weihua Tang. Efficient Ternary Polymer Solar Cells with Two Well-Compatible Donors and One Ultranarrow Bandgap Nonfullerene Acceptor. *Adv. Energy Mater.*, 8(11):1702854, apr 2018. ISSN 16146832. doi: 10.1002/aenm.201702854. URL http://doi.wiley.com/10.1002/aenm.201702854.

[407] Yuhang Liu, Cheng Mu, Kui Jiang, Jingbo Zhao, Yunke Li, Lu Zhang, Zhengke Li, Joshua Yuk Lin Lai, Huawei Hu, Tingxuan Ma, Rongrong Hu, Demei Yu, Xuhui Huang, Ben Zhong Tang, and He Yan. A Tetraphenylethylene Core-Based

3D Structure Small Molecular Acceptor Enabling Efficient Non-Fullerene Organic Solar Cells. *Adv. Mater.*, 27:1015–1020, 2015. ISSN 09359648. doi: 10.1002/adma.201404152. URL http://doi.wiley.com/10.1002/adma.201404152.

[408] Yuanpeng Xie, Tengfei Li, Jing Guo, Pengqing Bi, Xiaonan Xue, Hwa Sook Ryu, Yunhao Cai, Jie Min, Lijun Huo, Xiaotao Hao, Han Young Woo, Xiaowei Zhan, and Yanming Sun. Ternary Organic Solar Cells with Small Nonradiative Recombination Loss. *ACS Energy Lett.*, 4(5):1196–1203, may 2019. ISSN 2380-8195. doi: 10.1021/acsenergylett.9b00681. URL http://pubs.acs.org/doi/10.1021/acsenergylett.9b00681.

[409] Xin Song, Nicola Gasparini, Masrur Morshed Nahid, Sri Harish Kumar Paleti, Jin-Liang Wang, Harald Ade, and Derya Baran. Dual Sensitizer and Processing-Aid Behavior of Donor Enables Efficient Ternary Organic Solar Cells. *Joule*, 3 (3):846–857, mar 2019. ISSN 25424351. doi: 10.1016/j.joule.2019.01.009. URL https://linkinghub.elsevier.com/retrieve/pii/S2542435119300388.

[410] Robert A. Street, Daniel Davies, Petr P. Khlyabich, Beate Burkhart, and Barry C. Thompson. Origin of the Tunable Open-Circuit Voltage in Ternary Blend Bulk Heterojunction Organic Solar Cells. *J. Am. Chem. Soc.*, 135(3):986–989, jan 2013. ISSN 0002-7863. doi: 10.1021/ja3112143. URL http://pubs.acs.org/doi/10.1021/ja3112143.

[411] Sonya A. Mollinger, Koen Vandewal, and Alberto Salleo. Microstructural and Electronic Origins of Open-Circuit Voltage Tuning in Organic Solar Cells Based on Ternary Blends. *Adv. Energy Mater.*, 5(23):1501335, dec 2015. ISSN 16146832. doi: 10.1002/aenm.201501335. URL http://doi.wiley.com/10.1002/aenm.201501335.

[412] Luyao Lu, Tao Xu, Wei Chen, Erik S. Landry, and Luping Yu. Ternary blend polymer solar cells with enhanced power conversion efficiency. *Nat. Photonics*, 8(9):716–722, sep 2014. ISSN 1749-4885. doi: 10.1038/nphoton.2014.172. URL http://www.nature.com/articles/nphoton.2014.172.

[413] Luyao Lu, Wei Chen, Tao Xu, and Luping Yu. High-performance ternary blend polymer solar cells involving both energy transfer and hole relay processes. *Nat. Commun.*, 6(1):7327, nov 2015. ISSN 2041-1723. doi: 10.1038/ncomms8327. URL http://www.nature.com/articles/ncomms8327.

[414] Markus Koppe, Hans-Joachim Egelhaaf, Ewan Clodic, Mauro Morana, Larry Lüer, Anna Troeger, Vito Sgobba, Dirk M. Guldi, Tayebeh Ameri, and Christoph J. Brabec. Charge Carrier Dynamics in a Ternary Bulk Heterojunction System Consisting of P3HT, Fullerene, and a Low Bandgap Polymer. *Adv. Energy Mater.*, 3(7):949–958, jul 2013. ISSN 16146832. doi: 10.1002/aenm.201201076. URL http://doi.wiley.com/10.1002/aenm.201201076.

[415] Vinay Gupta, Vishal Bharti, Mahesh Kumar, Suresh Chand, and Alan J. Heeger. Polymer-Polymer Förster Resonance Energy Transfer Significantly Boosts the

Power Conversion Efficiency of Bulk-Heterojunction Solar Cells. *Adv. Mater.*, 27(30):4398–4404, aug 2015. ISSN 09359648. doi: 10.1002/adma.201501275. URL http://doi.wiley.com/10.1002/adma.201501275.

[416] Wei-Long Xu, Bo Wu, Fei Zheng, Xiao-Yu Yang, Han-Dong Jin, Furong Zhu, and Xiao-Tao Hao. Förster Resonance Energy Transfer and Energy Cascade in Broadband Photodetectors with Ternary Polymer Bulk Heterojunction. *J. Phys. Chem. C*, 119(38):21913–21920, sep 2015. ISSN 1932-7447. doi: 10.1021/acs.jpcc.5b06931. URL http://pubs.acs.org/doi/10.1021/acs.jpcc.5b06931.

[417] Petr P. Khlyabich, Beate Burkhart, and Barry C. Thompson. Efficient Ternary Blend Bulk Heterojunction Solar Cells with Tunable Open-Circuit Voltage. *J. Am. Chem. Soc.*, 133(37):14534–14537, sep 2011. ISSN 0002-7863. doi: 10.1021/ja205977z. URL https://pubs.acs.org/doi/10.1021/ja205977z.

[418] Jianqi Zhang, Yajie Zhang, Jin Fang, Kun Lu, Zaiyu Wang, Wei Ma, and Zhixiang Wei. Conjugated Polymer–Small Molecule Alloy Leads to High Efficient Ternary Organic Solar Cells. *J. Am. Chem. Soc.*, 137(25):8176–8183, jul 2015. ISSN 0002-7863. doi: 10.1021/jacs.5b03449. URL http://pubs.acs.org/doi/10.1021/jacs.5b03449.

[419] Pei Cheng, Cenqi Yan, Yang Wu, Jiayu Wang, Meng Qin, Qiaoshi An, Jiamin Cao, Lijun Huo, Fujun Zhang, Liming Ding, Yanming Sun, Wei Ma, and Xiaowei Zhan. Alloy Acceptor: Superior Alternative to PCBM toward Efficient and Stable Organic Solar Cells. *Adv. Mater.*, 28(36):8021–8028, sep 2016. ISSN 09359648. doi: 10.1002/adma.201602067. URL http://doi.wiley.com/10.1002/adma.201602067.

[420] Pei Cheng, Yongfang Li, and Xiaowei Zhan. Efficient ternary blend polymer solar cells with indene-C60 bisadduct as an electron-cascade acceptor. *Energy Environ. Sci.*, 7(6):2005, may 2014. ISSN 1754-5692. doi: 10.1039/c3ee44202k. URL http://xlink.rsc.org/?DOI=c3ee44202k.

Danksagung/Acknowledgements

Zum Schluss möchte ich mich bei all jenen bedanken, die mich auf dem Weg zum Abschluss dieser Dissertation unterstützt haben:

I want to thank PROF. DR. YANA VAYNZOF for the possibility to join her group at the Centre for Advanced Materials for this challenging project, summarized in this work. I would also like to thank her for her faith in me, mostly expressed with the words: "Vincent, you can do it", as well as the fruitful conversations and discussions. I am also grateful for the possibility of a research stay abroad and her advices for my future career.

PROF. DR. ANNEMARIE PUCCI möchte ich danken für die freundliche Übernahme des Zweitgutachtens und den schnellen E-Mail-Austausch trotz der Urlaubszeit.

PROF. DR. UWE BUNZ danke ich für den Zugang zu Laboren und Messgeräten.

I want to thank PROF. DR. NIR TESSLER for the possibility to visit his research group in Haifa and for the warm welcome during my stay. Special thanks to HIMANSHU SHEKHAR, GIL SHELEG, and DAN LIRAZ for the extremely interesting conversations and for showing me around in Haifa.

Ich möchte mich bei der HGSFP für die Möglichkeit bedanken am Winterschool und an den HGSFP Graduate Days teilnehmen zu dürfen und für die hilfreichen Informationen bezüglich der Abgabe meiner Arbeit.

Ich bedanke mich bei allen jetzigen und ehemaligen Mitgliedern der AG Vaynzof für die unvergessliche Zeit in den letzten Jahren. Insbesondere möchte ich mich bei DAVID LEIBOLD bedanken für seinen Prinzenrollen-Vorrat, die sehr angenehme Zusammenarbeit und die Diskussionen über nicht-fullerenen Akzeptoren. Des Weiteren möchte ich mich bei den besten Bürokollegen aller Zeiten bedanken, nämlich DOLLMANN, PAUL, ALEX B., DANIEL, LUKAS, ANDRES, JONAS und FRIGYES. Ein besonderer Dank geht natürlich an PAUL und ALEX B., mit denen es nie langweilig wurde, an DANIEL, mit dem ich die Schachpartien eindeutig vermissen werde und an FRIGYES, der mein letztes Jahr durch "Obstsalat mit Asanas" bereichert hat.

Ich möchte mich auch bei all jenen bedanken, die meine Arbeit Korrektur gelesen haben, insbesondere bei DR. ALEX TAYLOR und DR. KATELYN GOETZ, denen ich dafür mindestens ein Bier schulde. Ich möchte mich aber genauso bei DBK, JOSH, DR. FABIAN PAULUS, ANDI, FRIGYES, LUKI, JANNIS, JOHANNES, ÁKOS und ganz besonders bei DAVID L., YVONNE und SIMON REIFEGERSTE bedanken, die mir ihre Korrekturen immer (gefühlt) am gleichen Tag wieder schickten.

Ich möchte mich ganz herzlich bei ANNA bedanken, die auch in den stressigsten Zeiten zu mir stand! Köszönöm ÁKOSnak, akivel sikerült közösen megfejteni a kávéfogyasztás és az arduínó programozás rejtéjeit. Végül, de nem utolsó sorban szeretnék köszönetet mondani szüleimnek, elsősorban édesanyámnak, aki mindig támogatott. Nélküled nem sikerült volna!